THERMAL ENERGY STORAGE USING MOLTEN SALTS CONTAINING NANOPARTICLES

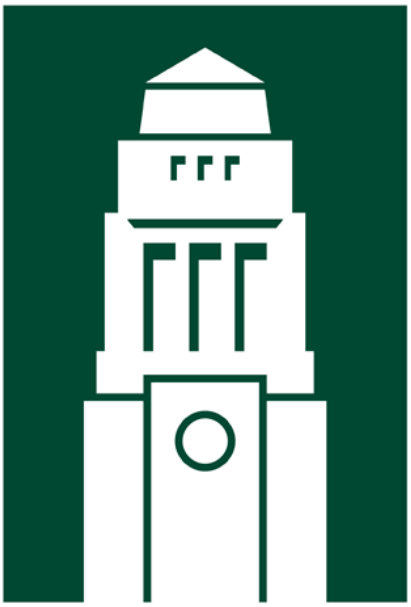

Bashar Hamad Mahmoud

The University of Leeds

School of Chemical and Process Engineering

Submitted in accordance with the requirements for the degree of

Doctor of Philosophy

December 2019

DECLARATION

The candidate confirms that the work submitted is his own, except where work which has formed part of jointly authored publications has been included. The contribution of the candidate and the other authors to this work has been explicitly indicated below. The candidate confirms that appropriate credit has been given within the thesis where reference has been made to the work of others.

Results chapter 1:

Journal paper - I&EC Research (ACS Publications) ***2019****, An acoustic method for determination of thermal conductivity of nanofluids - Mahmoud B.H.; Rice H.P.; Mortimer L.F.; Fairweather M.; Peakall J.; Harbottle D.*

Results chapter 2:

Journal paper - J. Phys. D: Appl. Phys. (IOP Publishing) ***2019****, Multiscale modelling of ceramic nanoparticle interactions and their influence on the thermal conductivity of nanofluids. Mahmoud B.H.; Mortimer L.F.; Fairweather M.; Rice H.P.; Peakall J.; Harbottle D.*

Conference proceedings - ESCAPE-29 ***2019****, Thermal conductivity prediction of molten salt-based nanofluids for energy storage applications. Mahmoud B.H.; Mortimer L.F.; Fairweather M.; Rice H.P.; Peakall J.; Harbottle D.*

Conference proceedings - ESCAPE-28 ***2018****, Prediction of stability and thermal conductivity of nanofluids for thermal energy storage applications. Mahmoud B.H.; Fairweather M.; Mortimer L.F.; Peakall J.; Rice H.P.; Harbottle D.*

Results chapter 3:

Conference proceedings - ESCAPE-29 ***2019****, Nanoparticle behaviour in multiphase turbulent channel flow. Mahmoud B.H; Mortimer L.F; Fairweather M.; Rice H.P; Peakall J.; Harbottle D.*

Conference proceedings - PARTICLES ***2019****, Turbulent heat transfer in nanoparticulate multiphase channel flows with a high Prandtl number molten salt fluid. Mahmoud B.H.; Mortimer L.F.; Colombo M.; Fairweather M.; Peakall J.; Rice H.P.; Harbottle D.*

For all jointly authored publications, other authors contributed to biweekly supervisory meetings, sharing ideas and offering guidance, as well as proof reading the papers. The experimental work, simulation and analysis work, as well as writing of the papers, is attributed to myself.

ACKNOWLEDGEMENTS

The author would like to acknowledge the guidance and help of the several individuals who in one way or another have contributed and extended their valuable assistance in the preparation and completion of this study. Therefore he would like to start by thanking his principle supervisor Prof. Michael Fairweather and co-supervisors Prof. Jeff Peakall and Prof. David Harbottle for their insightful discussions, understanding and encouragement, which have really added considerably to his graduate experience. He greatly appreciates their endless advice, motivation and guidance and that they have allowed him to develop his own research interests. It is doubtful that he will ever be able to convey his appreciation fully, but he owes them his eternal gratitude.

The author also recognizes that this research would not have been possible without the financial assistance of the Kuwait Institute for Scientific Research (KISR) and would like to express his sincere gratitude to them and to the Kuwaiti government as a whole for providing him with such a spectacular opportunity.

He is particularly indebted to his close colleagues Dr. Hugh Rice, Dr. Lee Mortimer and Dr. Marco Colombo whose ideas have contributed in filling up these pages and without whom motivation and help it would not have been possible to reach this level. It was with their assistance that the author has developed a focus and became more knowledgeable in the subject. Hugh provided the author with the experimental background and the knowhow of the acoustic technique development. While Lee and Marco provided him with the technical support, computational experience and the numerical codes required for this work and have both now become more of close friends than just tutors.

Furthermore, a special word of thanks goes on to his dear parents who have both supported him throughout his PhD. Last but not least, the author would like to show his gratitude to his dearest family, for their love and encouragement. Particularly, he would like to acknowledge his wife Mona for taking care of their children and for having to wait patiently for him to finish the writing of this thesis. He is confident that none of this could have happened without the endless emotional support of all the family members.

ABSTRACT

The growing interest in energy efficient and sustainable technologies has created significant demand for novel heat transfer and thermal energy storage materials, such as nanofluids. This research is therefore aimed at developing novel types of hybrid nanofluids that can be used as heat transfer fluid and thermal energy storage medium for solar power plants. The importance of nanoscience cannot be underestimated here, since the motivation for the manipulation, through nanoparticle addition, of the properties of existing thermal fluids (e.g. water and molten salt) arises from their poor thermal properties which represents a major limitation to the development of more energy-efficient processes. Special consideration is given to assess the stability of embedded nanoparticles in the base-fluid under different operating conditions, using appropriate ultrasonic diagnostic techniques (acoustic methods). This innovative approach allowed *in situ* high temperature ultrasonic probes to be used to measure the changes of thermophysical properties of nanofluids via speed of sound variations.

The work has also focused on combining the novel experimental development with the existing computational power to investigate the role of particle dynamic forces, mass and heat transfer of nanofluids in three-dimensional flows, using an advanced computational modelling approach (i.e. direct numerical simulation coupled to Lagrangian particle tracking). The advantage of the model developed is its ability to study in detail phenomena such as interparticle collisions, agglomeration, turbophoresis and thermophoresis, with the approach also of value in investigations of the long-term thermal stability of nanoparticle dispersions which as yet has not been considered in detail. The model has been applied to a stagnant nanoparticle dispersed fluid, as well as a turbulent channel flow with both non-isothermal and isothermal conditions.

The results of both computational and experimental investigations indicate that these effects are found to play a key role in the thermal behaviour of the nanofluid at various particle concentrations, with predictions in agreement with theoretical and experimental results obtained in similar studies. The outcome of this study allowed conclusions to be reached regarding the stability and heat transfer characteristics of nanofluids and their implications for thermal energy storage systems.

CONTENTS

List of Tables

List of Figures

NOMENCLATURE

Roman symbols:

A	Hamaker constant	J
a	Radius of a sphere	m
a_m	Fraction melted	kg
C	Velocity of a sound wave, also general concentration	m s^{-1}
C_A	Constants determined from experiment	-
C_D, C_L	Drag and lift coefficient	-
C_p	Specific heat (isobaric)	J kg^{-1} K^{-1}
$\overline{C_p}$	Average specific heat	J kg^{-1} K^{-1}
$\overline{C_{p_s}}$	Average specific heat of solid	J kg^{-1} K^{-1}
$\overline{C_{p_s}}$	Average specific heat of liquid	J kg^{-1} K^{-1}
C_v	Specific heat (isochoric)	J kg^{-1} K^{-1}
C_0	Mean initial concentration	%
d_1	Oscillatory period	m
d_2	Characteristic decay length	m
d_P	Particle diameter	m
d_q	Adiabatic pathway	m
e	Elementary electric charge	±1
F	General force vector	N
$\boldsymbol{F}_i^B$	The stochastic Brownian motion force	N
$\boldsymbol{F}_i^c$	The particle soft-sphere contact force	N
$\boldsymbol{F}_i^e$	The electric double layer repulsive force	N
$\boldsymbol{F}_i^f$	The fluid viscous drag force	N
$\boldsymbol{F}_i^v$	The van der Waals attractive force	N
$\boldsymbol{fc}$	Cell-dependent to accounts for momentum exchange	N
f^e	Repulsive electric double layer force	N
f^v	Attractive van der Waals force	N
f_D	Drag force empirical correlation function	N
f_L	Shear lift force empirical correlation function	N
g	Acceleration due to gravity vector	m s^{-2}

H	Interparticle distance (surface to surface)	m
h	Distance	M
h_{fus}	Heat of fusion	J kg^{-1}
h_m	Heat of fusion per unit mass	J kg^{-1}
j	Constituent phase	-
k	Thermal conductivity	W m^{-1} K^{-1}
k_{ag}	Thermal conductivity of the particle aggregates	W m^{-1} K^{-1}
k_{bf}	Thermal conductivity of the base fluid	W m^{-1} K^{-1}
k_{eff}	Effective thermal conductivity	W m^{-1} K^{-1}
k_L	Thermal conductivity, liquid	W m^{-1} K^{-1}
k_B	Boltzmann's constant	-
L	General characteristic length scale	J K^{-1}
l	General length, and eddy length scale	m
m	Mass, also constants determined from experiment	kg
m_p	Mass of particle	kg
N_P	Total number of particles	-
n	The number density of electrolyte ions	-
P_0	Particle osmotic pressure	Pa
Pe	Péclet number	-
Pr	Prandtl number	-
p	General pressure	Pa
Q_s	Quantity of sensible heat stored	J kg^{-1} K^{-1}
Q_l	Quantity of latent heat stored	J kg^{-1} K^{-1}
q_w	Wall heat flux	W m^{-2}
q_{vol}	Volumetric heat source term	W m^{-3}
R_a	Radius of gyration	m
Re	General Reynolds number	-
Re_B	Bulk Reynolds number	-
Re_P	Particle Reynolds number	-
Re_τ	Reynolds number based on shear flow scale	-
S	Entropy	J K^{-1}
St	Particle Stokes number	-

T	Temperature	K
T_2	Final temperature	K
T_{BF}	Base fluid temperature	K
T_i	Initial temperature,	K
T_m	Melting temperature	K
T_w	Wall temperature	K
T_τ	Friction temperature	K
$T*$	Instantaneous temperature	K
t	Time	s
t_F^*	Fluid timestep	s
t^*	Time in bulk units	s
U	General characteristic velocity scale	m s^{-1}
$\boldsymbol{u}^*$	Fluid velocity	m s^{-1}
$\boldsymbol{u}_F$	Instantaneous fluid velocity at particle location	m s^{-1}
$\boldsymbol{u}_{NP}$	Nanoparticle velocity vector	m s^{-1}
$\boldsymbol{u}_S$	Flow velocity relative to that of the particle	m s^{-1}
u_{NP}	Streamwise (x) instantaneous particle velocity component	-
u'_{rms}	Root mean square fluid velocity fluctuation	m s^{-1}
u_η	Kolmogorov velocity scale	-
u_τ	Shear velocity	m s^{-1}
V	General volume	m^{-3}
V_F	Fluid volume	m^{-3}
v	The molecular volume of the liquid	m^{-3}
ν_F	Fluid kinematic viscosity	m^2 s^{-1}
v_{NP}	Wall-normal (y) instantaneous particle velocity component	-
w_{NP}	Spanwise (z) instantaneous particle velocity component	-
x	General position vector	-
x^*	Streamwise direction	-
x^+	General position vector in shear units	-
y	Wall-normal direction	-
z	The ion valence or concentration of ions	-
z^*	Spanwise direction	-

Greek letters:

α	Thermal diffusivity	$m^2\ s^{-1}$
ε_0	Permittivity of a vacuum	$F\ m^{-1}$
ε_r	Relative permittivity of the medium	$F\ m^{-1}$
δ	Channel half-height	m
σ	Diameter of the smaller fluid hard spheres	m
α_p	Coefficient of thermal expansion (at constant pressure)	-
θ	General angle	°
Θ	Polarizability factor	$C\ m^2\ V^{-1}$
η	Kolmogorov length scale	-
ξ	Coefficient of Stokes drag for a sphere	-
ζ	Zeta potential of the nanoparticles	V
Π^{os}	Oscillatory structural force	N
Π^{el}	Electric double layer repulsive force equivalent to f^e	N
Π^{vW}	van der Waals attractive force, equivalent to f^v	N
ϕ	Particulate volume fraction	%
ϕ_{ag}	Aggregated particles volume fraction	%
φ	Volume fraction of the small fluid spheres	%
κ	Inverse Debye length	m
κ_S	Adiabatic compressibility	Pa^{-1}
κ_T	Isothermal compressibility	Pa^{-1}
γ	Heat capacity ratio (also known as the isentropic index)	-
μ	General viscosity	$kg\ m^{-1}\ s^{-1}$
μ_F	Fluid dynamic viscosity	$kg\ m^{-1}\ s^{-1}$
ρ	General density	$kg\ m^{-3}$
ρ_{BF}, ρ_{NP}	Fluid and particle phase density	$kg\ m^{-3}$
ρ_L, ρ_F	Liquid or fluid density	$kg\ m^{-3}$
ρ_p	Particle density	$kg\ m^{-3}$
ρ_s	Particle number density of the small fluid spheres	$kg\ m^{-3}$
$\boldsymbol{\tau}^*$	Viscous deviatoric stress tensor for a Newtonian fluid	-
τ_F	Fluid time scale	s

τ_P	Particle relaxation time scale	s
τ_η	Kolmogorov time scale	s
τ_W	Mean wall shear stress	Pa

Chemical Compounds:

Al_2O_3	Aluminium oxide
Ag	Silver
Au	Gold
Cu	Copper
CuO	Copper oxide
Fe_2O_2	Ferrous Oxide
HCl	Hydrochloric acid
K^+	Potassium
KNO_3	Potassium Nitrate
Na^+	Sodium
NO_3^-	Nitrate
$NaNO_2$	Sodium nitrite
$NaNO_3$	Sodium nitrate
NaOH	Sodium hydroxide
SiO_2	Silicon dioxide
Ti	Titanium
TiO_2	Titanium dioxide
ZnO	Zinc oxide

LIST OF ABBREVIATIONS AND ACRONYMS

Acronyms:

Symbol	Definition
AFM	Atomic force microscopy
BR	Buffer rod
CFD	Computational fluid dynamics
CNT	Carbon nanotubes
CSP	Concentrated solar power
DIW	De-ionized water
DLS	Dynamic light scattering
DLVO	Theory after Derjaguin & Landau, and Verwey & Overbeek
DNS	Direct numerical simulation
DSC	Differential scanning calorimeter
ECAH	Epstein-Carhart-Allegra-Hawley theory
EDL	Electric double layer
EDS	Energy-dispersive x-ray spectroscopy
EG	Ethylene glycol
ELS	Electrophoretic light scattering
ENG-TSA	Expanded natural graphite treated with sulfuric acid
GNF	Generalised Newtonian fluid
HTF	Heat transfer fluid
HTS	Heat transfer salt
HWA	Hot-wire anemometry
KISR	Kuwait Institute for Scientific Research
LCOE	Levelized cost of electricity
LFA	Laser flash analyzer
LPCS	Lithium and Potassium Carbonate salt
LPT	Lagrangian particle tracking / tracker
LTMS	Low temperature molten salt
MDS	Molecular dynamic simulation
M	Mole, for molarity in chemistry

MS	Molten salt
MSR	Molten salt reactor
Nek5000	Scalable high-order solver for computational fluid dynamics
NHTF	Nano-Heat-Transfer-Fluid
NP	Nanoparticle
NS	Navier-Stokes
NTA	Nanoparticle tracking analysis
PB	Power block, used for power generation
PCM	Phase change materials
RET	Renewable energy technologies
RMS	Root mean square
SCAPE	School of Chemical and Process Engineering
SEM	Scanning/Scattered electron microscopy, also Spectral element method
SOS	Speed of sound
SS	Solar Salt: binary nitrate mixture ($NaNO_3$:KNO_3, 60:40 wt.%)
TEM	Transmission electron microscopy
TES	Thermal energy storage
TGA	Thermogravimetric analysis
THW	Transient hot wire
TNT	Titanate nanotube
TSPTT	thermo-solar parabolic trough technology
UDVP	Ultrasonic Doppler velocity profiler
VDV	van der Waals

1 INTRODUCTION

1.1 Background

The reality of present and growing future energy shortage has stimulated intensive and wide-ranging development of so-called renewable energy sources, such as: solar, wind and biomass. However, the results of various techno-economic analyses[1] show that these sources may offer promise only if coupled with efficient and reliable storage options. Energy storage, and in particular thermal energy storage, has therefore received increased attention in the last few decades. Enormous interest in solar heating and molten salt heat storage technologies started primarily during the energy crisis of the early 1970's. From that time onwards the research and development of heat storage technologies became a significant part of the global solar energy programme[2].

Energy storage, in general, enables renewable power plants to have stable and non-dispatchable power deliveries with less need for any backup fossil fuel provision, for example as in burning natural gas. The use of energy storage could also improve the performance of these plants by smoothing the supply and increasing its reliability, and hence maximising the plant utilisation and efficiency. This, in turn, allows the generation of energy at lower operating costs.

Thermal energy has been the heart of the entire energy chain and, for decades, it has provided a link between the primary and secondary sources of energy. Thermal energy storage (TES) is one of these fast developing technologies that has the potential of maximising the utilisation of alternative energy and has become a key component of the global energy mix[3]. The concept of TES itself is not new, and it has been in use for centuries. It simply works by storing energy through a heating or cooling medium. The stored energy can then be released as needed for power and steam generation applications.

1.2 Overview of Kuwait's solar thermal energy storage plant

Developing efficient and more economical storage methods is as important as developing new sources of energy. The consideration of thermal energy storage, in particular, is expected to increase further in the next few decades, especially after reaching universal agreement on climate change (known as the Paris deal, 12 December 2015)[4]. In this agreement 195 Nations reached a landmark consensus that will, for the first time, commit

these nations to lowering planet-warming greenhouse gas emissions by about a half as is necessary to stave off an increase in atmospheric temperatures of 2°C[4]. This decision was taken to resolve the most crucial problem on earth that is climate change. In another words, to achieve the long-term goal of decarbonising the global economy before the end of the current century, phasing out the use of fossil fuels must now be initiated.

Kuwait as one of many other oil and gas producing countries decided to take the necessary steps towards reducing the demands on conventional energy sources. This is what the Renewable Energy Technologies (RET) programme of the Kuwait Institute for Scientific Research (KISR) is focussed on. One of the long-term objectives of this programme is to expand the range of energy resources, considering that a gradual move towards renewable energy would lower planet-warming greenhouse gas emissions and preserve oil reserves for the future. This would also help to safeguard Kuwait's energy supply prospects and fulfil its strategy of reducing the economic risk of heavy reliance on a single source of energy[5].

The Kuwait Institute for Scientific Research is now in the process of constructing two Concentrated Solar Power (CSP) plants, as part of the RET programme. The proposed 10 MW-direct and 50 MW-indirect CSP plants will be engineered by CHIYODA Corporation and TSK FLAGSOL, respectively. Both plants will use thermo-solar parabolic trough technology (TSPTT) with large thermal energy storage facilities (two large tanks capable of storing about 1,200 MWh_t energy in the form of molten salt). This storage installation will be sized to allow the plant to run at its full capacity for up to eight hours after sunset. In addition, the plant sites were explicitly selected due to their high proportions of Direct Normal Irradiance, and hence will be located in the western part of the country, as part of a mega project site known as 'Shagaya Renewable Park'[5]. The main purpose of building the plants is to enable Kuwait to assess the performance of this new technology under local climate conditions. In effect, investment in renewable technologies would benefit both Kuwait's passion for science in the service of society, and boosting the national economy by creating new solar companies and job opportunities.

In general, the intention of integrating the CSP plant with a TES unit is to permit the production of electricity during sunshine hours. In such a plant it is possible to generate electrical energy and store thermal energy at the same time. For that reason, the additional heat duty collected at the solar field is transferred via a thermal-fluid to the TES medium.

This heat is then used to produce electricity after sunset or in cloudy or even during dusty days, as often occurs in Kuwait. There are two types of CSP-TES arrangement's, known as 'indirect' and 'direct' systems, as shown in Figure 1. The similarities between the two arrangements are that they are both equipped with an auxiliary warm-up system to keep the minimum temperature required by the fluids, thus avoiding any freezing of salt and HTF (thermal oil) when energy is not produced.

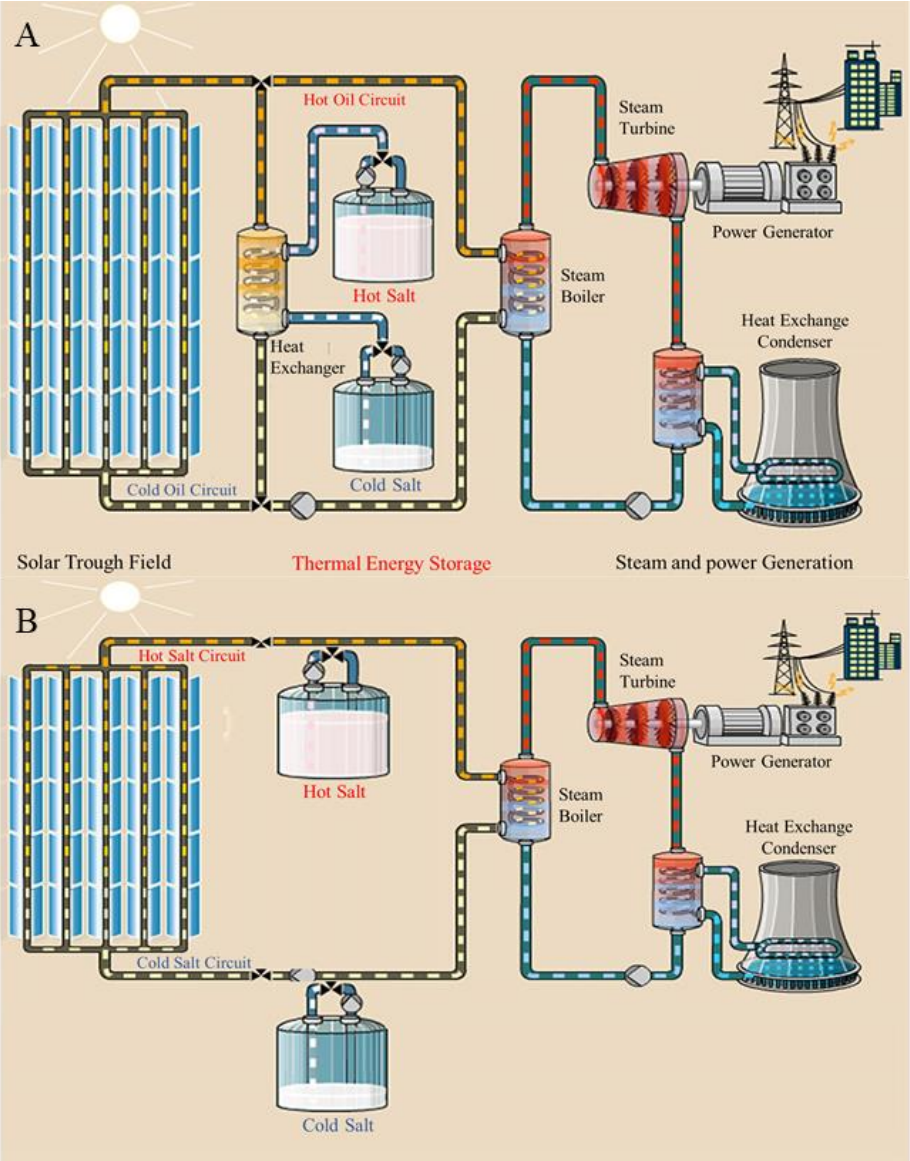

Figure 1. Concentrating solar power plant configurations with: A) Indirect, versus B) Direct heat storage systems. [Figure adapted from[6]].

The difference between the two is that an 'indirect' system consists of a cold storage tank, hot storage tank, two circulation pumps and an 'oil-to-salt heat exchanger'. The HTF oil cools from a nominal inlet temperature of 390^{o}C to an outlet temperature of about 298^{o}C. Nitrate salt from the cold storage tank flows in a counter-current arrangement through the

heat exchanger. The salt is heated from an inlet temperature of 290^{o}C to an outlet temperature of 384^{o}C, and is then stored in the hot storage tank. During a discharge cycle, this process is reversed in the oil-to-salt heat exchanger. Heat is transferred from the salt to the oil to provide thermal energy from the steam generator. The solar radiation from the field is carried to the thermal storage and steam generator system (Power Block, PB) back and forth by thermal oil. In 'direct' CSP arrangements, liquid salt leverages both the collection of energy and storage mechanisms, while still separating energy collection from electricity generation.

As can be seen in Figure 1, the salt flows from the solar field through the TES tanks and PB, where superheated steam is produced at the 'water-to-salt heat exchanger'. With this arrangement, the solar radiation is collected and concentrated in the solar field and turned directly into electricity. The main advantage of this arrangement can be seen in higher plant efficiency, as MS is an ideal heat capture medium capable of operating at a wide temperature range (250^{o}C to 550^{o}C). Nevertheless, the challenge of dealing with huge quantities of salts (storage tanks containing more than 31,000 tons of salt), together with extensive heat exchangers, piping and receiver networks filled with liquid salt, means that there are many difficulties to overcome, the major issue being the needed development of a reliable medium with less potential for freezing and decomposing, hence eliminating any probable risks within the TES network.

It is known that the use of molten salt for TES applications is still facing some scientific and technological challenges, which triggered this research initiative to address them. For instance, one of the downsides (of binary nitrate salt $NaNO_3$:KNO_3 in 60:40 wt. %) is its high solidification temperature, since it crystallizes at $T_{crys.}$ ~ 238°C and solidifies at $T_{frez.}$ ~ 221°C (freezing point)[7]. The associated risk of salt freezing is of major importance when it comes to plant operation. As a result, special consideration must be given to the possible operational difficulties associated with this phenomenon, and its negative consequences on plant continuity[8]. Currently, all CSP plants are equipped with a molten salt freezing protection system (extensive heat tracing around all molten salt equipment including; piping, collectors and receivers). However, running and maintaining such a system is an added cost to this technology. The second downside can be seen in salt disintegration where some studies have demonstrated that aged salts tend to decompose, as reported by Kruizenga et al.[9]. However, this problem is most evident when operating at elevated temperatures > 560°C.

These issues have encouraged many researchers to explore potential opportunities, and to find more innovative forms of salt storage materials with optimized thermo-physical properties. The type of improvements include: the enhancement of specific heat capacities; reduced melting temperature; improved thermal conductivity; and improved salt stability. What is important is the cost effectiveness of the improved molten salts, which can be seen in terms of improved process efficiency via increased energy storage capabilities and the ability to vary salt operating temperatures (both maximum and minimum thresholds). Controlling the material composites is one way towards achieving this goal. For instance, the use of ternary Nitrate-Nitrite salt composites (e.g. KNO-$NaNO_2$-$NaNO_3$) is an evolving technique capable of making such improvements. In this case, salt temperature thresholds change allowing the salt to be used as a TES medium as well as a heat transfer fluid at the same time (e.g. Direct Molten Salt TES).

Another typical solution to the problem involves the use of seeding particles (embedded into the molten salt base), as suggested by Siegel[10]. These fine particles of a high conductivity material are dispersed in the salt to improve its thermal properties. However, the suspension of 'big' colloidal particles (in the micrometre range) in the storage media has been found to cause undesired conditions. For instance, these particles tend to settle out of the fluid, causing clogging and other undesired flowability issues in the operating system[11]. As a result, the use of micron-sized seeding particles has not been commercially exploited. As an alternative, they can be replaced with nanoparticles to serve the same purpose.

1.3 Industrial considerations

The storage of energy is a major challenge when it comes to balancing the grid power supply, and it is more economically viable to store energy in the thermal form than in the form of electrical energy. Molten nitrate salts work on the concept of using earth abundant elements that can operate at elevated temperatures to serve as grid-level thermal energy storage medium, while still being emission-free. This storage option has therefore been considered by the solar energy producers, but with the need for more technological advancements. Solar thermal power plants with molten salt storage facilities are examples of this revised technology. These plants work on the concept of collecting heat from sunlight and preserving it thermally in the form of a molten salt, for power conversion at a later stage[12]. Spain and the USA have the largest number of commercial molten salt storage installations presently in operation[13]. The deployment of these storage facilities

allows uninterrupted electricity generation for 24 hours and have been reported as a flexible, efficient and cost-effective option for large scale energy production[8].

The reasons for selecting this specific storage option can be summarized as follows: i) molten salt operating temperatures are compatible with the requirements of modern steam turbines; ii) they have a very low vapour pressure as a liquid at atmospheric pressure; iii) they are non-flammable, non-toxic and environmentally safe, and are amenable to storing large amounts of thermal energy with quantities up to 900-1500 MWh_t; iv) they provide a low-cost medium to efficiently store thermal energy (current TES units run at an average cost of 15-30 $\$/kWh_{thermal}$ and with > 89% round trip efficiency, which is equivalent to 0.100-0.115 \$/kWh in terms of Levelized Cost of Electricity, LCOE)[14]. These factors have made molten salt one of the safest and most reliable storage options for solar thermal power processes[15].

Molten salts technologies also have other types of engineering applications, which have a wide-ranging scope, starting from their use in the nuclear power production (e.g. molten salt reactors, MSR), to metals and materials; batteries and fuel cells; the disposal of explosives and propellants, to name a few[16]. The use of molten salts in these applications led to the establishment of intensive technological experience in dealing with salts. In fact, the actual birth of molten salt usage in the area of power production was initially envisioned by the molten salt reactors research initiatives in the late 1940's, as part of the nuclear-powered aeroplane[16]. As a result of this, several conceptual techniques proposed for the development of large-scale solar collection assemblies and concentrators were found to be similar to those in MSR research activities.

According to Lovering[2], the marriage of solar and MSN nuclear technologies may practically be seen in the use of molten salts as a Phase Change Material, PCM. The synergistic nature of these two areas in the use of molten salt as a latent heat medium takes advantage of its applicability over a broad range of operating temperatures, thereby increasing the total amount of storable thermal energy. The difference between these two applications lies in the fact that nitrate salts are often employed in solar TES applications over working temperatures of 230ºC to 540ºC (e.g. typical solar nitrate salts have a density $\rho_l \sim 1899$ kg m^{-3}; heat of fusion $h_{fus} \sim 161$ J g^{-1}; specific heat capacity $C_p \sim 1.5$ kJ kg^{-1} $ºC^{-1}$; thermal conductivity just less than $k \sim 1$ W m^{-1} K^{-1})[17]. In contrast, for MSR nuclear applications the fuel is dissolved in a molten fluoride salt coolant to operate at temperatures of up to ~ 800ºC[18].

The main thermophysical properties of a salt such as its melting temperature, and thermal stability, define the lower and upper thresholds of usable temperatures in a sensible heat storage system[19]. The relation between the change in temperature and the stored heat is then given by the specific heat capacity (C_p; J $kg^{-1}\cdot K^{-1}$), which is defined as the heat capacity per unit mass of material[20]. While the specific heat capacity characterises sensible storage materials in regards to their ability to hold a particular amount of heat, the thermal conductivity (k; $W.m^{-1}\cdot K^{-1}$) quantifies their ability to transfer this heat[21]. Most conductors have relatively low specific heat capacity, whereas non-conductors have high values for specific heat capacity. The reason for this is that good conductors are frequently good radiators. Hence, they cannot hold their heat for a long time.

Molten salts are known as having a higher internal energy in the liquid phase than in the solid phase, since the molecules in the liquid phase experience weaker intermolecular forces and so they have a higher potential energy (a kind of bond-dissociation energy for intermolecular, with more internal degrees of freedom). This allows large quantities of energy to be stored in molten salts. The same energy can be released as the salt starts to reach the freezing temperature.

1.4 Experimental background

The development during the last few decades of state-of-the-art characterization techniques has allowed scientists to obtain quantitative information at time and length scales at and below nanosecond and nanometer scales. This technological evolution has opened the doors to new areas of science, such as nanoscience for energy technology and sustainability, which focuses its research on a number of key elements including the exploration of novel types of hybrid nanofluids to be used as heat transfer fluids and thermal energy storage media for renewable power plants.

Several in-depth studies[21-31] of nanofluids consider methods of manufacturing, and their fundamental characteristics, transport properties, thermal performance, heat transfer behaviour, and the practical application of thermal equipment to improve efficiency. Studies on fundamental characteristics have focused mainly on the dispersion stability, density and viscosity of nanofluids. Studies on nanofluid thermal performance have focused on the thermal conductivity, diffusivity and specific heat. The studies on the transport and heat transfer behaviour of nanofluids have focused mainly on their flow

behaviour, pumping power and heat transfer phenomena in various geometries, especially those found in the thermal industrial equipment and applications.

The underlying scientific challenge associated with nanofluids is complexity, specifically the complexity of their dynamics, behaviour and evolution under the large variety of physical, chemical and thermodynamic conditions that they are likely to encounter in the similarly large number of uses, including products, industries, emission and transport pathways. One of the biggest challenges facing science in this area is the behavior of nanomaterials and molecules as well as the precise characterization of the physical and chemical properties in the nanometric scale[28]. At the level of the physical mechanisms by which nanoparticles interact with each other and with a fluid, the following examples of idealized quantities that determine the nature and rate of interactions can be isolated with a view to experimental determination: collision rate and efficiency; and critical deposition concentration, at which aggregation rates are limited by diffusion. In turn, the physical properties of nanofluids thought to most strongly influence their transport are as follows: primary particle and aggregate state and size, shape, concentration; isoelectric point, zeta potential; surface charge and modifications; pH, ionic strength, concentration of the fluid.

The characterization of nanofluids in the nanometric scale can be achieved using two main approaches: direct-space techniques (i.e. microscopy), and indirect-space techniques (i.e. scattering). Both methods are not exclusive but complementary and as such can be used in combination not only for a complete characterization of a nanofluid, but also as a way to study the interactions between nanomaterials and the surrounding medium. There is also a large range of experimental techniques that are commonly used to characterise nanofluids[29], such as: high-resolution transmission electron microscopy (TEM) – structure, morphology, diffraction data; energy-dispersive x-ray spectroscopy devices (EDS) – elemental make-up of nanofluids; x-ray absorption spectroscopy methods – three-dimensional structure; atomic force microscopy (AFM) – surface morphology; small-angle x-ray scattering – phase and size, aggregation state; dynamic light scattering (DLS) – size, aggregation state, electrophoretic mobility; thermogravimetric analysis (TGA) – elemental composition; laser Doppler electrophoresis – electrophoretic mobility and zeta potential; nanoparticle tracking analysis (NTA) – size distribution and concentration measurement based on the light (laser beam) scattering and Brownian motion of nanoparticles in liquid suspension.

The use of light and sound in nanocolloidal science (nanofluids) is quite different. Light gained its importance as a characterization tool for colloids with the first microscopic observations of Brownian motion and the first measurement of electrophoretic mobility of particles in dispersion using electrophoretic light scattering (ELS)[22]. In contrast, sound remained unknown in colloidal science until ECAH theory (Epstein-Carhart-Allegra-Hawley) for ultrasound propagation through dilute colloids was developed[23]. In fact, according to Dukhin and Goetz[23] acoustics only attained some recognition in the field of colloidal science quite recently. The use of acoustic techniques are ideal for characterizing single- and multiphase elastic fluids due to the dependence of the speed of sound on a number of parameters such as density, compressibility and temperature[23]. Furthermore, acoustic measurements provide a multitude of data such as time-of-flight, acoustic impedance and attenuation, and variations in acoustic velocity which can be used to monitor particle settling, determine the particle concentration of a dispersion, and measure the critical transport velocity of a particle suspension in a flow.

A more detailed consideration of experimental studies of relevance to the present work is given in the literature review contained in Chapter 2.

1.5 Numerical simulation background

Advances in modern computing performance over the last few decades have contributed greatly to the improvement of computational fluid dynamic (CFD) capabilities. During this time, a large amount of work into simulation methods of turbulent fluid flow under a range of different geometries has been undertaken. This has generated great interest both in academic and industrial environments. In CFD, there are many simulation methods capable of modelling turbulence in singe- and multiphase fluid flows. The most accurate of these is direct numerical simulation (DNS) that solves the Navier-Stokes (NS) equations at all relevant turbulence length and time scales. In the DNS approach, pipe, duct and channel flow simulations in three-dimensions can be obtained to emulate the turbulent flow of representative practical media down to the Kolmogorov scale (the length scale of turbulent motion below which the effects of molecular viscosity are non-negligible). As a result, the amount of numerical grid points needed to solve the descriptive equations for a given domain in order to resolve these scales is very high. This technique therefore enables any quantity of interest to be analysed with great spatial and temporal precision, albeit at a large computational cost and for somewhat idealised conditions. Thus, DNS can generally be regarded as complementary to laboratory

experiments. For situations where interest lies in the physical behaviour of the system and in obtaining information useful in elucidating the fluid flow dynamics, DNS is an ideal option. However, and as noted, the amount of computations needed per timestep is very large.

The Lagrangian particle tracking (or in short the LPT method) is a numerical technique for tracking Lagrangian particles within an Eulerian framework. The LPT code recently developed at the University of Leeds has the capability of tracking representative groups of micro- and nano-sized spherical and non-spherical particles as they move through a flow field by solving the Newtonian equation of translational motion and the Eulerian equation of rotational motion. The LPT may also be coupled with DNS to form a powerful multiscale computational modelling capability, able of investigating the flow behaviour and heat transfer in nanofluids.

These types of simulations can be used to provide information where experiments are difficult to perform, which is particularly an issue in energy technology and sustainability research areas. Not only are nanofluids very difficult to observe and quantify experimentally in terms of their flow characteristics, their study is also limited to very specific setups. This removes the ability to determine the effect of modifying flow and material parameters. In contrast, numerical simulation allows us to be very specific and precise about the impact of system conditions. This means more efficient use of time and resources, and a greater focus on elucidating the dynamics of the system. In summary, results from high accuracy simulations can be used to reinforce experimental work, predict failures with current designs and provide insights into optimising future systems by determination of operating parameters for best performance, cost-effectiveness and safety. That in turn allows us to draw conclusions regarding the implications of nanofluids for sustainable energy systems and storage technologies.

A more detailed consideration of numerical simulation studies of relevance to the present work is given in the literature review contained in Chapter 2.

1.6 Project overview and objectives

As covered in the previous section, a combined experimental analysis and thermal testing with a computational modelling approach should provide the basis for an accurate investigation of nanofluids, which have great potential in enhancing the efficiency in the

renewable-energy industry, solar thermal systems and similar areas. This study, therefore, aims at determining the dynamic behaviour of nanofluids that utilize nano-thermo technology typical of that found in thermal energy storage systems, similar to that which exists in an actual CSP-TES plants. If a conventional fluid is to be doped with nanoparticles to enhance its thermo-physical properties, the physical stability and particulate dynamics of this dispersed system needs to be well understand, to reduce and prevent problems caused by the instability (i.e. settling) of nanoparticles in the storage system and transport pipelines. At the same time, it is important to insure that the heat flux stays uniform in the thermal storage system.

1.6.1 Experimental objectives

The main objective of the experimental programme is to address some of the existing gaps in knowledge, particularly with regard to nanofluid dynamics and thermal testing, developing methods for characterising nanofluids in model systems, and comparing results with those derived from a complementary programme of numerical modelling. This investigation therefore seeks to achieve the following set of objectives:

1. Formulate nanofluids by doping conventional fluids: water based and binary nitrate (mixture NaNO3:KNO3 in 60:40 wt. %) salt based mixtures with selected nanoparticles and test the thermal properties (thermal conductivity, diffusivity and specific heat capacity) of the mix;

2. Analyse the interaction and physical stability of nanoparticles in nanofluids, at varying particle concentrations ranging from 1 to 5 wt. %, typical of those found in industrial applications ;

3. Measure the speed of sound in nanofluids (based on the time-of-flight principle) and then use this data, together with measurements of density and predictions of thermal conductivity in relevant geometries (by simulating the nanofluid system), to determine mathematically the ratio of heat capacities using the relationship between experiments and computational models. This work will, therefore, be divided into two main parts as follows:

    a) Measuring the mobility of nanoparticles in ideal fluids (i.e. water). Proof-of-concept and optimisation to measure the stability of nanoparticles in static environments. This option involves the use of a stirred tank mixer and an *in situ*

based ultrasonic signal generator, equipped with a transducer-receiver system and an oscilloscope. The aim is to simulate a simplified industrial TES application with mixed nanoparticles. This technique is developed (in-house) to identify the most compatible measuring techniques needed to detect the nanoparticles in nanofluids as well as the relative speed of sound of the fluid in a temperature range of 25-95ºC.

b) The second experimental programme will investigate the speed of sound and thermal behaviour of molten salts nanofluids using a high-temperature stability rig. The thermal storage cell consists of a hot-molten-salt thermal cell fitted with an *in situ* high temperature ultrasonic transducer designed to investigate the behaviour of molten salt nanofluids over a temperature range of 250-500ºC. The effect of molten salt density and compressibility changes in relation to the nanoparticles suspensions will be considered. The measured speed of sound will then be used to determine mathematically the thermal properties of molten salt nanofluids.

c) To develop an ultrasonic waveguide sensor that can be used as buffer rods (BR) in high temperature molten salts testing cell.

4. Characterize the colloidal stability of the formulated nanofluids using Zeta potential and particle size distributions, which will be then be used for instrument calibration and high-precision measurements of selected parameters needed in the analysis of experimental data and numerical modelling results.

5. Testing for thermal properties includes: thermal conductivity, heat of fusion, melting point and specific heat capacity of nanofluids. These will be measured and analysed to guide formulation design, as follows:

   a) Measurement of heat of fusion, melting point and specific heat capacity will be performed experimentally using cutting-edge differential scanning calorimetry (DSC) techniques.

   b) Measurement of other thermal properties via acoustic speed of sound measurements (*in situ*). Develop a mathematical model to compute the thermal enhancements (thermal conductivity, heat capacity ratio) from SOS data at various nanoparticles concentrations and temperatures.

1.6.2 Numerical sumulation objectives

The main objective of the numerical investigation is to assess the stability, thermal properties, and turbulent flow behaviour of nanoparticle suspensions in both stagnant and flowing geometries. The investigation of nanofluids in both stagnant and flowing geometries will be conducted using Lagrangian particle tracking (LPT), and LPT coupled to advanced numerical simulation methods (DNS). The following set of objectives are set for the development of these predictive models:

1. To establish an LPT-based computational modelling capability based on the extension of an existing code, able to predict the motion of suspended nanoparticles in a three-dimensional, multiphase fluid-solid sample volume. The nanofluid is predicted using an Eulerian-Lagrangian hybrid approach with a constant timestep. This technique takes various multiscale forces into consideration in the calculations, whose characteristic scales are quite different, providing an analysis of all factors affecting the stability and thermal conductivity of nanofluids.

2. To establish a DNS capability, based on the spectral element method, for nanofluid flow in a channel, by adapting an existing code, Nek5000. Generate statistical moments up to fourth order for a shear Reynolds number flow of Re_τ = 180. More specifically, the multi-scale computational model will couple the aforementioned LPT with DNS to investigate the influence of dispersed nanoparticles on the surrounding carrier fluid, and the effect of the turbulence flow field on the dispersion and aggregation properties of the solid nano-particulate phase. The model will also be used to study in detail phenomena such as: interparticle collisions, concentration, turbophoresis and thermophoresis, with the approach also of value in investigations of particle-turbulence interactions and the long-term stability of nanoparticle dispersions in closed-conduit geometries.

3. To investigate the heat transfer behaviour of a nanofluid within a turbulent wall-bounded flow. Different simulations (non-isothermal/isothermal) will be performed with different heat flux boundary conditions. The first non-isothermal simulation will be for a fixed cold wall boundary, with an associated temperature of 250°C, whereas the second simulation is for a fixed hot wall boundary, with an associated temperature of 500°C. The fluid used in these simulations is set to have

a high Prandtl number (Pr = 5.0), representative of molten salt at 410°C. The third simulation is isothermal, and it is set for molten salt at a uniform temperature of 410°C. These simulations are used to study the effect of nanoparticles on the turbulent heat flux and temperature field, the nanoparticle concentration response to temperature variations and turbulence across the channel, allowing conclusions to be drawn on the impact of turbophoresis and thermophoresis in a turbulent particle-laden flow.

1.7 Thesis organisation

Chapter 1: Introduction

The rationale behind the study is explained and the main topics are introduced. The background to this study and the main objectives of it are presented, as well as the practical intent, which is to investigate the use of nanofluids as a heat transfer fluid and thermal energy storage medium for solar energy power plants.

Chapter 2: Literature review

In this chapter, the reader is provided with an overview of previous theoretical, experimental and numerical work related to nanofluids. The focus of the literature review is first on the scientific, engineering significance and potential industrial application of nanofluids. Different methods of preparing a stabile nanofluid will be explored. Key models related to nanofluids will be evaluated. In doing so, an understanding surrounding the thermophysical properties, particle dynamics and heat transfer mechanisms in nanofluids will be gained. Nanofluid experimental approaches will be highlighted, given prominence to the speed of sound characterization technique that has been applied in the current study. The review will then focus on nanofluid multiphase simulation work, underlining the most relevant parameters used to describe the heat transfer mechanisms of nanofluids in a stagnant environment. Finally, the mass and heat transfer behaviour of nanofluids in channel flows will be considered, with emphasis on DNS nanofluid simulation technique employed in this study.

Chapter 3: Methodology

Quite a considerable amount of time during this project was spent gathering the required data using a combined experimental and computational approach to investigate the role

of particle dynamic forces, and so in this section the details of the experimental facility and the numerical simulation methodology are both described. The basis of the acoustic experimental technique is explained, followed by nanoparticle characterisation studies used to select the most appropriate particle species. After that the principles of the computational technique used and processing of turbulent flow data, including velocity, temperatures and heat transfer profiles, is explained in detail. Finally, how this integrated system was used to generate useful results in both the experimental and computational set-ups is described, with measurement errors also discussed.

The content within the remaining chapters of this thesis is as follows. **Chapter 4** presents the acoustic method for determination of thermal properties of nanofluids and the thermal analysis obtained from differential scanning calorimetry experiments. **Chapter 5** will introduce the multiscale computational modelling of nanofluids. The focus of this section is to evaluate the stability of suspension of nanoparticles and their interactions within the system, as well as to determine the thermal conductivity of nanofluids in a stagnant configuration. The remaining results section, **Chapter 6** involves using numerical methods to simulate turbulent heat transfer behaviour of nanofluids in multiphase channel flows. The thesis will be summarised in **Chapter 7**, where conclusions will be drawn based upon the knowledge obtained throughout the project. Suggestions for extending the work presented here will also be discussed. Finally, **Appendix A** includes the derivation of thermodynamic relations between the ratio of heat capacities and the experimental values of the speed of sound and **Appendix B** discusses the propagation of experimental errors and uncertainty.

2 LITERATURE REVIEW

2.1 Introduction

A nanofluid is defined as a dispersion of nanoparticles, typical size range of 1-100 nm, in a base fluid. Nanofluids were first suggested by Choi[24] in 1995 to improve the heat transfer properties of conductive fluids (e.g. water, ethylene glycol, oil or molten salt), by doping them with small concentrations (1.0 to 5.0 vol. %) of nanoparticles. Nanofluid research has since received increased attention, with extensive experimental, theoretical and computational studies being completed[25], with the main objective being to achieve the highest possible thermal values at the smallest possible concentration of nanoparticles. The enhancement in heat transfer characteristics obtained using different types of nanoparticles such as: metals (Au, Ag, Cu) metal oxides (Al_2O_3, TiO_2), non-metallic oxides (SiO_2) and carbon nanotubes (CNTs) is described in the literature,[26-33] with substantial thermal properties improvements[34-38].

Due to the enormous thermal enhancement involved in nanofluids, they could potentially be used to solve one of the most important problem faced in the industry and that is the thermal management of high power systems (e.g. improving the heat transfer fluids and energy storage media). However, further investigations of this upcoming technology are needed to support the development of nanofluids both technically and economically. This in turn should pave the way for the industrial use of nanofluids, by making them more reliable, sustainable and energy efficient.

The mechanism of thermal enhancement in nanofluids is rather complicated[28] and can be explained by the behavior of dispersed nanoparticles and their interactions within the base fluid[39, 40]. This research area is now gaining a lot of interest by developers and in the academic community, since the evaluations of this technology relies heavily on understanding the fundamentals of such liquid-solid multiphase system. Currently the development of nanofluids is facing a number challenges such as: nanocolloidal stability; the degree of heat transfer enhancements; thermal stability; flow and heat transfer behaviour in the different process equipment and the overall cost of formulation. This section will introduce and discuss the current status of research on nanofluids and will identify the challenges and opportunities found within this ground breaking research area.

2.2 Objectives of the literature review

The purpose of this review is to consider and discuss the relevant terms and concepts of heat transfer and thermal energy storage by nanofluids, found within the literature. Due to the nature of the work presented in this thesis, the review will begin by underlining the scientific, engineering significance and potential industrial application of nanofluids. Different methods of preparing a stable (both physically and thermally) nanofluid will then be explained. The previous studies based on theoretical, analytical and numerical work will be introduced and evaluated. In doing so, an understanding surrounding the thermophysical properties, particle dynamics and heat transfer mechanisms in nanofluids will be given. The review will then focus on nanofluid experimental approaches, giving prominence to the speed of sound characterization technique that has been applied in the current study. After that, nanofluid multiphase simulation work will be highlighted, with the most relevant parameters used to describe nanofluids heat transfer properties in control volume, as in that used for the stagnant LPT nanofluid model, which forms part of this thesis. Finally, the mass and heat transfer behavior of nanofluid in channel flows will be considered, this include phenomena such as; nanoparticle interaction, agglomeration, turbophoresis and thermophoresis, with emphasis on the DNS simulation techniques performed as part of this study.

2.3 Scientific and engineering significance

The use of nanofluids presents the following advantages as compared with conventional (single-phase) fluids: (i) heat transfer intensification leading to reduced fluid volumes; (ii) high dispersion stability with predominant Brownian motion of particles (iii) reduced particle clogging as compared with conventional slurries, thus allowing system miniaturization; (iv) adjustable parameters, including flowability, thermal conductivity and heat capacity[40], by varying the particle type, size and concentration[41]; and (v) determinable acoustical and optical properties, enabling monitoring and diagnosis to be made in the process equipment.

Considering these enhancements and evidences, it is suggested that the employment of nanofluids as coolant and energy storage medium in renewable power plants seems promising and could result in increased efficiency and large energy savings. (e.g. high thermal capacity and conductivity when using nanofluids permits greater heat storage per unit mass)[42]. On the other hand, the industrial use of nanofluids may still pose some

challenges and these are: (i) increased pumping power due to greater pressure drop as a result of increased density relative to the single-phase fluid; (ii) long-term particle settling[43] and potential clogging of flow passages, if colloidal stability is not well maintained; (iii) possible damage to flow loop parts by erosion; (iv) high cost of nanoparticle suspensions; and (v) increased axial rise in wall temperature due to increased thermal conductivity and degraded specific heat[44]. Therefore, further investigation is required to address the issues associated with the industrial use of nanofluids.

2.4 Thermal energy storage concepts

In general, there are three basic methods of storing thermal energy: sensible, latent, and thermochemical heat storage. The main difference between the three methods is in the energy density (the amount of energy stored) and the time needed to charge and retrieve the stored energy. For molten salt studies, the focus is on both sensible and latent heat storage systems. The term sensible-heat indicates that there is a related change in temperature within the sensible heat storage process. The amount of heat stored depends on the heat capacity of the medium, the temperature change, and the amount of storage material. This can be expressed by the correlation given by Lane[19]:

$$Q_s = \int_{T_i}^{T_2} mC_p dT = m\overline{C_p}\,(T_2 - T_i) \qquad 2\text{-}1$$

where, Q_s is the quantity of sensible heat stored, T_i is the initial temperature, T_2 is the final temperature, m is the mass of heat storage medium, C_p is the specific heat (isobaric), and $\overline{C_p}$ is the average specific heat between T_i and T_2.

Latent heat differs from sensible heat in the fact that it is related directly to phase changing rather than just being related to changes in temperature. The absorbed energy of latent heat is stored or released by phase transition which takes place at a constant temperature, and so named latent. In practice, latent heat storage systems also make use of some sensible heat capacity in the system; this contribution is to be added as follows[19]:

$$Q_l = ma_m \Delta h_m + \int_{T_i}^{T_m} mC_p dT + \int_{T_m}^{T_2} mC_p dT \qquad 2\text{-}2$$

$$= m\left[a_m \Delta h_m + \overline{C_{p_s}}(T_m - T_i) + \overline{C_{p_l}}(T_2 - T_m)\right] \quad \text{2-3}$$

where a_m is the fraction melted, Δh_m is the heat of fusion per unit mass,T_m is the melting temperature, $\overline{C_{p_s}}$ is the average specific heat between T_i and T_m , $\overline{C_{p_l}}$ is the average specific heat between T_m and T_2.

For latent heat storage systems, the heat of fusion term is usually predominant. However, considerable heat can be added by sensible heat too. In such case, the melting point defines the threshold temperature at which the majority of heat is getting stored. The materials used for latent heat storage are often called PCMs (phase change materials) as they store heat using a phase change. Another important feature is the melting enthalpy (Δh_m; kJ·kg^{-1}) as it determines the amount of energy that can be stored in a given PCM. It is sometimes referred to as the enthalpy of fusion or latent heat of fusion, which is the change in enthalpy resulting from heating a given quantity of a substance to change its state from solid to liquid, the temperature at which this occurs is known as the melting temperature[20].

2.5 Applications of nanofluid

Nanofluids have gained a lot of interest because of their enhanced thermophysical properties, which can be a solution for a wide range of industrial issues. Unlike in conventional fluids, the significant enhancement of the heat transfer properties (thermal conductivity, heat transfer coefficient and heat capacity) reveals new pathways for its applications[28-29]. Recently, the number of industrial application potential of nanofluids technology, ranging from renewable energy, nuclear reactors, transportation, electronics, pharmaceutical, biomedicine and food, and their focus on increased energy efficiency have received much attention.

Initial reviews of this upcoming technology demonstrates a potential for utilization where straight heat transfer enhancement is paramount such as that faced by the renewable and thermal energy storage industry[31, 36, 38]. In this industry, the efficiency of the heat removal and thermal management system happens to be the greatest technological challenge. The progress in nanomaterials science, together with development in thermofluid engineering, suggests that enhanced thermal properties are technologically advantageous.

2.6 Nanofluid preparation

The preparation of a well-mixed and uniformly dispersed nanofluid is a key step for successful production of energy-efficient heat transfer fluid. Unstable dispersion of nanoparticles may lead to aggregation of particles and fouling in the thermal fluid heating systems (e.g. in the reservoir, heat exchanger and piping system), which will cause biphasic heat transfer[39]. To ensure the stability of working fluid in the thermal system, nanofluids can be prepared either by a single-step or two-step method[45], as will be explained in detail in the following parts.

2.6.1 Single-step method

The single-step process was first developed at Argonne National Laboratory[46]. In this process the nanoparticles are synthesised and directly dispersed into the base fluid. This method is sometime favourable, especially if drying, storage and logistic operations are to be prevented, when preparing nanofluids. Moreover, the undesired nanoparticle aggregation and non-uniform dispersion, can be minimized. For nanofluids containing high-conductivity nano-metals with relatively higher densities (e.g. gold, Au = 19.32 g. cm^{-3}; silver, Ag = 10.5; cupper, Cu= 8.94; titanium Ti= 4.5) the single-step process is preferable to the two-step processing, due to increased suspension stability of the particle in the base fluid[45].

Techniques for the one-step process include[30]: laser ablation method and submerged arc nanoparticles synthesis method, where metals are vaporized and cooled into liquids to obtain stable nanofluids. The results of the single-step method revealed the high purity of metal nanoparticles because they are submerged in de-ionized water, and thus not being contaminated or oxidized further. On one hand, this method is described to be excellent for research scale, but on the other hand it cannot be used to synthesise nanofluids in large scale. The process would be hard to scale up, for two reasons: processes that require a vacuum slow the production of nanoparticles and nanofluids significantly, and the cost of producing nanofluids by the single-step physical process is still considered to be high[46].

2.6.2 Two-step method

The two-step method is the most widely used for preparing nanofluids. In this method the nanoparticles are first produced in the form of dry powders by chemical, physical and mechanical methods. The nanoparticles will then be dispersed into a base fluid in the

second processing step with the help of intensive agitation force (i.e. direct sonication used to ensure dispersion and reduce the agglomeration of particles). Several other methods may also be applied to maintain the uniform nanoparticle dispersion in the fluid such as: magnetic, high-shear mixing, homogenizing, and ball milling.

The two-step method is currently recognized as the most economical for producing nanofluids on a large scale, as synthesis techniques have already been scaled up to industrial production levels. Also it is recommended to use the two-step process method[46] when preparing metal-oxide nanofluids with relatively lower density of nanoparticles (e.g. Al_2O_3 = 3.85 g. cm^{-3}; SiO_2 = 2.65; TiO_2 = 4.23), than those with heavy metallic nanoparticles[47]. However, it should be noted, that nanofluids produced by the two-step method have a higher tendency to form aggregates because of the high particles surface area and activity (van der Waals force among particles)[1], making it difficult to maintain the stability of nanofluid for a long time.

One way of improving the stability is to use surfactants[49]. However, the functionality of the surfactants under high temperature raises a big concern, especially for high-temperature nanofluid applications. Alternatively ultra-sonication or stirring process may be used to minimize agglomeration and deposition of nanoparticles on the inner wall of the thermal system and flow channels. It is also possible to maintain the homogenous mixture by varying the pH of concentration (e.g. formation of carboxyl groups on the surface of the nanoparticles for stability purpose).

Numerous other techniques have demonstrated promise in producing nanofluids[30, 38, 42] beside the single- and two-step methods, including: direct synthesis method; sol-gel method, chemical precipitation method, physical gas-phase; direct condensation method; mechanical stirring process; surface treated and functionalization acid treatment for carbon nanotube; and finally the chemical co-precipitation method. Ganvir et al.[30] also described other methods that have been employed by researchers to reduce agglomeration of nanoparticles, such as the use of different surfactants: as a surface modifiers.

The preparation of a stable Al_2O_3 nanofluid may be achieved with the two-step method without the use of dispersant or stabilizer as described by Zeinali Heris et al.[50], since the addition of any agent is likely to change the fluid properties. To prepare the required volume of nanofluid, Al_2O_3 nanoparticles can be mixed with the distilled water and

vibrated for 6–12 h by ultrasonic mixing system, without any observed sedimentation for all volume factions after 12 h at rest[50].

Furthermore, Chougule and Sahu[51, 52] prepared Al_2O_3/water and carbon nanotube CNT/water nanosuspensions. In their work two different types of fluids were also used, namely, functionalized water based nano-coolant and surfactant treated water based nano-coolant. Sonication is used, with ultrasonic vibration for 1 h to ensure the stable homogenisation of nanoparticles in the suspended fluid. Results of the thermal performance demonstrated that both nano-coolants exhibit enormous change Nusselt number, which was found to increase with the increase in the nanoparticle concentration and nanofluid velocity, when compared with pure water. Their results of functionalized CNT nano-coolant with 5.5 pH exhibits better performance compared to the nano-coolant with pH value of 6.5 and 9. The surface treated CNT nano-coolant exhibits the deterioration in heat transfer performance at higher temperature due to lower bonding strength between nanoparticles and surfactant[52].

2.7 Current status of research on nanofluids

Different fluids and nanoparticles will be considered throughout this study to serve the following purposes; firstly, water based nanofluids are to be used as heat transfer fluids in the cooling system at temperature ranging from 10 to 95°C. The second proposed type is a molten salt based nanofluid to serve as both heat transfer fluid and thermal energy storage medium at temperature ranging from 250 to 500°C. The study also aims to gain insight into the use of different nanoparticle characteristics that can be used interchangeably to improve the efficiency of the heat removal and thermal management systems in solar thermal power plant.

Nanofluid flow and heat transfer properties depend on various parameters such as: fluid–particle interfacial effects[53], base fluid properties[54], particle–particle interactions[55], nanoparticle aggregation into sparse of clusters[56-58], particle dimension and geometry[59], and particle distribution[60]. Correspondingly, the thermophysical properties of nanofluids, including thermal conductivity, specific heat capacity, density, viscosity and surface tension, are necessary to estimate the effectiveness of a nanofluid at a given thermal system. Changes in thermophysical properties of nanofluids compared with base fluids will be reviewed and discussed.

2.7.1 Thermal conductivity

Water based nanofluids

Several researchers studied experimentally the effects of volume fraction; nanoparticle size and type; and temperature dependency on nanofluids. Table 1 summarizes and compares measured thermal conductivity enhancement for nanofluids with different base fluids and nanoparticles. Some measurement of conductivity were made by transient hot wire (THW) method in which natural convection effects are eliminated to a large degree as indicated in the table below.

Table 1. Summary of measured thermal conductivity enhancement for different nanofluids

Ref. no	Reference	Base fluid	Nanoparticle material (size in nm)	Temp. range (°C)	Max. vol. (%)	Max. *k* enhancement
59	Beck et al. (2009)	Water	Al_2O_3 (12)	23–137	1–5	12% at 5% *
60	Lee et al. (1999)	Water	Al_2O_3 (18)	17-37	1–5	16% at 5%
60	Lee et al. (1999)	Water	CuO (24)	17-37	1–4	20% at 4%
61	Xie et al. (2002)	DIW, EG, oil	Al_2O_3 (60)	25	1–5	7.6% at 5%*
62	Pantzali et al (2009)	Water	Al_2O_3 (11)	75	1–4	18% at 4%*
		Water	CuO (30)	75	1–4	22% at 4%*
		Water	CNT(10-50)	75	1–4	10% at 4%*
63	Gherasim et al. (2009)	Water	Al_2O_3 (47)	21-23	1–4	12.1% at 2%*
64	Leong et al. (2012)	Air	Al_2O_3	100-240	1–7	23% at 7%*
		Air	TiO_2	100-240	1–4	23% at 4%*
65	Hung et al. (2012)	Water	Al_2O_3 (20)	30-60	0.5-1.5	40% at 1.5%*
66	Das et al. (2003)	Water	Al_2O_3 (38)	21–51	1–4	24.3% at 4%*
		Water	CuO	21–51	1–4	36% at 4%*
67	Eastman et al. (1996)	Water	Al_2O_3 (33)	25	1–5	30% at 5%
68	Nguyen et al. (2009)	Water	Al_2O_3 (36)	25	0-6	> 2.8%*
69	Asirvatham et al. (2011)	DIW	Silver (80)	25	up to 1	69.3% at 0.9%*
70	Naphon et al. (2008)	DIW, alcohol	Titanium (21)	25	0.01-1	10.60% at 0.1%

*Thermal conductivity measurement made by transient hot wire (THW)
DIW = De-ionized water
EG = Ethylene glycol

It is clear from Table 1 that the increment of thermal conductivity has been accomplished by many researchers on a wide diversity of nanofluids using different nanoparticles (ceramic, metallic and carbon-based nanostructures) as additives to the base fluids. A large number of publications have been devoted to the research of water based nanofluids[59-63, 65-70]. Other base fluids, such as ethylene glycol, air, alcohol and engine oil

have also been employed. These are all known as conventional nanofluids. The thermal conductivity *k* of water based nanofluids, for example, is usually found to be much greater than that predicted by classical models, such as the theoretical work of Maxwell[24]. The most significant enhancement in samples containing Al_2O_3 in water with volume fractions ranging between 1 and 5% is an increase in *k* of between 2 and 40%[61-65]. Conversely, the specific heat of nanofluids was reported to decrease gradually by 0.65% as the nanoparticle concentration increases from 0% to 5%[71], which will be discussed later.

Salt based nanofluids

Several industrial processes require the application of exceptional thermofluids that can operate at temperatures higher than those used when the working fluid is water. High temperature thermofluids are of special importance in solar thermal power plants, as the produced power in these plant depends mainly on the efficient conversion of the thermal energy collected from direct sunlight, into electricity at temperatures higher than ~ 250 °C. At present, the transport of the thermal energy in these plants is done through petroleum-oil-based heat transfer fluids, which are thermally stable up to ~ 360 °C. The use of molten salts as heat transfer fluids and storage medium has recently been considered by many researchers[72, 73] to allow a wider working temperature range (250-500 °C), in order to increase the process efficiency.

The use of molten nitrate salts and their mixtures (e.g. the binary mixture of 60 wt. % $NaNO_3$ and 40 wt. % KNO_3, commonly referred to as solar salt) as thermal energy storage material, for medium-to-high temperature, has become common practice in solar thermal power plants. The main advantages of using this type of nitrate mix are: the high energy density, thermal stability (up to ~ 680°C), and low cost. However, its application is often limited by poor heat transfer properties (i.e. thermal conductivity, specific heat, fast-cooling and phase segregation[74]). Of particular interest is the thermal conductivity of nitrate melts, which were reported by some researchers[75] to decrease with increased temperature, as salt molecules expands and move apart.

The technique of molten salt seeded with nanoparticles is relatively new and still on a research and development scale, a review of the recent literature displayed positive results[76-83]. The general intrinsic fact behind the use of nanoparticles is to acquire better thermophysical properties compared to its bulk state. The overall performance evaluation

for molten nitrate salt nanofluids was also reviewed, as reported in several studies[29, 76, 77] and found to be practically effective[78]. The recent literature displays clear enhancements in the thermal conductivity, specific heat capacities, and reduced onset salt melting temperature due to increased entropy[79-83].

For pure nitrate salts there is a focus on lowering the melting point by varying the composition of eutectic nitrate salt. With the addition of nanoparticles into the nitrate salt mix the melting point can be lowered, beside the enhancement of thermophysical properties. The particle concentration is found to be an important factor to consider when producing this type of nanofluids. The contribution of some nanofluid research studies was reviewed in that regards[79]. In particular molten salt nanofluids have been reported for their anomalous enhancement on the thermal conductivity, at concentrations of $0.1 < \phi$ (vol. %) < 5.0.

Comprehensive reviews on the use of molten nitrate salt nanofluids as heat transfer and storage materials, with different types of nanoparticles is described in the literature[85,86]. However, the main focus of the majority of these literature studies is on the enhancement of heat capacity, rather than the thermal conductivity. Little published work exists on the thermal conductivity of molten nitrate salt nanofluids. This is mainly because thermal conductivity measurement of these salt melts is difficult, due to the high melting temperatures ($\sim$ 221°C), the unavailability of a standard commercial device that can operate over a wide temperature range (250-500°C), and the corrosive nature of the nitrate salts. A summary of some measured thermal conductivity values of molten nitrate salt nanofluids containing different nanoparticles is shown in Table 2.

In fact, the availability of experimental data on thermal conductivity of molten salt nanofluids is limited. However, from those found (see Table 2) it is clear that significant enhancement are to be expected, the maximum of which was 47% as reported by Shin & Banerjee[93]. Moreover, Ueki et al.[89] used a THW technique to report an enhancement of 13% in the thermal conductivity of heat transfer salt (40% $NaNO_2$–7% $NaNO_3$–53% KNO_3, by mass fraction) at 200°C, on mixing with Silicon Carbide (SiC) nanoparticles at a particle loading of 1.2%. On the other hand, the THW techniques were reported in the literature as a significant source of unreliable data and some studies have highlighted some of these issues[90]. The main source of error is deposition of nanoparticles on the delicate hot-wire components.

Table 2. Summery of measured thermal conductivity enhancement for salt based nanofluids.

Ref. no	Reference	Base fluid	Nanoparticle material (size in nm)	Temp. range (°C)	Max. vol. (%)	Max. *k* enhancement
89	Ueki et al. (2017)	HTS	SiC (<100)	200	0.72-1.2%	13%
90	Ma & Banerjee (2017)	Solar salt	Al_2O_3 (40-60)	300-500	up to 4	20-25%
91	Sumair (2018)	LTMS	Graphene (60)	70-200	0.01-0.1	2.44%
92	Bellos et al. (2018)	Solar salt	CuO (50-100)	277-577	up to 4	13.9%
93	Shin & Banerjee (2015)	LPCS	SiO_2 (10-30)	150-300	Up to 0.5	37-47%
94	Jeyaseelan et al. (2019)	Solar salt	Al_2O_3 (unknown)	35-700	0.5-2.5	1.95-8.3%
		Solar salt	TiO_2 (unknown)	35-700	0.5-2.5	2.77-8.1%

Solar salt = a binary mixture of 60 wt. % (or 64 mol. %) $NaNO_3$ and 40 wt. % (or 34 mol. %) KNO_3.[87]

HTS = Heat Transfer Salt composed of 40 % $NaNO_2$, 7 % $NaNO_3$, and 53 % KNO_3 by weight.[89]

LTMS = Low Temperature Molten Salt composed of 5.76 % $NaNO_3$, 21.36 % KNO_3, 24.84 % $Ca(NO_3)_2$, 41.08 % $CsNO_3$ and $LiNO_3$ 7.44 % by weight. [91]

LPCS = Lithium and Potassium Carbonate Salt composed of 62 % Li_2CO_3, 38 % K_2CO_3) by weight.[93]

ENG-TSA = expanded natural graphite treated with sulfuric acid.[94]

It should also be noted that several measurements reported in the literature have shown an increase in the thermal conductivity of pure molten nitrate salts with increasing temperature, without the addition of nanoparticles as in that by Nagasaka and Nagashima[84]. However, this is not common for many other liquids, with the exception of water. In contrast, there was found to be no change in the thermal conductivity in the solar eutectic salt nanofluids doped with Al_2O_3 nanoparticles at several concentrations[88]. However, those thermal conductivity values were calculated from thermal diffusivity values measured in the solid state using laser flash analyser (LFA) at five temperatures (65, 85, 105, 125 and 145°C), which may explain the unchanged conductivity.

Moreover, the majority of molten salt nanofluid literature studies utilize the classical two-step synthesis protocol, which is challenging for large-scale industrial applications due to the high cost. Additionally, problems related to high temperature in the measuring instrument may arise when studying the effect of molten salt with nanoparticle at temperatures up to ~ 500°C. This factor introduces more complications in measuring instrument together with notable systematic errors (e.g. resulting from the combined effect of radiative and convective heat transfer phenomena). As a result, the use of indirect measurements, such as thermal, optical, and acoustic (i.e. speed of sound), have been the

applied solutions up until now[23]. Understanding the limitations of these techniques (in terms of accuracy) can lead to an acknowledgement of the need for further study, as will be explained latter.

2.7.2 Mechanism of thermal conduction in nanofluids

In this part of the literature survey, a special focus will also be given to explaining the mechanisms of thermal conduction in nanofluids. This topic is challenging, because of the debate found in literature in outlining the exact mechanism. The present understanding of thermal transport in nanofluids can be grouped into two main categories according to Wang and Mujumdar[26-28], who explained the different mechanisms involved, the details of which follow.

The first group[25, 54, 55] postulate, that the thermal conductivity of nanofluids is composed of the particle's conventional (static) part and a Brownian motion (dynamic) part which produces micro-mixing. These models take the dynamics of the particles into consideration, whose effect is additive to the thermal conductivity of a static dilute suspension. Thus, the particle size, volume fraction, thermal conductivities of both the nanoparticle and the base fluid, and the temperature itself are considered in the thermal conductivity model of nanofluids. These theories provide a means of understanding the particle interaction mechanism, which enhances the heat transfer via four possible routes: (i) the increased surface area due to suspended nanoparticles; (ii) the increased thermal conductivity of the fluid; (iii) the interaction and collision among particles; and (iv) the intensified mixing fluctuation and turbulence of the fluid, related to the dispersion of nanoparticles within the fluid.

Conversely, the second groups[39, 57] consider the influence of the solid–liquid interface in a nanofluid system and assume that the nanofluid is a composite, formed by the nanoparticle as a core, and surrounded by a 'nano-layer' as a shell, which in turn is immersed in the base fluid, and from which a three-component medium theory for a multiphase system is developed. Such models propose that the liquid in contact with a solid nanoparticle interface is more ordered than in a bulk liquid (liquid molecules close to the solid surface form a nanolayer structure), thus the liquid layering here is anticipated to lead to higher thermal conductivity in nanofluids. However, the exact mechanism for thermal conduction between a liquid and a solid interface is not yet well understood[28].

Wang and Mujumdar[28] then continued to explain that there are no general mechanisms to rationalize the overall thermophysical enhancements of nanofluids, including the greatly improved effective thermal conductivity and heat capacity, although many possible factors have been considered such as the ones highlighted above. It may also be related to the transport of electrons in a medium having negligible electrical resistivity caused by scattering (known as ballistic phonon transport)[28], or surface charge state. There are still several other possible macro-scale explanations such as heat conduction, particle-driven natural convection, convection induced by electrophoresis, thermophoresis, and perhaps some others.

The other argument made[28] is that most thermal conductivity measurements of nanofluids are made experimentally, and it depends on parameters including the thermal conductivities of the base fluid and the nanoparticles, the volume fraction, the surface area, and the shape of the nanoparticles, and the temperature and there are no theoretical formulas available as of now to account for all of these factors at the same time, and to predict the thermal conductivity of nanofluids.

The studies of Keblinski et al.[39,] and Eastman et al.[57] have proposed four possible mechanisms for the increase of the thermal conductivity in nanofluids, namely: Brownian motion of the nanoparticles; molecular-level layering of the liquid at the liquid/particle interface; the nature of heat transport in the nanoparticles; and the effects of nanoparticle clustering.

Particle forces

The interaction of nanoparticles in a nanodispersed system falls into the realm of colloids and interface science as "nanocolloidal fluids"[48]. Accordingly, the types of forces present in nanofluids are fall into two main categories. The first covers the classical forces that are governed by continuum mechanics, such as, those related to the momentum exchange between the solid and a fluid (primarily governed by Stoke's model to describe the fluid forces acting on a particle). In the second category, a number of dynamic interaction forces between nanoparticles are likely to be present and dominant at different time and length scales. An interesting study that addresses these interaction forces, responsible for enhancing the propensity for particle agglomeration and clustering in a nanofluid, is the one conducted by Sloan[58]. In his study the force are classified as: interfacial interaction (surface forces) - governed by DLVO theory (after Derjaguin and Landau[114], and Verwey

and Overbeek[115]), defines interparticle forces as the sum of van der Waals and electric double-layer contributions; random Brownian motion forces and collision forces. Although these forces were reported[58] to lead to uniformity in the viscosity (due to non-linear rheological behaviour), they were revealed to govern agglomeration and clustering of nanoparticles, leading to improved heat transfer by conduction, particularly in water based nanofluids.

When ionic liquids (i.e. molten salt fluids) are used as the base fluid, the oscillating layered structure force (represented by the matrix of liquid molecules around the nanoparticles) comes into play. An explanation of this phenomenon was first given by Israelachvili[49] who noted that the structural force arises once there is a change in the liquid density at the surface of nanoparticles, as they approach one other. This force may be thought of as the van der Waals force at small separations, with the molecular properties and density variations of the medium taken into account. This force is consequently dependent on the size, type and surface properties of the particles as well as the ionic concentration and density of the continuum. The influence of the interfacial layer thickness may then be used to describe the enhancement in the thermal conductivity in molten salt nanofluids.

2.7.3 Heat capacity

The literature on the heat capacity of nanofluids is extensive[100]. Bergman[101] studied the thermal properties of water–alumina nanofluids experimentally, and reported that the specific heat decreases substantially as the volumetric concentration of alumina nanoparticles increases. Conversely, the thermal conductivity of water–alumina nanofluids was enhanced, relative to the base fluid. Vajjha and Das[102] studied three different types of nanofluids with 2–10 vol. % of Al_2O_3, SiO_2, and ZnO nanoparticles in a 60:40 ethylene glycol–water base fluid. The specific heat of the three nanofluids were found to substantially decrease as the volumetric concentration of nanoparticles was increased. However, the specific heat was found to increase moderately with temperature for all nanoparticle types. Additionally, Zhou and Ni[103] observed that the specific heat of an alumina–water nanofluid decreased by 40–50% at a particle concentration of 21.7% by volume. The numerical model of Puliti et al. also predicted a lower specific heat of nanofluids with increasing concentration[100].

Other results were reported by Nelson et al.[104] who conducted an experimental study of polyalphaolefin nanofluids using a flow loop. They observed that the specific heat of nanofluids was increased by 50% with a dispersion of exfoliated graphite nanoparticles at a concentration of 0.6%, by weight. Also, Shin and Banerjee[105] reported a 26% enhancement of the specific heat of a molten salt (eutectic of 62% lithium carbonate and 38% potassium carbonate by weight) with a suspension of silica nanoparticles at a concentration of 1%, by weight. Shin and Banerjee[105] have reported a 14.5% enhancement in the specific heat of a chloride salt eutectic as well, using a dispersion of 1% by weight of silica nanoparticles (20–30 nm nominal diameter). In the latter, the dispersion behaviour of the nanoparticles was confirmed by scanning electron microscopy SEM. On the bases of their observations, Shin and Banerjee[105] proposed three independent thermal transport mechanisms (modes) to explain the enhancement of the specific heat and these are:

- Mode 1: enhancement due to higher specific surface energy of nanoparticles surface atoms, compared to the bulk material. At the surface of a nanoparticle, the energy is higher due to low vibrational frequency and hence higher amplitudes of the vibrations.

- Mode 2: enhancement due to interfacial interactions between nanoparticles and the liquid molecules that act as virtual spring–mass systems. This effect is present due to the extremely high specific surface area of the nanoparticles.

- Mode 3: liquid layering, already discussed in the earlier section with regard to the thermal conductivity enhancement. Solid-like liquid nanolayers adhering to the nanoparticles are more likely to have an enhanced specific heat due to a shorter intermolecular mean free path compared to the bulk fluid.

Because the specific heat is a fundamental property for many thermal engineering applications, there is a great need for additional experimental studies as well as numerical models on this key thermal property of nanofluids[100].

2.7.4 Viscosity

Beside nanofluid thermal conductivity and heat capacity, viscosity is an important transport property in the application of mass and heat transfer in nanofluid thermal systems such as heat exchangers, cooling and energy storage media. A review of the

available literature reveals that the viscosity of nanofluids increases with an increase in nanoparticle volume fraction and shear rate[96] but decreases with the temperature[97]. The smaller the diameter of the nanoparticles the more they interact with the surrounding fluid over a greater surface area, thus increasing the viscosity as the particle diameter decreases[98]. Additionally, the viscosity of nanofluids decreases with an increase in temperature causing the Reynolds number to rise, which leads to an increase in Nusselt number[99]. It has also been noted that an increase in viscosity will increase the Prandtl number but decrease the Reynolds number influencing heat transfer and pumping power[30]. Further, viscosity at the wall reduces due to migration of particles towards the centre of the tube[116].

Viscosity is an essential parameter for nanofluids flow since both the pressure drop and pumping power depends on it, thus a significant increase in nanofluids viscosity is highly undesirable. The general trends observed in nanofluids studies[43, 124, 203] indicate that the viscosity of nanofluids remains higher than the base fluid. Viscosity is typically higher in nanosuspensions with smaller particles and depending on the particle concentration and the strength of particle−particle interactions). Extended agglomeration and clustering of nanoparticles could result in a significant viscosity increase as the fluid microstructure provides resistance to fluid flow. Additionally, the shape of nanoparticle could affect the viscosity of suspensions. For instance, the use of elongated nanoparticles, showing higher viscosity than spherical particles, at the same operating conditions and volume concentrations. This behavior was explained by Sen et al.[43] as related to the presence of the boundary layers between nanoparticles and the liquid molecules, which are negligible in suspensions of micron-sized particles, but could contribute significantly to fluid properties at the nanoscale.

Prasher et al.[124] reported experimental results on the effect of shear rate on nanofluids' viscosity. Experiments were conducted using alumina (Al_2O_3) nanoparticles of three different diameters: 27, 40, and 50 nm, at three nanoparticle mass concentrations: 0.5%, 2%, and 3%. Then to observe the non-Newtonian behavior for dilute suspensions the viscosity measurements were carried out at various shear rates 0.7 – 100 s^{-1} and over a temperature range of 30-60°C. The results revealed that nanofluids behave as Newtonian fluids for up to 3% particle loading. The viscosity of nanofluids were found to be higher than can be predicted by Einstein's model, but this is likely due to nanoparticles aggregation. The analysis of Prasher et al.[124] also show that the relative increase in the

viscosity has to be more than four times larger than the relative enhancement in the thermal conductivity for nanofluids to be worse than the base liquid.

Sekhar and Sharma[203]. conducted a study investigating the correlation between viscosity and specific heat capacity characteristics of nanofluids. In their study, the non-Newtonian behaviour of nanofluids was discussed[203]. It was pointed out that the concentration of nanoparticles, can greatly affect the Newtonian behaviour of nanofluids. For example, the viscosity measurements on Al_2O_3 nanofluids in the volume fraction range of 1%–5% suspended for a fortnight, were found to behave as non-Newtonian fluids since they were forming agglomerates, which made the nanofluids highly viscous. However, up on re-ultrasonication of the same nanofluid samples they became Newtonian fluids again and so they have suggested more detailed studies to be conducted for the influence of agglomeration on the viscosity of nanofluids.

Up to the present time, achieving a high concentration of nanosuspension without a dramatic increase in viscosity remains a key challenge in nanofluid engineering. As to the use of surfactants to improve colloidal stability and viscosity of nanosuspensions, they were found to have an adverse effects on other useful properties, such as thermal conductivity of nanosuspensions[43]. This is attributed to the low thermal conductivity of surfactants that are formed on the surface of nanoparticles and act as a thermal insulator (resistance layer), therefore reducing the thermal conductivity. There is a pressing need for more investigation of nanofluid viscosity, which has major effects on the heat transfer and thermal conductivity of such multiphase flows.

2.8 Acoustic characterization of nanofluids

At present, little is known about the behaviour of nanofluids[133] in process equipment, particularly those with potential use in high-temperature applications (e.g. solar thermal plants). Measurements of nanofluid properties are usually limited by either the ability of available instrumentation or material compatibility of the sensing element. This is unfortunate as such measurements can provide critical information about optimal operating conditions, which is required if nanofluid technology is to be scaled-up for practical use. Acoustic techniques are ideal for characterizing single- and multiphase elastic fluids[134] due to the dependence of the speed of sound (acoustic velocity) on a number of parameters such as density, compressibility and temperature. Furthermore,

acoustic measurements provide a multitude of data such as time-of-flight, acoustic impedance, attenuation, and variations which can be used to monitor particle settling[135, 136], determine the particle concentration of a dispersion[137], and measure the critical transport velocity of a particle suspension in a flow[138].

The speed of sound in liquid mixtures and homogenous particle dispersions is affected by two critical properties; mean compressibility and mean density of the components in the system. This fundamental observation, according to Povey[134], was first made in 1941 by Wood[139], who applied it to liquid mixtures. However, the relationship between the sound velocity in a particle-liquid dispersion can be attributed to Urick[140]. In addition, the thermal conductivity of a liquid depends on the very rapid transmission of energy via molecular interactions[141]. This mechanism is best understood by considering the speed of sound in liquids, which is five to ten times larger than the speed of motion of the molecules themselves as determined by kinetic theory[141]. The best way to understand the speed of sound in liquids is by considering two colliding molecules, where the energy is transferred instantaneously from the centre of one molecule to the centre of another[141].

Most semi-empirical and theoretical methods used to determine the thermal conductivity, *k*, of liquids (and suspensions) are based on the empirical relation of Bridgman[142], which assumes that liquid molecules are arranged in a cubic lattice of a particular dimension, and that energy is transferred from one lattice plane to the next at the speed of sound for the given fluid[143]. According to Lin and Pate[144], the theoretical equation of Bridgman[142] was later justified by Powel et al.[145] for the thermal conductivity of liquids.

The work conducted by Chakraborty et al.[146] shows how an ultrasonic technique can be used to measure the concentration of nanoparticles in water based nanofluids, with the underlying principle being that the speed of sound in nanofluids is a function of its density and compressibility. Other research on the velocity of ultrasonic vibrations in molten salt was performed by Bockris and Richards[147], whose study gives details of the isothermal compressibility, speed of sound and specific heat ration of molten nitrate salts, as a function of temperature over the range of 300-500°C.

2.9 Theoretical studies of nanofluid

A variety of theoretical models have been developed for explaining the different heat transport mechanisms responsible for the enhancements reported from nanofluids

experimental studies[100], including: (i) collision of the base fluid molecules with each other; (ii) thermal diffusion of nanoparticles within the fluid; (iii) collision of nanoparticles with each other; and (iv) Brownian motion-induced nano-convection of particles (as a secondary dynamic mechanism). Further details of each of these mechanisms, and models of them, are given by Lee and Jang[117]. However, the disparities between conductivity data measured experimentally and model predictions suggests that conventional heat conduction models, developed for multiphase fluids containing larger particles (three to six orders of magnitude in diameter greater than nanoparticles) are inadequate for nanofluids, as detailed by Das et al. [46]. The current lack of a reliable theory capable of making accurate predictions of the thermal enhancement in nanofluids (with relatively low solid volume fractions) is therefore evident, as reported by Wang and Mujumdar[28].

With the aim of overcoming this issue, many researchers have tried to combine the static and dynamic mechanisms of thermal conductivity enhancement in nanofluids. Among the first to undertake such work were Ren et al.[118] who considered interfacial nano-layering and Brownian motion-induced convection. This was followed by Murshed et al.[119] in an attempt to derive a combined thermal conductivity model consisting of nanolayer, Brownian motion, surface chemistry and interaction potential elements. Xuan et al.[120] proposed a different thermal conductivity model that considers stochastic Brownian motion and nanoparticle aggregation, whilst Prasher et al.[121] combined aggregation kinetics with a Brownian motion-induced micro-convection model. The theoretical predictions of the latter model were later expanded to include nanofluid dependency on fluid chemistry and pH, time and viscosity effects[122-124].

2.10 Analytical & numerical studies of nanofluid

Some numerical models have been proposed to justify the enhancement of the thermophysical properties of nanofluids. CFD modelling of nanofluid systems fall into two categories. The single-phase approach assumes that continuum principles are still valid for the fluid. Here, it is assumed that suspended nano-sized particles follow the flow, and as such this methodology is simpler to implement and computationally much less expensive than explicitly resolving both phases. It should be noted that the assumption made in some CFD models that nanofluids behaved like as single-phase fluids maybe valid at very low solid concentration[106].

The alternative multiphase technique better models each phase separately, however this method is not commonly used[95] due to its computational complexity and limitations associated with long computing times. The latter technique is to be preferred when modelling nano-suspensions, as it is able to describe the key mechanisms and dynamic processes involved in such multiphase fluids. A number of researchers have used the two-phase assumption[58, 107]. Although both classical theories of single- and multiphase fluids may be applied to a certain extents, some numerical studies simulate nanofluids with different approaches from the single- or two-component non-homogeneous models[108, 109].

Also, the lattice Boltzmann model for nanofluids was adopted, by Xuan and Yao[110]. This interesting numerical investigation by Xuan and Yao[110] considered simulating the nanoparticle distributions and the flow of nanofluids using the lattice Boltzmann model. Their results showed that a higher temperature improves the diffusivity of nanoparticle within the fluid, which is an important factor responsible for the heat transfer enhancement in nanofluids. The same study also shows that the random motion of nanoparticles tends to flatten the temperature distribution near the boundary wall. Another numerical investigation was conducted by Xue et al.[111] using non-equilibrium molecular dynamics simulations. This study looked at the effect of liquid-solid interface on the interfacial thermal resistance and found that the simple monatomic liquid around the solid particle had no influence on the thermal transport either normal or parallel to the surface. The study suggested that the large improvement of thermal conductivity in nanofluids cannot be explained by thermal transport in the liquid-solid interface layer as previously highlighted by Wang and Mujumdar[28]. It is also possible that the improvement of the thermal conductivity of nanofluids occurs at an atomic scale, since it can be related to the transport of electrons in a medium having negligible electrical resistivity caused by scattering (known as ballistic phonon transport), or surface charge state[28].

A further development of these models and simulations with a higher number of combinations of nanofluids is necessary. The obtained predictions must be confirmed by experimental results and vice versa. More investigations involving combined simulation and experimental work at the same time are required.

2.10.1 Multiphase models

The suspension of nanoparticles in fluids is governed by the basic physical laws of conservation of mass, momentum and energy. Accordingly the forces acting on a solid

nanoparticle submerged in a liquid continuum can be expressed mathematically by means of a force-balance equation. Likewise, the forces exerted by the solid particles on the carrying liquid can be expressed in a similar way. These forces will depend on the physical properties of the carrier fluid, the system parameters (e.g. settling velocity) and particle concentration. Thus they can be categorized as follows, where our primary interest is in cases 1 and 2:

1) Collision-free (dilute) flows (also sometimes called one-way coupled): particles of low Stokes number and so they follow the fluid motions to a greater extent. As a result, particles do not influence turbulence, and so it is possible to compute the behavior of the fluid-phase and integrate the particle equation of motion without any coupling between the two[112];

2) Collision-dominated (low-to-medium concentration) flows (also known as two-way coupled): the statistical behaviour of the carrier phase (such as Reynolds stresses and turbulence energy spectrum) are affected by the presence of particles through momentum exchange between the solid and the liquid phases. However, the hydrodynamic or collisional interactions between particles are not significant[113];

3) Contact-dominated (dense) flow (or four-way coupled): particle-particle interactions are present and at higher volume fractions they might dominate the rheology of the system[113];

4) Particles moving in the system may also interact with the container boundary where other types of forces may apply.

One way of exploring these forces is by the use of numerical modelling. This approach will allow a multiscale system demonstration to be performed so as to determine the dominant transport mechanism that are responsible in nanofluids, to that observed in the experimental work.

2.10.2 Turbulent flow and heat transfer models

Various models were considered by researchers, to describe the mechanisms of flow and heat transfer of nanofluid, including fluid particle interaction in laminar flow and turbulent flow regions. Brownian motion and thermophoresis found to play an important role in laminar and turbulent nanofluid flow[126], whereas in the highly turbulent region, eddies affect the motion of nanoparticles as in a shallow cavity[125]. The numerical investigation

of Mohammed et al.[127] using Al_2O_3/water nanofluid, found that the wall temperature decreased and the wall shear stress increased with an increase in particle volume fraction at extreme heat fluxes of 1000 W/m^2. Whereas in the case of de-ionised water based nanofluids with CuO and Al_2O_3 nanoparticles, the three-dimensional steady state equation, Naviere Stokes equation and energy equation during SIMPLE algorithm, results into significant heat transfer enhancement[128]. For Al_2O_3, CuO, CNT and titanate nanotube (TNT) nanofluid at 0 – 6 vol% flows in laminar flow regime at constant heat flux[129], shows heat transfer coefficients of nanofluid was lower than the experimental data while the effect of Brownian motion of nanoparticles predicts the heat transfer coefficient more accurately.

The CFD approach, by solution of the continuity, momentum and energy equations shows that the highest enhancement in heat transfer is around 43.9% at Re = 200 and 5 vol. % over the base fluid, may likely lead to design of more compacted heat exchangers[130]. Additionally, for water- Al_2O_3 nanofluid (100 nm) at particle concentrations of 1–4 wt% under constant heat flux, using single and two-phase models, it was observed that heat transfer was enhanced by increasing the concentration of nanoparticles[131]. Further, Gori and Boghi[132] used DNS to study the three dimensional domains on nanofluid (treated as non-Newtonian fluids) at different Reynolds numbers. The investigation used a generalised Newtonian fluid (GNF) turbulence model, with the predictions showing that the relation between the viscosity fluctuation and its derivatives indicted the non-Newtonian behavior of nanofluid.

Turbulent heat transfer in a channel is characterised not only by the Reynolds number but also by the Prandtl number of the fluids. Kawamura et al.[133] undertook DNS simulations of turbulent heat transfer for various Prandtl numbers ranging from Pr = 0.025 to 5 with a Re_τ = 180 flow using a finite difference method-based solver. They assumed a constant volumetric heating with a uniform wall temperature. Profiles of the mean temperature, temperature variance and turbulent heat flux were obtained, with detailed budgets within the transport equations for these quantities reported.

The difficulties in identifying an established theory to predict accurately the heat transfer characteristics of nanofluids is emphasised by many researchers. Thus some researchers deal with nanofluids as a single phase fluid rather than a two-phase mixture. However, others deals with nanofluids as a multiphase system whereby the particle-liquid

interaction and the relative movement between particle and liquids is believed to play an important role in affecting the convective heat transfer performance of nanofluids.

2.11 Concluding remarks of the literature review

In this chapter, the key pieces of literature relevant to studying nanofluids have been summarised and detailed. Upon doing so, it becomes clear that there is a sufficient amount of work carried out over the last couple of decades surrounding nanofluids. From an analysis of the direction of both numerical and experimental work, it seems that there is great interest in the thermal conductivity of nanofluids, not to mention the flow behaviour and heat transfer mechanism, and the interaction between the base fluid and solid nanoparticles. To resolve these, highly resolved simultaneous three-dimensional velocity and temperature fields must be captured. This is a very difficult process to achieve in a real system, but is quite feasible with a highly-resolved numerical simulation.

For the effective use of nanofluids in thermal engineering systems, new technologies are needed to monitor and maintain the degree of physical and thermal stability of nanofluid. In this study the use of acoustic techniques has therefore been proposed since they are ideal for characterizing nanofluids due to the dependence of the speed of sound on a number of material properties such as density, compressibility and temperature. In the past decade new experimental and computational methods have become possible, forming the majority of fundamental nanocolloidal and multiphase flow research.

Present simulation work is mainly focused on systems with single-phase approach such as that of Azari et al.[106] and Kawamura et al.[133], whereas multiphase simulations carried out at different volume concentration (1-5 vol %) and over a wide temperature range are sparse. This gap in the literature can be filled by carrying out a piece of work directed towards accurately simulating the interactions of nanoparticles and their influence on the thermal conductivity of nanofluids. In fact, a strong understanding of the stability and thermal conductivity of nanoparticle suspensions in fluids using a multi-scale computational technique (LPT) would not only benefit and build upon the current literature, but it is also capable of generating new avenues for analysis and discussion such as the influence of Brownian motion, fluid viscous drag, interparticle collisions and DLVO attraction and repulsion forces on the level of nanofluid thermophysical stability for instance. This in turn should provide explanations of the enhanced thermal behaviour of the nanofluids in both stagnant and flowing environments.

The proven enhancement in the conductivity of fluids affected by the addition of nanoparticles has great potential to assist the development of commercial nanofluid technology aimed at energy efficient and sustainable processes. Despite these advances in the field, there remains a need to investigate the exact flow and heat transfer behaviour of nanofluids in the process equipment. In the present work, therefore, a study is made of multiphase turbulent channel flows (of both water and molten salt liquids) containing a nanoparticulate phase, using a high-accuracy DNS simulation technique. Simulations will be performed with an emphasis on elucidating the dynamics surrounding how particles interact with both the turbulence itself and other particles in the presence of turbulence and a temperature gradient. Combining the recent interest in nanofluid simulation with the newly developed experimental techniques would allow detailed elucidation of nanofluid behaviour, at a level of detail surpassing that of previous work.

3 METHODOLOGY

3.1 Introduction

This chapter gives a detailed description of the relevant theory, experimental technique and numerical methods used within this project to investigate nanofluids. First, the acoustic technique used to determine the speed of sound and thermal properties of nanofluids will be explained. The multiscale computational modelling of nanofluids in a stagnant environment will be described. The spectral element-based fluid phase DNS solver, Nek5000, shall be introduced. To simulate the particulate phase an LPT is developed to run alongside the DNS solver and so these shall also be explored.

3.2 Nanofluid characterization by speed of sound

3.2.1 Speed of sound of nanofluids

The variation of the sound speed in water is anomalous[134] in that it does not vary monotonically with temperature[134, 148], yet the ultrasound speed in water is routinely measured as it is easy to obtain, is used for the calibration of many acoustic instruments, in manufacturing and laboratory applications,[149] and water is a fundamental component of many products and reactions used in the chemical industry

The most likely explanation of these anomalous characteristics is the nature of the structure of liquid water molecules, which are linked together by weak hydrogen bonds to give a complex long range structure[148]. Of particular importance in this connection is the relationship between the compressibility and density of water molecules versus temperature (at standard atmospheric pressure), as given by Kell[150], see Figure 2. As a result, both the compressibility and density of water are relatively high at low temperatures (0-10°C). However, as the temperature of water increases, the compressibility decreases sharply, while density shows an inverse exponential decline over the temperature range 10-100°C. Considering these effects in terms of the sound speed formula as given by the Urick[140] (Eqn. 3-1 below), it is clear that the change in density with temperature brings an attendant change in the sound speed of the medium.

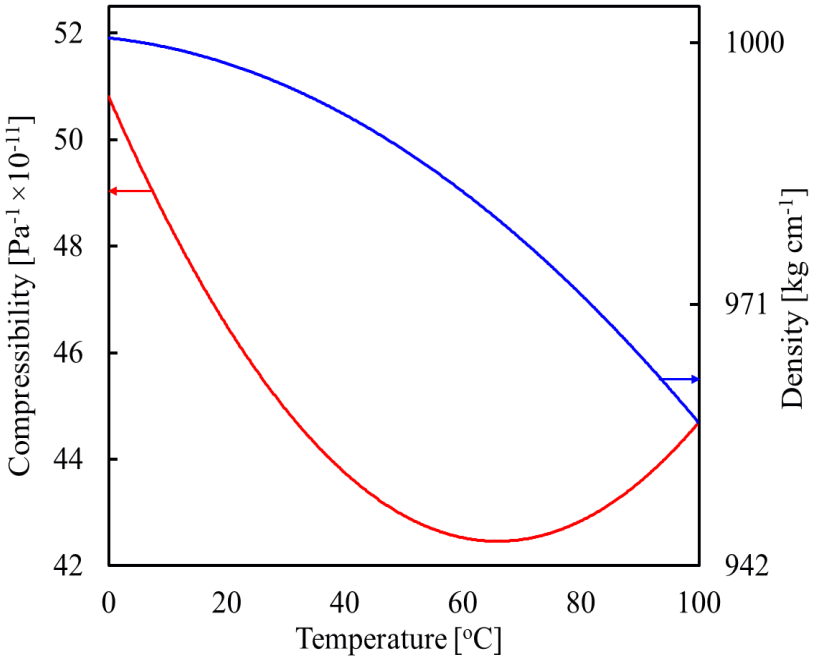

Figure 2. Compressibility and density of water with temperature at standard atmospheric pressure.

Liquid mixtures and homogenous particle dispersions in water are treated by assuming that the speed of sound is mainly affected by the mean compressibility and mean density of the components in the system. This fundamental observation, according to Povey[134], was first made in 1941 by Wood[139], who applied it to liquid mixtures. However, the relationship between the sound velocity in a particle-liquid dispersion can be attributed to Urick[140], hereafter referred to as the Urick equation:

$$C = \frac{1}{\sqrt{\kappa_s \rho}}, \qquad \kappa_s = \sum_j \phi_j \kappa_{sj}, \qquad \rho = \sum_j \phi_j \rho_j, \qquad 3\text{-}1$$

where C is the velocity of a sound wave in the dispersion, κ_S the adiabatic compressibility, ρ the density, ϕ the volume fraction of the dispersed phase and the subscript j refers to the constituent phases. As stated by Povey[134], for one material dispersed within another, the compressibility and density can be written as:

$$\kappa_s = \phi\kappa_{s_2} + (1-\phi)\kappa_{s_1}, \qquad \rho = \phi\rho_2 + (1-\phi)\rho_1, \qquad 3\text{-}2$$

in which the subscripts 1 and 2 refer to the continuous and dispersed phases, respectively. Eqn. 3-1 and 3-2 can be used to determine C if κ_s and ρ of both phases are known.

Another form of the Urick equation is[140]:

$$C = \sqrt{\frac{C_p(\gamma - 1)}{\alpha_p^2 T}}, \qquad 3\text{-}3$$

where C_p is the specific heat at constant pressure (isobaric), α_p the coefficient of thermal expansion (at constant pressure), T the absolute temperature, and γ the ratio of heat capacities (also known as the isentropic index), defined as $\gamma = C_p/C_v$, with C_v being the specific heat at constant volume (isochoric). For water at atmospheric pressure C_p, α_p and γ vary considerably with temperature, the net result being an increase in the sound velocity with temperature.

Sound waves propagate as a series of compressions and expansions that change the local kinetic energy of the medium that they pass through. As temperature is a measure of the internal energy of the system, it varies during sound wave propagation. However, the variations in density of the liquid medium take place rather more rapidly with temperature. As a result, the process of heat flow through the test cell (described below) is assumed to be adiabatic. On this basis, Eqns. 3-1 to 3-3 are used throughout this study to calculate the sound velocity in both pure water and water based nanofluids, assuming the propagation of sound to be adiabatic[134]. For an adiabatic process involving a liquid, both the pressure and volume remain constant.

In principle, measured values of the speed of sound and density of the medium can be used to calculate other thermodynamic parameters that are useful for the modelling of nanofluids. The variation of these parameters with temperature can be calculated from a set of thermodynamic relations using the equation of state (see Appendix A).

3.2.2 Predictive correlation between speed of sound and thermophysical properties

The thermal conductivity of a liquid depends on the very rapid transmission of energy via molecular interaction[135]. This mechanism is best understood by considering the speed of sound in liquids, which is five to ten times larger than the speed of motion of the molecules themselves as determined by kinetic theory. The best way to understand the

speed of sound in liquids is by considering two colliding molecules, where the energy is transferred instantaneously from the centre of one molecule to the centre of another[135].

Most semi-empirical and theoretical methods used to determine the thermal conductivity, k, of liquids (and suspensions) are based on the empirical relation of Bridgman[142], which assumes that liquid molecules are arranged in a cubic lattice of a particular dimension, and that energy is transferred from one lattice plane to the next at the speed of sound for the given fluid[143]. According to Lin and Pate[144], the theoretical equation of Bridgman[142] was later justified by Powel et al.[145] for the thermal conductivity of liquids. The resulting equation, which can be used for pure fluids, is as follows:

$$k = 2.8K_B v^{2/3} C, \qquad 3\text{-}4$$

where K_B is the Boltzmann constant and v the molecular volume of the liquid, that is, the molecular mass divided by the density.

The second formulation is due to Eyring[135], who supposes that only the rotational and translational degrees of freedom are effective in transferring the energy in a polyatomic liquid (e.g. water). Accordingly, the empirical relation of Bridgman[142] can be expressed as:

$$k = 2.8K_B v^{2/3} \gamma^{-1/2} C. \qquad 3\text{-}5$$

Here, the heat capacity ratio γ (also referred to as the Eucken correction[135]), should be taken as the predicted value from both model simulation and speed of sound measurements. In other words, it is used to convert the isothermal compressibility κ_T to the adiabatic compressibility κ_s measured in speed of sound experiments[135, 152], since sound compression waves are adiabatic in reality, rather than isothermal. According to Hirschfelder[141], Eqn. (3-5) applies extremely well with a mean deviation of around 10% for a large number of liquids. Bridgman also pointed out that his formula gives the correct temperature dependence of the thermal conductivity of liquids at atmospheric pressure[135].

Although most published data on γ are for gases, the importance of γ for liquids is highlighted in a number of studies[135, 153, 154], and it has been referred to as a fundamental physical property of fluids with great importance in reversible adiabatic processes. The

value of γ typically varies from 1.30 to 1.66 in gases[152] and from 1.1 to 1.36 in liquids[155], as a function of temperature and pressure. On account of its contribution to sound absorption in liquids, it has been suggested that γ in liquids might be referred to as the sonic anisotropy[153] (the phenomenon that determines the direction of ultrasonic wave propagation and its asymmetry).

As to the theoretical framework and the use of the Bridgman equation[142] (i.e. Eqn. 3-5), Chebbi[156] developed a model to correlate the speed of sound and thermal conductivity in nanofluids. The results suggest that the enhancement of thermal energy and heat transfer were at the speed of sound in nanofluids (e.g. via consecutive collisions between nanoparticles).

From this it follows that the speed of sound using the Urick equation, Eqns. (3-1 to 3-3), can be related to $\gamma, \kappa_s, \kappa_T$ and density as follows:

$$C = \frac{1}{\sqrt{\kappa_s \rho}} = \left(\frac{C_p}{C_v}\frac{1}{\kappa_T \rho}\right)^{1/2} \qquad 3\text{-}6$$

Eqn. (3-4) can now be re-written in terms of the thermodynamic properties as:

$$k = 2.8 K_B v^{2/3} \frac{1}{\sqrt{\kappa_s \rho}} \qquad 3\text{-}7$$

Eqn. 3-5 can be treated similarly:

$$k = 2.8 K_B v^{2/3} \left(\frac{\gamma}{\kappa_T \rho}\right)^{1/2}. \qquad 3\text{-}8$$

Measuring the heat capacity at constant volume C_v can be extremely difficult for liquids and solids because small temperature changes typically produce large pressure changes, meaning that the containing vessel must be able to withstand very high pressure variations. Instead it was decided here to predict the thermal conductivity *k* for nanofluids at different concentrations and constant pressure using a numerical simulation[157] together with experimental measurements of density and the speed of sound, *C*, over a range of

temperatures. The modified Bridgman equation, Eqn. (3-8), is then used to solve for the heat capacity ratio γ at constant volume, by fitting to equations of the form $\gamma = \gamma(\Phi,T)$ and $k = k(\Phi,T)$.

3.2.3 Materials

Alumina nanoparticles (Al_2O_3, 80 % α/ 20 % γ - mixed-phase crystalline, 99.9 % purity) were purchased as a powder from US Research Nanomaterials Inc.[158] The differences between α- and γ-Al_2O_3, are mostly related to their specifications and structural properties. In terms of structure, the α-Al_2O_3 is trigonally structured and γ-Al_2O_3 on the other hand has a cubic shape coupled with a face-centered cubic. As to the specifications, α- and γ-Al_2O_3 differ in the followings: α-Al_2O_3: amorphous, color-white, crystal form-α, purity-99.9 %. In γ-Al_2O_3, the form is nano-powder, color-white, purity-99.97 %. There is also a difference in the temperature behavior between the α- and γ-Al_2O_3 structures (or phases) with temperatures ranging from 1050 to 1100 and 400 to 600°C, respectively. The supplier reported average particle size was d_p = 50 nm and this was experimentally verified using the Zetasizer Nano ZS90 (Malvern Panalytical Ltd.), see Figure 4. Scanning electron microscopy (SEM) of the powder (Figure 3) confirmed particle clusters composed of the primary particles.

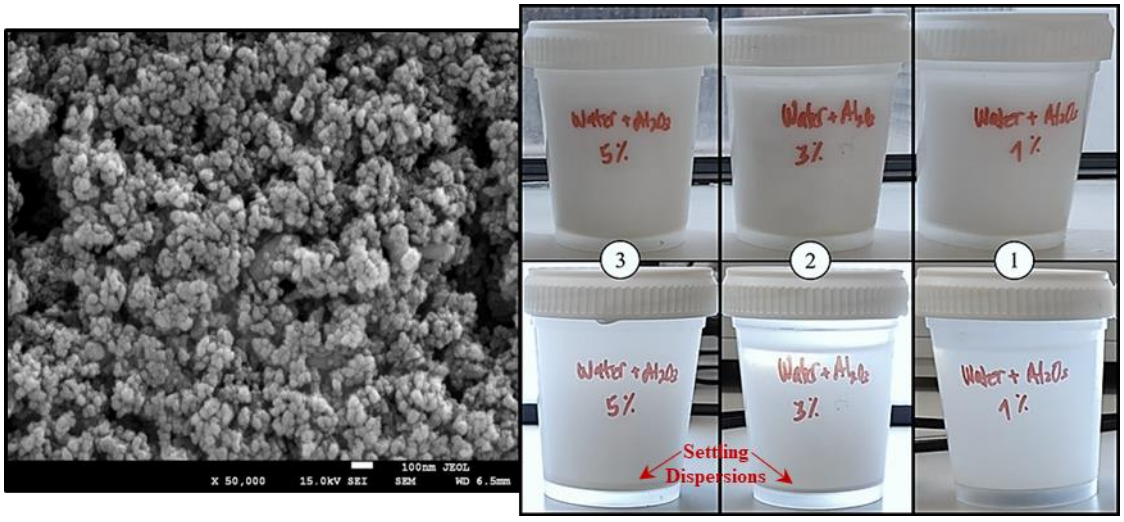

Figure 3. (Left) SEM image of Al_2O_3 nanoparticles (99.9% pure, d_p = 50 nm). (Right) Images of Al_2O_3 water-based nanofluids, from right to left: 1 water with 1 vol% nanoparticles; 2 with 3 vol%; and 3 with 5 vol%. Samples on the top have been sonicated, samples at the bottom after settling for 4 weeks in the laboratory.

3.2.4 Preparation of water based nanofluids

The nanofluids were prepared (through a two-step method) in distilled water at pH 6.8. Two different ultrasonic systems were used to disperse the nanoparticles in the base fluid, namely, a probe-type sonicator (505 Sonic Dismembrator, Fisher Scientific) for 12 min and a bath-type sonicator (XUBA Analogue Ultrasonic Bath, Grant Instruments) for 250 min, to disperse the primary particles. As the probe sonicator is directly immersed in the suspension, it is expected to deliver a higher power (≈ 500 W) to the nanosuspension than the ultrasonic bath (≈ 35 W). In contrast to bath sonication which was performed at room temperature, the probe sonicator operates at higher amplitudes and is more effective at inducing cavitation and generate heating. Thus for experiments using the ultrasonic probe, the nanofluid was placed in a separate glass container to prevent evaporation of the fluid and container damages caused by the elevated temperature. It should also be noted that for both sonication methods the total amount of energy delivered to the sample was constant.

To enhance particle dispersion and suspension stability, the suspension pH was set at pH = 8.5-9.2 and the particle zeta potential = 24 mV, as measured using the Zetasizer Nano ZS90. Under these conditions it was possible to disperse the particles to ~50 nm by sonication and the resulting particle suspension was visually assessed to remain stable during the acoustic measurements. Figure 3 (right) shows the results of sonicated specimens versus those at the bottom to settle for four weeks in the laboratory (Figure 3, samples 1, 2 and 3). Although the level of brightness is different between the two sets of images, the photographs clearly show the settled bed of nanoparticles after settling for four weeks. Without sonication the particle size distribution was found to be very broad (Figure 4, noting that the abscissa is logarithmic) with particle clusters greater than a few microns.

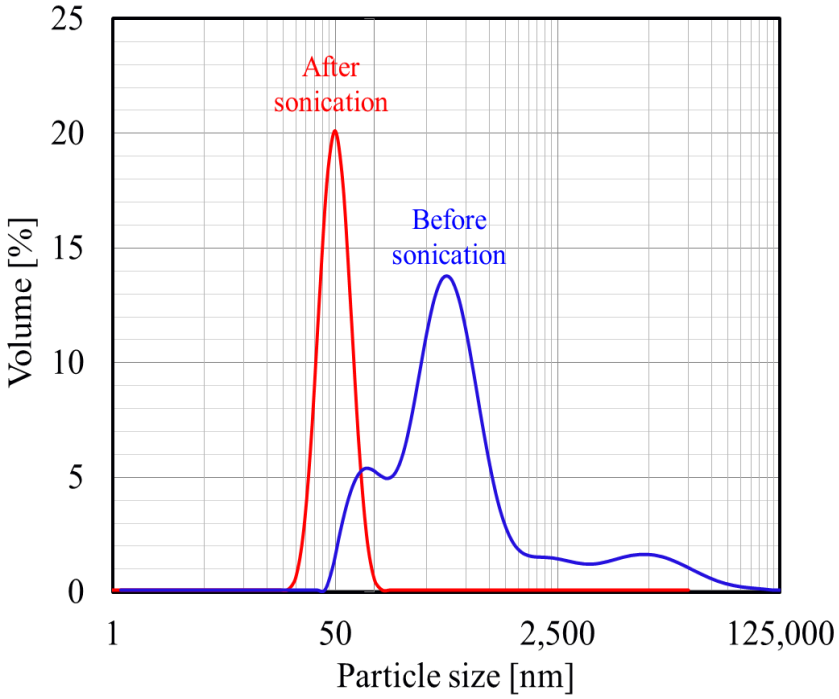

Figure 4. Particle size distribution of Al_2O_3 nanoparticles (99.9% pure, dp = 50 nm) measured with Zetasizer Nano ZS 90 before (blue) and after (red) sonication with 505 sonic dismembrator – high power tip sonicator for increased time periods.

With the exception of the sample before sonication, which shows primary and secondary peaks in the range $100 < d_p < 2500$ nm, the distribution for all other sonicated samples showed a single peak at $d_p = 50$ nm, similar to the manufacturer's quoted size. This means that significant aggregation is expected to take place, as a high sonication power was needed to break-up all the aggregates.

To quantify the stability characteristics of the nanofluid, the zeta potential was measured under different pH conditions. Tests were also conducted in a Zetasizer Nano ZS 90 (Malvern Panalytical Ltd, Worcestershire, UK), using 0.01wt.% of alumina nanofluid at a temperature $T = 25^{o}$C. The pH value of the system was adjusted with NaOH and HCl solution using a precise pH meter S220 (Mettler-Toledo Ltd. Leicester, UK). The isoelectric point was found to be in the region of pH = 8.5-9.2.

3.2.5 Physical properties of the materials

A detailed description of the physical properties of pure water and the particle species is given with sources in Table 3 and Table 4, respectively.

Table 3. Physical properties of pure water used as the base fluid.

Parameter	At T=25°C
Sound speed[a], C / ms^{-1}	1493
Thermal conductivity[b], k / W $m^{-1}K^{-1}$	0.608
Heat capacity[b], C_p / kJ $kg^{-1}K^{-1}$	4.1796
Density[b], ρ / kg m^{-3}	997.1
Compressibility[c], κ_S / Pa^{-1}	44.8×10^{-11}

The above parameters can be expressed as function of temperature T (in K) as follows:

$C = 1.40238744\times10^{3} + 5.03836171T - 5.81172916\times10^{-2}\,T^{2} + 3.34638117\times10^{-4}\,T^{3} - 1.48259672\times10^{-6}\,T^{4} + 3.16585020\times10^{-9}\,T^{5}$ (C in ms^{-1}, 273 - 373 K) (3-9)[a]

$k_L = -0.2758 + 4.6120\times10^{-3}T - 5.5391\times10^{-6}T^{2}$ (k in W $m^{-1}K^{-1}$, T_{min} = 273 K ($k_L = 0.57$) and T_{max} = 633 K ($k_L = 0.424$)) (3-10)[b]

$C_p = 92.053 + -3.9953\times10^{-2}T + (-2.1103\times10^{-4}T^{2}) + 5.3469\times10^{-7}T^{3}$ (C_p in J $mol^{-1}K^{-1}$, 273 - 615 K) (3-11)[b]

$\rho_L = 0.14395 / 0.0112^{1+(1-(T/649.727)\text{^}0.05107}$ (ρ in kg m^{-3}, 273 - 648 K) (3-12)[b]

$\kappa_S = (50.88496 + 0.6163813T + 1.459187\times10^{-3}T^{2} + 20.08438\times10^{-6}T^{3} - 58.47727\times10^{-9}T^{4} + 410.4110\times10^{-12}T^{5}) / (1 + 19.67348\times10^{-3}T)$ (κ_S in bar^{-1}, 273 - 423 K) (3-13)[c]

[a] See Ref.[159]

[b] See Ref.[160]

[c] See Ref.[150]

Table 4. Physical properties of the particles Al_2O_3 (d_p= 50 nm, component purity 99.9%).

Parameter	At T=25°C	Remarks
Sound speed[d], C / ms^{-1}	6420	longitudinal waves
Thermal conductivity[e], k / W $m^{-1}K^{-1}$	37	
Heat capacity[e], C_p / kJ $kg^{-1}K^{-1}$	0.775	
Density[d], ρ / kg m^{-3}	3850	
Compressibility[d], κ_S / Pa^{-1}	39.4×10^{-13}	

The above parameters can be expressed as function of temperature T (in K) as follows:

$k = 5.5 + 34.5 \times \exp.[-0.0033\times(T - 273)]$ (k in W $m^{-1}K^{-1}$, 273 - 1573 K) (3-14)[e]

$C_p = 1.0446 + 1.742\times10^{-4}T - 2.796\times10^{4}T^{2}$ (C_p in kJ $kg^{-1}K^{-1}$, to 1773 K) (3-15)[e]

[d] See Ref.[161]

[e] See Ref.[162]

3.2.6 Acoustic test cell

A high-temperature test cell was designed to study the thermal performance of nanofluids under both static and dynamic conditions. It consisted of a temperature-controlled cylindrical vessel fitted with an axial agitator (IKA LR 1000, Germany). The cell had a flat base which acted as an acoustic reflector, and the ultrasonic transducers were placed at the top end of the cell facing downwards. The cell was fitted with temperature sensors

that allowed measurements to within ±0.01°C. The basic principle of the experimental setup is shown schematically in Figure 5.

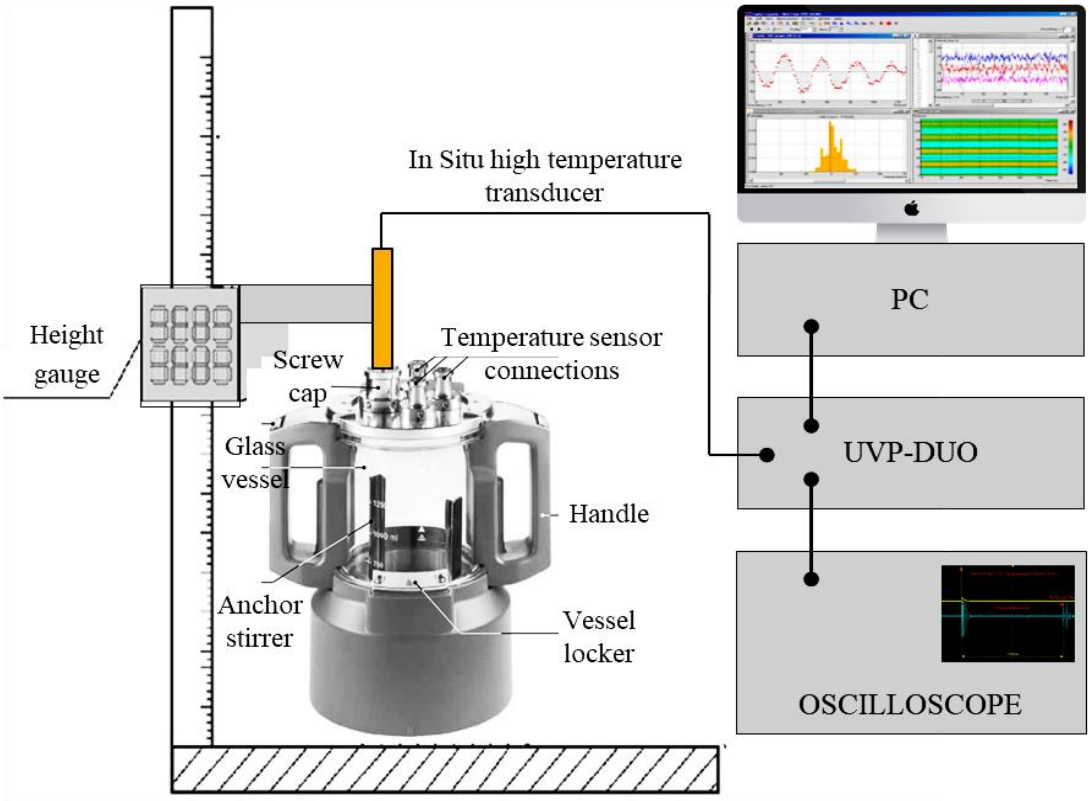

Figure 5. Schematic of the test cell experimental setup for nanofluid sound velocity and thermal conductivity measurements.

An ultrasonic signal processing unit (UVP-DUO, Met-Flow, Lausanne, Switzerland) was used as a signal generator with two ultrasonic emitter-receiver transducers. This ultrasonic systems is capable of characterizing nanofluids with high precision, with the main sources of uncertainty being the probe position height and the orientation accuracy of the probe giving a combined error of (±0.17mm), the oscilloscope peak-to-peak resolution (±0.18μs) and the uncertainty in temperature measurements (±0.1°C); for further details, see Appendix B. Analysis of these errors demonstrates that the temperature variation is negligible compared to other sources of error such as probe position, based on the error analysis presented in Appendix B.

Two types of emitter-receiver probes were used in this study, both operating at 4 MHz: standard (0-60°C) 4 MHz probes (Imasonic SAS, Besançon, France), active diameter 5 mm; and a high-temperature model (Ionix, Huddersfield, UK) to operate over a wider range of temperatures (–40 °C to +380°C), active diameter 10 mm. A backscattered

pressure wave is produced by suspended particles which produces a voltage in the transducer. This echo signal was monitored and displayed on a digital oscilloscope (WaveSurfer 3024, Teledyne LeCroy, Glasgow, UK).

3.2.7 Measurements of speed of sound

The test cell was designed such that the transducers were in contact with the nanofluid. The cell operates on a time-of-flight basis over a known distance. The echo voltage signal was recorded by an oscilloscope through the test section of the cell in a vertical, one-dimensional profile. The test section and ultrasonic probe are shown in Figure 6.

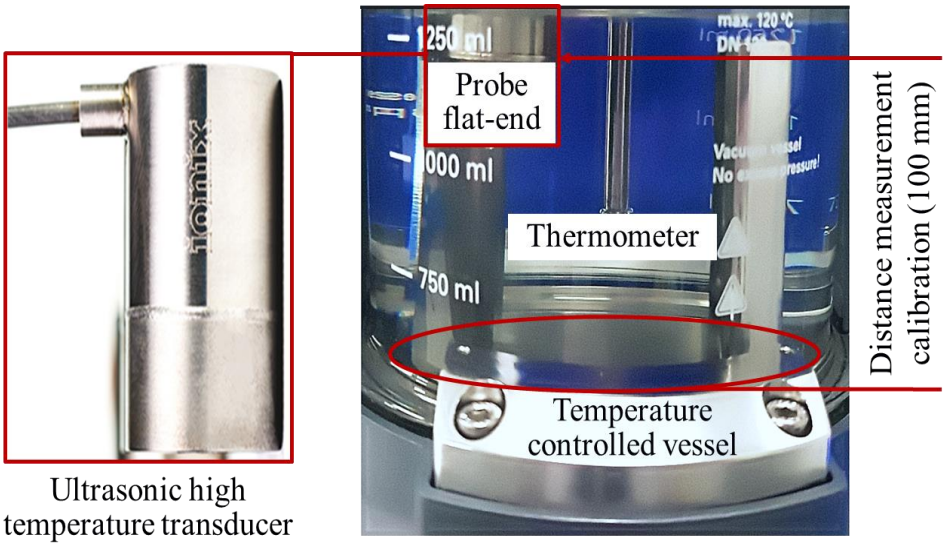

Figure 6. (Left) High-temperature transducer used for the speed of sound measurements. (Right) Photograph of the test section of the nanofluid thermal cell.

A 1 L volume of nanofluid was used so that the system could be well controlled and all dispersions were degassed and well mixed.

3.2.8 Distance calibration

Pure water was used to validate the measurement method because the test fluid is reliable and reference data is available. The distance between the probe tips and the base of the cell was set to 100 mm using a height gauge, (with accuracy including orientation of probe of ±0.17 mm; see Appendix B) as shown in Figure 6, giving a total measurement distance of 200 mm (after travelling through distance h = 100 mm, total = 2h). Figure 7 shows the reflected signal between the ultrasonic probe and base of the cell.

The ultrasonic signal processing unit was used as a signal generator, and triggered the oscilloscope; see the left side of Figure 7. It was found most appropriate to acquire a waveform within only one triggering interval (the repetition frequency) and repeat the acquisition a number of times for multiple measurements, which were then averaged. There are two indications, one from the initial pulse of the probe, and the second due to the back wall echo.

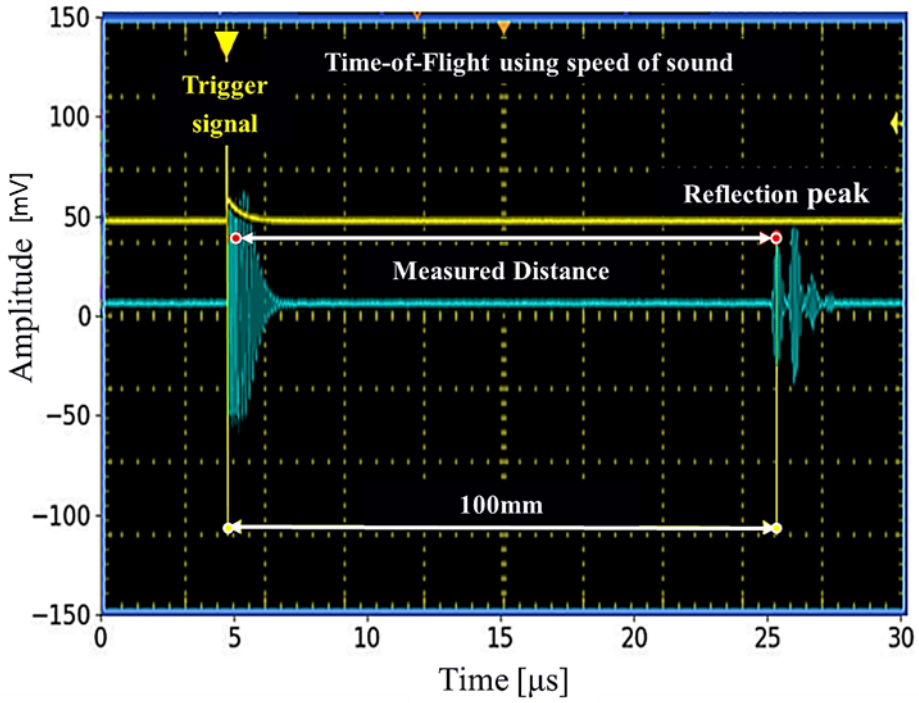

Figure 7. Screenshot of ultrasonic pulse captured by oscilloscope over test distance of 100 mm. Trigger signal in yellow, received signal in blue.

The complete measurement principle of this experimental setup is illustrated in Figure 8, showing how an ultrasonic pulse is emitted by the probe into the fluid inside the testing cell and then how this signal is captured by the oscilloscope.

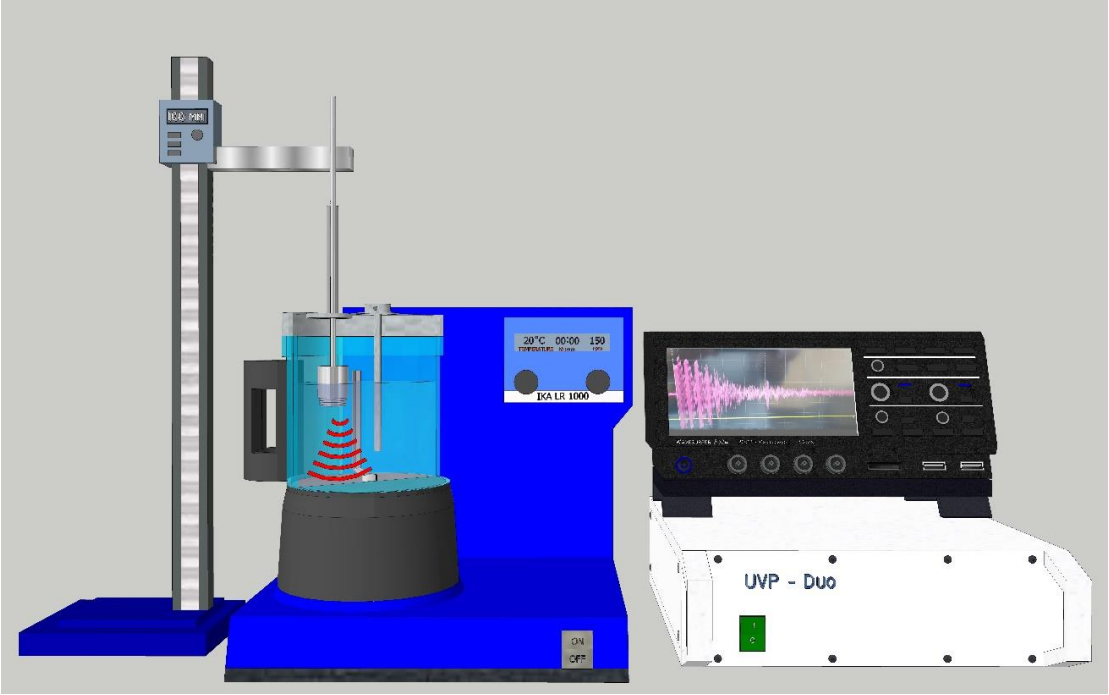

Figure 8. Measurement principle of the water based experimental setup showing an ultrasonic pulse emitted by the probe into the testing cell and captured by oscilloscope.

The steps followed to perform the water based nanofluid speed of sound experiments is illustrated in Figure 9.

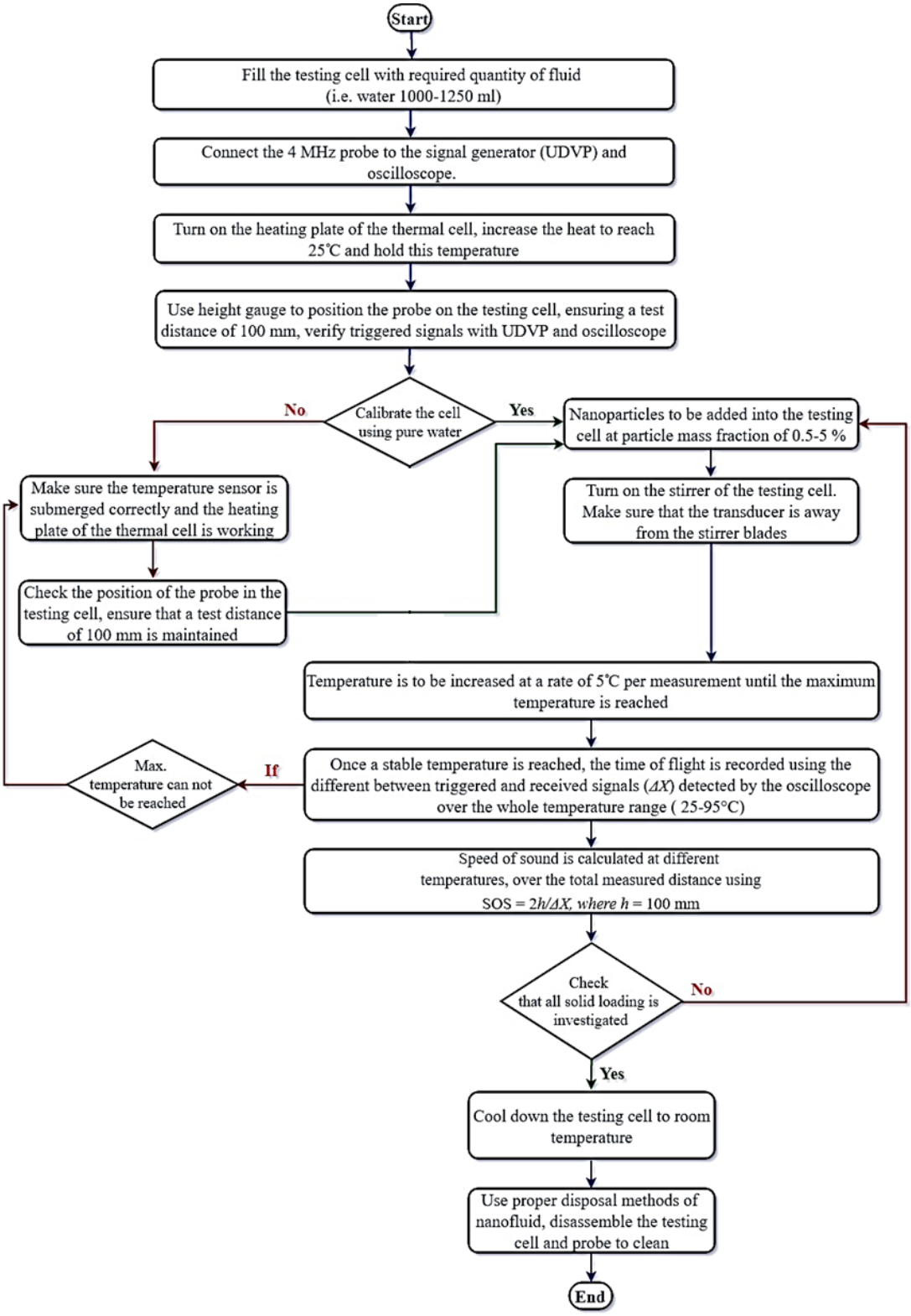

Figure 9. The procedure of the water based speed of sound experiment is illustrated with a flowchart.

3.2.9 Molten salt nanofluids

In-situ characterization of the molten salt nanofluids is considered using a high-temperature crucible furnace and the same transducer and ultrasonic signal processing unit, explained in Section 3.2.6. The basic principle of the experimental setup is schematically illustrated in Figure 10. Both speed of sound and thermal properties of the formulated molten salt nanofluid is studied across a range of conditions including temperature 250 – 500°C. The speed of sound measurement is then correlated with molten salt thermophysical properties from numerical simulation and DSC characterization studies at the same temperatures. The molten salt stability rig is also used to verify the formation of aggregates and to examine nanoparticles dispersion stability in nanofluids. The main equipment used to build a high-temperature thermal storage cell is shown in Figure 10. The measurement principle of the high temperature experimental setup is illustrated in Figure 11, showing how an ultrasonic pulse emitted by the transducer (in the form of mechanical vibrations) gets transmitted through the fluid in the testing cell and captured by the oscilloscope.

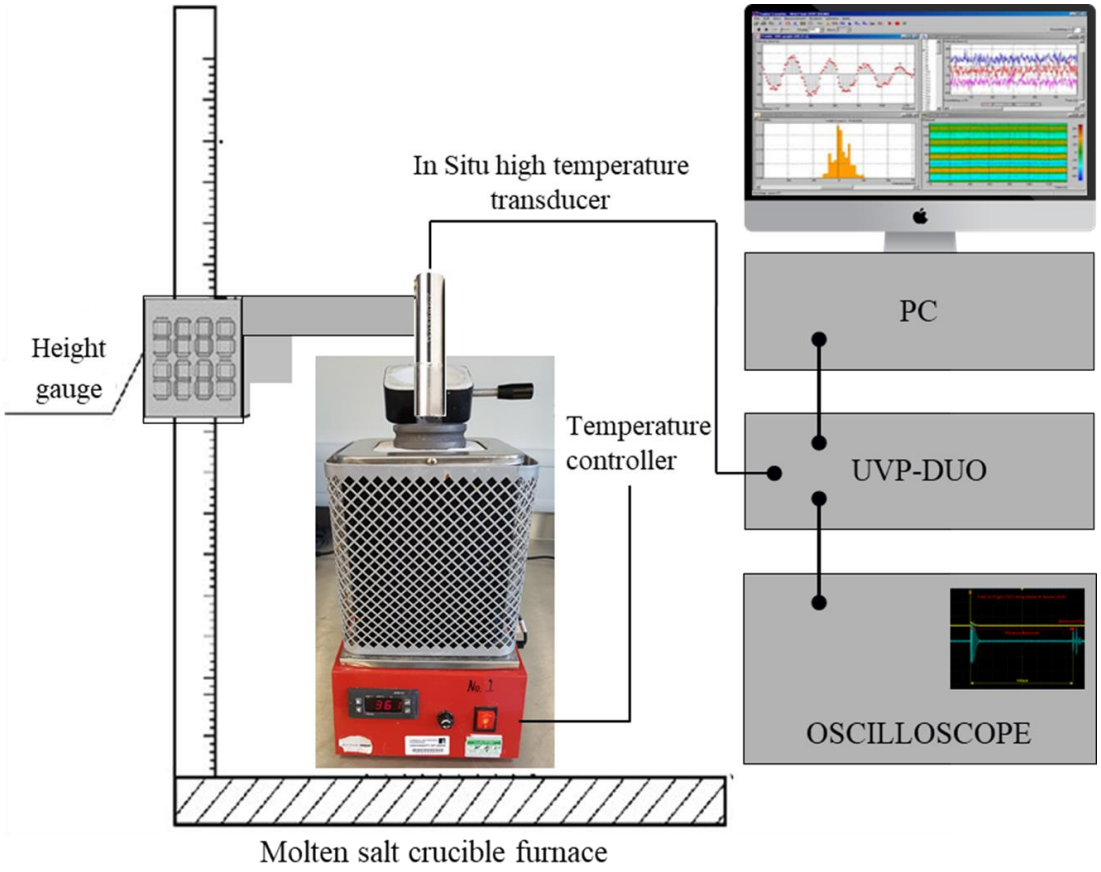

Figure 10. Schematic view of the experimental setup for molten salt nanofluid sound velocity and thermal conductivity measurements.

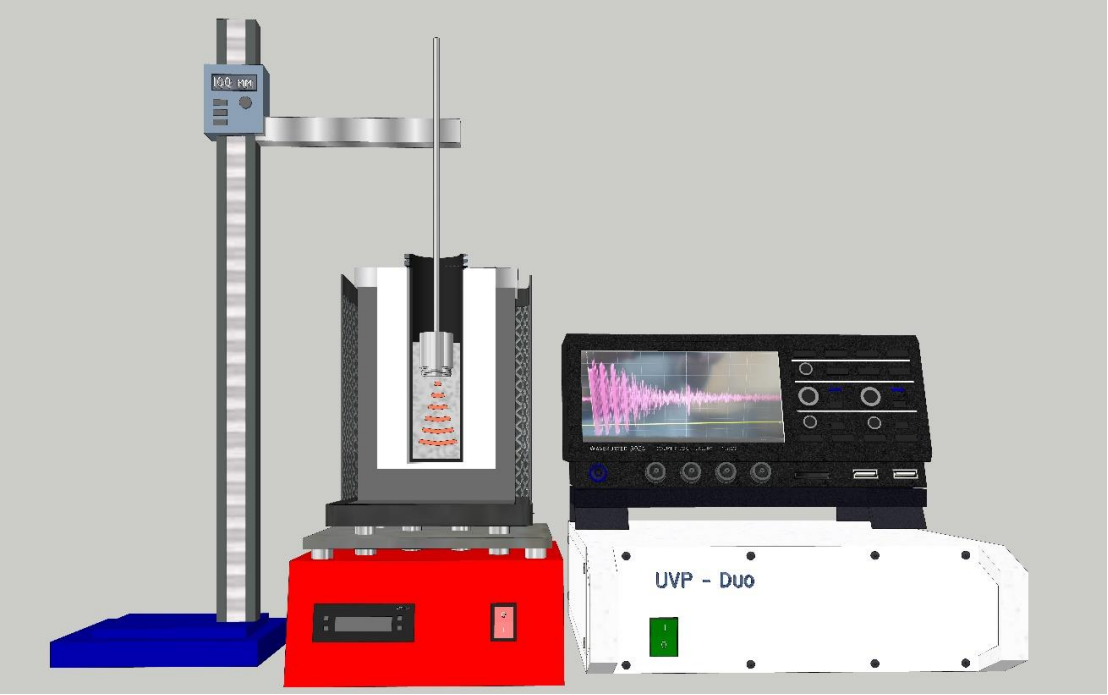

Figure 11. Measurement principle of the molten salt experimental setup showing an ultrasonic pulse emitted by the probe into the testing cell and captured by oscilloscope.

3.2.10 Preparation of salt based nanofluids:

The molten salt mixtures were prepared from Sodium nitrate ($NaNO_3$, ReagentPlus®, ≥99.0 %) and Potasium nitrate (KNO_3, ReagentPlus®, ≥99.0 %) obtained from Sigma-Aldrich Company Ltd., these were assorted into the right solar salt (a binary mixtures of nitrate salts $NaNO_3$:KNO_3 in 60:40 wt. %) (See Figure 12).

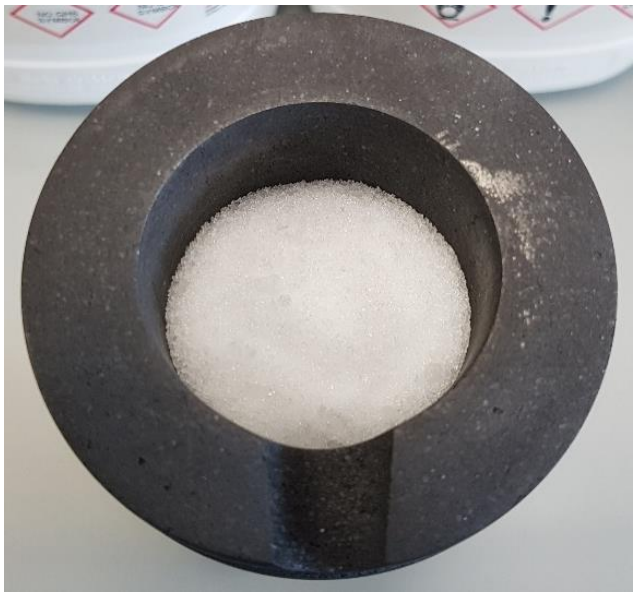

Figure 12. Nitrate salt mixture consisting of 60 wt. % sodium nitrate ($NaNO_3$) and 40 wt. % potassium nitrate (KNO_3), known as “Solar Salt” placed in a graphite furnace crucible.

A detailed description of the physical properties of the solar salt mixture is given with sources in Table 5.

Table 5. Physical properties of pure solar salt (in the liquid phase) used as the base fluid.

Parameter	At T=410°C
Sound speed, C / ms^{-1}	1680
Thermal conductivity[f], k_L / W m^{-1}K^{-1}	0.5
Melting temperature[f], °C	222
Heat capacity[f], C_p / kJ kg^{-1}K^{-1}	1.513
Density[f], ρ / kg m^{-3}	1830
Compressibility[g], κ_S / Pa^{-1}	19.8×10^{-11}
The above parameters can be expressed as function of temperature T (in K) as follows:	
k_L = 0.075439 - 2.77×10^{-4}(T -273) + 3.49×10^{-7}(T -273)^2 – 1.474 ×10^{-10}(T -273)^3 (k in W m^{-1}K^{-1}, T_{min} = 573 K (k_L = 0.43) and T_{max} = 873 K (k_L = 0.63))	(3-16)[f]
C_p = 1396.044 + 0.172 T (C_p in J mol^{-1}K^{-1}, 573 - 873 K)	(3-17)[f]
ρ_L = 2263.628 – 0.636 T (ρ in kg m^{-3}, 573 - 873 K)	(3-18)[f]

[f] See Ref.[163]

[g] See Ref.[164]

After obtaining a homogenous binary nitrate salt mixture, alumina nanoparticles (Al_2O_3, 80 % alpha / 20 % gamma, 99.9 % pure, d_p = 50 nm) obtained from US Research Nanomaterials Inc. in dry powder form were introduced in the salt mixture with the following ratio: 1 wt. %; 3 wt. % and 5 wt. %. This was followed by uniform mixing for around 35-45 minutes to ensure that nano-particles had been well dispersed within the salt mix (see the left side of Figure 13). The mixtures were then sieved to remove the few large aggregate remaining and kept in labelled jars ready for testing (see the right side of Figure 13).

Figure 13. Example of binary nitrate salt doped with alumina nanoparticles (Al_2O_3, 80% alpha / 20% gamma, 99.9% pure, d_p = 50 nm) samples produced using the dry mixing process (1 wt. %; 3 wt. % and 5 wt. % from left to right, respectively). (Left) In this particular case, glass jars ware used to mix a total amount of 350 g solar salt per batch, each consisting of 210 g of $NaNO_3$ and 140 g of KNO_3. (Right) samples kept in labelled glass jars.

To melt the required quantities of the nitrate salt mixtures (of binary nitrate salt $NaNO_3$:KNO_3 in 60:40 wt. %) for speed of sound measurements, weighed amounts of the individual salts were loaded into high-purity crucibles (graphite, EG75), the crucible is then placed in the furnace chamber and were heated in the crucible open to the atmosphere (Figure 14). The temperature was initially maintained at approximately 150°C to allow the water of hydration of these nitrates constituent to evolve slowly. After visual indications of vapour evolution ceased, the melts were heated to 350°C to 450°C, periodically stirred, and maintained at an elevated temperature for at least one overnight period before cooling and being ready for thermal property determinations.

It should be noted here that we first produced the molten salt nanofluid at different particle concentrations 0.5 – 5.0 wt. %. We then focused on the particle weight fraction of 0.5 and 1.0 wt. %, which corresponds to the volume fraction of 0.25 and 0.49 vol. %, respectively. The particle mass fraction 1.0 wt. %. was found to be an upper bound that we were able to test with the present speed of sound experimental setup. However, for other thermal testing (i.e. DSC) the full range of particle concentrations 0.5 – 5.0 wt. %. was conducted.

Figure 14. Solar salt mixture when the graphite crucible is placed in the furnace. (Left) pure salt being melted; (Right) nanofluid with 1 wt. % Al_2O_3 nanoparticles fully melted.

3.2.11 Test parameters

Here we describe the experiment for measuring the speed of sound in molten salt nanofluids for temperatures between 250 and 500°C. Prior to loading a new working nanofluid into the furnace, the graphite crucible was properly flushed and dried to clean any residues from the components in the testing section of the cell. In each experiment,

measurements were performed after steady-state conditions were achieved. Steady-state condition was defined in these experiments to be when a stable temperature is reached, at a rate of 25°C per hour until the maximum temperature of 500°C is reached. The digital thermostat of the thermocouples attached to the heating element of the furnace, was monitored and used to verify the basis for the steady-state temperature measurement, as shown in Figure 15.

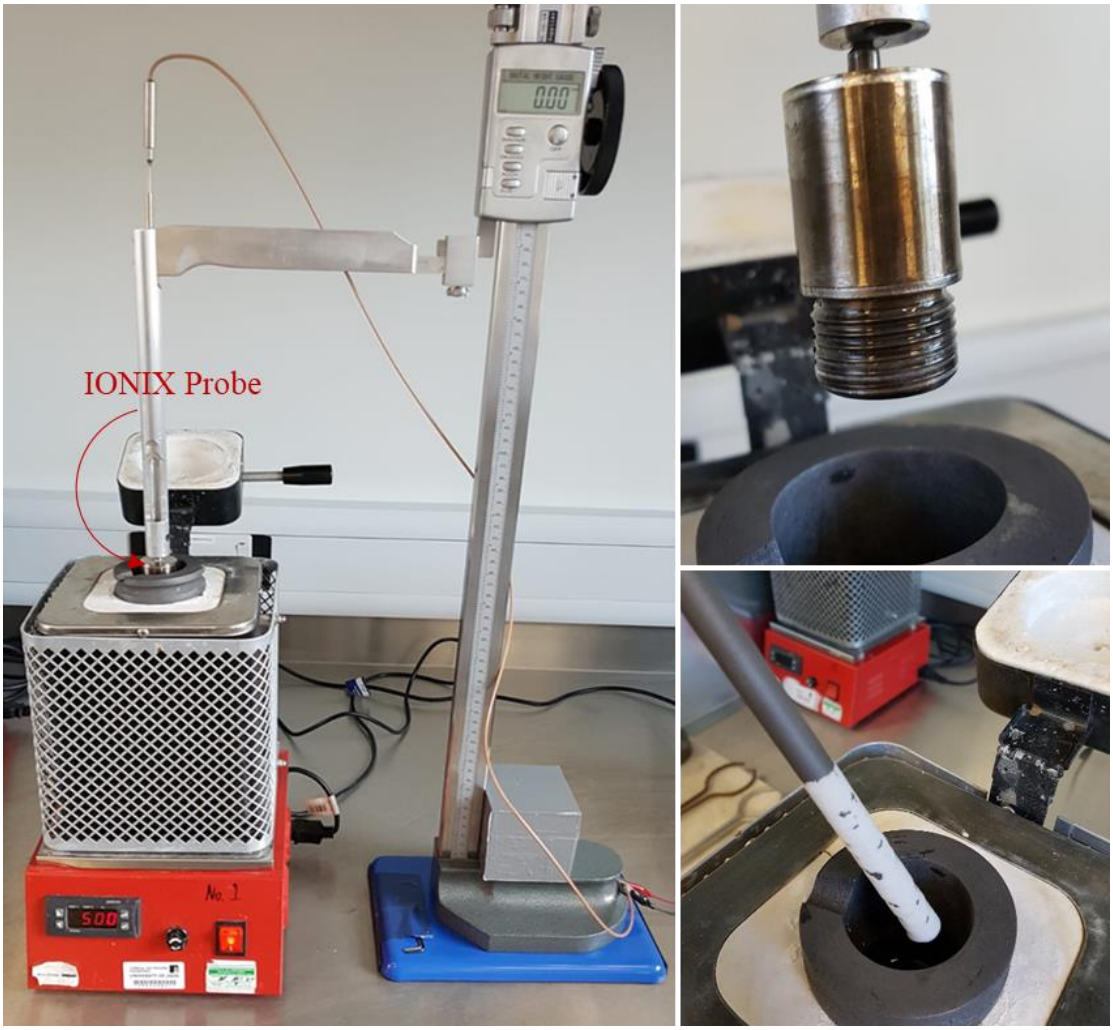

Figure 15. Molten salt experimental setup. (Left) Temperature monitored with the digital thermostat and distance of the probe was monitored/maintained at a constant value using the digital readout of the height gauge. (Top-right) ultrasonic probe being retracted from the molten salt. (Bottom-right) molten salt mixing rod.

Each test was run at a given temperature that was maintained constant throughout the entire test. As discussed in section 3.2.8, the range of speed of sound measurements attainable by the ultrasonic probe was the limiting parameter in the experiments. In addition to measuring the speed of sound at a constant temperature, the distance of the probe through the fluid was also kept constant at a predetermined value (see section

3.2.8). The distance of the probe was maintained at a constant value using the digital readout of the height gauge shown in Figure 15. Once the melting temperature of the salt mixture (222°C) is reached, the ultrasonic probe was wheeled down insuring that the probe is submerged into the molten salt for all experiments. This temperature range was chosen to conform to the typical operating conditions on a thermo solar plant that utilize molten salt as the energy storage medium.

To verify the accuracy of the results experiments were performed in triplicate and repeated three times with similar results. The probe distance calibration and the operation of the signal generator and oscilloscope through the test section of the cell can be found in section 3.2.9. The procedure of the molten salt nanofluids experiments is schematically presented in Figure 16.

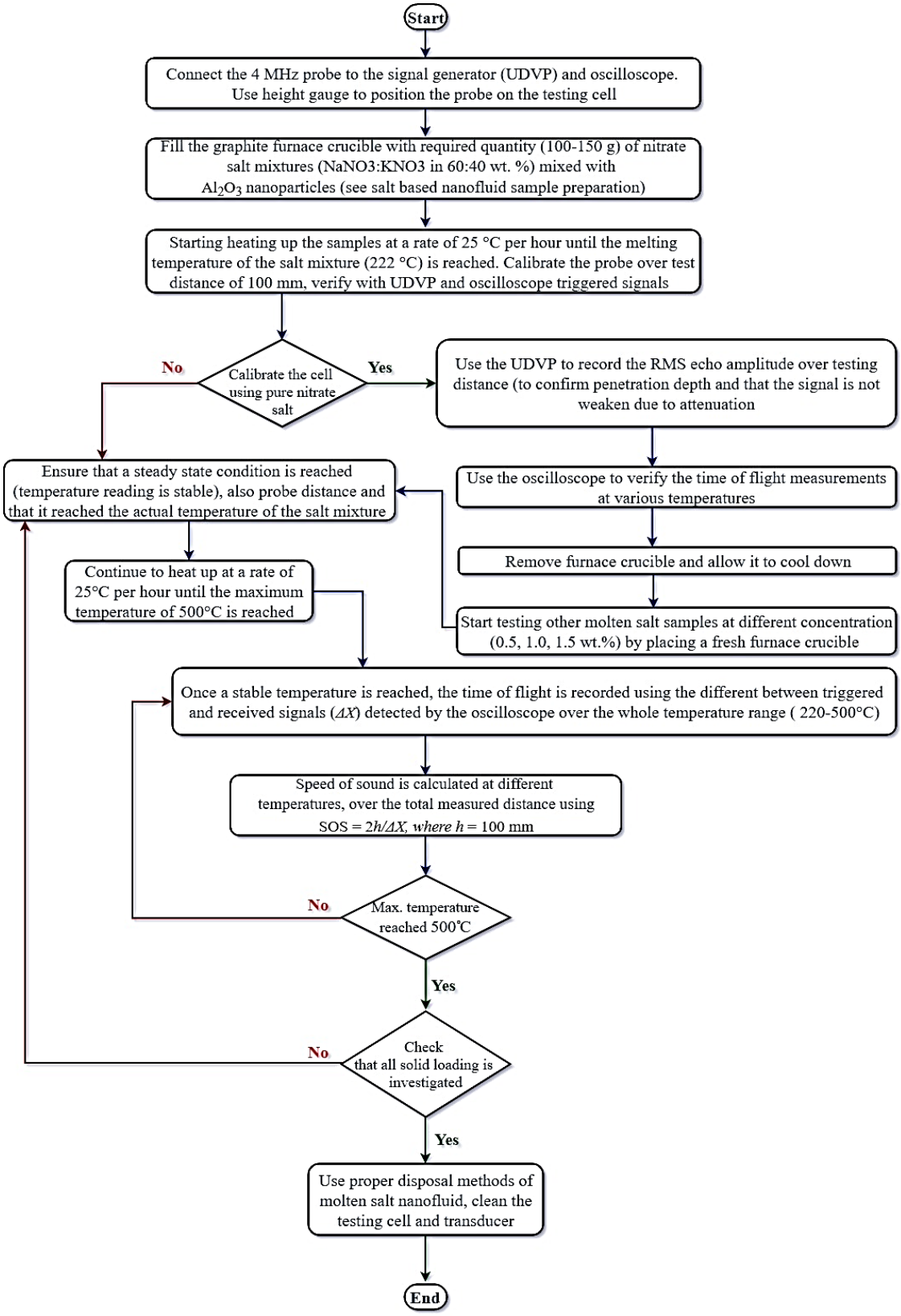

Figure 16. The procedure of the salt based speed of sound experiment is illustrated with a flowchart.

3.2.12 Ultrasonic waveguide

Part of the experimental research focussed on developing novel acoustic methods for measuring the material and flow properties of high temperature multiphase suspensions. One of which was the development of a novel ultrasonic waveguide sensor that can be used as buffer-rod in high temperature molten nitrate salts. The main idea of using the waveguide is to protect the piezoelectric crystal in the ultrasonic transducer against salt, chemicals, and high-temperature corrosive environments. Several design aspects were initially considered including: material and acoustic properties; geometrical parameters; wettability (used as an indicator of the mutual coupling properties between the solid and liquid); corrosion resistance; thermal properties; cladding and transducer/BR interface with the ultrasonic coupling agent (e.g. using specific type of acoustic gel).

The most important properties when creating a suitable waveguide is the proper selection of the material of construction and the geometric shape. These properties are crucial for the accuracy and reliability of the acoustical measurements. Previous studies[165-167] and from our own work revealed that in a cylindrical geometry near the tip of the waveguide, the main signal can be reflected, hence a huge amount of trailing-waves are generated. These trailing-waves will therefore interfere with signals used in the measurements and result in additional measurement errors. After careful consideration, and with the intention of improving the propagation of acoustic signal we were able to design the optimum configuration, of two different types of waveguides to be used for different purposes. Both are tapered waveguides; the first is single tapered, while the second is double tapered, as shown in Figure 17.

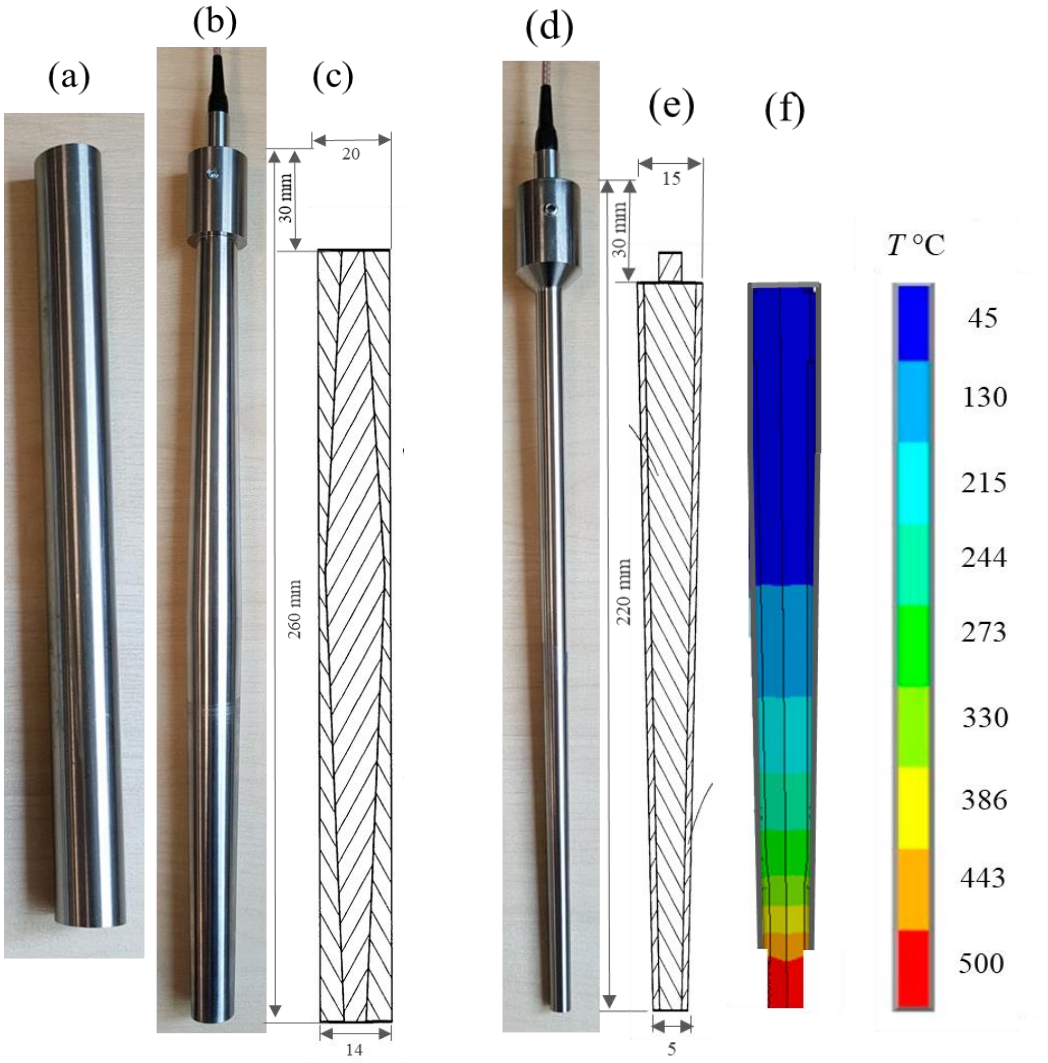

Figure 17. High temperature ultrasonic waveguide made out of: (a) Original titanium buffer rod. (b) External view of the double-tapered waveguide and (c) schematic view. (d) External view of the single-tapered waveguide and (e) schematic view. (f) Temperature distribution along the waveguide. Note that temperature profiles are only indicative of expected changes.

These waveguides are made out of special titanium alloy and were designed and fabricated in-house at the University of Leeds. With the newly developed devices several technical challenges were overcome, allowing online ultrasonic testing in the desired media without damaging the ultrasonic probes. Moreover, the waveguides did not only serve the lab-scale requirements, but could be scaled up to suite other industrial applications, especially those where conventional ultrasonic transducers cannot be directly placed in contact with the process media, due to high temperature, incompatible chemicals, rough surfaces and in harsh environments (i.e. molten metals, nuclear waste, to name a few).

3.3 Differential scanning calorimeter

Using the differential scanning calorimeter (DSC) (Mettler Toledo, DSC1/700), various thermo-physical properties of the both water based and salt based nanofluids were investigated. Regarding DSC tests, it should be noted that these tests are performed using the Mettler Toledo, DSC platinum 30 µL crucibles (ME-51140842) with lead. These crucibles were selected because of their superior thermal characteristics and thermochemical compatibility. In addition, this type of pan displays both very high melting point (i.e. with maximum temperature range up to 1600°C) and resistance to corrosion. The consistency of these pans for high temperature nanofluid testing were reported in similar studies[168] and they were compared with other available standard types (i.e. Aluminium, Alumina and Stainless Steel). The current study proved that these pans are very stable over repeated heating and cooling cycles. These pans can be described as very rigid, and will not be affect by the DSC robotic hands, hence will always keep their original shape, see Figure 18.

The cleaning procedure for the pans involved sonication of the crucibles in deionised water for 30 minutes followed by transferring the pans to a beaker containing 5M hydrochloric acid that should then be sonicated for another 30 minutes. The pans are then cleaned in water to remove any acid contamination, and finally dried in an oven at 80°C for 1-2 hours.

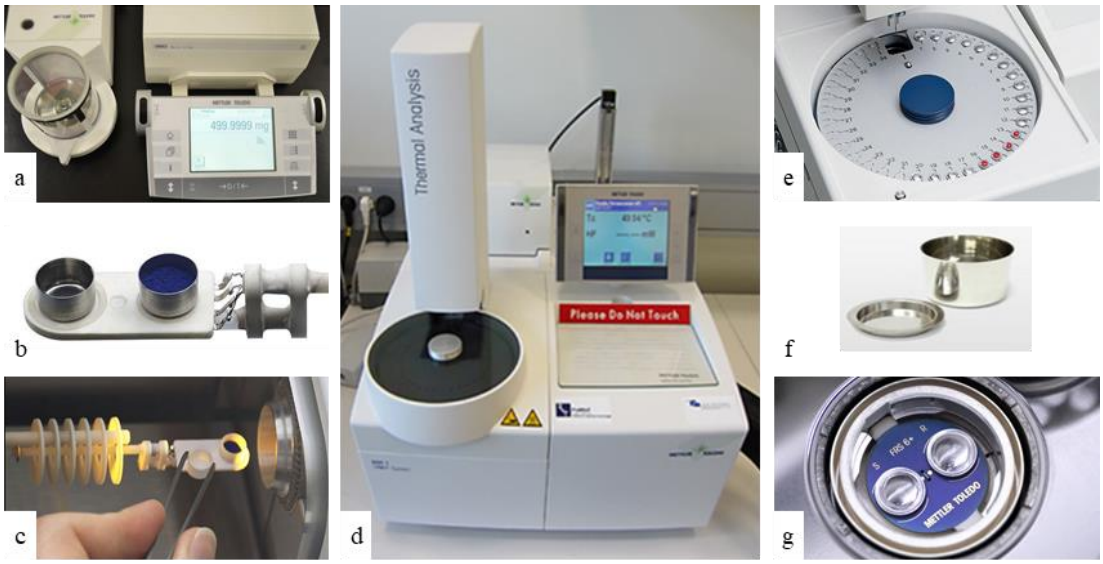

Figure 18. TGS/DSC Device and components: a) Ultra-micro-balance; b) TGA pans sensor; c) reference pan robotic arm; d) TGA/DSC thermogravimetric analyser with small furnace; e) samples rotary disc; f) Platinum 30 µl crucible (Pan); g) reference pan compartment.

Differential scanning calorimetry (DSC) analysis was performed using the setup shown in Figure 18, in which both pure fluids and fluids with nanoparticles were analysed at concentrations ranging from 0.5-5 vol. %. Follows is the procedure developed for DSC sample preparation and testing.

1. Bulk nanofluid sample preparation:

    a. Here are the steps to prepare water based nanofluid samples for DSC testing:

    - The required quantity of water (100 mL) is placed in 4 sample containers

    - Nanoparticles equivalent to 0.5, 1 and 2 wt. % are weighed

    - Nanoparticles are mixed with 100 ml of water

    - Samples are sonicated for 3-4 hours to minimize nanoparticle settling.

    b. The steps to prepare salt based nanofluid samples for DSC testing are:

    - The required quantity of a salt mixture (100 gm) is placed in 4 sample containers

    - Nanoparticles equivalent to 1, 3 and 5 wt. % are weighed

    - Nanoparticles are mixed with nitrate salts in the dry powder form

    - Mixing is applied to insured the uniform distribution of nanoparticles (see section 3.2.10.).

2. DSC sample preparation:

    - Empty crucible and lid are weighed and recorded

    - Dispersed water based samples are transferred into standard DSC testing crucible (40µL), and salt based samples into high temperature platinum crucible (30µL), containing 15-30 mg each

    - Using the sample sealing crimp press, testing crucible is placed on the press die, the lid is then replaced, and both crucible and lid are positioned correctly before pressing the plunger down

    - For salt mixture, the crucibles are filled to around 50% and the lid is placed in

    - Salt samples are weighed with crucible and lid

- Samples net weight are recorded and subtracted from the total weight.

3. Define temperature program (on the experiment window of STARe software):

   -Two temperature program are created for water and salt samples

   -The isothermal temperatures is set, heating and/or cooling rates, dynamic temperature, and type of sample holder.

4. Blank curve subtraction:

   - Two empty crucibles are placed on DSC (one used as a reference and the other contains the tested sample)

   - The temperature program on the experiment window is created

   - The run blank curve for experiment is marked

   - The starting temperature, crucible weight, position of the blank crucible are defined.

5. Heat flow measurement:

   - The prepared samples are loaded on the DSC

   - Temperature program created on the experiment window is switched on

   - The starting temperature, crucible weight, position of the blank crucible are defined

   - Water based samples are heated from $0^{o}C$ to $95^{o}C$ at a rate of 10 ^{o}C /min, and was held for a given time before it was cooled down from $95^{o}C$ to $0^{o}C$ at a rate of -10 ^{o}C /min

   - A complete cycle of heating/cooling per water sample takes about 30 minutes

   - Salt based samples are heated from $0^{o}C$ to $500^{o}C$ at 5 ^{o}C/min rate, and were then set in isothermal for 5 minutes before cooling them down from $500^{o}C$ to $0^{o}C$ at a heating rate of -5 ^{o}C/min

   - A complete cycle of heating/cooling per salt sample takes about 205 minutes

   - An average of four trials for every mass fraction were performed to achieve precise measurements

- Typical heat flow curves are shown in Figure 19.

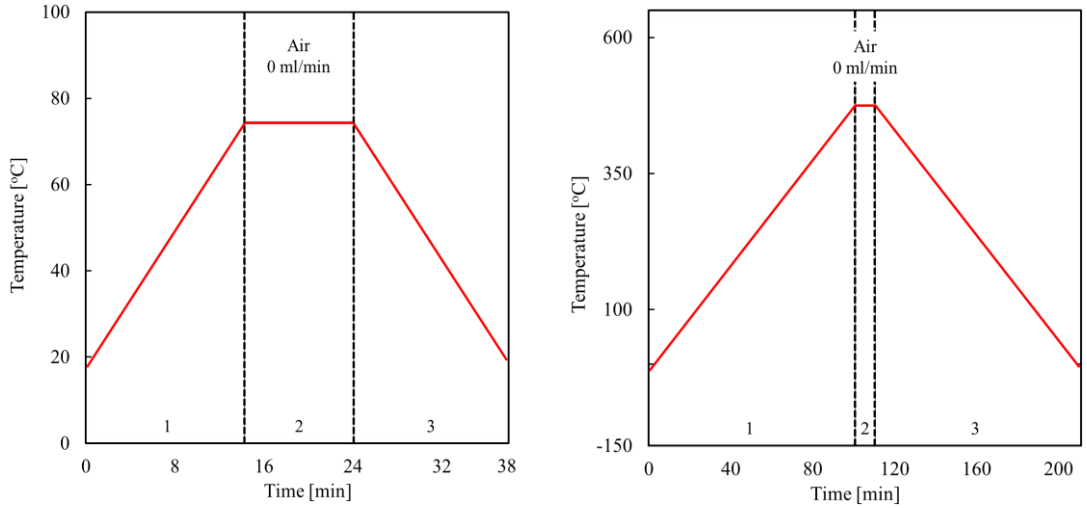

Figure 19. Differential scanning calorimetry curve showing the heating and cooling curve of samples: (Left) water based nanofluids; (Right) molten salt based nanofluid.

6. Specific heat measurement (direct method):

   - Heat flow values are viewed on evaluation window

   - Specific heat values from the STARe software are automatically generated, after obtaining heat flow values

   - Specific heat values resulting from direct method measurements can be viewed on DSC tab.

- Steps 5 and 6 are repeated three times on the DSC for each sample prepared.
- Steps 2, 4, 5 and 6 are repeated on the DSC for each set of trial.
- For salt samples, the platinum crucibles are cleaned after every trial, and dried before repeating step 2 onwards.

The procedure of the DSC experiment is schematically presented in Figure 20.

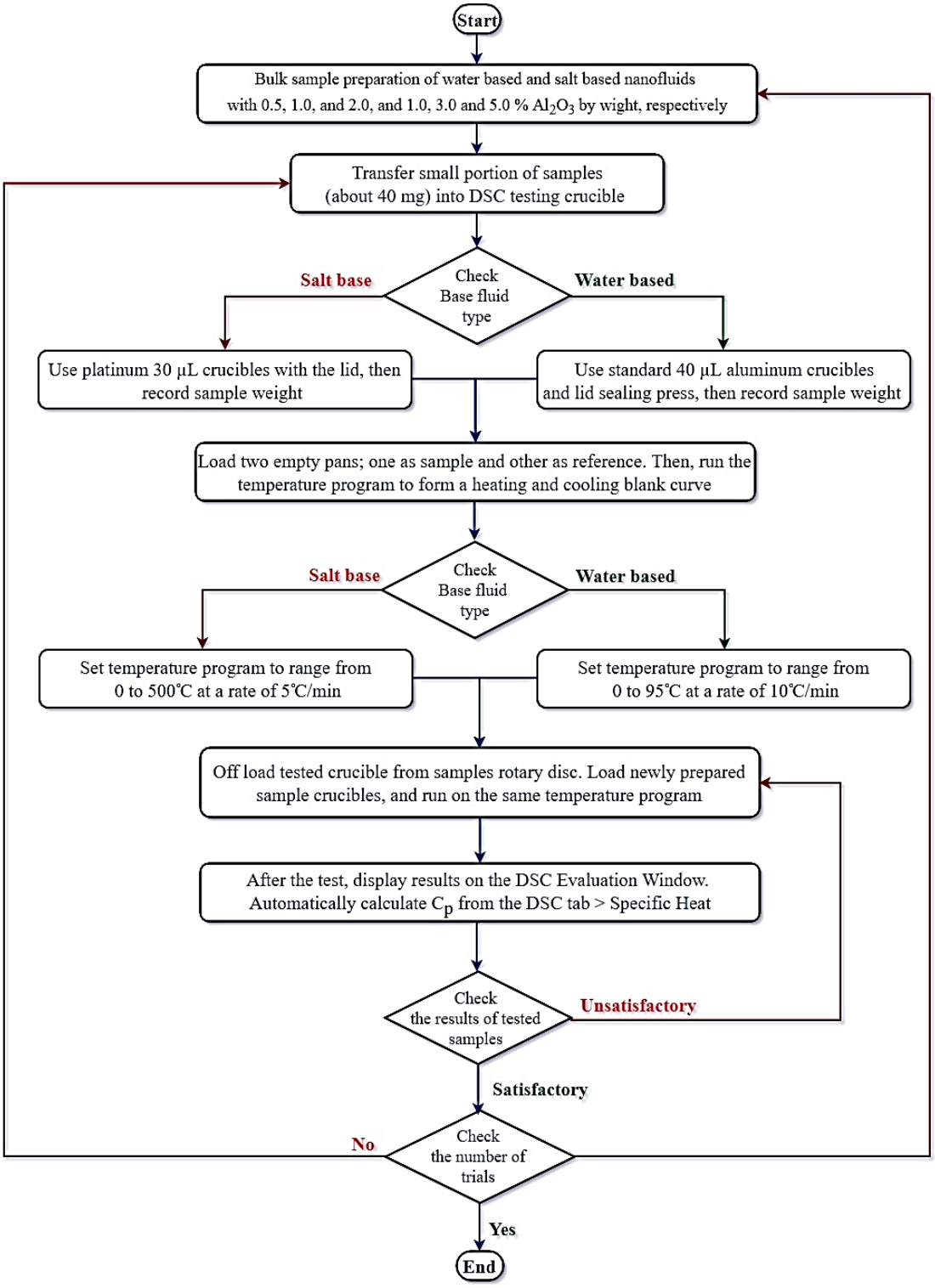

Figure 20. The procedure of the DSC experiment is illustrated with a flowchart.

3.4 Methods of determining nanofluid thermal properties

Quoted values of the thermophysical properties of specific types of material are usually given at specific temperatures. However, no data exists in the literature for the thermal properties of this particular type of Al_2O_3 nanoparticle suspension (using water or salt as the carrier fluid) at the required operating conditions, thus it can only be obtained experimentally or by using numerical simulation. Although the conductivity of Al_2O_3-nanofluids can be measured directly via experiments, such measurements are difficult and so the numerical method (described in the section 3.4.4) is presented as an alternative approach. Simulation of nanofluids also has the advantage of validating experimental results or vice versa, as well as enabling a more detailed understanding of the underlying processes, i.e. the dynamics involved in the enhancement of thermal properties via nanoparticle loading and varying the temperature.

The combined experimental-numerical method presented here was used for generating the thermal values of Al_2O_3-nanofluids at different operating conditions and particle sizes. With the use of the speed of sound measurement, the method enables the ultrasound technique to generate key thermal property date of nanofluids (i.e. the ratio of heat capacities). A more detailed consideration of this method and the predictions made is given in the results and discussions contained in Chapter 4 and Chapter 5.

3.4.1 Fluid-phase modelling

The temporal evolution of the fluid phase is modelled based on solutions to the fundamental equations that arise due to enforcing conservation of mass, momentum and energy across a small three-dimensional fluid element. For all simulations performed for the work presented in this thesis, it is assume that the fluid is incompressible and Newtonian. With these conservation laws and assumptions in place, the resulting equations are the Navier-Stokes (NS) equations. These are fundamental to the field of fluid dynamics, and are presented below:

Mass: $$\boldsymbol{\nabla} \cdot \boldsymbol{u}^* = 0,$$

Momentum: $$\frac{\partial \boldsymbol{u}^*}{\partial t^*} + \boldsymbol{u}^* \cdot \boldsymbol{\nabla} \boldsymbol{u}^* = -\boldsymbol{\nabla} p^* + \frac{1}{Re_B} \boldsymbol{\nabla} \cdot \boldsymbol{\tau}^* + \boldsymbol{f} c. \qquad 3\text{-}19$$

Here, $\boldsymbol{u}^*$ is the fluid velocity, p^* is the fluid pressure, Re_B is the bulk Reynolds number defined as $Re_B = U_B\delta/\nu_F$, ν_F is the fluid kinematic viscosity and $\boldsymbol{\tau}^*$ is the viscous deviatoric stress tensor for a Newtonian fluid. The additional term, $\boldsymbol{fc}$, is cell-dependent and accounts for two-way momentum exchange between particles in a cell and the surrounding fluid. The calculation of this term will be detailed later.

3.4.2 Direct numerical simulation

Since the focus of the work is on fundamental dynamics and small-scale nanoparticle interactions in turbulence, it is important that all relevant spatial and temporal scales are resolved when obtaining a mathematical description of the fluid phase. This means that the Kolmogorov scale, η, up to the integral length scale, L, must be resolved on the computational solution mesh. By ensuring this condition is met upon the solution grid, and by utilising a time-stepping procedure which resolves the smallest time scales associated with the turbulent eddies, a direct numerical simulation is being performed. This creates a high-fidelity solution for the fluid velocity and pressure fields and all elements and structures associated with the turbulence should be captured accordingly.

3.4.3 Nek5000 solution algorithm

The simulations were performed using the open source spectral element-based DNS code, Nek5000, as described in detail by Fischer et al[169]. The numerical code is a combination of finite element and high-order accuracy spectral methods, and was chosen based on its extensive testing, efficient parallelization capabilities and strong validation history. Thus it was used extensively throughout this project in order to obtain a high-resolution representation of the carrier phase through DNS.

The SEM is a high-order weighted residual technique which is implemented by splitting the domain into multiple hexahedral subdomains or ‘elements’ which form the full flow geometry of the system. This provides enhanced flexibility in the case of complex geometries. The solution is then represented as N^{th} order tensor-product polynomials within each of these elements. For all simulations performed within this project we choose polynomial $N = 7$ which is equivalent to 8^3 solution grid points per element.

Within the SEM, the Navier-Stokes equations undergo a weak formulation transformation, which entails multiplying them by test functions before integrating over each element in the domain. Spatial discretization is obtained via use of the Galerkin

approximation. Solution bases for velocity and pressure are Nth and (N-2)th order Lagrangian polynomial interpolants, respectively[170]. The calculations within each of these elements are capable of being performed in parallel, allowing for optimal time efficiency when carrying out the necessary computations.

Time-stepping is treated semi-implicitly. The non-viscous terms use a third-order extrapolation scheme and the viscous terms use implicit third-order backward differentiation. Upon solving the equations at each time-step, a velocity and pressure field is obtained across the element geometry as specified by the user.

3.4.4 Multiphase stagnant fluid particle tracking

The present section describes the governing equations solved in the computational model. The numerical technique developed in the present investigation defines each element of the solid phase as a computational sphere. The Lagrangian particle tracker solves the non-dimensional Newtonian equations of motion for each particle in order to calculate their trajectories (position and velocity at every computational time-step). The acceleration equation is derived by considering the force-balance between a particle's inertia and that of the fluid. The nanoparticle velocity vector is $\boldsymbol{u}_{NP} = (u_{NP}, v_{NP}, w_{NP})$, and the coordinates of the particle position are $\boldsymbol{x}_{NP} = (x_{NP}, y_{NP}, z_{NP})$, vectors in the absence of particle rotation are given in the Lagrangian reference frame as[171]:

$$\frac{\partial\, \boldsymbol{x}_{NP}}{\partial\, t} = \boldsymbol{u}_{NP}. \qquad 3\text{-}20$$

The motion of each nanoparticle is described using the Langevin equation[58], where the derivative of the translational velocity of the i-th particle is obtained from standard Newtonian dynamics:

$$m_p \frac{\partial \boldsymbol{u}_{NP,i}}{\partial t} = \boldsymbol{F}_i \qquad 3\text{-}21$$

where,

$$\boldsymbol{F}_i = \boldsymbol{F}_i^c + \boldsymbol{F}_i^e + \boldsymbol{F}_i^v + \boldsymbol{F}_i^f + \boldsymbol{F}_i^B \qquad 3\text{-}22$$

Here, m_p and $\boldsymbol{u}_{NP,i}$ are the mass and translational velocity vector of the *i*-th nanoparticle, respectively. $\boldsymbol{F}_i^c$ is the particle soft-sphere contact force; $\boldsymbol{F}_i^e$ the electric double layer repulsive force; $\boldsymbol{F}_i^v$ the van der Waals attractive force; $\boldsymbol{F}_i^f$ the fluid viscous drag force and $\boldsymbol{F}_i^B$ the stochastic Brownian motion force. Additional body forces such as gravity and buoyancy are assumed to be negligible for all length and time scales relevant to the present study, since their magnitudes are much smaller than the aforementioned interparticle and hydrodynamic forces. The present model predicts the dynamics and interaction mechanisms responsible for nanoparticle aggregation, including interparticle collisions and DLVO interparticle van der Waals attraction and electric double layer repulsion forces[172], as well as fluid drag and Brownian motion forces. The fluid drag force is calculated based on the stagnant liquid in which the particles are suspended, and is proportional to the instantaneous particle velocity. In all simulations performed a Newtonian incompressible fluid with a constant kinematic viscosity is assumed. In this sense other carrier fluids can be considered via modification of the fluid parameters (viscosity and density). Furthermore, it is assumed that the drag force is dominant, which is realistic since only stagnant systems with a zero fluid velocity are considered.

A soft-sphere approach is used to model interparticle collisions as described by the Hertzian normal contact theory[173]. The model describes the collision force between the *i*-th and *j*-th spheres in the unit normal direction, $\boldsymbol{n}_{ij}$, according to the approach of Fujita and Yamaguchi[174], with a two-dimensional schematic given in Figure 21.

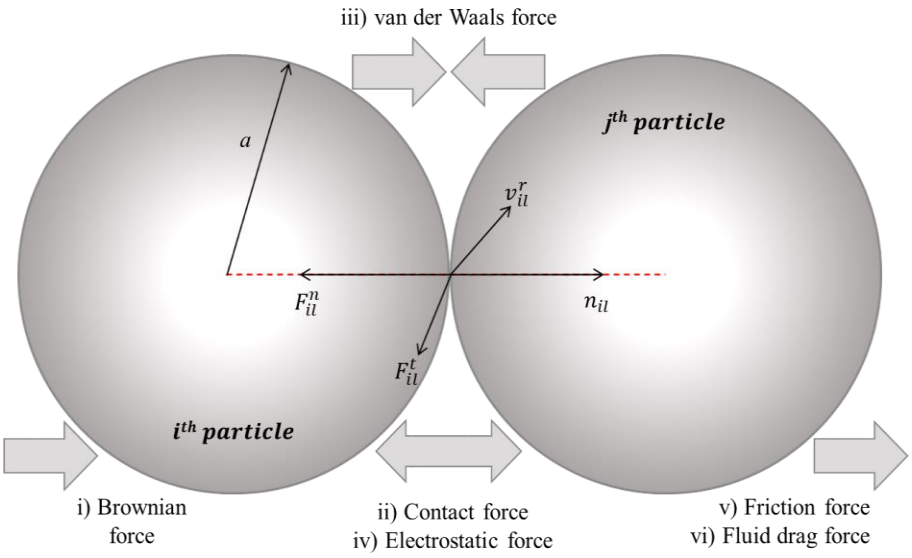

Figure 21. Hydrodynamic forces acting on two spherical solid particles submerged in a fluid continuum: (i) Brownian force; (ii) contact force; the instantaneous balance of the DLVO forces (iii) van der Waals and (iv) electrostatic; and the resulting (v) friction and (vi) fluid drag forces.

To predict interparticle forces, DLVO theory is used, with intersurfacial separations considered down to 5 nm. These consist of a repulsive electric double layer force exerted between the two spheres, together with an attractive van der Waals forces that can be expressed mathematically as:

$$\boldsymbol{F}_i^e + \boldsymbol{F}_i^v = \sum_j (f_{ij}^e + f_{ij}^v)\, \boldsymbol{n}_{ij} \qquad 3\text{-}23$$

The magnitude of the electrostatic repulsive force exerted between each of two homogeneously charged spheres can be determined using Derjaguin's approximation[172] using:

$$f_{ij}^e = -\frac{64\pi a n k_b T \Theta^2 e^{-\kappa H_{ij}}}{\kappa} \qquad 3\text{-}24$$

and for the attractive van der Waals forces[172]:

$$f_{ij}^{v} = \frac{Aa}{12H_{ij}^{2}} \qquad 3\text{-}25$$

with a the radius of a sphere; n the number density of electrolyte ions; k_b the Boltzmann constant; T the temperature; A the Hamaker constant; H the interparticle distance (surface to surface) and Θ the polarizability factor, expressed as:

$$\Theta = \tanh\left(\frac{ze\zeta}{4k_bT}\right) \qquad 3\text{-}26$$

Here, κ is the Debye parameter (inverse of the Debye length), given as:

$$\kappa = \sqrt{\frac{2nz^2e^2}{\varepsilon_0\varepsilon_r k_b T}} \qquad 3\text{-}27$$

where z is the ion valence (a number representing ion concentration that is either a positive or negative integer); e the elementary electric charge; ζ the zeta potential of the nanoparticles; ε_0 the permittivity of a vacuum and ε_r the relative permittivity of the medium.

It should be noted that the magnitude of the van der Waals forces is limited below a maximum value to prevent divergences at zero separations, thus the inter-surface distance is given a lower limit close to zero. These forces for two identically sized spherical particles are effective from a few angstroms to several hundred angstroms according to Butt[175]. Furthermore, Eqns. 3-23 to 3-26 are valid for $\kappa a < 5$, and so it is necessary to have a large Debye length for the medium, κ^{-1}, or small particle radius, a, such as occurs for nanoparticles in water. Moreover, these equations can only be applied for low electrolyte concentrations. In fact the electrolyte conditions in salts and ionic liquids are actually effectively zero. Different expressions are available in the colloidal literature for the repulsive force, for higher $\kappa a > 5$ values. For water based nanofluids κ is relatively small and related to the concentration of ions, z, by[176]:

$$\kappa = 5.023 \times 10^{11}(z)^{0.5}/(\varepsilon_r T)^{0.5} \quad \text{3-28}$$

Equation 3-27, used in the present work, allows evaluation of κ for an aqueous solution at different values of electrolyte concentration and valence of ions, such that $z = 10^{-\mathrm{pH}}$ for pH ≤ 7 and $z = 10^{-(14-\mathrm{pH})}$ for pH > 7.

The Brownian force exerted on a spherical nanoparticle is modelled using a Gaussian white noise process given by Kim and Zydney[177]:

$$F^B = \xi \sqrt{\frac{12\pi a \mu_f k_b T}{\Delta t}} \quad \text{3-29}$$

in which ξ is the coefficient of Stokes drag for a sphere and μ_f is the dynamic viscosity of the fluid. The magnitude of the fluid force responsible for nanoparticle aggregation can be determined in a quiescent system using the following Stokesian equation[58]:

$$F^f = 6\pi a \mu_f \boldsymbol{u}_S \quad \text{3-30}$$

where $\boldsymbol{u}_S$ is the flow velocity relative to that of the particle ($\boldsymbol{u}_S = \boldsymbol{u}_F - \boldsymbol{u}_{NP}$). Here, $\boldsymbol{u}_F$ is the instantaneous fluid velocity at the location of the particle and $\boldsymbol{u}_{NP}$ is the particle velocity.

3.4.5 Heat transfer property modelling

To predict the overall heat transfer properties of the system, the above nanofluid dynamic model is further coupled to a thermal energy model, which works on the basis of mean interparticle distances. These are tracked concurrently with the fluid phase at each timestep in the simulation. The volume of aggregates formed at each time step was calculated using a depth-first search method to iterate through aggregated particle chains and clusters. The applied technique links to the thermal model by considering both Brownian motion (responsible for induced micro-convection) and aggregation kinetics (responsible for the formation of particle percolation pathways). These physical phenomena are both found to be responsible for modulating the effective thermal

conductivity, k_{eff}, in nanofluids, as noted by Prasher et al.[122], and can be expressed mathematically as:

$$k_{eff} = (1 + C_A Re^m Pr^{0.333} \phi) \left\{ \frac{[k_{ag} + 2k_{bf} + 2(k_{ag} - k_{bf})\phi_{ag}]}{[k_{ag} + 2k_{bf} - (k_{ag} - k_{bf})\phi_{ag}]} \right\} k_{bf} \qquad 3\text{-}31$$

where Re is the Brownian Reynolds number; Pr the Prandtl number defined as the ratio of momentum diffusivity to thermal diffusivity ($Pr = C_p \mu / k$), and C_A and m are constants determined from experiment; k_{ag} and k_{bf} represent the thermal conductivity of the particle aggregates and the base fluid, respectively. The dynamic properties of both phases were coupled to the ambient temperature of the fluid suspension, that being water at 25-95°C or molten salt at 250-500°C. The particle volume fraction is given by ϕ for a primary particle and as ϕ_{ag} for aggregated particles, which are characterized by their radius of gyration, R_a, determined using the mean free path (average distance a particle travels between collisions) and the depth-first search method, as illustrated in Figure 22.

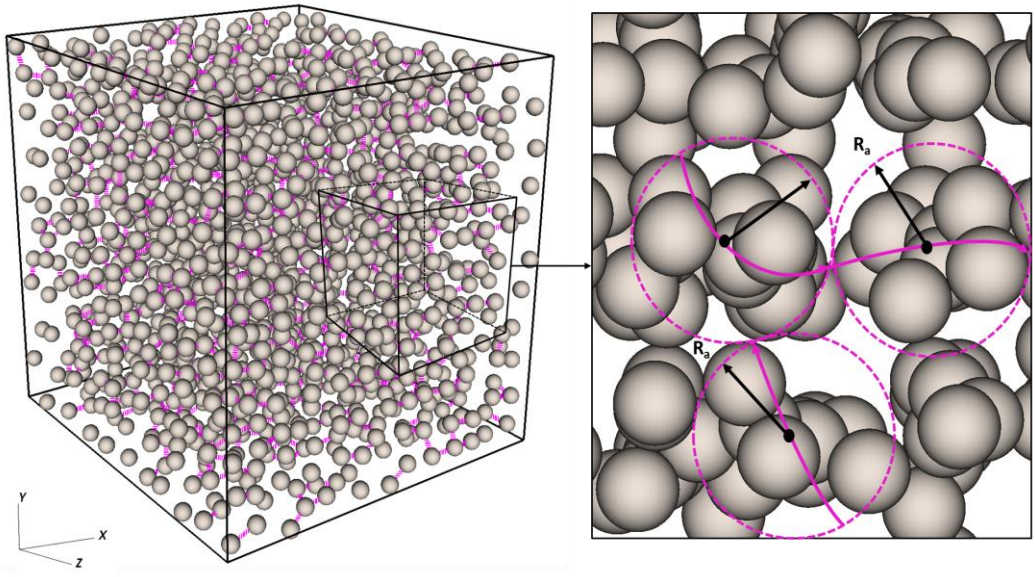

Figure 22. Schematic of aggregated particles in a three-dimensional computational cell (left). The aggregates are characterized by their radius of gyration (R_a) and shown to have a higher interacting mass than an individual nanoparticle (right), thereby creating a high conductivity percolation path.

The thermal conductivity enhancement of a nanofluid is correlated to nanoparticle aggregation using the dimension of the aggregates and their radius of gyration, which is the mean of the displacement of each constituent in the agglomerate from the centre of

mass. This treatment allows the effect of cluster morphology to be evaluated in terms of the mean radius of gyration, of the aggregates, as those described by Prasher et al.[122].

3.4.6 Structure and dynamics of ionic liquids

The binary mixtures of $NaNO_3$:KNO_3, like many other salts, contain ionic compounds such as sodium (Na^+), potassium (K^+) and nitrate (NO_3^-) ions and are, therefore, classified as alkali metal nitrates. When two nanoparticles (with smooth surfaces) are immersed in an ionic liquid such as molten nitrate salt, an oscillatory force exists between the particles due to the ordering of the confined liquid molecules in the thin film between the two surfaces. Theoretical predictions demonstrate that the ordering of liquid molecules reaches an energetic minimum at separations which correspond roughly to the diameter of a liquid molecule, as illustrated in Figure 23. At present, little is known about the thermal properties of this interfacial layer, however, theoretical analyses and numerical simulations predict that it acts as a thermal bridge, particularly in high temperature ionic fluids like molten salts. It is believed that these layered fluid molecules are in an intermediate physical state between that of the bulk fluid and the solid surfaces, thus forming a solid-like nanolayer of liquid molecules which leads to higher thermal conductivity than that of the bulk fluid[24].

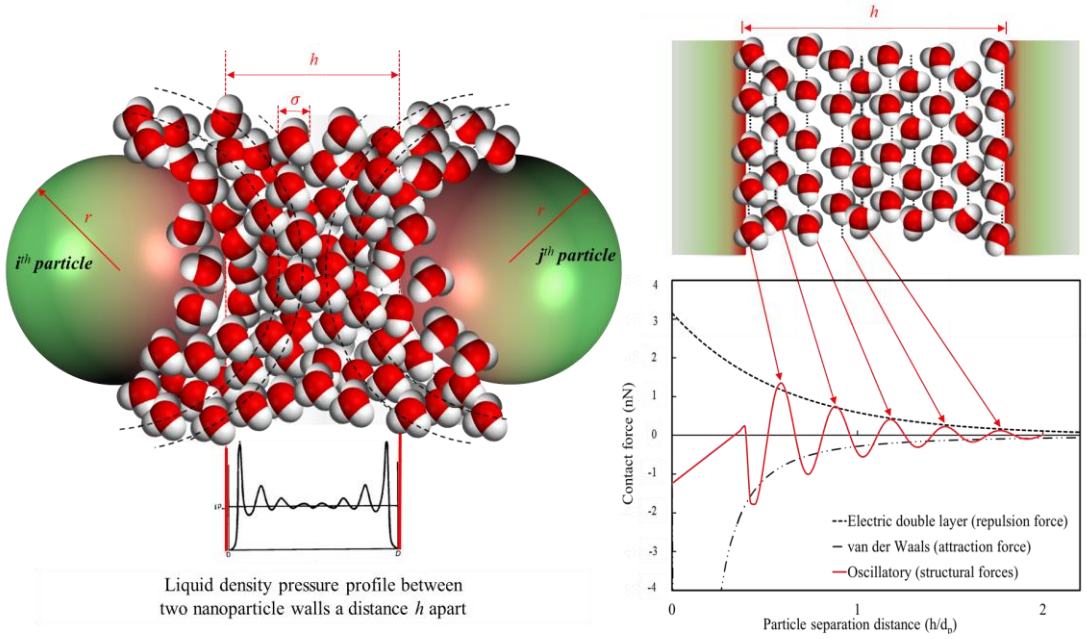

Figure 23. Schematic of structuring of molten nitrate molecules between two smooth spherical particles submerged in an ionic continuum (left); and period of force, i.e. diameter of small liquid molecules, causing oscillatory structural forces with monotonically decaying amplitude (right).

Extending the LPT model, a novel method is used to describe the oscillating layered structure of molten salt fluids (represented by the matrix of liquid molecules around the nanoparticles), and the influence of the interfacial layer thickness on the system conductivity. An explanation of this phenomenon was first given by Israelachvili[172] who noted that the structural force arises once there is a change in the liquid density at the surface of nanoparticles, as they approach one other. This force may be thought of as the van der Waals force at small separations, with the molecular properties and density variations of the medium taken into account. This force is consequently dependent on the size, type and surface properties of the particles as well as the ionic concentration and density of the continuum.

To account for the motion of solid nanoparticles suspended in an ionic fluid the addition of the structural force is needed. The structuring of molten nitrate molecules between two smooth Al_2O_3 spherical particles submerged in an ionic continuum is schematically illustrated in Figure 23. Interparticle collisions are resolved using the previously described soft sphere approach[173]. The oscillatory structural force is considered by adding an extra term, Π^{os}, to the classical DLVO expression for the disjoining pressure[178]:

$$\Pi(h) = \Pi^{el}(h) + \Pi^{vW}(h) + \Pi^{os}(h) \qquad 3\text{-}32$$

where Π^{el} is the electric double layer repulsive force, equivalent to f_{ij}^{e} (Eqn. 3-24), and Π^{vW} is the van der Waals attractive force, equivalent to f_{ij}^{v} (Eqn. 3-25).

The dependence of the oscillatory structural component of disjoining pressure on the film thickness can be specified using the formula of Denkov and Kralchevsky[178]:

$$\Pi^{os}(h) = P_0 \cos\left(\frac{2\pi h}{d_1}\right) \exp\left(\frac{d^3}{d_1^2 d_2} - \frac{h}{d_2}\right), \ for\ h > d$$
$$\Pi^{os}(h) = -P_0, \ for\ 0 < h < d \qquad 3\text{-}33$$

where σ is the diameter of the smaller fluid hard spheres (≈ 0.45 nm for molten salt molecules), d_1 the oscillatory period and d_2 the characteristic decay length, which are related to the particle volume fraction, φ, as follows:

$$\frac{d_1}{d} = \sqrt{\frac{2}{3}} + a_1 \Delta\varphi + a_2 (\Delta\varphi)^2; \quad \frac{d_2}{\sigma} = \frac{b_1}{\Delta\varphi} - b_2 \qquad 3\text{-}34$$

Here, $\Delta\varphi = \varphi_{max} - \varphi$, with $\varphi_{max} = \pi/3\sqrt{2}$ the value of φ at close packing, and a_1, a_2, b_1 and b_2 are correlation coefficients determined theoretically with respect to φ. The particle osmotic pressure, P_0, is taken from the formula of Carnahan and Starling[179]:

$$P_0 = \rho_s k_b T \frac{1+\varphi+\varphi^2-\varphi^3}{(1-\varphi)^3} \qquad 3\text{-}35$$

in which ρ_s is the particle number density of the small fluid spheres given by $\rho_s = 6\varphi/\pi\sigma^3$. For $h > \sigma$ the structural disjoining pressure oscillates around P_0 as defined in Eqn. (3-35). However, for $h < \sigma$ the small particles are expelled from the gap into the neighbouring bulk suspension by the depletion attraction, described by Eqn. (3-33). When $h = \sigma$ there is a finite discontinuity as the interaction switches from an oscillatory to a depletion regime. The contribution of the interaction free energy per unit area of the film can be obtained by integrating the oscillatory structural forces:

$$f_{os}(h) = \int_h^\infty \boldsymbol{\Pi}^{os}(h')\, dh' \qquad 3\text{-}36$$

and from Eqns. (3-33) and (3-36) one obtains:

$$f_{os}(h) = \boldsymbol{F}(h), \ \textit{for } h \geq \sigma$$
$$f_{os}(h) = \boldsymbol{F}(\sigma) - P_0(\sigma - h), \textit{for } 0 \leq h \leq \sigma \qquad 3\text{-}37$$

where

$$\boldsymbol{F}(h) = \frac{P_0\, d_1\, exp(d^3/d_1^2 d_2 - h/d_2)}{4\pi^2 + (d_1/d_2)^2} \left[\frac{d_1}{d_2}\, cos\left(\frac{2\pi h}{d_1}\right) - 2\pi sin\left(\frac{2\pi h}{d_1}\right)\right] \qquad 3\text{-}38$$

It should be noted that although soft sphere particle collisions are assumed, Eqns. (3-33) and (3-38) are applicable for hard sphere fluid molecules of diameter σ. However, the interparticle potential may still be 'soft' due to the actions of some long range forces.

3.4.7 Stagnant fluid in 3D cell computational method

The multiscale model outlined in the previous section applies a Lagrangian particle tracking approach in order to investigate the heat transfer mechanisms in, and the dynamics of, nanofluids[157]. The three-dimensional computational region examined consists of a 1μm (i.e. $\Delta l = 1\times10^{-6}$ m) cube filled with stagnant water or molten nitrate salt. This volume element contains a collection of 25-71 nm diameter Al_2O_3 spherical nanoparticles (40-2000 in number) that are initially located uniformly within the computational domain ensuring equal spacing between neighbouring particles. Periodic boundary conditions are applied in all directions. This system geometry is used throughout the second results chapter of this thesis.

The dynamic properties of both phases are coupled to the ambient temperature of the fluid suspension, that being water at 25 to 85°C and molten nitrate salt at 250 to 600°C. The thermophysical characteristics of the multiphase system are also modelled dynamically, whereby the mechanical characteristic (e.g. modulus of elasticity, rigidity and Poisson's ratio) of the alumina ceramic nanoparticles in the fluid change as a function of temperature[161]. The nanofluid dynamic model was further coupled to a thermal energy model (Eqn. 3-31) to predict the overall heat transfer properties of the system which works on the basis of interparticle distances, h, which are tracked at every time step in the simulation.

The motion of the embedded nanoparticles in the fluid is treated using an Eulerian-Lagrangian hybrid scheme with fixed time stepping. To advect the particles, the equations of motion for velocity and acceleration (Eqns. 3-20 and 3-21) are integrated using the fourth order Runge-Kutta algorithm with a very small time step, $\Delta t = 10^{-11}$ s, to fully capture the timescales associated with the short-range inter-particle forces of importance. The equation for acceleration is calculated using the relevant force terms in Eqn. 3-22. Each timestep, the terms in Eqn. 3-22 are recalculated using Eqns. 3-23 to 3-30, accounting for attractive and repulsive DLVO forces, inter-particle soft sphere collisions, Brownian forces and fluid viscous drag. Since there is no fluid flow, fluid velocity interpolation is unnecessary, and in Eqn. 3-30, which requires the local fluid velocity, this

value is set to zero ($\boldsymbol{u}_F = 0$) to indicate a stagnant fluid. To determine whether soft-sphere collisions take place, a deterministic binary collision algorithm is used. The algorithm divides the domain into a coarse mesh, wherein overlapping particle pairs are searched for within each coarse cell. Finally, if a particle moves outside the fluid domain, it is reinjected into the corresponding location at the other side of the computational cube, satisfying periodicity. Model output is recorded each timestep and corresponding statistical quantities such as mean free path, particle velocities and inter-particle forces are calculated in post-processing.

3.4.8 CFD prediction of fluid flow and turbulence onset

The flow is driven and maintained by a constant pressure gradient in the streamwise (x^*) direction. Using non-dimensional parameters, its magnitude is:

$$\frac{\partial p^*}{\partial x^*} = \left(\frac{Re_\tau}{Re_B}\right)^2 \qquad 3\text{-}39$$

where $Re_\tau = u_\tau \delta / \nu_F$ is the shear Reynolds number, which uses the shear velocity, $u_\tau = \sqrt{\tau_W / \rho_F}$, where τ_W is the mean wall shear stress. This equation, along with the appropriate boundary conditions, formulate a fluid dynamics system, and the bulk of the single-phase study revolves around solving such problems.

Multiple levels of coupling are used between the fluid and particles. Consideration of solely fluid forces acting upon the particulate phase is known as one-way coupling. Two-way coupling was achieved by implementing the point-source-in-cell method whereby particle forces are fed back to the local fluid cells. Particle collisions (four-way coupling) were resolved using the soft sphere approach, as described by Hertzian normal contact theory[180]. Finally, four-way coupled predictions were extended to include DLVO interparticle van der Waals attractive and electric double layer repulsive forces to allow the prediction of particle-particle agglomeration events.

3.4.9 Channel flow computational method

In the final results chapter of this study, the system geometry consists of a rectangular channel. The geometry of the channel was $14\delta \times 2\delta \times 6\delta$, with $\delta = 0.1$ mm, as illustrated in

Figure 24. For the purpose of this study, the computational coordinates (x, y, z) were used to represent the three-dimensional geometry of the channel, with x being the streamwise direction (runs between $x^* = -7$ to $x^* = 7$), y the wall-normal direction (runs between $y^* = -1$ to $y^* = 1$), and z the spanwise direction (runs between $z^* = -3$ to $z^* = 3$).

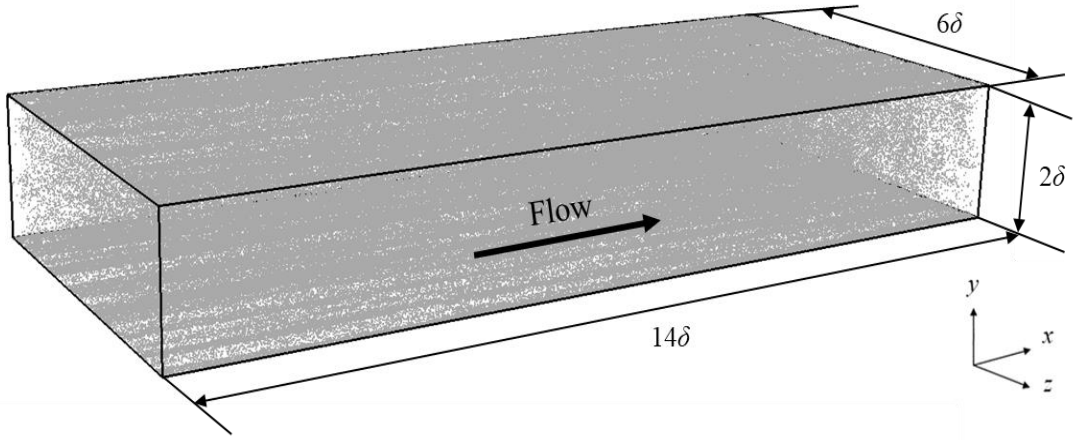

Figure 24. Schematic of multiphase turbulent channel flow computational domain.

Periodic boundary conditions were enforced in the streamwise and spanwise directions, while the wall-normal axis used no-slip conditions at $y = \pm\delta$. Within the code, the incompressible Navier-Stokes equations (mass and momentum conservation) are solved to high accuracy, with the code applied to a Cartesian grid consisting of 27×18×23 8th order elements (i.e. 5.7 M nodes) used to represent a turbulent channel flow at shear Reynolds number Re_τ = 180 (equivalent to a bulk Reynolds number $Re_B = 2800$). A constant fluid timestep of $\Delta t_F^* = 0.01$ was used throughout.The elements were scaled such that those closest to the wall were distributed more densely. This is important since the near-wall regions (viscous sublayer and buffer layer) contain most of the smallest turbulence scales, which must be resolved completely to take into account their effects on the dispersed phase. The element distribution is illustrated in Figure 25. More information on the computational mesh and time-steps used in the flow simulations can be found elsewhere[227, 232].

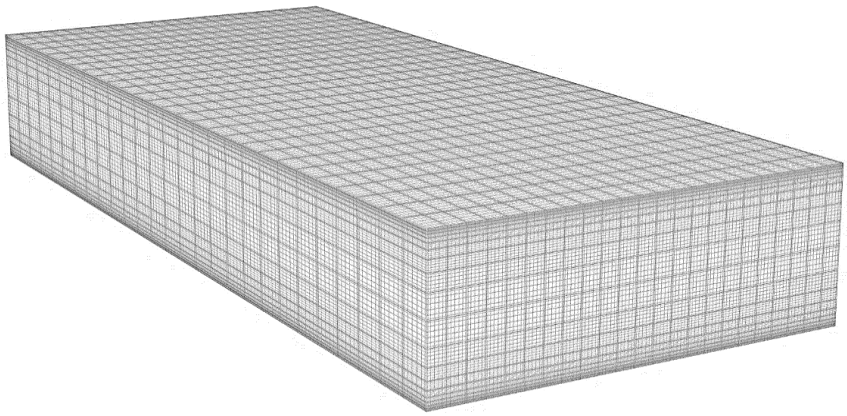

Figure 25. Computational mesh demonstrating element spacings and increased near-wall nodal density.

3.4.10 Turbulent heat transfer in channel flows

In addition to the fluid flow, Nek5000 solves the following non-dimensional conservation equation for energy transport via heat:

$$\frac{\partial T^*}{\partial t^*} + \mathbf{u}^* \cdot \nabla T^* = \frac{1}{Pe} \nabla \cdot \nabla T^* + q_{vol} \qquad 3\text{-}40$$

where T^* is the temperature, q_{vol} is the volumetric heat source term and $Pe = LU/\alpha$ with $\alpha = k/\rho_F C_p$, in which α is thermal diffusivity, Pe is the Péclet number based on bulk properties, L is a characteristic length, U the local flow velocity, k the thermal conductivity, ρ_F the fluid density, and C_p the heat capacity. For the temperature to be made non-dimensional the following expression was used:

$$\bar{T}^* = \frac{\overline{T_w(x)} - T}{T_\tau} \qquad 3\text{-}41$$

here, T_w is the wall temperature and T_τ is the friction temperature defined by

$$T_\tau = \frac{q_W}{\rho C_p u_\tau} \qquad 3\text{-}42$$

where u_τ is the friction velocity given by $u_\tau = \sqrt{\tau_w/\rho}$, where τ_w is the statistically averaged wall shear stress and ρ is the density. At the wall conductive flux, u_τ can be chosen to be positive or negative in the *y* direction. According to this definition the wall thermal boundary condition in the case of an imposed heat flux reads:

$$-k\left(\frac{dT}{dy}\right)_w = q_w \tag{3-43}$$

$$-\left(\frac{d\left(\overline{T_w(x)} - \bar{T}^+ T_\tau\right)}{dy}\right)_w = \frac{q_w}{k} \tag{3-44}$$

$$\frac{T_\tau}{\delta}\left(\frac{d\bar{T}^+}{dy^+}\right)_w = \frac{q_w}{k} \tag{3-45}$$

$$\left(\frac{d\bar{T}^+}{dy^+}\right)_w = \frac{\delta q_w}{k}\frac{u_\tau \rho C_p}{q_w} = \frac{\delta u_\tau \rho}{\mu}\frac{\mu C_p}{k} = Pe_\tau \tag{3-46}$$

where Pe_τ is related by $Pe_\tau = Pe\ Re_\tau/Re_B$.

4 AN ACOUSTIC METHOD FOR DETERMINATION OF THERMAL PROPERTIES OF NANOFLUIDS

4.1 Introduction and background

An ultrasonic technique is developed herein for the analysis and characterization of nanofluids using the sound speed dependence on temperature and nanoparticle concentration[181]. This technique is promising for the characterisation of multi-phase systems such as nanofluids because it is flexible, cost effective, non-destructive, non-invasive and can operate in dense and optically opaque nanosuspensions[182] with fewer restrictions than optical methods. The results demonstrate the potential of acoustic methods to determine the thermophysical properties of nanofluids. This is achieved by first measuring the speed of sound in nanofluids, and then using the data, together with measurements of density and predictions of thermal conductivity derived from Lagrangian particle tracking (LPT) simulations (see section 3.4), to determine the ratio of heat capacities of nanofluids using a modified version of the Bridgman equation. This *in situ*, online method has potential applications in energy storage where thermofluids such as water and molten salts dosed with nanoparticles are used as thermal transfer fluids and storage media, with their application requiring effective monitoring. To support the findings of the previous ultrasonic technique, differential scanning calorimetry (DSC) was used to measure the specific heat capacity and enthalpy of fusion values in the nanofluids. The variation in the sensible and latent heat values was shown to depend on the nanoparticle concentration and temperature.

The study provides a theoretical background of the acoustic properties of different nanofluids, before discussing the corresponding experimental analysis using the speed of sound variations. From the ultrasonic experimental results, the two different nanofluids were compared and shown to exhibit different trends with regards to the speed of sound variation with temperature and particle concentration, and as such their thermophysical parameters were calculated to verify this result. Such a technique could provide both a more in-depth understanding of important acoustical properties of nanofluids, as well as laying the foundations for investigating nanofluid thermal properties at a more fundamental level, as will be discussed in this Chapter.

4.2 Experimental method

The first objective was to measure the speed of sound in nanofluids at different solid concentrations and temperatures. The second objective was to use the speed of sound data, together with measurements of physical properties to determine the thermal properties of nanofluids. A general description of the experimental methods used in this study are given in Section 3.2. The experimental procedures that were specific to this part of the study are described throughout Section 3.2.1 to 3.3, in particular nanofluid characterization by speed of sound (Section 3.2.1), the predictive correlation between speed of sound and thermophysical properties (Section 3.2.2), preparation and testing of water based nanofluids (Section 3.2.4), acoustic test cell (Section 3.2.6), preparation and testing of salt based nanofluids (Section 3.2.10 and 3.2.11), ultrasonic waveguide (Section 3.2.12), and differential scanning calorimeter (Section 3.3).

The main results are presented in two sections: water based nanofluids (Section 4.3), and salt based nanofluids (Section 4.4). Other results are also presented in the following section: ultrasonic waveguide (Sections 4.5), and differential scanning calorimeter (Section 4.6). A summary of all the results is given (Section 4.7).

4.3 Water based nanofluids

4.3.1 Measured speed of sound of pure fluid and nanofluids

All sound velocity measurements of water based nanofluids were made using the acoustic test cell described in Section (3.2.6), and the results shown in Figure 26. The figure shows the change in acoustic time measured by the oscilloscope in pure water, over the temperature range of 25-85°C. These data were used to find the peak-to-peak resolution needed for the propagation of error analysis, and were also used for the thermometer sensor calibration over a given temperature range (see Appendix B).

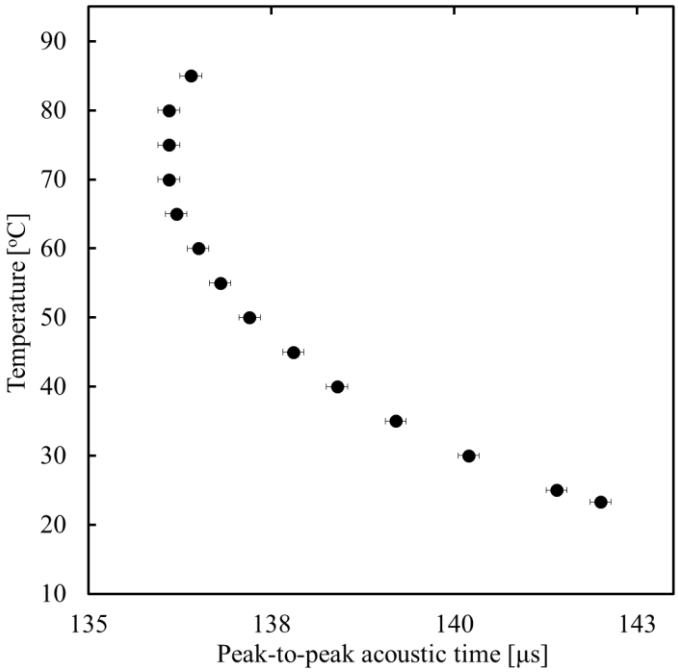

Figure 26. The change in the peak-to-peak time base of ultrasonic signals collected by the oscilloscope with temperature, for pure water.

The influence of Al_2O_3 particle concentration on the speed of sound was measured up to 5 vol%, using both transducers, as illustrated in Figure 27.

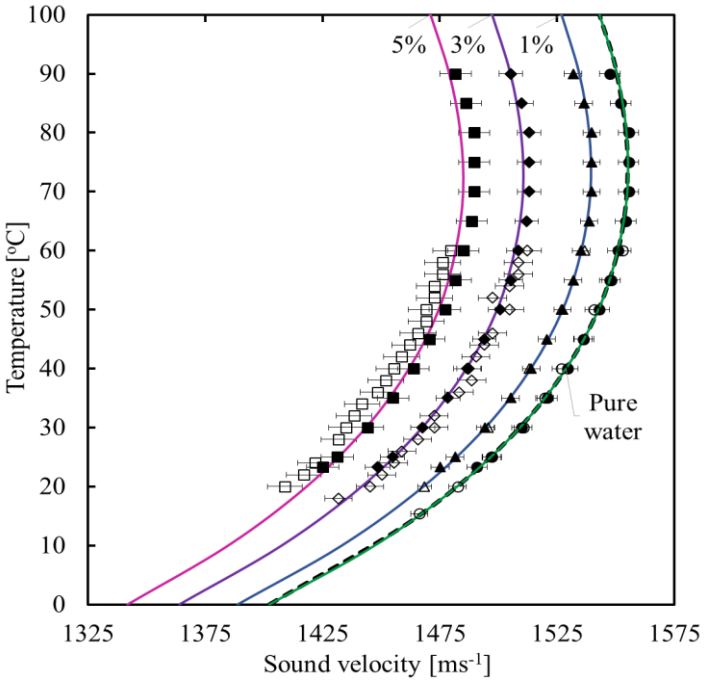

Figure 27. Measured sound velocity in pure water and water based nanofluids containing d_p = 50 nm alumina (Al_2O_3) as a function of temperature and concentration. Open symbols: standard transducer. Closed symbols: high-temperature transducer. Circles: pure water; triangles: 1 vol%; diamonds: 3 vol%; squares: 5 vol%. Colours indicate theoretically calculated values at various solid concentrations using Urick[140] equation. Dashed line: experimental data of Bilaniuk and Wong[159].

As shown in Figure 27, the results confirm the accuracy of the sound speed measurements for pure water, when compared to predictions of the Urick[140] equation and the data of Bilaniuk and Wong[159]. The sound velocity increases until it reaches a maximum at ~74°C. The temperature coefficient dC/dT is positive up to this temperature. The velocity then decreases with increasing temperature >74°C, hence dC/dT is negative at higher temperatures. The variation in the measured water speed-of-sound can be explained by the changes in water compressibility as shown earlier in Fig. 2. Figure 27 also shows the sound velocity in water based nanofluids containing d_p = 50 nm Al_2O_3 nanoparticles. The sound velocity increases with increasing temperature to ~74°C, similar to that shown for pure water (See also Figure 2).

The slight differences between the standard and high temperature transducer results (Fig. 27) may be the result of their different frequency of operation, since the high temperature transducer has a centre frequency ≈ 3.45 MHz, whereas the standard transducer has a corresponding frequency ≈ 4.0 MHz. Different temperature ranges were used for the different probe types (due to temperature limitations of the Imasonic probes ~60°C). The result demonstrates that the velocity of sound is frequency-dependent[140] for this type of nanosuspension system. It should also be noted that very minor influences of distance measurements when using the two probes are likely to impact on the value of the sound velocity in the test mixture. Such errors are indicated by the error-bars, with the variation of ultrasonic velocity with probe distance discussed in detail in Appendix B.

Additionally, the strength of the signal of standard probe was found to be more sensitive to the effect of reflection and attenuation of ultrasound waves caused by the presence of high nanoparticle concentrations. This can be seen by the minor discrepancies between the two transducer types at a solids concentration of 3 vol%, and more noticeably at 5 vol%. Other potential errors (as those discussed in Appendix B) could have contributed to the differences, although the small volumes of nanofluid tested, especially with the high-temperature transducer, were continuously calibrated, very well mixed, and fully dispersed. Accordingly, the Urick[140] equation is in close agreement with the more reliable high temperature transducer data.

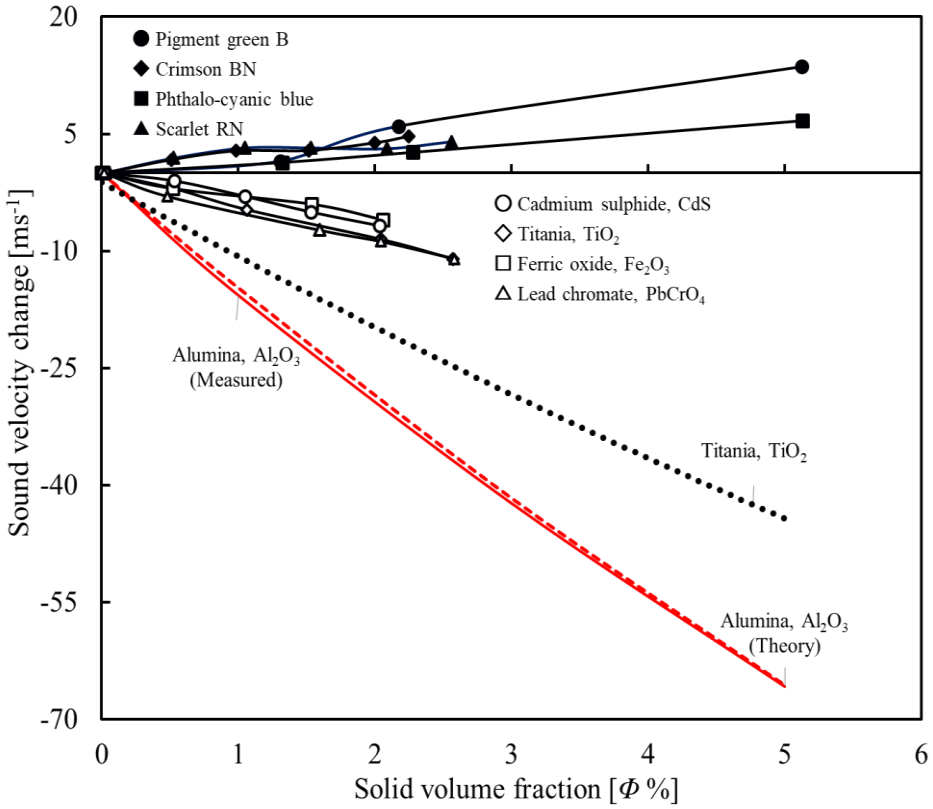

Figure 28. Relation of ultrasound velocity change through dispersions of low- and high density solid particles in water or Turkish oil. Present study: Red solid: sound velocity in alumina (Al_2O_3) nanofluid. Red dashed: theoretically calculated values using Urick[140] equation. Data of Piotrowska[183] (Closed symbols: low-density solids. Open symbols: high-density solids). Dotted: experimental data of Kim et al.[181].

The main observation from these results (Figure 27) is the decrease in sound velocity with increasing particle concentration. To describe this phenomenon, the change in sound velocity measurements at room temperature is plotted against the concentration of alumina particles (d_p = 50 nm), together with the results obtained by Piotrowska[183] and Kim et al.[181], in Figure 28.

It should be noted that Piotrowska[183] used a mixture of distilled water and Turkish oil (stabilizer) as the dispersive phase for the particle species, with the exception of TiO_2, and scarlet RN, where distilled water was used alone. The study[183] reported that it was possible to obtain accurate results at low concentrations up to 2 vol% using an interferometric method, whereas the method used here can go up to 5 vol% and is only limited by attenuation and the thermal interaction at higher voltages. It is clear that the sound velocity in suspensions of low-density species (e.g. pigment green B, Crimson BN, see densities Table 6), which are also partly soluble in water, was higher than that of suspensions of high-density species (i.e. TiO_2, Fe_2O_2) that are not soluble either in water

or in water and Turkish oil. The physical properties of all particle species used in the figure are shown in Table 6.

Table 6. Physical properties of particle species.

Species	Density, ρ / kg m^{-3}
Alumina, Al_2O_3	3850
Titania, TiO_2*	3840
Ferric oxide, Fe_2O_3*	4740
Lead chromate, $PbCrO_4$*	4540
Cadmium sulfide, CdS*	4820
Pigment green B*	1560
Crimson BN*	1460
Phthalo-cyanic blue*	1600
Scarlet RN*	1400
Titania, TiO_2**	3980

*Species used by Piotrowska[183] had irregular shapes and undefined particle size in the micrometer range. **Species used by Kim et al.[181] were spherical and had an average size of 55 nm with a secondary peak at ~200 nm.

The data of Kim et al.[181] for water based TiO_2 nanofluids shown in Figure 28 indicate that in the concentration range 0 to 5 vol. % the velocity decreases as the solids concentration increases. An important implication of this finding in the case of low particle concentrations is the wide interparticle distance, which was thought by Kim et al.[181] to be the cause for the reduction of ultrasound wave propagation (due to scattering). Kim et al.[181] also showed that the sound velocity decreases up to ~30 vol%, above which the sound velocity increases due to the reduction in interparticle distance and rapid wave propagation through the particles. Further details of this complex multiple scattering phenomena are given by Kim et al.[181]

It is also seen that the nano-sized TiO_2 used by Kim et al.[181] decreased the speed of sound more than the micron-sized TiO_2 particles used by Piotrowska[183] (i.e. by 30 ms^{-1}), which is an important observation supporting the effect of particle size on the speed of sound measurements (Figure 28).

4.3.2 The ratio of heat capacities

The modified Bridgman equation (3-8) is combined with experimental speed of sound measurements to give a very simple yet accurate semi-empirical model for the prediction of thermal properties. This model is used with predicted thermal conductivity values from simulations (as will be discussed in detail in the following Chapter) to determine the ratio

of specific heats (using Eqns. 3-8) of Al_2O_3-nanofluids at different temperatures and concentrations. Results for the specific heat ratio in the temperate region 25-90°C are shown in Figure 29 alongside the predicted conductivity values.

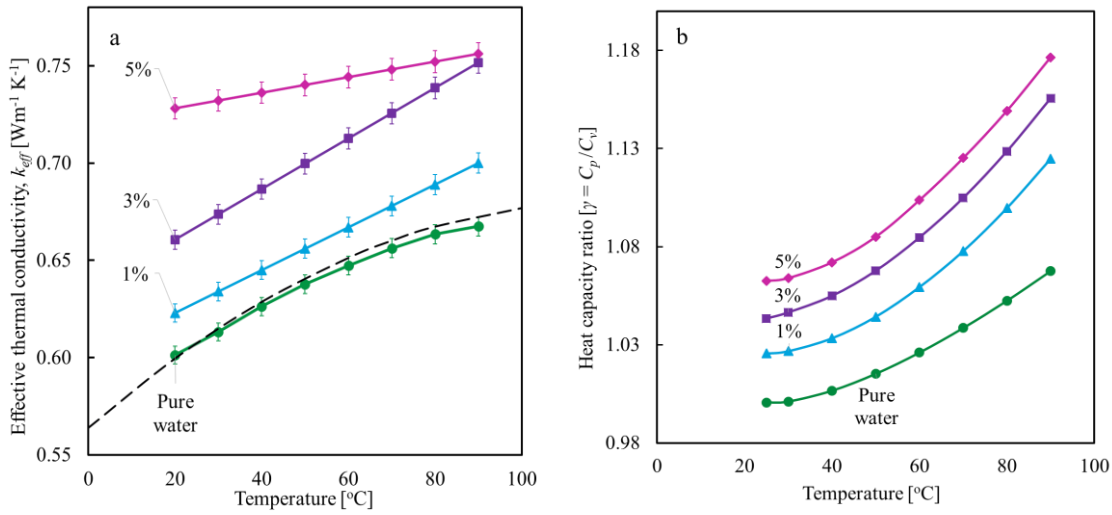

Figure 29. (a) Comparison of thermal conductivity values (— predictions using numerical model, – – experimental data of Coker[184]). (b) Determined heat capacity ratios as function of temperature and concentration of nanofluids (water and spherical d_p = 50 nm Al_2O_3 particles) using Eqn. (3-8).

The predicted thermal conductivity values increase with increasing temperature, supporting the contention that the increases are due to increased probability of particle collisions and the effect of Brownian motion. The predicted values, at different volume fractions and temperatures, show an almost 12.5 % increase for 5 vol. % of particles relative to pure water. Although these predictions were made over a temperature range of 25 to 90 °C, they suggest that further enhancement is to be expected with temperature as a result of increasing kinetic energy and hence in the fluid drag and Brownian motion forces.

The other interesting observation from Figure 29 is that the variation of thermal conductivity with temperature tends to follow a transition from curved for pure fluid to linear at concentrations of 3 vol. %, then to a smaller gradient at 5 %., i.e. a change in slope is indicated above such volume fractions, with this behaviour transitioning from pure liquid at low concentrations to linear behaviour beyond 1 vol. %. From the model predictions this demonstrates that the system is entering a different regime where particle-particle interactions (particle collisions) driven by Brownian motion start to increase resulting in induced micro-convection, leading to a substantial increase in thermal

conductivity[121]. The increased colloidal forces[41] and aggregation kinetics (collisions; van der Waals forces; electric double layer forces) are also responsible for the formation of nanoparticle percolation pathways, generating more conductive pathways for thermal energy transfer. Similar results were obtained using a combined mechanism-based model of aggregation kinetics with Brownian motion-induced micro-convection.[157]

Figure 29 shows that the ratio of heat capacities γ for pure water increases with temperature. Similarly, with the addition of nanoparticles the heat capacity ratio shows an increase with temperature that is most pronounced at 5 vol%. The reason for this is that at higher particle concentrations there are more particles in the system, therefore there is a greater chance the particles will collide; this in turn increases the collision frequency and thus increases the heat capacity ratio. Moreover, an increase in temperature will increase the average kinetic energy of the particles in the system. Therefore, a greater proportion of particles will have the minimum energy necessary for an effective collision. This ratio can therefore be used in the calculation of the thermal conductivity of Al_2O_3-nanofluids using the modified Bridgman equation (Eqn. 3-8), and vice versa.

These results emphasise the significant effect of temperature and particle concentration on the thermal conductivity and ratio of specific heats. In order to better represent the modification of these thermal parameters with temperature and concentration, the data shown in Figure 29 were used to construct three dimensional plots, plotting both T– k –Φ and T– γ –Φ surfaces, as illustrated in Figure 30.

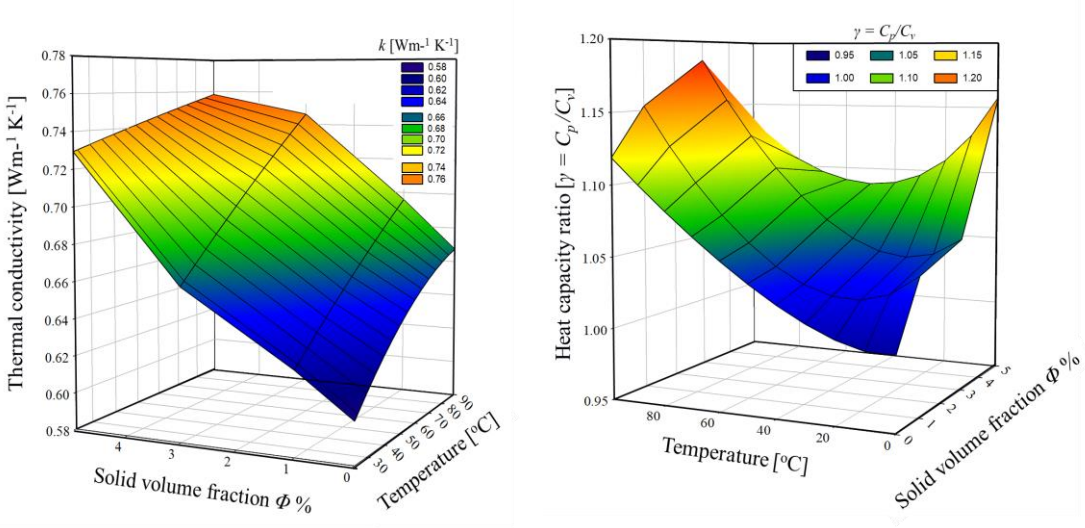

Figure 30. (Left) Dependence of thermal conductivity k on temperature T and solid volume fraction Φ. (Right) Dependence of heat capacity ratio γ on T and Φ, for Al_2O_3 nanofluids.

The effect of particle volume concentrations $\Phi > 3$ vol. % on both k and γ is clear from the results. The enhancement of thermal properties in nanofluids at higher concentrations can be explained by the increased interaction of nanoparticles, as explained above. As to the temperature dependence of the system, which was found to be strong, previous results[157] demonstrated that the enhancements were due to Brownian motion (induced micro-convection) and collisions between nanoparticles as well as aggregation kinetics (the formation of particle percolation pathways) in the base fluid. The increase in temperature leads to an increase in kinetic energy that intensifies both the Brownian motion and particle collisions of Al_2O_3-nanofluids.

These new results confirm the temperature and concentration dependence of both k and γ and the influence of Brownian motion, interparticle collisions and particle size. They confirm that heat transfer enhancement through the use of nanoparticles is a valuable approach for a wide variety of industrial applications, with the use of Al_2O_3-nanofluids in heat exchange devices showing significant promise and offering increased efficiency and significant energy savings, compared to conventional heat transfer fluids.

Lastly, it may be noted that the ratio of heat capacities derived from the combined LPT simulations and experimental values (see Figure 29) for the speed of sound used in this study may also be used together with P-V-T relations as a method to obtain values of C_p or C_v for nanofluids using Eqn. (8-15) and Eqn. (8-16), as described in Appendix A.

4.4 Salt based nanofluids

In this section, the speed of sound in salt based nanofluids is investigated, using the high temperature acoustic test cell described in the methodology section (3.2.9). First, the attenuation of a sound wave is considered. Attenuation is a useful quantity for the ultrasonic characterisation of nanofluids, especially nanofluids at high temperatures. The presence of nanoparticles in such a high temperature fluid can produce an effect that weakens the sound. Such weakening results from scattering and absorption (which are the underlying physical mechanisms)[182, 188]. Scattering is defined here as the reflection of sound wave in directions other than its original direction of propagation (or can also be in the same direction as the incident radiation), while absorption is defined as the conversion of the sound energy to other forms of energy. Signal weakening may also be due to attenuation (these are the result of scattering and attenuation, but vary according

to the measurement method, e.g. angle between emitter and receiver). The combined effect of these physical mechanisms is referred to here as ultrasonic attenuation.

Ultrasonic attenuation was obtained experimentally using the method explain earlier in section 3.2.9, from voltage measurements (RMS amplitude of the echo signal as a function of probe distance), and is then used to verify experimental results; a typical display is shown in Figure 31. The result in Figure 31, exhibits a clear variation in amplitude with increased probe distance (from probe tip to testing cell reflected base). The intensity of sound waves (the decay rate of the wave as it propagates through the media) is clearly decreasing with distance as it travels through the testing cell.

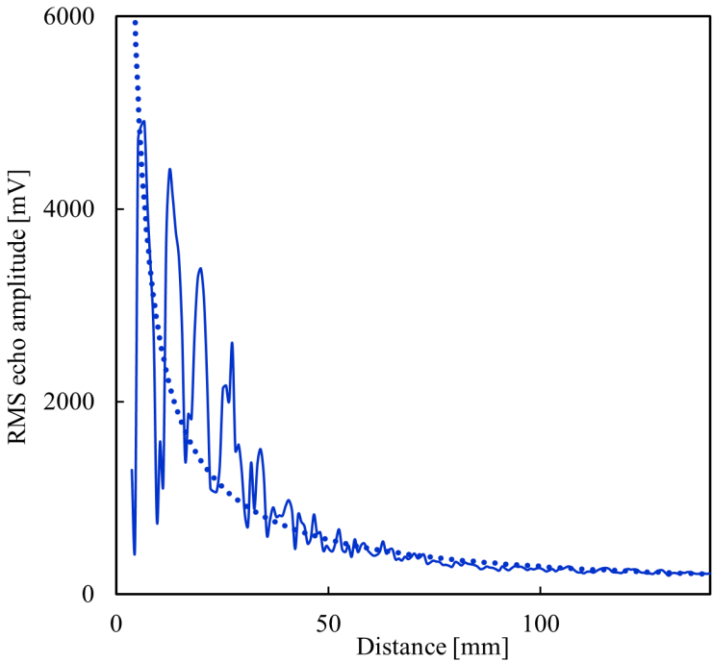

Figure 31. RMS echo amplitude of ultrasonic scattering signals (Ionix f = 4 MHz) displayed over the travel time (penetration depth) within the suspension of nanoparticles (Al_2O_3: particle size d = 50 nm ; particle concentration 1 wt. %) in molten solar salt (60 wt. % $NaNO_3$ + 40 wt. % KNO_3), at 300 °C.

A further effect that weakens ultrasonic waves is the increased temperature of the molten salt nanofluids in the testing cell, as it enhances the Brownian motion of nanoparticles producing more inter-particle interaction, and hence attenuation of sound is increased. It is also likely that there is an internal friction (acoustic impedance) or energy absorption in the tested medium, which may give rise to attenuation of wave propagation through the cell, as it is proportional to square root (RMS) of sound frequency[188]. Both the fluid and particles can contribute to attenuation, and so in some cases, acoustic attenuation can be related to particle concentration. However, this may only be achieved when there is less number of particles present in the testing cell and so the interaction between these

particles is less. Such ideal conditions of an experiment are difficult to control, especially in the case of high temperature nanofluids. This phenomenon is further explained by Rice et al.[188]. It should be emphasized that the likely influence of nanoparticle aggregation on the overall suspension attenuation in the molten salt system is very complicated. This is due to the ambiguous relationship between aggregations versus total attenuation in this specific case. Large increases in size will enhance attenuation from scattering, but small changes in aggregation will be difficult to detect. Other differences may be due to the density ratio of the nanoparticle to the fluid phase. A more detailed consideration of these effects is given by Bux et al.[235]

In Figure 32 attenuation can also be seen as a function of temperature, for pulse spreading (distinct from attenuation by scattering and absorption) from an acoustic probe over distance, leading to magnitude reduction, especially when temperature is increased from 300 to 400°C. This test was conducted specifically since the high temperature probe (Ionix, Huddersfield, UK) is rated to 380°C for long term use. Excursions at ≥ 400°C are fine as we have observed during the experiments, but with longer periods of probe exposure in the molten salt at such high temperature, the signal amplitude reduction was noticed. Therefore it has been decided to keep exposure periods as limited as possible at temperatures above 380°C, to avoid damaging the probe.

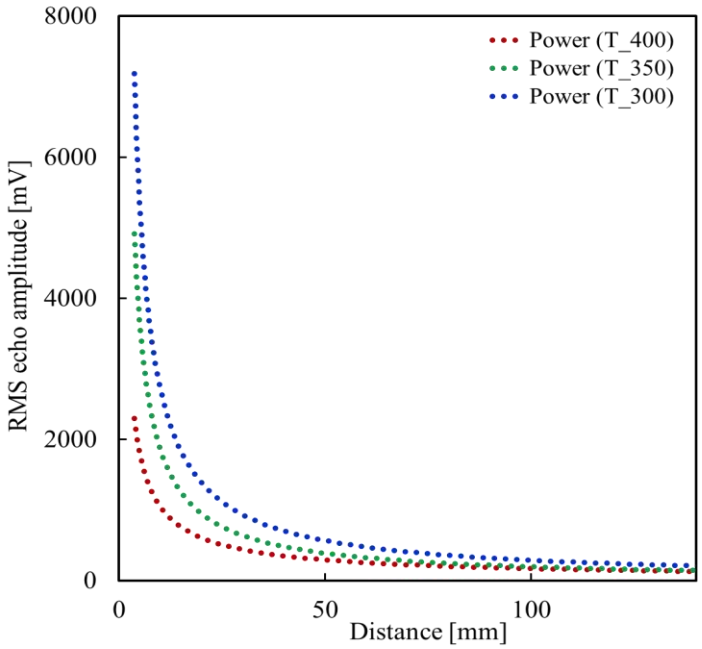

Figure 32. Variation of RMS Echo Amplitude of ultrasonic signal (Ionix f = 4 MHz) displayed over the travel time (penetration depth) within the suspension of nanoparticles (Al_2O_3: particle size d = 50 nm; particle concentration 1 wt. %) in molten solar salt (60 wt. % $NaNO_3$ + 40 wt. % KNO_3), at different

temperatures: Blue: 300°C; Green: 350°C; Red: 400 °C. Note that an approximate fit is used plot the RMS as an exponential function of distance.

4.4.1 Measured speed of sound of salt based nanofluids

Sound velocity measurements were made for pure molten salt and molten salt nanofluid at different particle mass fraction of 0.5 and 1.0 wt. %. From these experiments the speed of sound data as a function of temperature ranging from 250 to 500°C, are presented in Figure 33. The sound velocity data reported by other researchers[147, 155] on individual nitrate salts, for both $NaNO_3$ and KNO_3, are also included in the plot. It is clear from the result that the sound velocity is in good agreement with the ultrasonic data which can be seen in the figure. The results of pure binary nitrate salt mix ($NaNO_3$:KNO_3 in 60:40 wt. %) lies between the individual nitrate salts, and slightly closer to the $NaNO_3$ data, since it forms the higher fraction of the nitrate salt mixture. Our results show that the speed of sound is temperature dependent and similar to the previous results it decreases with temperature.

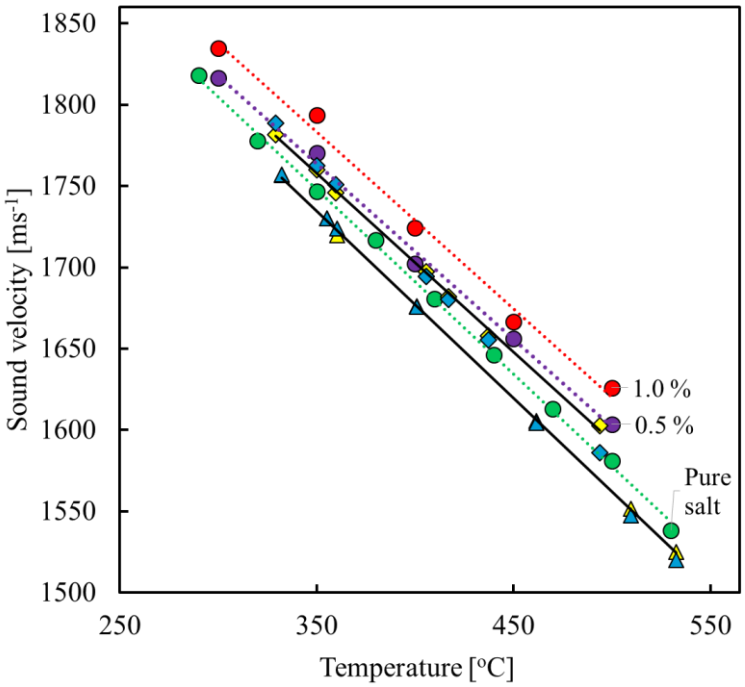

Figure 33. Measured sound velocity in solar salt (60 wt. % $NaNO_3$ + 40 wt. % KNO_3) and the suspension of nanoparticles (Al_2O_3: particle size d = 50 nm), as a function of temperature. Present study, Green circles: pure solar salt; Purple circles: with 0.5 wt. % nanoparticles; Red circles: with 1 wt. % nanoparticles. (Yellow) Experimental data of Bockris and Richards[147]; (Blue) Experimental data of Richards et al.[155], for individual molten alkali-metal nitrates. Diamond: $NaNO_3$; Triangle: KNO_3.

The other interesting aspect of the results is the sensitivity of the measurements to the change in particle concentration. It is clear from all these results that the speed of sound of salt based nanofluid at a given temperature, increases roughly linearly as concentration increases from 0.5 to 1.0 wt. %. The likely cause of the observed increase in the speed-of-sound for nanofluids versus pure molten salt can be explained by the influence of compression and density effects, as those defined in Eqn. (3-1). Also it is not possible to calculate the speed of sound from the model directly, due to lack of compression data for the molten salt. It should finally be noted that molten salt nanofluids were also tested at higher concentration (i.e. 3.0 wt. %). However, the received signal was observed to be too weak, due to excessive attenuation which causes the acoustic energy to extinguish (by scattering and absorption, explained in Figure 31) before it reaches the transducer.

4.4.2 The ratio of heat capacities

The modified Bridgman equation (using Eqn. 3-8) is then combined with experimental speed of sound measurements to predict the thermal properties. Predicted thermal conductivity values from simulations (discussed and validated in Chapter 5 of this thesis) are used to determine the ratio of specific heats (using Eqn. 3-8) of molten salt Al_2O_3-nanofluids at different temperatures and concentrations. Results for the specific heat ratio in the temperate region 250-500°C are shown in Figure 34 alongside the predicted conductivity values.

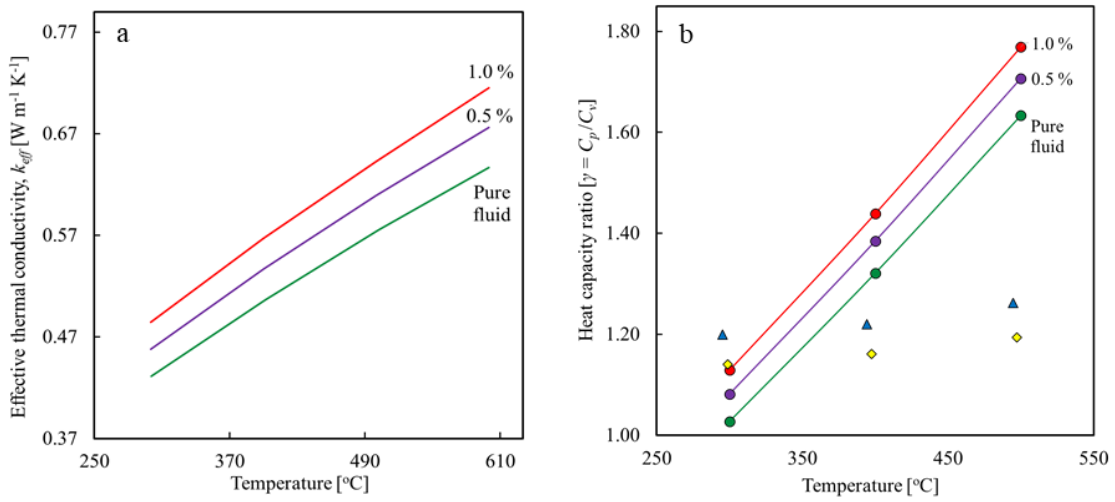

Figure 34. (a) Comparison of thermal conductivity values of solar salt and the suspension of nanoparticles (Al_2O_3: particle size d_p = 50 nm) (— predictions using numerical model, Green: pure solar salt; Purple: with 0.5 wt. % nanoparticles; Red: with 1 wt. % nanoparticles). (b) Determined heat capacity ratios as function of temperature and concentration of nanofluids using Eqn. (3-8). Experimental data of

Bockris and Richards[147] for individual molten alkali-metal nitrates, Yellow diamond: $NaNO_3$; Blue tringle: KNO_3.

It can also be seen from Figure 34 – b that the ratio of the heat capacities γ for pure molten salt increases with temperature. Similarly, with the addition of nanoparticles the heat capacity ratio shows an increase with temperature that is most pronounced at 1 wt. %. This can be explained by the rise in average kinetic energy of the particles present in the system, particularly when temperature is increased. Also because the thermal conductivity values shown in Figure 34 – b used in these predictions came from simulations (see section 5.3), the reason can be explained from a modelling perspective with high particle concentrations, as there are more particles in the system, therefore there is a greater chance that the particles will collide; this in turn increases the collision frequency and thus increases thermal conduction. Therefore, a greater proportion of particles will have the minimum energy necessary for an effective collision. More details of predicted thermal conductivity values from simulation are given in Chapter 5.

4.5 Ultrasonic waveguide

Earlier methods for the measurement of the speed of sound in nanofluids involved techniques with contact between the acoustic source and the test fluid and are thus not to be considered for high temperatures fluids ($T > 500^oC$). The main problem in devising a technique applicable to molten salt is the elimination of contact between the sound source emitter (using the standard ultrasonic probe) and the tested fluid. Consequently, it was decided to fabricate a high temperature titanium buffer rod and to propagate the ultrasonic longitudinal waves in and out of the fluid along the rod on which the source and receiving transducers were mounted out of contact with the high temperature fluid.

The fabricated waveguides were tested using an oscilloscope and the nanofluid calibration and testing cell. The results from it appear to be reasonable in respect of echo signals resulting from the propagation across the waveguide. In fact the results showed that the single-tapered prototype has a weak detection sensitivity with a lot of background noise, whereas the double-tapered BR demonstrated a better capability, but signals still contained significant noise as illustrated in Figure 35. The pulse-echo signal was also found to be reasonable with respect to temperature, with high signal to noise ratio. As part of the continuous improvement of the devices, work is ongoing on cladding them, which it is thought will help to improve the received signal. This will also help in reducing

the trailing echoes further, making the waveguides more promising and cost-effective not just for the desired application but also for many other industrial applications.

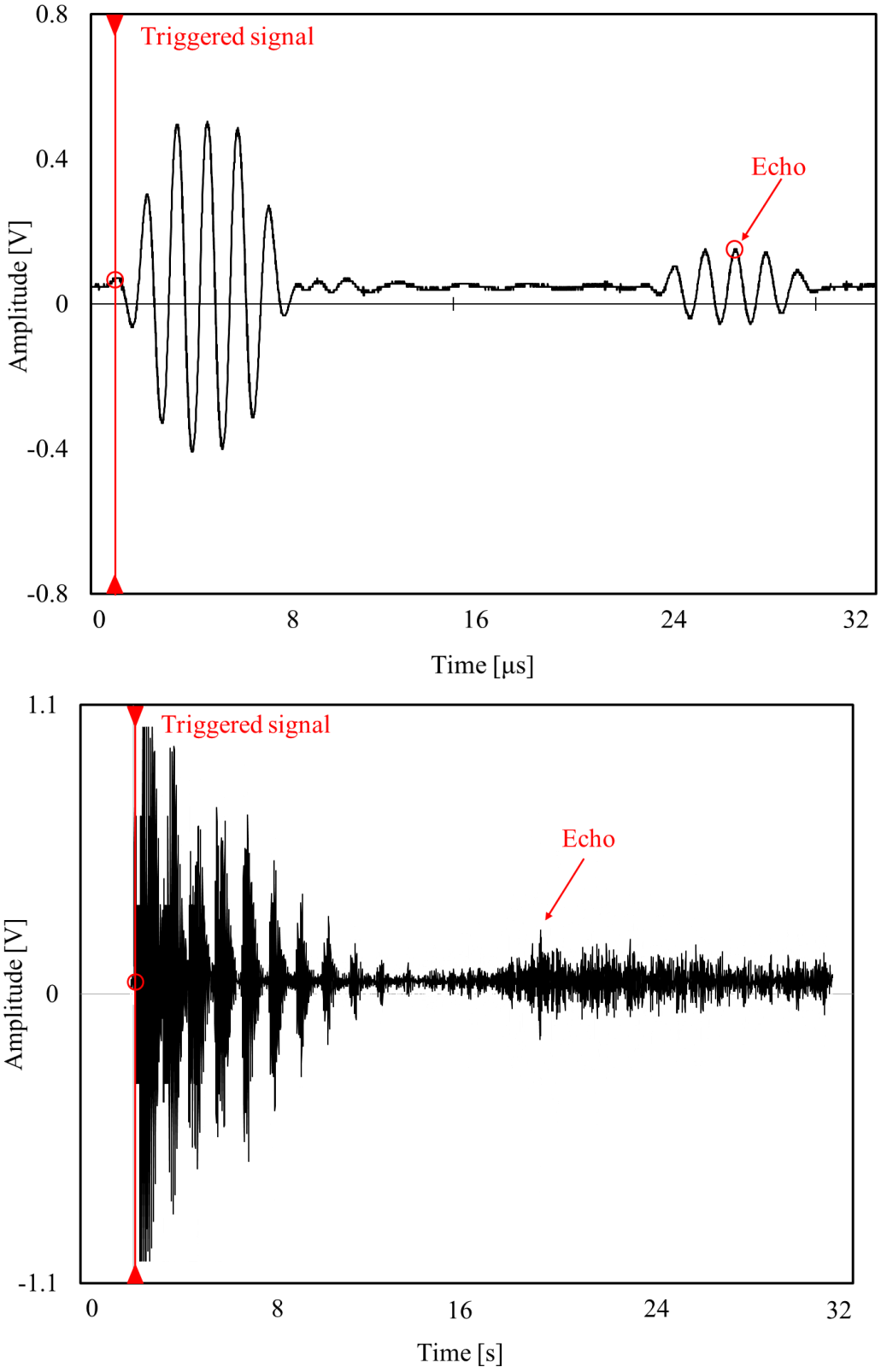

Figure 35. Plots of a pulse measurement received by the ultrasonic transducer. (Top) Standard transducer; (Bottom) Single-tapered waveguide.

4.6 Differential scanning calorimeter

Differential scanning calorimetry (DSC) analysis was performed using Mettler Toledo (DSC-1/700). The experimental setup and procedure which is detailed in Section (3.3). This technique is usually used for a wide range of application, and considered for the off-line thermal analysis for solids, liquids, solid-liquid suspensions (i.e. nanofluids). In this section, the thermophysical data obtained from the characterization of both water based nanofluids (temperature ranges from 0^{o}C to 85^{o}C) and salt based nanofluids (temperature ranges from 0^{o}C to 500^{o}C), with and without additives are provided and discussed.

The specific heat capacities and melting points of the samples were thermally tested, as a function of temperature, using the DSC technique. The measurements were made under atmospheric air with a flow rate of 15 cc/min and at a heating/cooling rate of 5 ^{o}C/min for salt based samples, and 10 ^{o}C/min for water based samples. The prescribed heating rate was chosen to avoid temperature increase due to thermal inertia as described by Ferrer et al.[189]. Both heat flow and temperature were recorded in the instrument with an accuracy of ±140 mW and ± 0.2 K, respectively. Each sample was weighed to an accuracy of 0.1 mg using a Mettler Toledo Microbalance (MX5). With regards to other measurement uncertainties, the manufacturer provided a value of ±5%, which was applied to the DSC data.

4.6.1 High temperature salt based nanofluids

First the two types of nitrate salts were analysed individually: Sodium nitrate ($NaNO_3$) and Potassium nitrate (KNO_3) "ReagentPlus®, ≥99.0 %, obtained from Sigma-Aldrich Company Ltd". Each salt sample was placed and crushed thoroughly in a 30µl platinum crucible, as described in section (3.3). Later, they were heated up from 0^{o}C to a temperature at which both salt melts (up to 360^{o}C). Under these conditions both nitrate salts were thermally tested for melting points and latent heat. Different melting temperatures and enthalpies were observed for each one of the salt samples, with sharp peaks during the DSC endothermic melting process. The obtained thermal data of each single salt sodium $NaNO_3$ and potassium salt KNO_3 are presented in Figure 36 and Figure 37.

As to the $NaNO_3$ salt sample, the larger and broader peaks are found at the temperature range of 305-315^{o}C, and the melting point at 306.03^{o}C, the details of which are shown in

Figure 36. Also the integration of the area under the heat flow curves represents the total heat that is $29.01x10^3$ mJ with the latent heat reported as 183.49 Jg^{-1} at the specified range of temperature, as illustrated in the same figure.

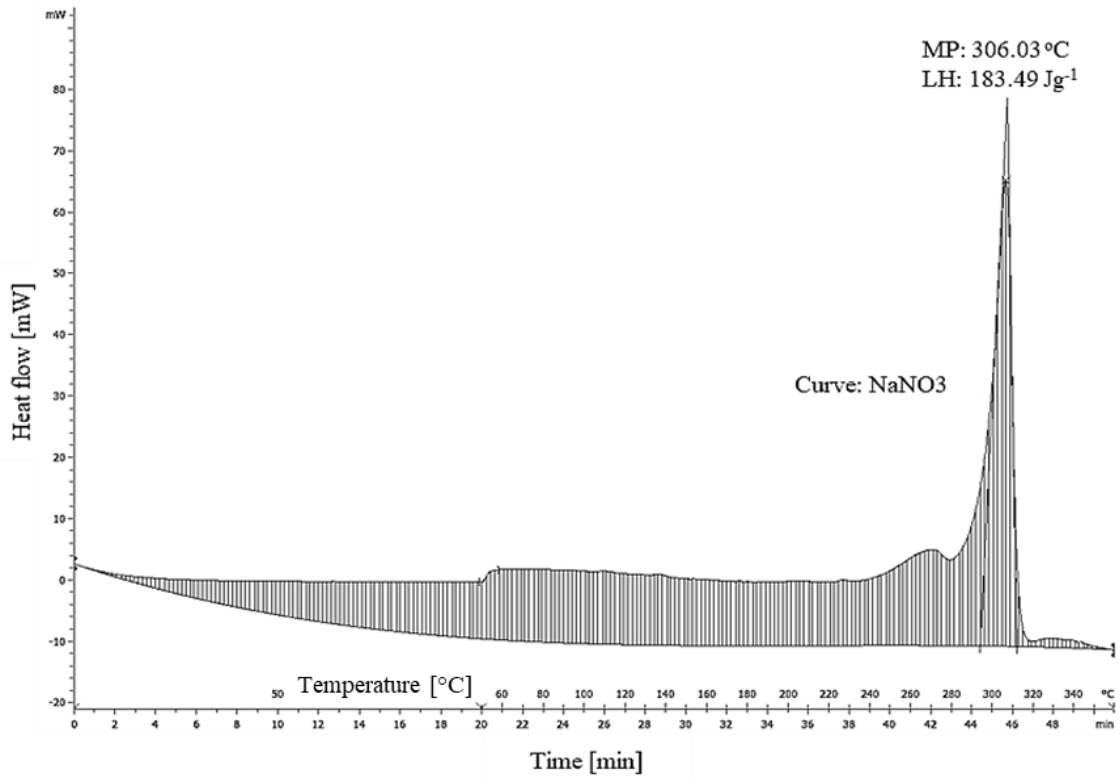

Figure 36. DSC heat flow curves for the melting temperatures and latent heat of $NaNO_3$ salt.

In the case of KNO_3 salt, two peaks were observed per sample just like the condition illustrated in Figure 37. Normally, the temperature of transition (melting point of solid into liquid) is taken from the first peak of the heat flow curve. However, in this case the first small endothermic peak (ranging from 135-155^{o}C) refers to the solid-state phase transition of the salt[12]. Whereas the second larger endothermic peak (ranging from 335-345^{o}C) refers to the melting of the salt (i.e. liquid state), as can be seen in the heat flow curves of Figure 37. This phenomenon is common for melting point measurement (with the existing type of DSC set-up) and it is likely to occur especially with KNO_3 samples, due to the presence of moisture. In detail, in the first cycle of the enthalpies of fusion curve, the moisture caught by the salt particles, was removed in the process of heating. As a result, the sample underwent partial solidification during the loading process, and was then re-homogenized in the first heating cycle. This is also believed to be the reason for the sample discolouration after it has been tested (from white to light brown) as shown in Figure 38. Moreover, for the pure KNO_3 salt sample, and based on the second peak the

melting point is reported at 338.24ºC (Figure 37). The total heat is $35.83x10^3$ mJ and the latent heat is 226.73 Jg^{-1} (Figure 37).

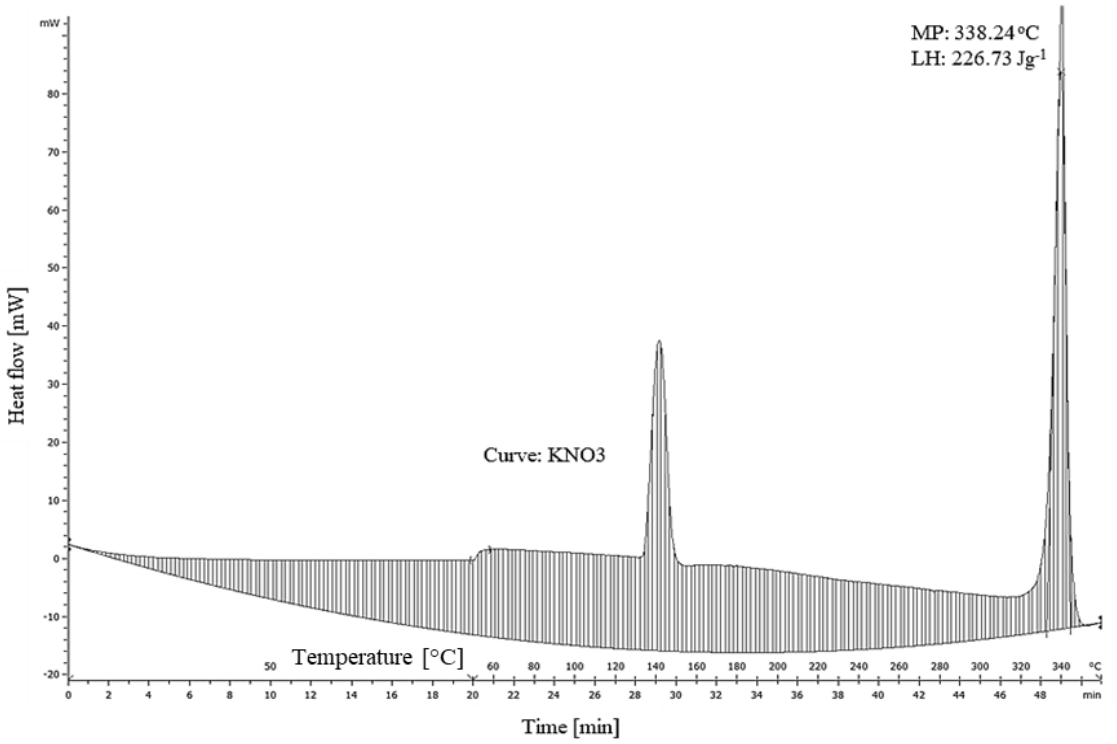

Figure 37. DSC heat flow curves for the melting temperatures and latent heat of KNO_3 salt.

Figure 38. DSC testing disc with 3 samples numbered on the tray as: 1) Empty pan used as a main reference; 2) $NaNO_3$ sample; 3) KNO_3 sample. The four pans at the corner of the figure are the same sample, with an extra empty pan number-4 used inside the DSC reference compartment.

Table 5 summarises the experimental findings for melting points and enthalpies of fusion, which reveal similar values to those in the literature, e.g. Tian et al[190]; Pfleger at al[191], and Lasfargues[12]. The majority of the results shows excellent agreement with these studies

and it demonstrate that the variation of melting point are within 0.31-1.55 % and the variation of the change of enthalpy is less than 0.322-6.26 %. The slight variations in the melting point and specific heat capacity of the different salts might be due to differences in the major impurities present within each salt, as described in Bauer et al[192] and Pfleger at al[191]. The main significance here is to confirm the suitability of the salts that are going to be used for the production of the binary solar salt mixture ($NaNO_3$:KNO_3 in 60:40 wt. %).

Table 7. DSC experimental data for melting points and enthalpies of fusion of the sodium nitrate $NaNO_3$ and potassium nitrate KNO_3 salts, in comparison to literature.

Reference	Manufacturer	Compound purity	Melting point [^oC]	Density [km m^3]	Latent heat [J g^{-1}]
			$NaNO_3$		
This Study	Sigma-Aldrich Ltd	≥ 99 %	306.03	≥ 2260	183.49
Lasfargues[12]	Fisher Science	98 %	308.01	-	172.84
Tian[190]	Commercial PCM	-	307	2260	172
Pfleger at al[191]	Commercial PCM	-	306	-	-
			KNO_3		
This Study	Sigma-Aldrich Ltd	≥ 99 %	338.24	≥ 2110	226.73
Lasfargues^[12]	Sigma-Aldrich Ltd	98 %	336.03	-	-
Tian et al[190]	Commercial PCM	-	333	2110	226
Pfleger at al[191]	Commercial PCM	-	334	-	-

4.6.2 Specific heat capacity of high temperature salt based nanofluids

DSC tests were then performed on the binary nitrate salt mixture ($NaNO_3$:KNO_3 in 60:40 wt. %) and salt based nanofluids with nanoparticle mass fraction ranging from 1.0 to 5.0 wt. %. For these tests the DSC was used to measure specific heat directly. The temperature program was set between 0 to 500°C.

The heat flow curve for the pure nitrate salt mixture is shown in Figure 39. It displayed two peaks per sample just like the condition illustrated previously in Figure 37 for the KNO_3 salt. The first small endothermic peak refers to the solid-state phase transition of the binary salt mix (temperatures ranging from 120 to 135^{o}C), whereas the second, larger endothermic peak (ranging from 223 to 236^{o}C) refers to the melting point of the salt (liquid state) that peaked at 228°C. It is also clear from the curves obtained in Figure 39 that over many heating cycles (three trials of the same salt mixture) that the obtained data were sharp and almost overlapping. Moreover, the data of Wu et al.[193] for the same binary salt mixture is included in the plot and found to be in good agreement with the results,

especially at the range of temperatures in which the two sharp peaks are spiking. Beyond these two endothermic peaks the data of Wu et al.[193] begin to deviate from the results.

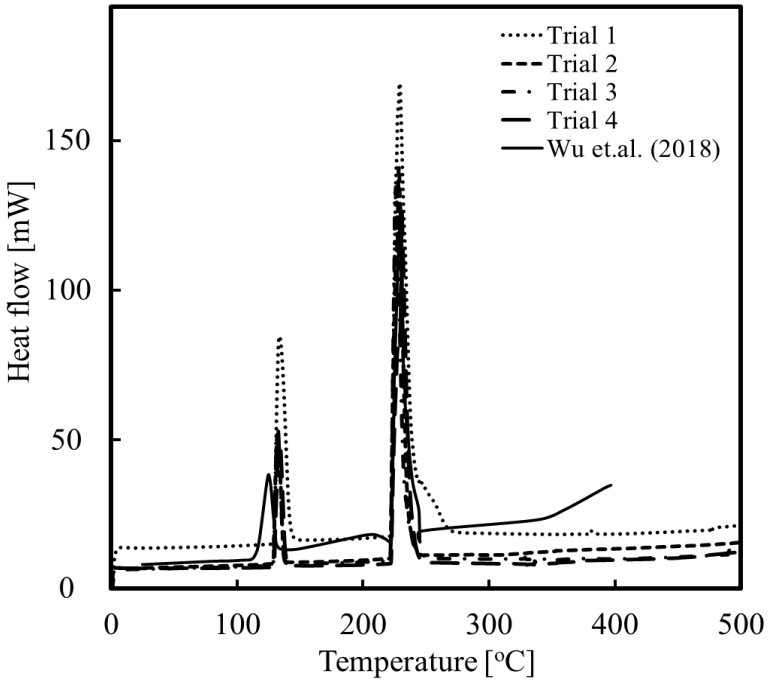

Figure 39. DSC heat flow curves for the melting temperatures of solar salt (60 wt. % $NaNO_3$ + 40 wt. % KNO_3) as a function of temperature, compared against the experimental data of Wu et al.[193].

After this, the specific heat capacities of the binary salt mix were measured, the results of which are plotted in Figure 40. The results of three different samples tested at least four times each (12 tests in total) were compared with other similar studies found in the literature[193-196] for the same type of binary salt mixture; the discussion of findings follows. For the lower temperature range ($0 \leq T \leq 160^oC$) since the salt mixture is still in the solid state, the specific heat values are directly proportional to temperature. When salt particles begin to change phase (from solid into liquid) at temperatures > 183°C, the slope of the heat capacity curve tends to flattens. This can be explained by the amount of endothermic energy (i.e. latent heat) required to complete the phase change, and thus to change all solids into liquid salt. Then the data gathered when all salt particles were converted into the liquid state (temperatures $230 \leq T \leq 300\ ^oC$) showed heat capacity values varying from 1.25 to around 1.37 $Jg^{-1}{}^{\circ}C^{-1}$. The closest heat capacity data, found to be as close as 5 % to 8 %, are those of Dudda and Shin[194.] The second closest result found in the literature are those by Perry[195], and though they were found to be different by 7 % to 10 %, they get close to 1.5 % at $375 \leq T \leq 395^oC$. A few other similar studies have been included in Figure 40 such as those by Wu et al.[193] and Zavoico[196]. The last two studies were found to have a variation of 10 to 13 % in the heat capacity values.

To the best of the author's knowledge, there are only a few studies reported for this type of nitrate salt mixture. It was also difficult to judge the accuracy of the available data found in literature. Thus, it is expected that the trace minerals and different composition of impurities found in the salts used, can have an impact on the thermodynamic properties of nanofluids. However, the identification of these impurities and their effect on the thermal properties would have to be investigated both experimentally and theoretically, over a wide range of temperature. Typically, variation in the thermophysical results of nanofluid may also be due to the: different instrumentation techniques, sample preparation and the actual physical characteristics of nanoparticles used. It can therefore be said that this issue is yet to be explored and more work is necessary on this topic.

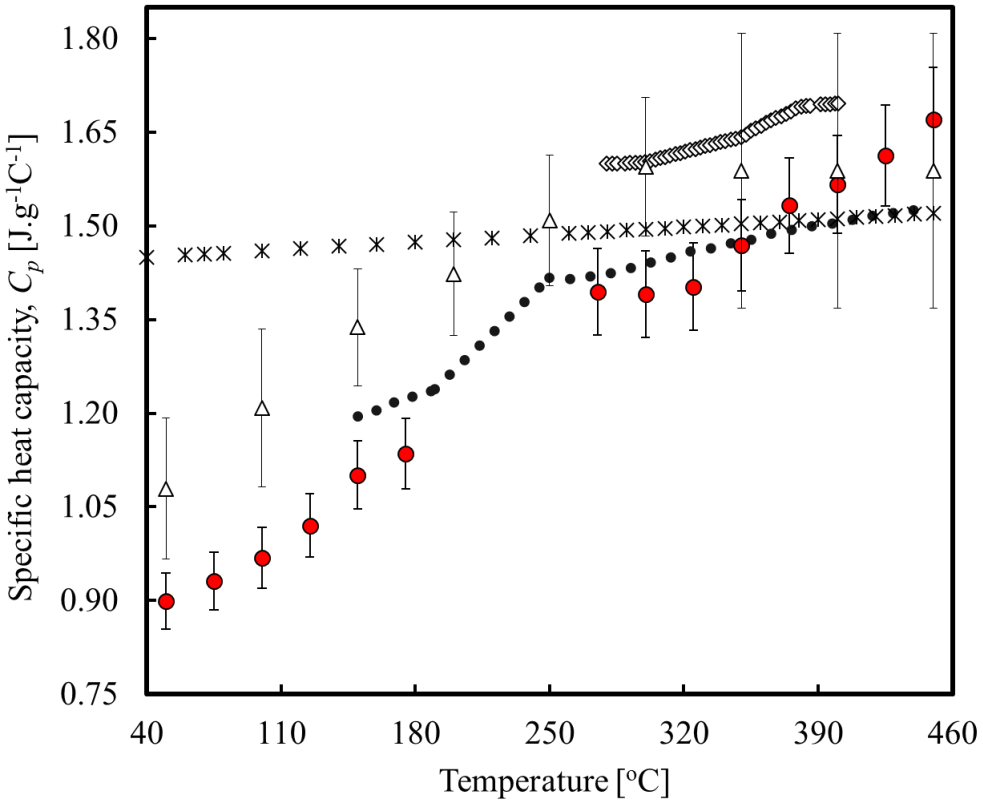

Figure 40. Specific heat capacity of pure solar salts (60 wt. % $NaNO_3$ + 40 wt. % KNO_3), as a function of temperature. Red circles: Present work. ∗∗: Experimental data of Zavoico[196]; ◇◇ : Wu et.al.[193]; ● ● Dudda & Shin[194]; △△: Perrys[195].

To explore the effects of dispersing nanoparticles on the specific heat capacity, samples containing solar salt with 1.0 to 5.0 wt. % Al_2O_3 nanoparticles were tested, and the results are illustrated in Figure 41. It is clear that the addition of 1.0 wt. % Al_2O_3 nanoparticles displayed a slight reduction (of around 2.1 %) in the specific heat capacity curve. Then as the concentration of nanoparticles was increased from 1.0 to 3.0 wt. %, further

reduction in the heat capacity curve was noticed. Similarly with 5.0 wt. % the heat capacity value tend to reduce further. In fact, at regions beyond the melting point of salt ($T \geq 228°C$) there seemed to be a clear relationship between the addition of nanoparticles and the change in specific heat curves as it increases. This may also be related to the heat capacity ratio data (Fig. 34) as the trends are consistent, and that may indicate performance of the molten salt as a heat transfer fluid.

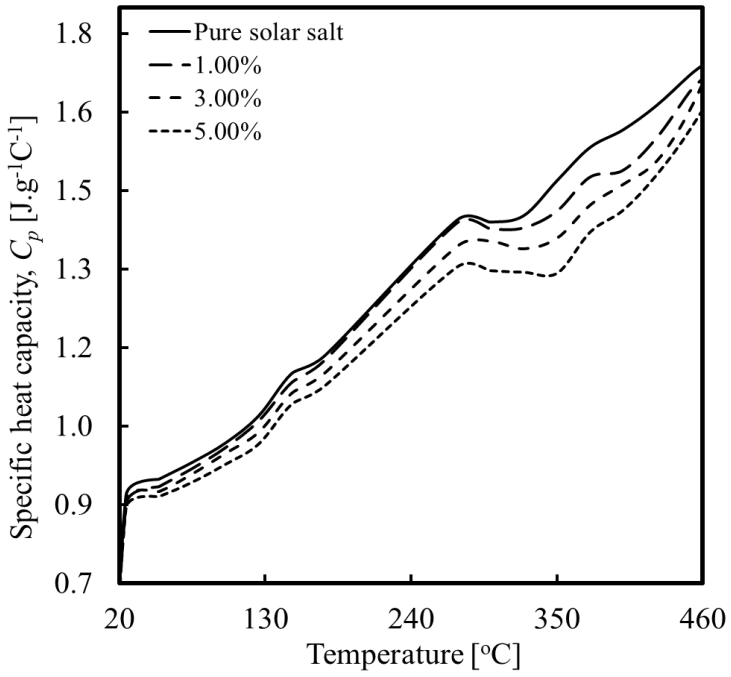

Figure 41. Specific heat capacity of solar salt (60 wt. % $NaNO_3$ + 40 wt. % KNO_3) and the suspension of nanoparticles (Al_2O_3: particle size d = 50 nm), as a function of temperature.

To explain the reduction in heat capacity and to verify the effect of temperature, particle concentration is plotted versus nanofluids heat capacity normalized by the heat capacity values of the base fluid, with Figure 42 giving results (coloured) for salt based nanofluids which are in good agreement with the experimental data of Chierruzi et al.[79], Lu and Huang[197], Schuller et al.[198].

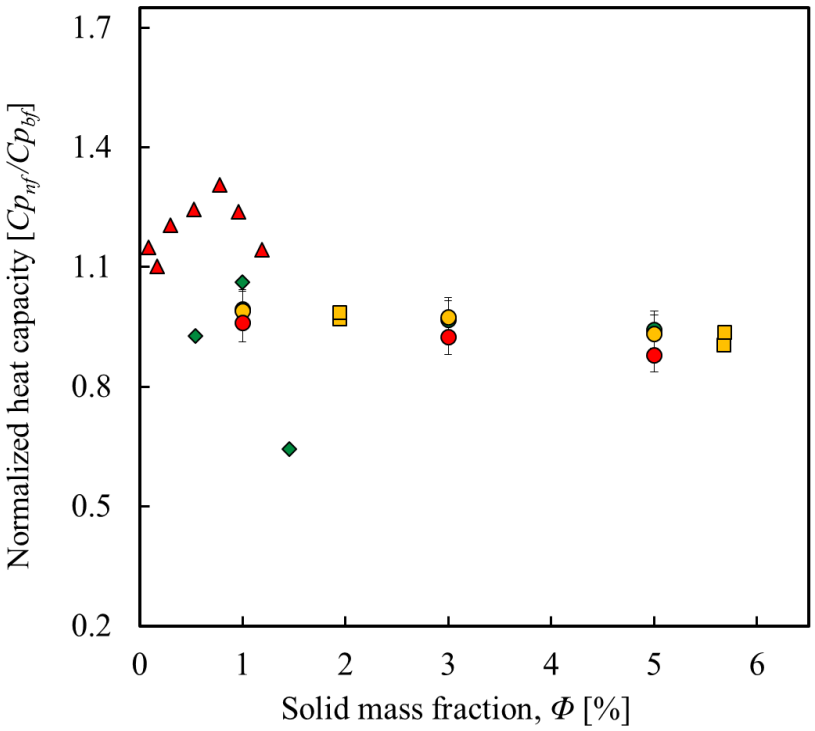

Figure 42. Normalized specific heat values versus nanoparticles (Al_2O_3: particle size d = 50 nm) concentration for salt based nanofluids at three distinct temperature. Circles: present work at: 220 ˚C (green), 300 ˚C (yellow) and 350˚C (red). Green diamond: experimental data of Chierruzi et al. (2013)[79]; Yellow square: Lu & Huang (2018)[197]; Red triangles: Schuller et al. (2013)[198].

In Figure 42 the heat capacity values of salt based nanofluids are normalised by the heat capacity of the base fluid, to allow comparison with other studies. In fact, the present results agrees well with these findings[197]. The study of Lu and Huang[197] that uses both 13 nm and 90 nm Al_2O_3 nanoparticles dispersed in the same solar salt, showed a decreasing effect in the specific heat with the increase in mass fraction. Moreover, a decrease in specific heat was reported by Lu and Huang[197] for a mass concentrations from 0.5 to 2.0 % at 300°C. It is also clear from the studies of Chierruzi et al.[79] and Schuller et al.[198] that the specific heat capacity only increases up to a certain mass fraction $0 \leq \Phi \leq 1$ %. Beyond the mass fraction of 1 wt. % it is clear that the heat capacity begin to decrease.

Other research, on the other hand, observed an increase in specific heat of molten salt containing nanoparticles. For instance, Dudda and Shin[194] reported a 27 % increase in the specific heat of salt base nanofluid with the addition of 1.0 wt. % of SiO_2, using various particle sizes. Ho and Pan[200] have also looked for the optimal concentration of alumina nanoparticles in a molten ternary salt mixture, and obtained a specific heat capacity increase of about 20 % at a very small nanoparticle concentration, i.e., 0.063 wt. % using

50 nm Al_2O_3 nanofluids. A still larger increase of heat capacity (with an average enhancements of ~9 %, ~28 %, and ~62 % of 0.5, 1, and 2.5 wt. % respectively) has been reported by Paul[201], who studied different nanoparticle enhanced ionic liquids containing spherical Al_2O_3 nanoparticles.

With regard to the effect of temperature on heat capacity of salt based nanofluid, it is clear that there is no suitable correlation from previous work. Researchers such as Lu & Huang[197] related this to the effect of nanolayer formation. In an explanation to this phenomenon they stated that the addition of nanoparticles increases the surface area and so the formation of a nanolayer resulted in a decrease in specific heat capacity. An alternative explanation of this phenomenon by the same researchers[197] relates this phenomenon to the thermal equilibrium model, stating that as the nanoparticles employed have a lower heat capacity than the base fluid, the dispersion of these particles may decrease the overall heat capacity of the mixture. Shin et al.[199] also considered the fact that formation of a nanolayer may be one of the possible mechanisms to explain the variation of specific heat. However, their study suggested interfacial thermal resistance between particles and liquid molecules, which will act as an additional thermal storage in nanofluids increasing the specific heat of these mixtures.

Salt based nanofluid, as an ionic liquid, behaves differently than a water based one, particularly at higher temperatures, thus the mechanism that alters specific heat capacity is as yet uncertain and more work is required on this subject.

4.6.3 Low temperature water based nanofluids

To measure the specific heat capacity of water based nanofluids the DSC procedure explained in section (3.3) was followed. Each sample was placed in a 40 µl sealed aluminum crucible (Mettler Toledo standard for thermal analyst). Later, samples were heated up from 0^{o}C to 85^{o}C, and ramped at 10 °C/min. Water was used as the reference material. For each sample of nanofluid at three different Al_2O_3-nanoparticle concentration of 0.5, 1.0, and 2.0 wt. % six measurements were taken. These values were then averaged to yield the data points and related uncertainty presented in Figure 43 and Figure 44.

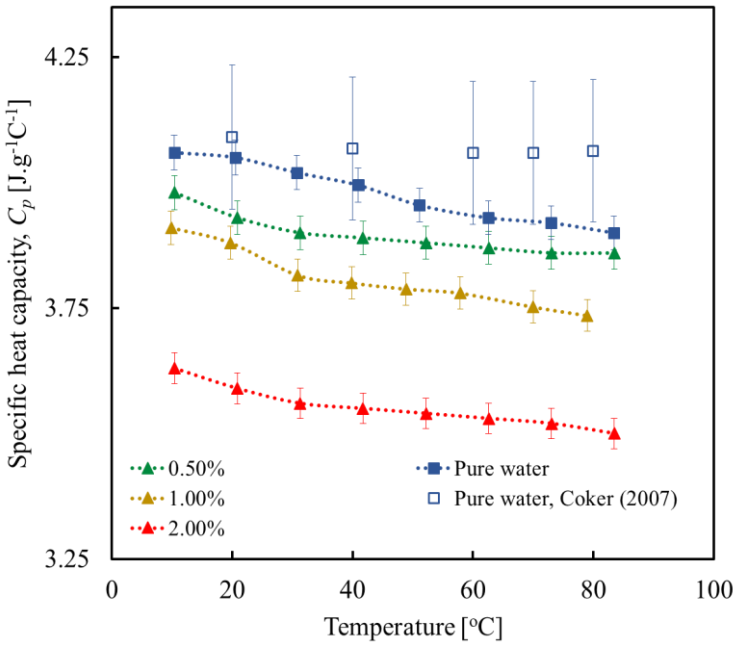

Figure 43. Specific heat capacity of water and the suspension of nanoparticles (Al_2O_3: particle size d = 50 nm) of varying concentrations, as a function of temperature.

It can be seen from Figure 43 that the specific heat capacity of pure water ranges from 3.90 to 4.06 Jg^{-1} °C^{-1}. This was found to be in good agreement with those obtained by Coker[184], (Figure 43) with an average of 0.125 Jg^{-1} °C^{-1} for the same temperature range (20°C to 80°C). Importantly, the present results are within Coker's[184] error bars and only started to deviate from those when it reached the upper part of the temperature range. Figure 43 also shows the specific heat capacity of water based nanofluids versus nanoparticle mass percent. It is clear that by increasing the mass percent, specific heat decreases from a minimum of 1.53 % at 0.5 wt. % to around 11.44 % at 2.0 wt. %. This means that for a lower specific heat, less energy is needed to raise the temperature. It can also be noted from Figure 43 that with the increase of temperature the specific heat capacity of nanofluids is decreasing. These findings have an important role on the thermal efficiency of nanofluids.

The properties of nanofluids at different mass percentage were then compared with theoretical values obtained from literature, as shown in Figure 44. To allow the use of these correlations the parameters were selected at a temperature of 40°C, thus the heat capacity value 4.18 Jg^{-1} °C^{-1} was used for the base fluid and for the nanoparticles it was 0.803 Jg^{-1} °C^{-1}. The specific heat correlation of Xuan and Roetzei[202] is based on the assumption of thermal equilibrium between the solid-liquid suspensions. The correlation of Sekhar and Sharma[203] formed an equation, based on the experimental results of earlier

researchers. Finally, the correlation of Vajjha and Das[204] is included which was based on the findings of their own conducted experiments, using various nanofluid combinations. For example, nanoparticles suspended in two different base fluids, Al_2O_3 and ZnO nanoparticles were suspended in a base fluid of 60:40 ethylene glycol/water mixture, and the SiO_2 nanoparticles were suspended in water. The uncertainties of the last two datasets are ±8.0% and ±2.8%, respectively.

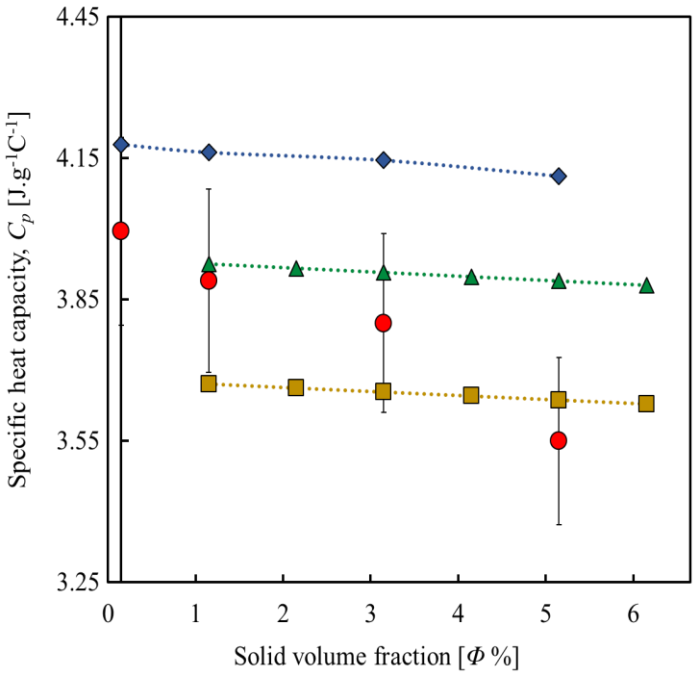

Figure 44. Specific heat capacity of water and the suspension of nanoparticles (Al_2O_3: particle size d = 50 nm) as a function of volume fraction, at T= 40 °C validated using correlations form literature. Red circles: Present work. Blue diamond: Xuan & Roetzel[202]; Green Triangle: Sekhar & Sharma[203]; Yellow square: Vajjha & Das[204].

From Figure 44 it can be seen that for pure water and up to 0.5 wt. % the present results were within the range of the theoretical model of Xuan and Roetzei[202]. However, at 0.5 wt. % and above the closest model to the present experimental results was that of Sekhar and Sharma[203], followed finally by that of Vajjha and Das[204].

Based on the study of Xuan and Roetzei[202], the reduction in specific heat capacity of Al_2O_3-water nanofluids with increased mass fraction can be explained by the difference between the specific heat capacity of Al_2O_3-nanoparticles (e.g. Cp_{np} = 0.79 Jg^{-1} ^{o}C^{-1}), which is significantly lower than that of the water base fluid (e.g. Cp_{fl} = 4.184 Jg^{-1} ^{o}C^{-1}), both at room temperature. It is also worth noting that although sonication of samples was performed, Al_2O_3-nanoparticles may slowly start to settle to the bottom of the DSC crucible (sample container) during testing, which may have slightly affected the results.

4.7 Summary and conclusions

The limited availability of methods for measuring the thermophysical properties of nanofluids online calls for the development of reliable techniques. The results of a combined experimental and numerical investigation aimed at determining the properties of water based Al_2O_3-nanofluids using high-temperature ultrasonic transducers, based on the time-of-flight principle, and thermal conductivity data from the Lagrangian particle tracking model were presented. The results show that this combined technique can be used as a reliable method of measuring the speed of sound in nanofluids up to a solid loadings of 5 vol. %. The variation of the speed of sound with nanoparticle concentration and temperature was found to be large compared to that in pure water. It was also shown that use of a thermal conductivity model of nanofluids (using a modified version of the Bridgman equation) with measured speed of sound values and the heat capacity ratio gives accurate predictions.

In addition, new data has been generated that is in line with some past work on Al_2O_3 nanofluids. These data demonstrate that the addition of nanoparticles to the base liquid enhances the thermal conductivity, with that enhancement increasing with increasing particle concentration and decreasing particle size. This trend is explained by numerical considerations of two mechanisms responsible for thermal conductivity and heat capacity ratio enhancement: Brownian motion (responsible for induced micro-convection) and aggregation kinetics (responsible for the formation of particle percolation pathways).

The thermophysical properties of molten salt based nanofluids were investigated by means of the speed of sound method. At particle mass fractions of 0.5 wt. % and 1.0 wt. % (corresponding to volume fractions of 0.25 and 0.49 vol. %) the presence of Al_2O_3 nanoparticles increased the heat capacity ratio by approximately 6 % and 12 % respectively. The salt based nanofluid was able to enhance thermal conductivity, similar to the enhancement of water based nanofluids reported earlier in this study. The increase in the thermal conductivity by the addition of nanoparticles is in line with the theoretical nanofluid thermal conductivity, described in the next Chapter-5. Based on the outcome of the combined experimental and modelling approach, it is suggested that the thermal enhancement is dominated by the formation of nanolayers between particles, particularly at 1.0 wt. %, and at such concentrations aggregates (nanoclusters) form in addition to the nanolayers between the particles. This leads to the conclusion that at high concentrations

the percolation effect dominates due to reduced interparticle distances (See further discussion in Chapter 5).

In this study, differential scanning calorimetry heat flow tests were conducted, with the aim of investigating the effect of particle mass fraction and temperature on the heat capacity values of nanofluids. The results of the low temperature (0 to 85ºC) water based nanofluids revealed that the addition of Al_2O_3 nanoparticles decreased the heat capacity from a minimum of 1.53 % at 0.5 wt. % to around 11.44 % at 2.0 wt. %. On the other hand, the specific heat capacity of the high temperature (0 to 500°C) nanofluids increased with increasing temperature. Addition of 1.0 wt. % Al_2O_3 nanoparticles, to binary nitrate salt based nanofluids displayed a slight reduction of around 2.1 % in the specific heat capacity. Then as the particle mass fraction was increased from 1.0 to 3.0 wt. % further reduction in the heat capacity curve was observed. A similar decrease in the specific heat capacity was reported in various nanofluids studies[197, 199], and thought to be due to solid-liquid interfaces and the interactions of fluid molecules (the formation of nanolayers around the surface of the nanoparticles). This type of solid-liquid interaction may have altered the specific heat capacity, especially those with an ionic liquid base such as molten salt. It should finally be emphasized that the thermal property mechanism in both water and molten salt nanofluid requires further investigation. A key task for future work will be to extend the advances made in the current study to include a broader selection of thermofluids such as ionic liquids under a wide range of operating conditions, especially temperature, to cover the full range of conditions found in solar thermal heat storage systems.

5 NANOFLUID STABILITY AND THERMAL CONDUCTIVITY USING MULTISCALE COMPUTATIONAL MODELLING

5.1 Introduction and background

In the previous chapter, we considered the experimental investigation of nanofluids, with the primary focus being on how nanofluid properties are dependent on nanoparticle concentration, dispersion stability, and temperature. However, understanding the dispersion and deposition behaviour of particles in nanofluid flows is quite challenging if it is to be performed only experimentally. Aside from the constraints associated with size and harsh environmental issues (i.e. high temperature setups for the molten salt nanofluid), many other complications arise from the responsible forces that are likely to take place at varied magnitudes and with multi-time scales, which are near impossible to resolve and quantify experimentally. The use of a numerical approach is therefore proposed to investigate these phenomena. More specifically, a multiscale computational model using Lagrangian particle tracking (LPT) simulation is developed to investigate the dispersion stability and thermal properties of nanofluids. The other benefit of the CFD model is that is allows the long-term stability of the dispersion to be studied. It is thought that agglomeration of nanoparticles to form larger particles could lead to surface impact, deposition and erosion, although evidence of this in the literature is conflicting[205, 206], with very few quantitative studies reported.

There is currently a lack of a reliable theory capable of making accurate predictions of the thermal enhancement properties in nanofluids (with relatively low solid volume fractions, down to 1 vol. %). The work described here therefore assesses the thermal conductivity of nanoparticle suspensions in fluids using a LPT-based computational modelling technique. A three-dimensional, multiphase fluid-solid model is developed which predicts the motion of suspended nanoparticles. The nanofluid is predicted using an Eulerian-Lagrangian hybrid approach with a constant timestep[58, 174]. This technique takes various multiscale forces into consideration in the calculations, whose characteristic scales are quite different, providing for the first time an analysis of all factors affecting the stability and thermal conductivity of nanofluids.

The system considered consists of 25-71 nm diameter Al_2O_3 ceramic nanoparticles, at various volume fractions ranging from 1.0 to 5.0 % suspended in fluids of different density ratios, with homogeneous temperature distributions from 25-85°C for water-based nanofluids and from 250-600°C for molten nitrate salt-based nanofluids. In addition, these salt-based nanofluids (nano-salts) form an important class of thermal fluids that can act as both heat transfer and thermal energy storage media for high temperature applications, including solar thermal systems[191]. Among these, the class of binary nitrate salts (60:40 wt. % $NaNO_3$:KNO_3) and their mixtures with metal oxide nanoparticles are the most prominent.

The results of the simulations aim to demonstrate the usefulness of the presented technique, with predictions elucidating the role of Brownian motion, fluid viscous drag, inter-particle collisions and DLVO forces on nanofluid stability. Results indicate that aggregated nanoparticles, at various particle concentrations, formed in the suspensions play an important role in the thermal behaviour of the nanofluids. Predictions are in agreement with theoretical and experimental results obtained in related studies. The thermal characteristics of nanofluids are also considered as a function of temperature, system chemistry and time (measured from an initially homogeneously dispersed state). As to the evaluation of the stability of nano-salts, the same computational technique was used, but with the addition of the oscillatory structural force to the model. This approach was undertaken to account for the motion of solid nanoparticles suspended in molten salts that are classified as ionic liquids. The technique enables the aforementioned multiscale forces, with different characteristics, to be established with predictions elucidating the influence of the crucial oscillatory structural force on the enhancement of thermal conductivity in such ionic liquids. The liquid structuring of salt melts around the embedded nanoparticles is found to play a key role in the nano-salts' thermal behaviour, with predictions in agreement with previous theoretical and experimental studies.

The outcome of this research forms the basis for the potential use of nano-salts in solar thermal systems. The proven enhancement in the conductivity of fluids affected by the addition of nanoparticles has great potential to assist the development of commercial nanofluid technology aimed at energy efficient and sustainable processes.

5.1.1 Novelty of the extended LPT model

There are a number of novel features in the model developed and described in this work. The parameters considered include particle size, physical interactions between the nanoparticles (collisions) and the dynamics between the particles and the carrier fluid, and the particle surface (zeta potential) and related nanocolloidal properties. The significance of the enhanced thermophysical properties is considered, with emphasis on the solid-liquid characteristics (e.g. specific heat, thermal conductivity and coefficient of thermal expansion), and mechanical properties (e.g. modulus of elasticity, rigidity and Poisson's ratio), of the alumina ceramic nanoparticles (α-Al_2O_3, 25-71 nm diameter) in water and molten salt. These characteristics are modelled dynamically as a function of temperature using data from Auerkari[161] in an attempt to understand the dynamics of nanoparticles in such multiphase systems. Ceramic oxide nanoparticles have been chosen for consideration in this study since they are available at reasonable commercial rates compared to other types of nanoparticles (e.g. carbon nanotubes and graphene), and hence are more likely to be adopted in practical systems. Additionally, α-Al_2O_3 ceramic nanoparticles possess strong ionic interatomic bonding giving an excellent combination of desirable thermophysical properties and thermal stability at elevated temperatures (i.e. usable in both oxidizing and reducing atmospheres up to 1900°C).

The kinetics of nanoparticles, such as aggregation, clustering and the resultant radius of gyration of the aggregates, are analysed using a depth-first search aggregate classification method. Finally, the thermal conductivity of nanofluids is predicted using an approach similar to that developed by Prasher et al.[122], but using a more justifiable Brownian velocity (by applying a Gaussian white noise process) for nanoparticles in a liquid rather than an approach based on the kinetic theory of gases.

Furthermore, the model is able to track the motion of embedded nanoparticles in the suspended fluid, which is modelled using an Eulerian-Lagrangian hybrid scheme with fixed time stepping, based on the work of Fujita and Yamaguchi[174]. This approach enables quantification of the various multiscale forces (Brownian motion, particle collision, fluid drag and DLVO forces) whose length and timescale characteristics are quite different.

The study presented here improves and significantly extends previous preliminarily research[157]. First, the simulations are performed for significantly longer timescales in order to obtain more stable and converged predictions. The present work also includes: a

validation of the computational model; further in-depth analysis to more comprehensively elucidate the key dynamics associated with thermal conductivity predictions; and significantly more results for the situations considered. As far as the authors are aware, there is no published analysis of the key dynamic factors affecting the stability and thermal conductivity of nanofluids using a similar multiscale computational modelling approach. Below, the combined mechanism-based model is described, and used to evaluate the most significant dynamic forces involved in nanofluids, with results and findings discussed. General conclusions are also drawn on the three-dimensional multiphase liquid-solid model's ability to predict aspects of thermal property enhancement in nanofluids, and their potential applications in industry.

Ultimately, the model can be used together with experimental investigations to provide more detailed insights into the fundamental dynamics of nanosuspensions, and can also be used in this regard in its own right. In addition, the present model allows different operating scenarios to be examined, and the impact of modifications to them established, again providing a better understanding of the particle dynamics, and hence the heat transfer characteristics of potential nanofluids. The final practical outcome is a model that can be used to establish the optimum characteristics for both coolants and thermal energy storage media.

5.2 Modelling of ceramic nanoparticle interactions and their influence on the thermal conductivity of water based nanofluids

Various simulations were performed using the described model, with results analysed to determine the forces and mechanisms responsible for nanoparticle interaction dynamics, aggregation and subsequent thermal property enhancement. The spontaneous ordering process of the particles in the suspension was first examined, followed by clustering and agglomeration as a function of time. Timestep snapshots of the simulations at 5 vol. % are presented in Figure 45. Figure 45(a) presents the initial homogeneous distribution of single particles within the computational cell. Small aggregate clusters begin to form at later times, as in Figure 45(b), and subsequently large aggregates gradually form with increasing time (Figure 45(c)).

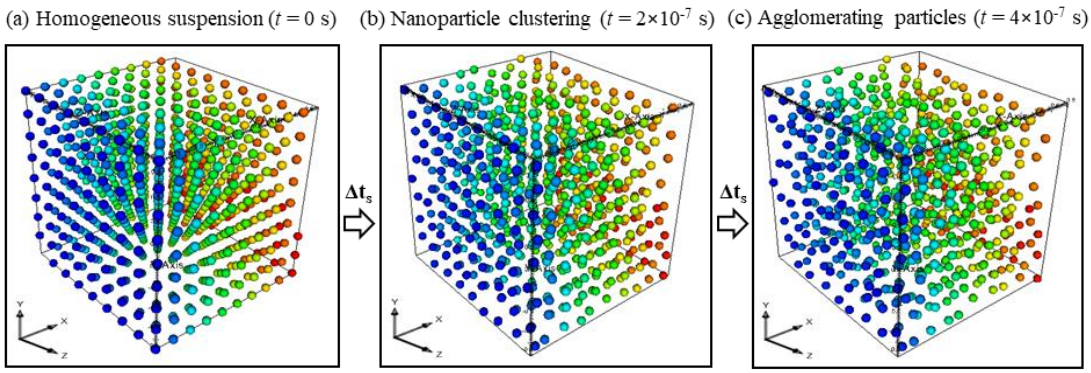

Figure 45. Representation of three-dimensional spherical 71 nm Al_2O_3 particles in 1 µm cubic cell filled with water showing: a) homogenous distribution of particles; b) formation of clusters; and c) nano-aggregation.

With the aim of investigating the influence of particle size on aggregation, the interaction of two suspended nanoparticles (with charged surfaces) was examined using three different sizes of particle, the results of which are presented in Figure 46.

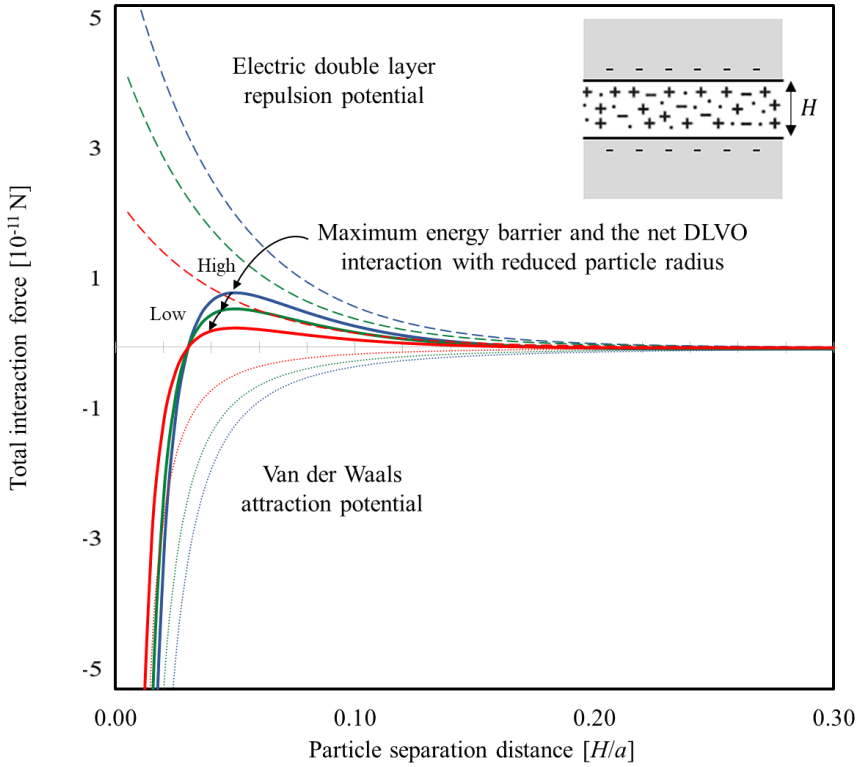

Figure 46. Interaction potential energy versus distance profiles of two colliding nanoparticles (spherical Al_2O_3 particles at 1 vol. % and 25°C) at three different sizes: 25 nm (red); 50 nm (green); and 71 nm (blue). Electric double layer (– –); maximum or total energy barrier (—) and van der Waals (···). The actual magnitude of the energy is proportional to the particle size (radius, *a*) or interaction area (between two planar particles surfaces, *H*).

The figure illustrates the potential energy of two colliding nanoparticles caused by the two attractive and repulsive interparticle forces[172]. For the different particle sizes used in the simulations it is clear that, as the separation distance becomes smaller, the electric double layer (long-range) force is initially dominant, decaying exponentially. Then at very small inter-particle distances, the attractive van der Waals (short-range) forces begin to dominate, leading to a collision between the two particles and subsequent adhesion. In addition, for a constant volume fraction, aggregation increases with decreasing particle size as the average inter-particle distance between nanoparticles decreases. This is exemplified by the reduction in the potential energy observed for 71nm-sized particle as compared to 25nm-sized particles, where the maximum energy barrier (the sum of all the repulsive and attractive potentials) that the particles must overcome to collide and form an aggregate decreases with the reduction in size. Computational limitations were strongly dependent on particle number, therefore we were restricted to using particle sizes $\geqslant$ 25nm.

The model also allows for the magnitude of the different hydrodynamic and interaction forces exerted on nanoparticles in a suspension to be predicted, given a set of material and fluid properties. Figure 47 illustrates each of the multiscale forces plotted as a function of the intersurfacial distance, H, normalized by the particle radius, a. The results show the magnitude of the various forces exerted on the particles which drive particle collision and aggregation in the computational cell. They illustrate that when sufficient distance is maintained between nanoparticles, the effects of both the fluid (drag) and Brownian random motion forces dominate over other contributions since these forces are dependent on the velocity of the nanoparticles and interactions between the particles and the fluid. As the intersurfacial distance between particles becomes small ($H/a < 0.1$), the electric double layer repulsive force starts to have a significant effect on particle interactions. When two particles are close to colliding, the attractive van der Waals forces becomes dominant over all others. After a collision of two nanoparticles, the repulsive soft-sphere collision force increases rapidly and is of a similar magnitude as the attractive force.

The main conclusion is that the van der Waals attraction always exceeds double-layer repulsion at small enough separations since it represents a power law interaction, while the double-layer interaction energy remains finite or rises much more slowly as the relative inter-particle distance tends to zero. These findings are in line with observations

within the existing literature on DLVO theory (i.e. Eqns. (3-23)-(3-27)), as noted by Israelachvili[172] for the various types of interaction potential and the sequential phenomena that occur between two similarly charged or colloidal particles. These equations can therefore be used to describe how the colloidal dispersion stability is affected by the electrolyte concentration and surface charge density.

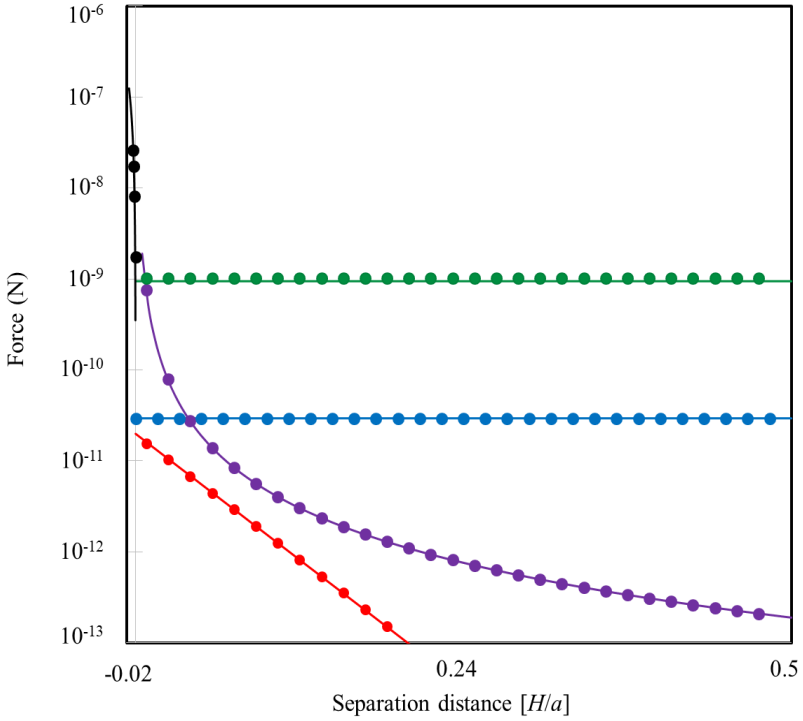

Figure 47. Verification of modelled colloidal forces across the control volume (1 μm cubic cell filled with water and spherical 71 nm Al_2O_3 particles at 1 vol. % and 25°C), showing the magnitude of the following forces: electric double layer (purple); van der Waals (red); fluid drag (blue); Brownian motion (green); and collision (black), as functions of intersurface distance. Theory[58, 174] (—); and numerical (●).

The magnitude of the forces with inter-particle distance shown in Figure 47 leads to the conclusion that every force noted should be considered in the dynamic modelling of nanofluids, as they are all relevant at different interparticle separations. Moreover, the values given are in excellent agreement with similar results in the literature[58, 174]. The results of Figure 48, which demonstrates the effect of varying temperature, also confirm and validate the numerical implementation of the theory described above.

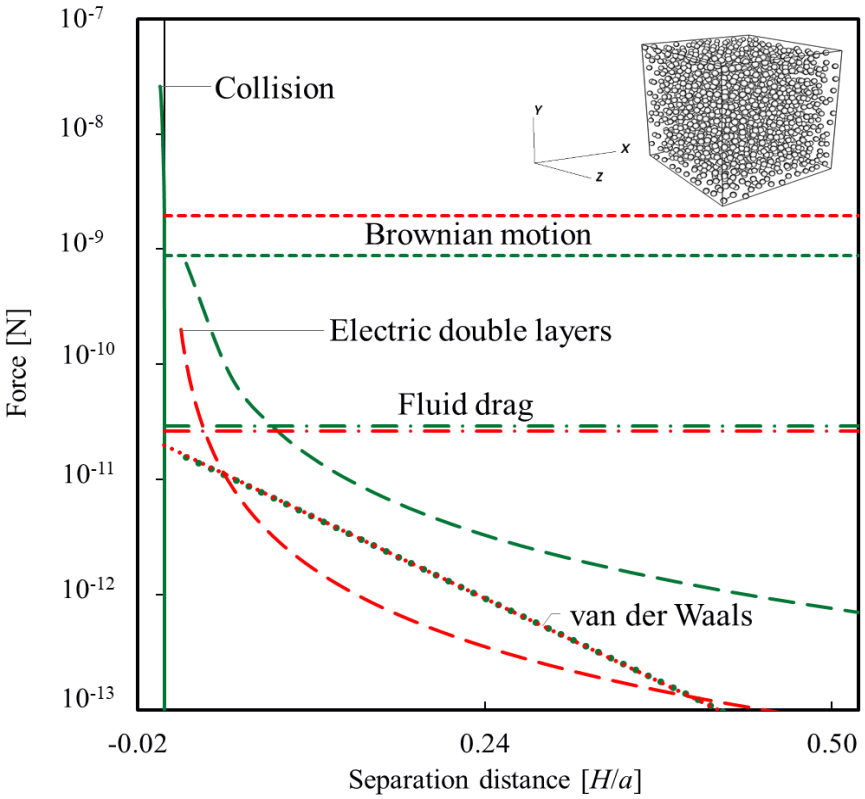

Figure 48. Magnitude of modelled colloidal forces acting on spherical nanoparticles submerged in a fluid continuum across the control volume (1 μm cubic cell filled with fluid and spherical d_p = 50 nm Al_2O_3 particles at 1 vol. %, and 25°C (green) and 90°C (red), as in the insert) showing the magnitude of the forces as functions of inter-surface distance.

5.2.1 Interaction between nanoparticles and aggregate formation

The model allows for determination of the precise number of various dynamic events via post-processing. Firstly, collision events are defined to be an event in which two particles 'intersect' and then separate during which the soft-sphere interaction forces are active. The mean free path between particles together with the aggregate number (using the depth-first search to identify chains of particles) can then be calculated, as explained in previous sections 3.4.5 and 3.4.7. Figure 49 provides predictions of the mean number of aggregates formed in the system as a function of solid volume concentration and temperature, together with mean free path values.

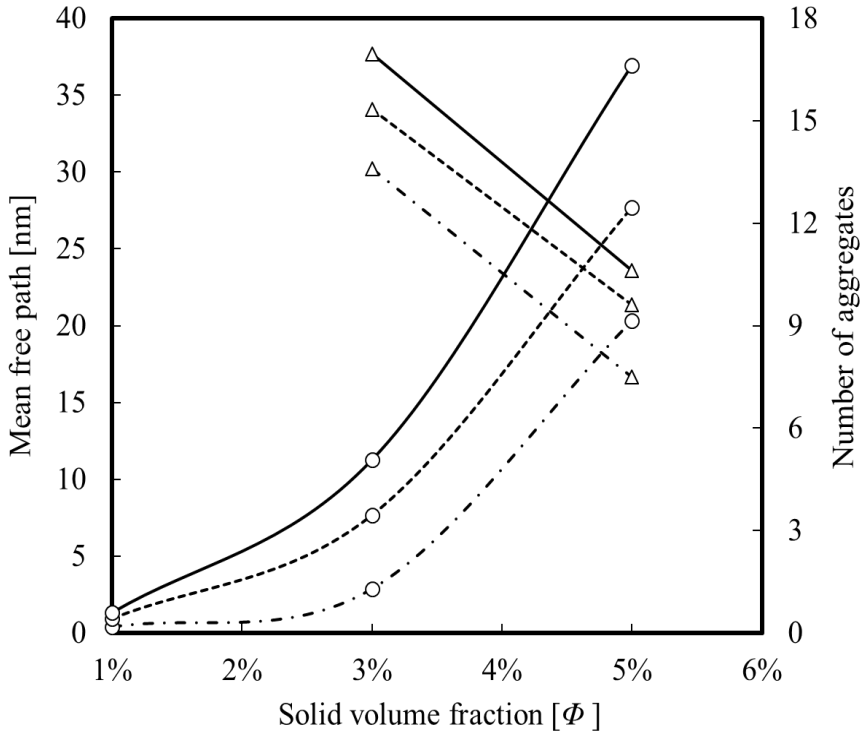

Figure 49. Number of aggregates (○) and mean free path (△) versus particle concentration across the control volume (1 μm cubic cell filled with water and spherical 71 nm Al_2O_3 particles): at 25°C (- · -); 55°C (----); and 85°C (—).

It is clear from the results of Figure 49 that very few aggregates are formed when the concentration is 1 vol. %, which is due to very few collisions occurring over the time simulated. Due to this, the mean free path predictions are not shown for this case. At 3 vol. %, the mean free path clearly decreases due to increased collision and agglomeration events. Above 3 vol. %, the system enters a regime where both collisions and agglomerations begin to take place more frequently, leading to a substantial increase in the average number of aggregates. The probability of collision and aggregation rises with increasing temperature due to the effect of Brownian motion. In terms of the fundamental dynamics, it is clear that particles at increased temperatures exhibit an increased mean free path, and therefore cover a larger distance in the same period of time, increasing their collision cross section, which further increases the aggregation rate.

Corresponding results for the nanoaggregate mean radius of gyration, R_a, were determined using the depth-first search method as described in the methodology. The results are presented in Figure 50, together with predicted effective thermal conductivity, k_{eff}, values, at various volume fractions and temperatures.

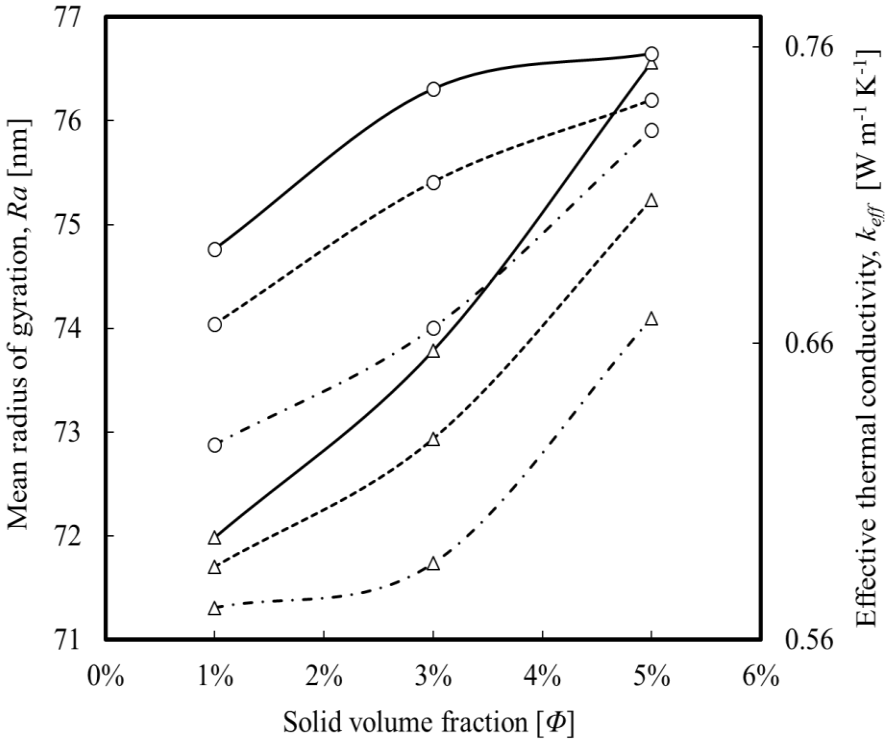

Figure 50. Mean radius of gyration (△) and thermal conductivity (○) versus particle concentration across the control volume (1 μm cubic cell filled with water and spherical 71 nm Al_2O_3 particles): at 25°C (- · -); 55°C (----); and 85°C (—).

The results for the thermal conductivity given in Figure 50 indicate an almost 13 % increase in k_{eff} for 5 vol. % of particles over the solid volume fraction range considered. These predictions were made over a temperature range of 25 to 85°C, and show that enhancement is therefore to be expected. The exhibited temperature dependency is likely a result of increased kinetic energy and hence Brownian motion forces, encouraging collisions and providing more chances for aggregation. Although the Brownian motion force decreases as the mass of aggregates increases over time, the increase in k_{eff} is still evident, as highly conducting ceramic nanoparticles come in contact with each other. Thus, with increasing collisions and aggregation with time, the concentration and temperature variations indicate the effect of direct particle contact and the agglomerates' percolation effects on the conductivity. The observed combined effects of convection and conduction on thermal enhancement in nanofluids have been reported by Prasher et al.[122], and are of the same magnitude as exhibited in the predictions of Figure 50. This leads to the same conclusion regarding the percolation effect in nanoaggregates and the dominant dynamic forces which are believed to govern thermal behaviour in nanofluids. The other interesting behaviour in the trend in conductivity is that it tends to plateau at concentrations of 3 vol. %, and temperatures of 55°C, and above, which can be explained

by the simultaneous increase in the mass of the aggregates and the decrease in the nanoparticles' Brownian motion. As might be anticipated, the predicted mean radius of gyration of the aggregates increases significantly with both the solid volume fraction and temperature, although the temperature dependence is lower for increased volume fractions, likely due to the reduced interparticle separation decreasing the necessity for increased particle speeds to instigate collisions.

5.2.2 Effect of time on aggregate radius of gyration

As noted, analysis of the size distribution of nanoparticle aggregates within the computational cell shows that there is a significant dependency of the nanoaggregates' mean radius of gyration, R_a, on temperature and solids concentration. Figure 51 presents the time sequence of R_a values over 400 ns of simulation time at 25 to 85 °C. The system seems relatively stable after the first 50 ns. Then at a given time point it is clear that a rise in temperature results in an increase of the nanoaggregate size. This occurs at all concentrations, but most significantly at 5 vol. %.

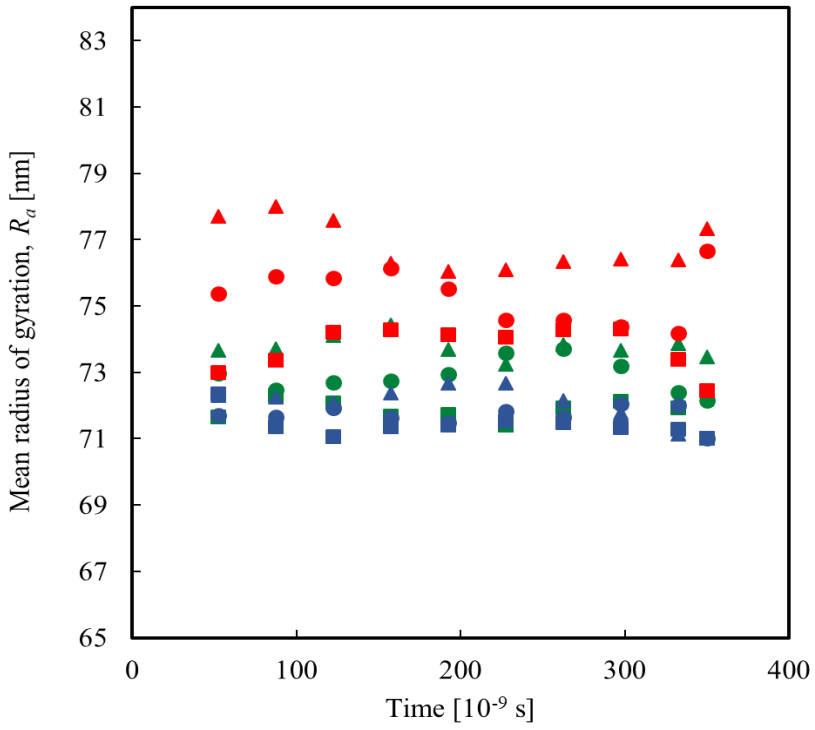

Figure 51. Time dependence of aggregate mean radius of gyration at: 25°C (■); 55°C (●); and 85°C (▲); and for 1 vol. % (blue); 3 vol. % (green); and 5 vol. % (red).

Aggregation is known to be a time-dependent phenomenon. Similar conclusions as those noted can be reached from the nanoaggregate size distribution inferred from R_a values

over time, as shown in Figure 52, which gives the trend of the aggregate mean radius of gyration for the 3 vol. % and 5 vol. % concentrations at three different temperatures between 25 and 85°C. The temperature dependence of R_a is quite evident from the increase in the relatively stable time dependent R_a values with temperature. Moreover, for the 3 vol. % and 5 vol. % concentrations it is observed that the mean radius of gyration be going down for increased temperatures, which can be explained by the increased kinetic energy separating the particles over time (e.g. in the case of 5 vol. % concentration, at 85°C, 2000 nanoparticles are injected into the computational cell, and so R_a is found to be around 77 nm, based on the radius of 16 nanoparticles held together in an aggregate. The same applies to all nanofluids at different temperatures and concentrations.

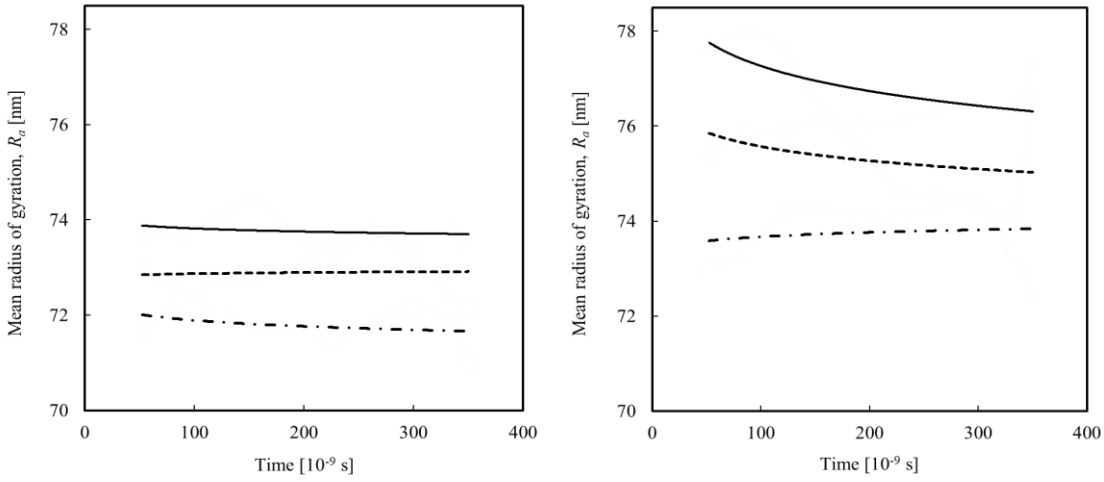

Figure 52. Variation of mean radius of gyration with time. The figure shows the variation in R_a for the 3 vol. % concentration (left) and 5 vol. % concentration (right): 25°C (- · -); 55°C (----); and 85°C (—).

5.2.3 Effect of temperature and concentration on thermal conductivity

The great potential for thermal conductivity enhancement using nanofluids has encouraged many researchers to undertake comprehensive investigations using various methods and techniques. In this section, results of the LPT methodology used to underpin predictions of the thermal conductivity of Al_2O_3-nanofluids are validated in order to provide confidence in the accuracy and ability of the method.

The thermal conductivity values predicted by the present model are therefore compared against relevant experimental measurements and other model predictions from a number of sources[59, 207-211], with good agreement found throughout. This comparison is shown in Figure 53, with both the data and predictions from the latter sources showing the same

trend in thermal conductivity enhancement with increasing volume fraction of nanoparticles as the present model.

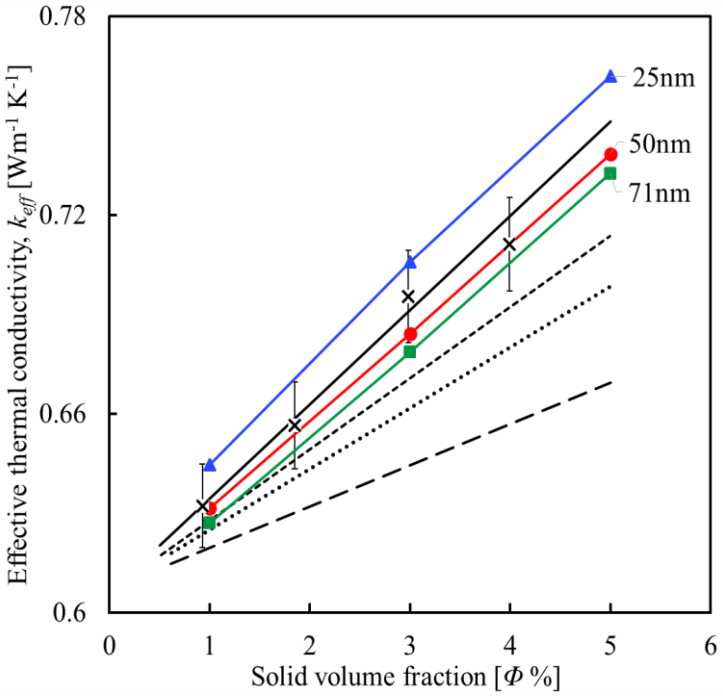

Figure 53. Effective thermal conductivity of nanofluid containing spherical Al_2O_3 particles as a function of solid volume fraction Φ. Experimental data of Beck et al.[59] (×), with error bars from that source. Theoretical work of Maxwell[207] is shown for a spherical nanoparticles (⋯). Lines represent predictions of Nan et al. [208] (– –); Yu and Choi[210] (----); and Warrier et al.[211] (—).Present work: predictions using numerical model[157] at different particle sizes: 71nm (-■-); 50nm (-●-); 25nm (-▲-).

Furthermore, the present model is also capable of predicting the effect of concentration and nanoparticle size on the overall thermal conductivity of the system, giving predictions (coloured) which are in good agreement with experimental data (Beck et al.[59]) that examined heat conduction in nanofluids using seven sizes of alumina nanoparticles ranging from 8 to 282 nm in diameter.

Regarding size dependence, the present model predicts that the conductivity of nanofluids containing d_p = 25 nm Al_2O_3 particles is greater than those containing 50 nm and 71 nm particles, by nearly 8% and 15%, respectively, although no systematic experimental investigation of size-dependant conductivities has been performed. Conversely, in Beck et al.[59] it is indicated that the thermal conductivity enhancement decreases as the particle size decreases below about 50 nm and they attributed this decrease in enhancement to a decrease in the thermal conductivity of the nanoparticles themselves (as the particle size becomes small enough to be affected by increased phonon scattering). Their

measurements showed a clear effect of the particle size and dispersion method (e.g. mixing/sonication) and indicate that there is an expected limit of enhancement for nanofluids containing larger nanoparticles. Their results were found to be marginally within the predictions of the present study. It should be noted that although the results given in Figure 53 show the effect of volume fraction on the thermal conductivity, the existing model exhibited more sensitivity to particle size in predictions of conductivity than the model of Beck et al.[59].

The theoretical values of the static model of Maxwell[207] presented in Figure 53 were found to be slightly below the predictions of the present model. This classical model of Maxwell[207] is widely used to determine the effective electrical or thermal conductivity of liquid-solid suspensions of monodisperse, low volume fraction mixtures of spherical particles. It involves the particle size/shape and volume fraction and assumes diffusive heat transfer in both fluid and solid phases. The model may give good predictions for micron-sized particles, but generally underestimates the magnitude of thermal conductivity enhancement in nanosuspensions as a function of volume fraction[117].

Figure 53 gives predictions made using the numerical model by Nan et al.[208] which accounts for the effects of particle size, shape, distribution, volume fraction, the orientation of inclusions and the interfacial thermal resistance on the conductivity of particulate composites. In addition, their model was developed in terms of an effective medium approach combined with Kapitza's thermal contact resistance concept, suitable for the prediction of the thermal conductivity of mineral matrix composites[208]. This may explain the discrepancy between predictions of their model and those of the present work since the Nan et al.[208] model characterizes the conductivity of particulate composites within an interfacial thermal resistance without accounting for all the possible mechanisms involved and the dynamic forces present in nanofluids.

The predictions of Yu and Choi[210] were derived using a modified version of the Maxwell equation which includes the effect of liquid molecules close to the solid surface of nanoparticles on the thermal conductivity of solid-liquid suspensions. This effect assumes the formation of layered solid-like structures (known as ordered nanolayers) which have a major impact on nanofluid conductivity[210], in particular when the particle diameter is less than 10 nm. Although their predictions are found to be slightly below the results derived from the present model, they follow the same overall trend, as shown in Figure 53.

Warrier et al.[211] also modelled the thermal conductivity of nanoparticle suspensions and examined the effect of the two phases present in the heterogeneous system. Their model takes into account adjustable parameters such as the temperature dependence of the thermal conductivities of the individual phases, as well as the size dependence of the dispersed phase. Using this modified version of the geometric mean model allowed the effect of a wide range of particle sizes (11 to 302 nm), volume fractions and temperatures to be studied. The model is also capable of predicting the effect of different base fluids and the decrease in the thermal conductivity of semiconductor nanoparticles, especially when the particle size is of the same order as the phonon mean free path. It can be seen that the Warrier et al.[211] model predictions fall between the Beck et al.[59] error bars. Although the predictions of Warrier et al.[211] are slightly above those of the present results, they show approximately the same rate of change in conductivity with solid volume fraction.

It can therefore be concluded that the numerical model described is in good agreement with the experimental data of Beck et al.[59], and the numerical model of Warnier et al.[211], with all these showing very similar gradients in conductivity with solids volume fraction. In contrast, the models of Maxwell[207], Nan et al.[208], and Yu and Choi[210] all under-predict the influence of solid volume fraction on effective thermal conductivity by comparison. This is in agreement with previous work that shows that the Maxwell equation, of which Yu and Choi[210] is a variant, underpredicts this relationship. The Nan et al.[208] simulations underpredict to a far greater degree than any of the other models, suggesting that the approach is not well suited to Al_2O_3 nanoparticle suspensions. It should be noted that dynamic models of nanofluid thermal conductivity represent an enhancement of some of the classic models and thereby provide additional physical insight into the phenomena considered. Undoubtedly, it is necessary to consider not only one possible mechanism but combine several in order to explain enhancement in the thermal conductivity of nanofluids.

With the aim of further verifying the above predictions, values of the normalized thermal conductivity, k_{eff} / k_{bf}, are plotted against temperature and volume fraction in Figure 54. The predicted thermal conductivity values are found to be in good agreement with experimental data and the predictions made by the other researchers noted[60, 66, 212] , and particularly the data of Lee et al.[60] and Das et al.[66] at the same operating temperature (25ºC). This is in addition to agreement with the theoretical model of Hamilton and

Crosser[212] for both cylindrical and spherical particles. The probability of combined collision and aggregation increases linearly as the concentration increases from 1 to 3 vol. %. The other interesting aspect of the results is observed at 3 vol. % and above, where a rise of the conductivity values with increasing volume fraction is evident. It is clear from all these results that the thermal conductivity increases roughly linearly as concentration increases from 3 to 4 vol. %. This demonstrates that the system is entering a different regime where energetic collisions driven by Brownian motion start to weaken and instead agglomeration starts to dominate, leading to the substantial increase in conductivity values.

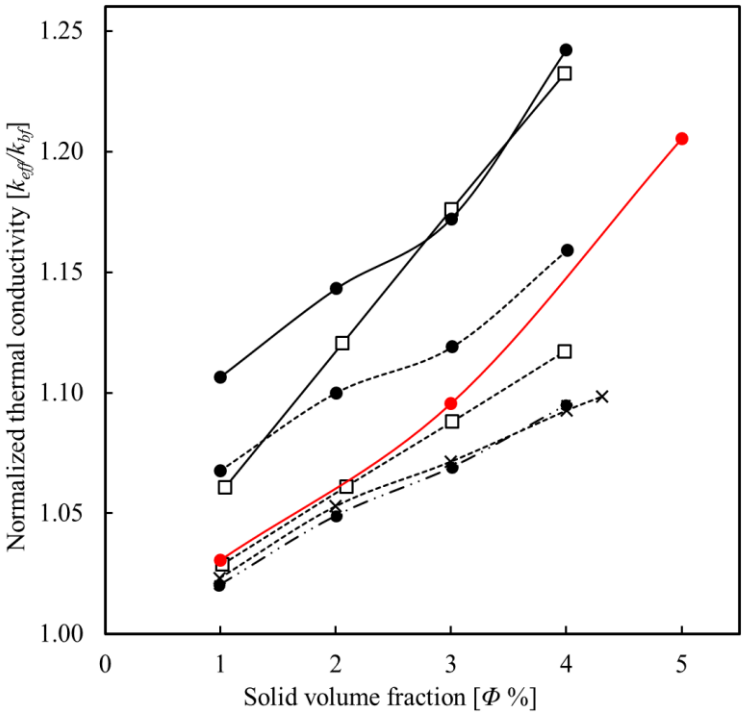

Figure 54. Thermal conductivity ratio of nanofluid containing spherical d_p = 50 nm Al_2O_3 particles as a function of volume fraction Φ. Experimental data of Lee et al.[60] at 21°C (--×--). Lines represent the predictions of Das et al.[66] at 25°C (– · · –●), 33°C (--●--) and 51°C (–●–). The theoretical work of Hamilton and Crosser[212] at 21°C is shown for both cylindrical (–□–) and spherical (--□--) models. Present work: predictions using numerical model at 25°C (-●-).

The approximately linear relationship between the thermal conductivity and temperature, and particle concentration, is another behaviour that is predicted by the model, as illustrated in Figure 55. It is clear from these results that the temperature dependence is not as strong at concentrations < 3 vol. %, but for larger values a stronger dependence is apparent. This reflects the role of intermolecular forces, dominated in this case by Brownian motion, that are strongly temperature- and concentration-dependent[211]. A

similar increase in the normalized thermal conductivity with temperature has also been reported by Das et al.[66], and is thought to be caused by the stochastic motion of the nanoparticles. Figure 55 also shows the effect of the volume concentration of nanoparticles on thermal conductivity enhancement: it increases with volume concentration from 1 to 5 vol. % of nanoparticles. Similar effects have been reported for different nanofluids based on experimental measurements and model predictions[59, 60, 209, 210, 211]. The thermal conductivity enhancement in nanofluids at higher concentrations is believed to be due to the increased interaction of nanoparticles in the base fluid, and the interactions that occur as more nanoparticle chains are formed. The same figure also illustrates the variation in thermal conductivity enhancement with respect to temperature (ranging from 25°C to 85°C). The maximum conductivity was obtained at 85°C and the enhancements are 4 %, 6.7 % and 25 % for 1 vol. %, 3 vol. % and 5 vol. %, respectively, compared with pure water. The thermal conductivity is enhanced at higher temperatures due to Brownian motion and collisions between nanoparticles[213].

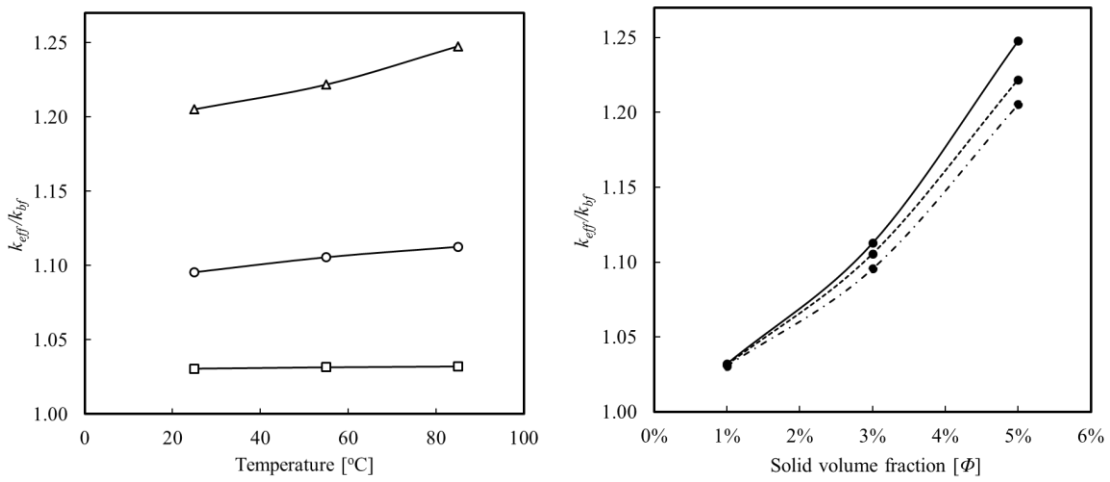

Figure 55. Normalized thermal conductivity enhancement as a function of temperature (left) at: 1 vol. % (–□–); 3 vol. % (–○–); and 5 vol. % (–△–), and as function of concentration (right) at: 25°C (– · –); 55°C (----); and 85°C (—).

Similar results were obtained by Prasher et al.[121], in agreement with the previously explained combined mechanism-based model of aggregation kinetics with Brownian motion-induced micro-convection. These findings support the superiority of nanofluid dynamic models as they take the effect of the nanoparticles' random motion into account, while static models assume that the nanoparticles are stationary relative to the base fluid, which is not physically realistic.

For the nanofluids considered, k_{eff} was found to increase with temperature over the range 25 to 85°C. This can be seen from the simulation results presented in Figure 56.

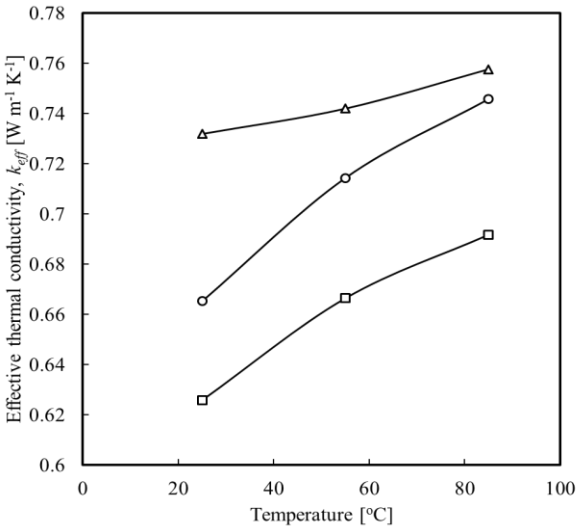

Figure 56. Effective thermal conductivity enhancement as function of temperature at: 1 vol. % (–□–); 3 vol. % (–○–); and 5 vol. % (–△–).

Similar behaviour was reported by Das et al[46], who noted that the variation in the thermal conductivity of the nanofluid with temperature closely follows that of the base fluid. To investigate this observation, the present simulations were extended to cover a wider range of temperatures than previously considered, from 0 to 100°C, and the results, together with values of the conductivity of pure water and Al_2O_3, are compared in Figure 57.

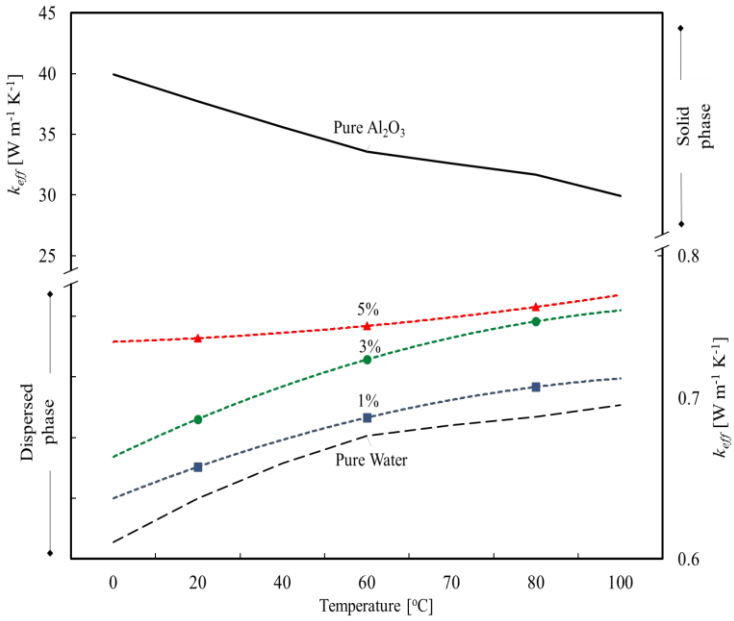

Figure 57. Predictions of thermal conductivity as a function of temperature at: 1 vol. % (--■--); 3 vol. % (--●--); and 5 vol. % (--▲--). Lines represent standard reference data for pure water of Ramires et al.[214] (– –) and experimental data for pure aluminium oxide of Touloukian[215] (—).

It can first be noted that the gradual increase in the conductivity of pure water, such as that reported by Ramires et al.[214], from the hydrogen bonded structures could, to a large extent, be responsible for the increase in k_{eff} in water based nanofluids at relatively low particle concentrations of around 1 vol. %. Also, research has shown that k_{eff} for pure water is relatively high and rises to a maximum value at approximately 130°C, starting to fall at higher temperatures[216]. A partial decrease in k_{eff} with increasing temperature is therefore expected above this value, even when other types of base-fluids are used. For instance, for oil-based nanofluids the thermal conductivity of oil is expected to decrease with increasing temperature, and so the overall k_{eff} of the mixture will be slightly affected[217]. Adding additional nanoparticles to the mixture could compensate for the drop in thermal conductivity caused by the base fluid.

Secondly, the general trend in the nanofluid conductivity shows an increase in k_{eff} with temperature as the particle concentration increases up to 3 vol .% which is qualitatively in line with the trend for pure water. Above this value, however, the k_{eff} variation with temperature begins to move away from that observed for pure water to more closely resemble that observed for pure solid Al_2O_3. The conductivity of pure solid Al_2O_3 decreases with an increase in temperature, an effect due to the gradual accompanying phase change. This implies that the mechanism for thermal conductance in nanofluids at high concentrations above 5 vol. % will likely move away from the liquid mixture behaviour and become more similar to that of pure solid composites, as described by Keblinski et al.[56].

5.2.4 Effect of pH variation of nanofluid on thermal conductivity

The thermal conductivity of the nanofluids considered was found to be highly dependent on changes in pH which is one of several important factors which determine the isoelectric point of a nano-suspension (as it varies the surface potential and hence controls the magnitude of the repulsive force), with this point defined as the pH at which the surface of the nanoparticles exhibit a neutral net electrical charge or, equivalently, a zero zeta potential, i.e. $\zeta = 0$ V. For this particular value of ζ, only attractive van der Waals forces are significant, and the solution is not stable as the repulsive forces between particles tend to decrease to zero. This is referred to as the point of zero charge, for which a colloidal particle is found to be electro-kinetically uncharged leading to poorer dispersion and increases in particle attraction and agglomeration[46, 61]. In this study,

established isoelectric point values from experimental investigations on colloids were employed to provide guidance for model development[122, 218]. Thus, the pH value corresponding to the isoelectric point of an Al_2O_3-water nanofluid has been determined[219] to occur at pH ≈ 8.5 - 9.2 (for α-Al_2O_3, purity > 99.9 %, suspensions). Similar values were reported by Kim et al.[220] for α-Al_2O_3 suspensions with ζ potentials ranging from -55 mV at a maximum pH = 10.5, 22 mV at pH = 7, and 75 mV at pH = 1. Clearly, an increase in pH lowers the zeta potential in a ceramic α-Al_2O_3 nano-suspension.

The dynamics of nanoparticle suspensions are affected by all of the parameters noted earlier, including those related to the DLVO energy profile. Correspondingly, nanoparticle stability and agglomeration in the present model is controlled by changing the ionic concentration valence, z. As such, a variation from 1 to 5 in z is representative of a change in pH from neutral or acid (pH ≤ 7), which promotes stability, to values outside the region of the isoelectric point at pH ≈ 8.5 - 9.2. Figure 58 gives predictions of the conductivity against pH values, and with respect to R_a and Φ, demonstrating the strong pH-dependence of the system. This is equivalent to changing the valency which changes the Debye length (the screening potential), with a high valency corresponding to high screening, hence poor stability (i.e. more aggregation).

From the figure it can be seen that the range of electrostatic surface potentials decreases as the valence of the ions in solution increases. This demonstrates that the dispersion of Al_2O_3 is affected by the electrostatic repulsion force which is in agreement with classical DLVO theory. Regarding the increase in thermal conductivity due to percolation effects (direct contact between the particles) in the aggregates, this effect is also illustrated in the results of Figure 58 where a clear enhancement in conductivity values occurs as a function of pH at a given temperature and concentration.

The results in the figure also clearly indicate the thermal conductivity enhancement due to the combined effect of collision and aggregation as concentration increases from 1 vol. % to 3 vol. %, in line with Eqn. (3-31). Another interesting feature of the results is the shift observed at concentrations of 4 vol. %, where a change in the ionic concentration valence from 1 to 5 causes a rise in the conductivity from 0.70 to 0.735 $Wm^{-1}K^{-1}$. An increase in conductivity values at higher volume fractions is evident, but when the system is forced to form aggregates (by moving away from the isoelectric point), it enters a different regime. Up to that point, collisions driven by Brownian motion have begun to diminish and instead agglomeration hasarted to dominate, leading to the substantial

increase in conductivity values observed, resulting from percolation effects and heat transfer by conduction through the nanoaggregates. Nevertheless, at concentrations ≥ 5 vol. % the system enters a limiting region, where a clumped nano-suspension (congested aggregates) starts to form due to the presence of too many nanoparticles in the control volume. This demonstrates that although aggregation can enhance the conduction contribution compared to a well-dispersed system, it needs to be controlled to ensure the formation of well dispersed aggregates (chain-like clusters), rather than large congested aggregates.

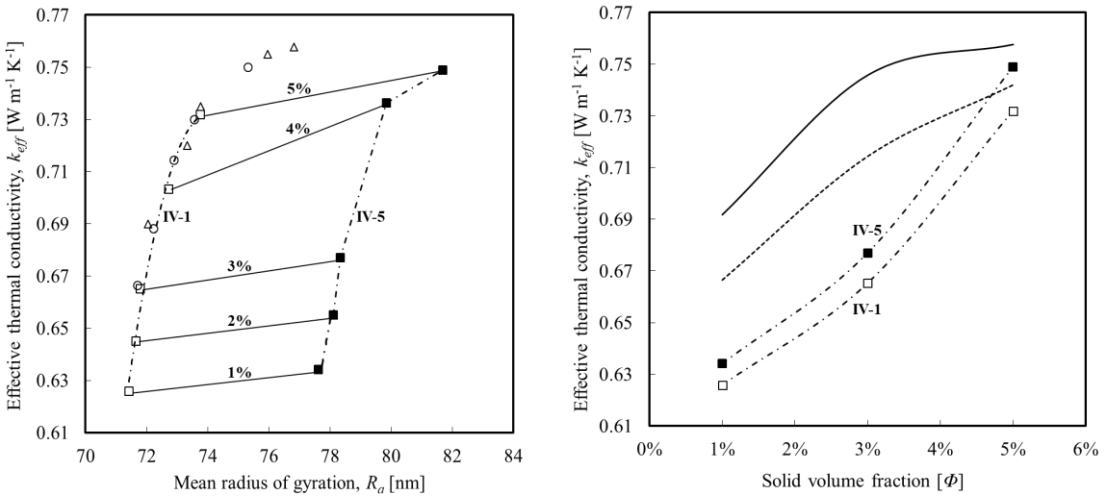

Figure 58. Thermal conductivity dependence on the mean radius of gyration (left) – effect of pH presented as a function of changes in z from $z = 1$ corresponding to pH ≤ 7 (– · □ · –) to $z = 5$ outside of the isoelectric point at pH ≈ 8.5-9.2 (– · ■ · –) at 25°C (□); 55°C (○); and 85°C (△). Note that R_a is higher at the isoelectric point as energy potential for Al_2O_3 particles at this pH reaches zero. Thermal conductivity dependence on solid volume fraction (right) – dependence is represented at different ion valencies IV-1 (– · □ · –) and IV-5 (– · ■ · –) at 25°C against particle concentration, and: ion valency IV-1 at 55°C (----); and 85°C (—).

Figure 58 also shows that the thermal conductivity increases with an increase in particle concentration, as well as with the difference between the pH value of the aqueous suspension and the isoelectric point of Al_2O_3 particles. It can clearly be seen that at 25°C, and at 1 vol. % to 3 vol. %, the change in pH (screening potential) is still significant even if the system is optimally aggregated. Thus, a slight change in pH leads to a clear enhancement in the thermal conductivity of the system. At higher concentrations ≥ 4 vol. % the effect of full nanoparticle aggregation leads to combined convective and conductive effects and hence an improved thermal conductivity. Conversely, at higher concentrations (≥ 4.5 vol. %) the thermal conductivity curve starts to flatten and the effect of increasing pH causes the 25°C curve to overlay the 55°C curve. This leads to the conclusion that at

higher concentrations the effects of Brownian motion are reduced and instead percolation effects dominate due to increased nanoparticle aggregation in the system.

In general, the numerical simulations indicate that a change in zeta potential (determined in part by the valence and pH of the solvent phase) is an important parameter as it affects the level of agglomeration in nanofluids. Similar behaviour in ceramic nano-suspensions was reported by Lee et al.[221] who studied the effect of the surface charge on the thermal behaviour of nanofluids. The study indicated that this basic parameter is primarily responsible for the thermal conductivity enhancement of nanofluids. It also highlighted how colloidal nanoparticles can be destabilized as the pH of the solution moves closer to the isoelectric point, eventually altering the thermal conductivity of the nanofluid. It is concluded that the pH of the colloidal liquid strongly affects the suspension stability and hence the performance of thermal nanofluids

5.3 Role of oscillatory structural forces: non-DLVO forces between ceramic nanoparticles and their influence on the thermal conductivity of molten salt based nanofluids

When ionic liquids (i.e. molten salt fluids) are used as the base fluid, the oscillating layered structure force (represented by the matrix of liquid molecules around the nanoparticles) comes into play. An explanation of this phenomenon is given in section 3.4.6, pointing out that the structural force arises once there is a change in the liquid density at the surface of nanoparticles, as they approach one other. Simulations were performed using the model described in Section 3.4.6, with results analysed to consider the forces and mechanisms responsible for nanoparticle dynamics, structural and surface property effects, and thermal conductivity enhancement. First, the spontaneous ordering process of nanoparticles in a suspension was examined, followed by the formation of a structured nanolayer (of liquid molecules around the seeded nanoparticles) and of percolation networks of nanostructures using a system under forced aggregation conditions.

A plot of the interaction energy between two colliding particles in the molten salt fluid is given in Figure 59, illustrating the dynamic properties of the salt melts (liquid films confined between two smooth nanoparticle surfaces). It can also be seen that the resulting oscillatory structural force is monotonically decaying in amplitude with particle separation distance.

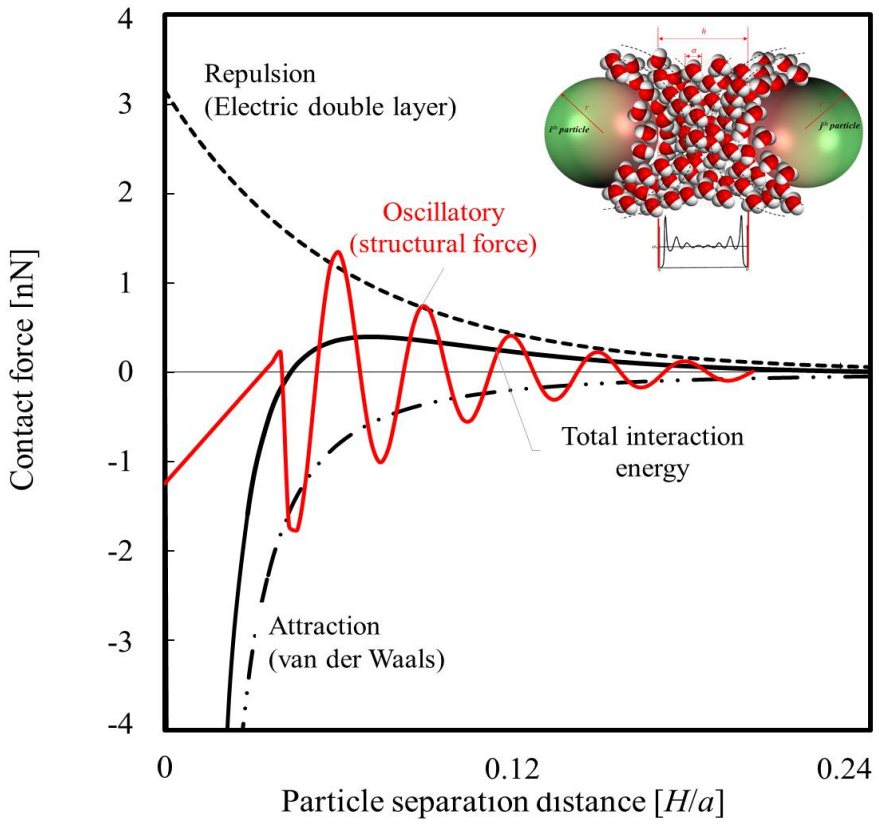

Figure 59. Plot of the interaction energy between two colliding particles in molten salt, presenting the resulting oscillatory structural force is monotonically decaying in amplitude with particle separation distance.

Figure 59 also shows the concentration dependence of the structural force in the oscillatory regime and how it is dominated by the oscillatory period d_1, and the characteristic decay length d_2.These findings are in line with the existing literature on oscillatory theory (i.e. Eqns. (3-34)-(3-38)). The period of the force is equivalent to the diameter of the small liquid molecules σ, and shows an oscillatory nature close to the particle surface with an amplitude that decays monotonically with H (e.g. for a given H, the disjoining pressure increases almost five times for a 10 % increase in the volume fraction φ of the liquid molecules).

The model also allows for the magnitude of the different hydrodynamic and interaction forces exerted on nanoparticles in suspension to be predicted as illustrated in Figure 60. Each of the multiscale forces shown in the figure is plotted as a function of the intersurfacial distance, H, normalized by the particle radius, a similar to that previously described in Figure 47.

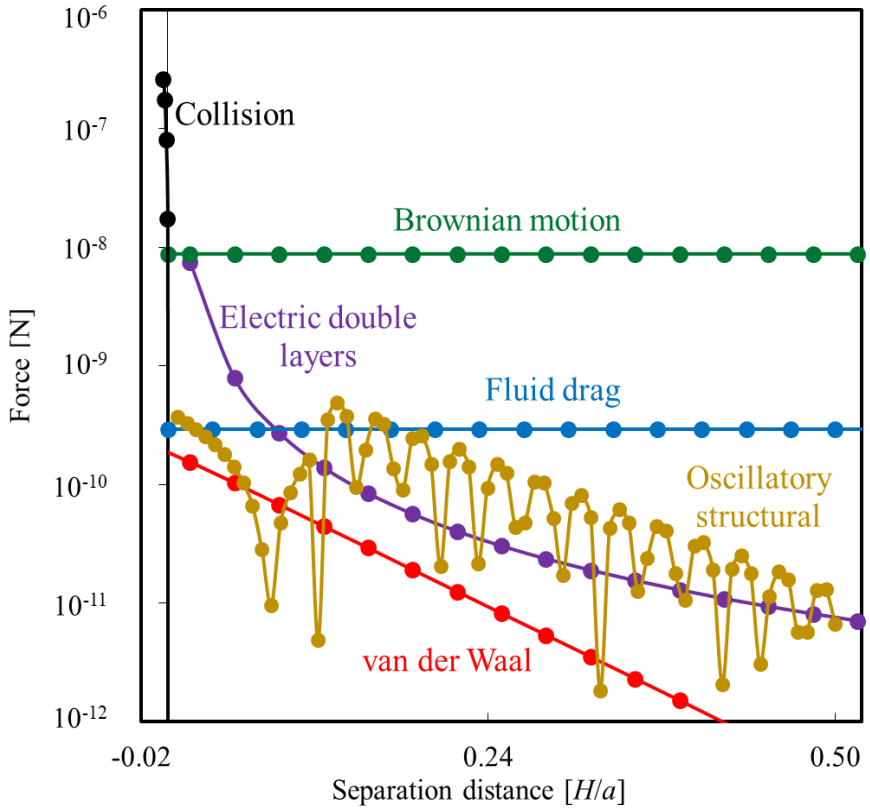

Figure 60. Verification of modelled colloidal forces across the control volume (1 µm cubic cell filled with molten salt and spherical 71 nm Al_2O_3 particles at 1 vol. % and 350 °C), showing the magnitude of the following forces: electric double layer (red); van der Waals (purple); fluid drag (blue); Brownian motion (green); Oscillatory (mustard) and collision (black), as functions of intersurface distance. Theory[58, 174] (—); and numerical (●).

Furthermore, the model predicts the effect of temperature and nanoparticle size on the overall thermal conductivity of the system, with Figure 61 demonstrating model predictions (coloured) for pure molten salt which are in good agreement with experimental data of Ma and Banerjee[90].

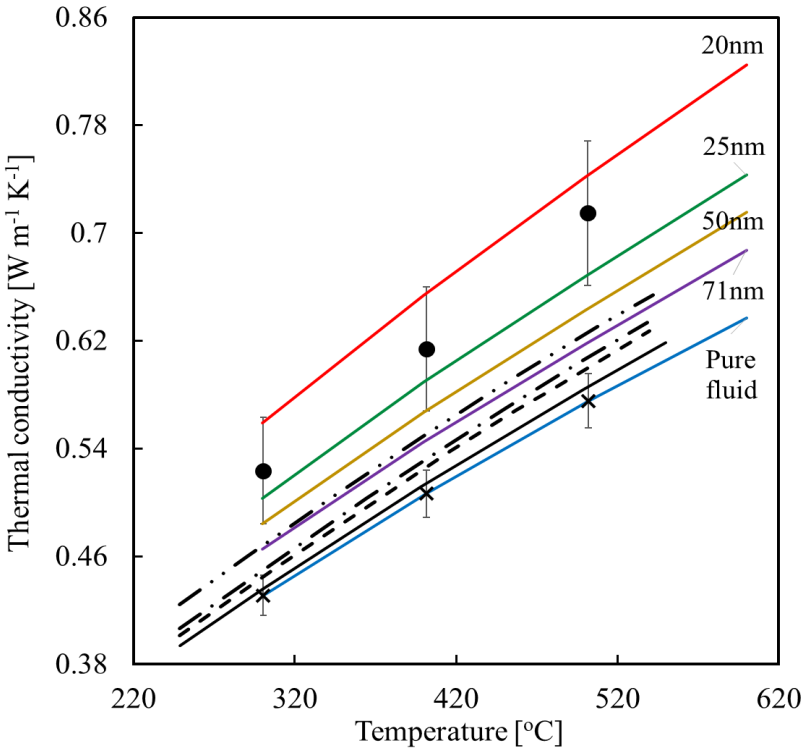

Figure 61. Comparison of model predictions of thermal conductivity with experimental measurements and analytical models for molten salt (Al_2O_3) nanofluids. Pure molten salt (blue); molten salt with 1.0 wt. % nanoparticles sizing from: 20nm (red), 25nm (green), 50nm (mustard), 71nm (purple). The experimental measurements of Ma and Banerjee[90] of pure fluid (×) and with d_p=25nm particles (●). The theoretical work of Maxwell[207] (—). Black lines represent predictions of Xuan and Li, 2000 (– - - –); Pang et al. [224], (– - –); and Prasher et al.[121], (– –) models.

The figure also gives predictions of thermal conductivities of nanofluids for a fixed concentration of 1 vol. % and temperatures over the range shown. The results are compared with the theoretical models of Maxwell[207], the data of Ma and Banerjee[90] and other model predictions (Xuan and Li[25]; Pang et al.[224]; Prasher et al.[121]), with good agreement found. It should be noted that the existing model showed more sensitivity to particle size in predicting conductivity than the other theoretical models illustrated in Figure 61.

Regarding size dependence, the model predicts that the conductivity of nanofluids containing 20nm Al_2O_3 particles is significantly greater than those containing 25nm and 71nm particles, by nearly 11 % and 22 %, respectively, although no systematic experimental investigation of size-dependant conductivities has been performed. Figure 62 illustrates the thermal conductivity of the nanofluids, normalised by the conductivity of the base fluid, plotted as a function of the solid volume fraction, Φ, for the 71nm Al_2O_3 particles.

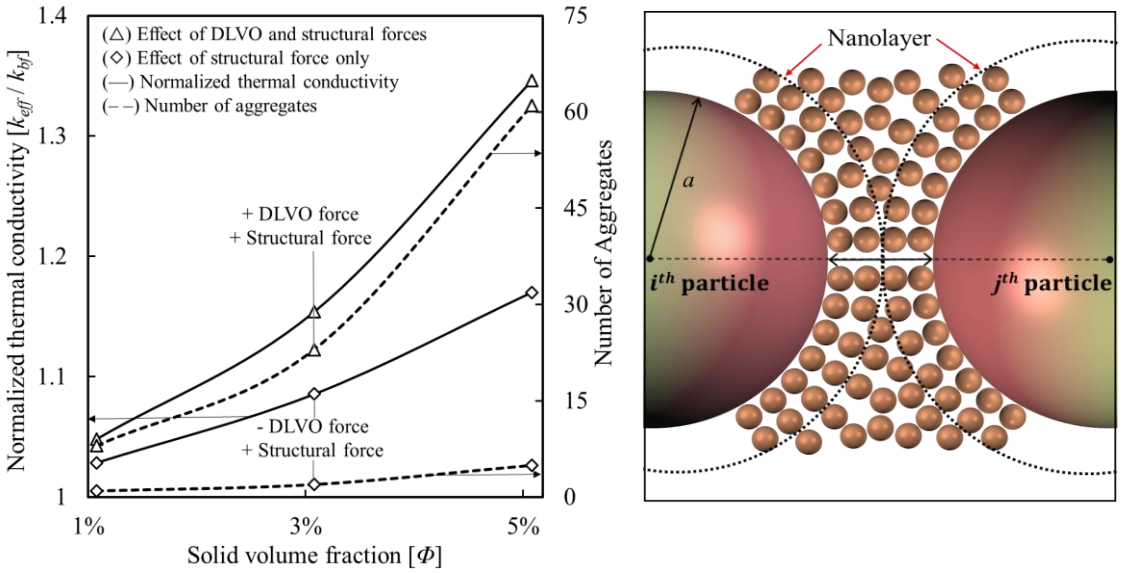

Figure 62. (Left) Nanoparticle concentration dependent thermal conductivities and number of aggregates formed at 350 ºC. (Right) salt liquid molecules forming a solid-like nanolayer around nanoparticle surface.

The results is Figure 62 show the contribution of the structural force, which form layered structures of liquid molecules[209] close to a nanoparticle surface (i.e. referred to as nanolayer, see Figure 62-Right) and DLVO force responsible for the aggregation of nanoparticles, to the thermal conductivity, and how this increases with particle volume fraction. Additionally, the number of aggregates appears to be considerably higher when van der Walls forces is included, which appears to dominate the behaviour, suggesting a minor contribution from structural forces, given evidence in Figure 62.

With regards to the effect of the nanolayer, at concentrations < 3 vol. % the majority of nanoparticles collide, although the formation of aggregates remains low. Hence, the thermal conductivity enhancement is dominated by the formation of nanolayers between particles. At $\Phi \geq 3$ vol. %, however, the combined effect curves show that the conductivity is enhanced by a factor of two to three, and at such concentrations aggregates (nanoclusters) form in addition to the nanolayers between them, although the interparticle distance is very small (0.5-1 nm). This leads to the conclusion that at high concentrations the effect of Brownian motion is dramatically reduced and instead percolation effects dominate due to reduced interparticle distances and increased particle nanolayering and aggregation.

Figure 63 shows the effect of particle diameter on the thermal conductivity for $\Phi = 1$ vol. %. The predictions indicate that thermal conductivity increase at low particle sizes. This

can be explained by the fact that as the particle size is decreased, the interparticle distance decreases. Consequently, conduction-like effects become dominant, increasing the conductivity. The thermal conductivity of nano-salts is hence enhanced by the addition of smaller nanoparticles. Such size-dependent behavior makes nanofluids more promising for many practical application than ever. Similar finding were also reported by Lee and Jang[117] for various nanoparticles as shown in Figure 63.

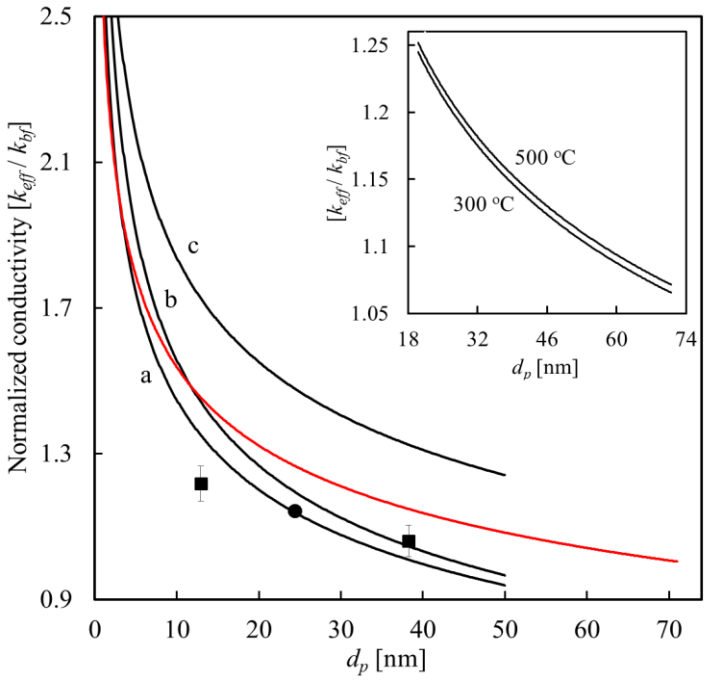

Figure 63. Effect of particle diameter d_p on thermal conductivity ratio. Present work: predictions using numerical model with AL_2O_3 nanoparticles (Solid red curve). Insert shows conductivity ratio of nanolayer plotted as function of temperature. Data of Lee and Jang[117]: model predictions (solid curve a) with experimental data (solid squares) for nanofluids containing AL_2O_3 nanoparticles; model predictions (solid curve b) and the experimental data point (solid circle) for nanofluids containing CuO nanoparticles; model predictions (solid curve c) for nanofluids containing Cu nanoparticles.

Corresponding results for the effect of particle diameter on the nanolayer thickness are given in Figure 64, with predicted values at different temperatures. These results demonstrate that the thickness of the nanolayer increases with reducing particle diameter, and with temperature due to Brownian motion effects. Hence both particle size and system temperature can be used to enhance the thermal conductivity of nanofluids.

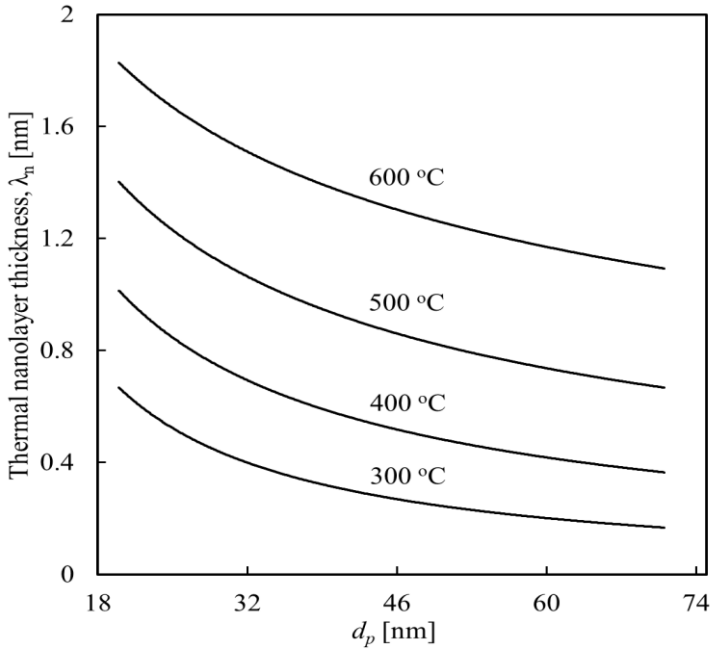

Figure 64. Thermal conductivity ratio of nanolayer as function of particle diameter at fixed concentration of 1 vol. %.

5.4 Summary and conclusions

Key parameters related to the stability and thermal conductivity of nanofluids have been examined using multiscale simulations. The novel model developed enables the prediction of the various dynamic forces acting in nanofluids, and provides quantitative predictions of the magnitude of those forces, including their role in particle aggregation. The model has been found to perform well in comparison with similar studies, and provides predictions of nanofluid dynamic properties, including the effect of the base fluid, and nanoparticle characteristics such as size[222], concentration, temperature, pH and external driving forces, on the thermal conductivity of the system.

The model provides confirmation of the effect of temperature and concentration on the enhancement of thermal conductivity. In addition, high temperatures are found to enhance nanoparticle interactions, collisions and aggregation which, ultimately, can inhibit higher conductivities in nanofluids. Such increases in conductivity are desirable for practical applications of nanofluids, for example if they are to be used in thermal applications. With regards to nanoparticle concentration, at low loadings (< 1 vol. %) it appears that the effective conductivity is dominated by that of the water base fluid. However, at moderate concentrations (≈ 3 vol. %) the thermal conductivity enters a zone of intensive interactions between nanoparticles, with the combined effects of aggregation (responsible for conduction) together with Brownian motion-induced convection governing the

conduction of heat in the system. At higher concentrations (≥ 5 vol. %) the system starts to behave in a fashion more akin to that found in pure solid composites. This leads to the conclusion that the conductivity of nano-suspensions is dependent on the physical properties of the nanoparticles and their interactions, including the interaction between nanoparticles and the liquid, and the conductivity of the base fluid and nanoparticle material.

These new findings, not previously predicted through multiscale simulation, also demonstrate the importance of particle agglomeration and how it leads to extended pathways (chain-like clusters) with a higher effective thermal conductivity. The impact of aggregate structures is therefore found to be positive in terms of the conduction of heat. However, aggregation into sparse but large clusters is known to increase the viscosity of the fluid and can become significant when the aggregates start to touch one another[56, 124, 223]. For this reason, nanoaggregates may not be as favourable in some practical applications involving fluid flow, if high viscosity is of concern. To overcome this, appropriate physical and surface charge modifications can be implemented, using pH adjustment techniques, to ensure that the level of nanoparticle aggregation always remains under control. Various researchers[51, 52] discussed the influence of pH and the addition of surfactants chemical on the suspension stability and thermal behavior of nanofluids. However, only few thermal conductivity models such as that by Prasher et al.[122], have considered the influence of pH and surfactants. Practically the use of surfactant and chemicals (for altering the pH) might be feasible for water based nanofluids at lower temperatures. However, there use for high temperatures nanofluids such as molten salt, might likely lead to decomposition and decrease of surfactant's concentration, thus exhibiting poor thermal performance.

In addition, key variables related to the oscillatory structural force acting between two spherical nanoparticles, and the thermal conductivity of salt based ionic nanofluids, have been examined using multiscale simulation. The thermal properties of nanofluids were found to be enhanced compared to those of the pure molten salt bulk fluid. The model has been found to perform well in comparison with similar studies, and provides confirmation of the effect of interparticle distance, particle concentration, temperature, and the formation of nanolayer and percolation networks, on the thermal conductivity of nano-salts. Although the thickness of the aligned solid-like layer of liquid molecules at the interface of a nanoparticle is at a magnitude of nanometer, it could play an important role

in heat transport from solid to adjacent liquid. Further work will extend the current model's application to include the hydrodynamic forces considered to be important in three-dimensional flows, as found in solar thermal heat storage systems, by coupling the tracking approach with direct numerical simulations. A more detailed consideration of this approach is given in Section (6.4) contained in Chapter 6.

The variation of the temperature-dependent properties (e.g. density and viscosity) of both base fluids used in this study, are causing the Al_2O_3 nanoparticles to behave differently in water- to molten salt-based systems. For instance, the impact of interfacial nanolayer (demonstrated by the oscillatory structural force) was shown to have effects on the enhanced thermal conductivity of the molten salt-based nanofluids. With regard to the influence of nanoparticle size, it was revealed that the conductivity of molten salt nanofluids containing 20nm Al_2O_3 particles is greater than those containing 25nm and 71nm particles, by nearly 11% and 22%.

In terms of limitations, the present model only applies to stagnant fluids (as it is computationally expensive to solve for the fluid phase evolution), simple geometries and limited numbers of particles. Future work should extend the model's application to include other base-fluids such as ionic liquids and molten salts (used as hydride nanofluids for thermal energy storage applications), and to flow situations by coupling the tracking approach described with direct numerical simulations. This will involve optimization of the properties of the nanofluid by considering different nanoparticle materials, and different particle sizes, shapes and concentrations. Experimental research should also be conducted to support the development of this numerical model – to track, characterise and model the dynamics and thermal enhancement of potential nanofluids. Further research initiatives in this area will assist in the design of renewable-energy power plants and other thermal management systems that involve nanofluids.

6 NANOPARTICULATE BEHAVIOUR AND TURBULENT HEAT TRANSFER IN MULTIPHASE CHANNEL FLOWS

6.1 Introduction and background

Particle-laden flows containing micro-/nano-sized particulate structures (e.g. particles, colloids and surfactants) have gained increasing attention recently because of their wide range of industrial applications. Of particular interest are nanofluids, which are prepared by dispersing nanoparticles in conventional thermofluids such as water and molten salt. Unlike conventional fluids, nanofluids have been shown to exhibit significant enhancement of the thermophysical properties[24] of the base fluid, which has been discussed in previous Chapters 4 and 5. Such enhancements open up new pathways for the use of nanofluids in high temperature applications, particularly in the energy sector where efficiency of heat transfer and thermal management systems is presently the greatest technological challenge. In fact, the use of nanofluids as a heat transfer fluid and energy storage medium for power generation and storage is potentially promising and could result in increased efficiency and large energy savings[225]. The flow and heat transfer of such nanofluids is therefore gaining a lot of interest by researchers in the academic community due to their inherent improved thermal transport properties and the current lack of a robust theoretical framework for their prediction.

Understanding of the hydrodynamics, heat transfer and thermal enhancement of nanofluids is quite challenging if it is to be investigated only experimentally. Apart from the restrictions of size and harsh environmental regimes (i.e. high temperature differences), many other complications arise from the responsible hydrodynamic and interaction forces which are likely to take place at varied magnitudes and across multiple time scales. The use of a numerical approach is therefore proposed to investigate these phenomena. More specifically, a multiscale computational model based on Lagrangian particle tracking (LPT) (discussed earlier in Section 3.4.4) is used together with the direct numerical simulation (DNS) (described in Section 3.4.8), to investigate the following nanofluid flow and heat transfer behaviours: i) the influence of dispersed nanoparticles on the surrounding carrier fluid, ii) the effect of the turbulence field on the dispersion stability, iii) aggregation properties of the solid nano-particulate, and iv) thermal

properties and turbulent heat flux in nanofluids in a channel flow. The other benefit of this computational fluid dynamic (CFD) model is its ability to investigate more intrinsic phenomena such as interparticle collisions, turbophoresis (the tendency for particles to migrate in the direction of decreasing turbulence kinetic energy) and thermophoresis (particle motion induced by thermal gradients), and hence the long-term thermal stability of nanofluids that has not yet been comprehensively studied elsewhere.

The method proposed (detailed in Sections 3.4.8 to 3.4.10), uses a channel flow configuration in three-dimensions which is used to simulate turbulent flows representative of those encountered in industry by providing a full solution which solves for all relevant length and time scales, down to the Kolmogorov scale[227]. This technique enables any quantity of interest to be analysed with great spatial and temporal precision, albeit at a large computational cost and for somewhat idealised conditions. DNS can generally be regarded as a complement to laboratory experiments. Particle-particle interactions are represented using detailed surface interactions based on DLVO interaction forces[228]. DLVO theory (after Derjaguin and Landau[114], and Verwey and Overbeek[115]) defines inter-particle forces as the sum of van der Waals and electric double-layer contributions, and these are fully resolved in the computations.

It is thought that agglomeration of nanoparticles to form larger particle clusters could lead to surface impact, deposition and erosion, although evidence of this in the literature is conflicting[226], with few quantitative studies reported. To capture these effects using CFD, a comprehensive description of both the fluid phase and solid nanoparticle phase evolution is necessary. Since these particles are very small, with Stokes numbers $St \sim 0$, they are expected to behave like tracers within the carrier phase. Hence, the focus here is on the fluid phase that dictates the spatial distribution of solid particles relative to the turbulent flow. The evolution of the particles' distribution is therefore highly dependent on the turbulent flow and temperature fields, and physical interactions between the particles and between the particles and the cold or hot wall heat flux boundaries. Moreover, whereas most transport models are not explicit and do not account for feedback between the turbulence and particle distributions, the model proposed here does so.

This chapter aims to expand on the recent work by more realistically investigating the nanoparticulate behaviour and turbulent heat transfer of nanofluid in a channel flow, for which four main simulations were performed. The configuration of all the simulations studied here is a fully developed channel flow with one of the following conditions: i) an

isothermal boundary condition of water based nanofluid with a uniform fluid temperature at 25°C, ii) a simulation of isothermal boundary condition of molten nitrate salt based nanofluid at 410°C, iii) non-isothermal boundary condition of molten nitrate salt simulation with uniform cold wall boundaries at 250°C, and iv) non-isothermal boundary condition of molten nitrate salt simulation with uniform hot wall boundaries at 500°C.

The operating conditions of the four simulations were chosen to match those found in a real solar thermal power plant. The dispersed phase in these simulations was represented by 500,000 (100 nm diameter) Al_2O_3 particles, which were tracked through the fluid flow field. The work performed provides both a more in-depth understanding of nanofluid flow behaviour, as well as laying the foundations for investigating the heat transfer phenomena of nanofluids within a channel flow, at a more fundamental level. The statistics obtained from these simulations are presented and discussed in the following sections.

6.2 Isothermal water nanofluid simulation, T= 25°C

For this section, a water-based nanofluid will be investigated. The simulation parameters are chosen to represent those typically found inside a thermo-solar power plant. Knowledge from this type of study can be obtained and used regarding how particles affect the turbulence properties of water, and how the latter impact of the dispersion of the nanoparticles (in such systems as a cooling and heat transfer fluid). The simulation has therefore been set to have an isothermal boundary condition with a uniform fluid temperature. Chemical and mechanical properties were chosen to match Al_2O_3 in water at 25 °C, with the parameters used in the simulations provided in Table 8.

Table 8. Parameters used in the Al_2O_3 in isothermal water simulations.

Parameter	**Carrier phase (water)**	**Particle phase (Al_2O_3)**
Shear Reynolds number, Re_τ	180	-
Bulk Reynolds number, Re_B	2800	-
Particle diameter, d_p / nm	-	100
Number of particles, N_p	-	500,000
Volume, V / m^3	1.58×10^{-10}	4.07×10^{-13}
Volume fraction, Φ / vol %	-	0.26
Temperature, T / °C	25	25
Bulk velocity, U_B / m s^{-1}	25.67	25.68
Density, ρ / kg m^{-3}	997.1	3850
Viscosity, η_F / m^2 s^{-1}	0.917×10^{-6}	-

The simulations were first performed as an unladen single-phase flow using a standard initial turbulence profile with added chaotic terms in the wall-normal and spanwise

directions. Once turbulence was established, fluid statistics were monitored every 1.95 ns until the mean and fluctuating velocities reached a statistically steady state. Particles were then injected uniformly throughout the channel and given an initial velocity equal to that of the local fluid. Particle statistics in the wall-normal direction were obtained by splitting the domain into 120 equal volume cuboidal regions, and by averaging various dynamic properties such as velocity and velocity fluctuations over all particles within each statistical region. The statistics presented below represent those at a state where the near-wall particle concentration was approximately stationary with respect to time, which occurred around t = 150 µs. From this steady state condition, two-way coupled runs were performed, reducing the fluid and particle time step initially to avoid divergences in the flow field due to the impact of particle forces. Fluid and particle statistics were then recorded to determine when the system had finished responding to the addition of the momentum-coupling mechanism. Once satisfied, statistics were determined as noted above. This approach was repeated to obtain four-way coupled simulations, and results for four-way coupling plus particle agglomeration.

The results of each simulation were analysed to elucidate the behaviour of the fluid and the nanoparticles within the channel flow. The predictions demonstrate how particle concentrations increased in the near-wall regions due to turbophoresis, as illustrated in Figure 65. Preferential concentration of particles within low speed streaks close to the walls is also observed [227, 232].

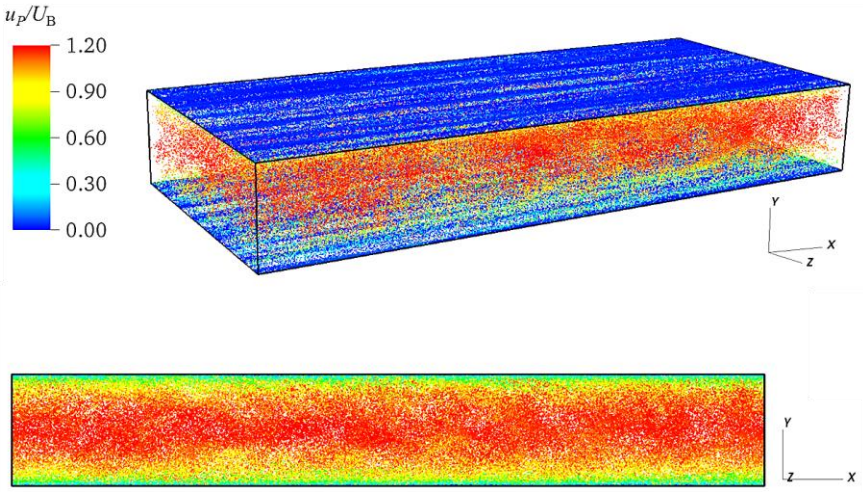

Figure 65. Particle distribution within Re_τ = 180 channel flow, colours indicate particle to bulk velocity ratio, u_P/U_B (top); and snapshot of streamwise particle velocity on vertical plane (bottom).

Figure 66 compares the fluid mean streamwise velocity profile, and normal and shear stress profiles, for the single phase flow with those obtained by Moser et al. (1999) who also used DNS. Throughout, excellent agreement is obtained.

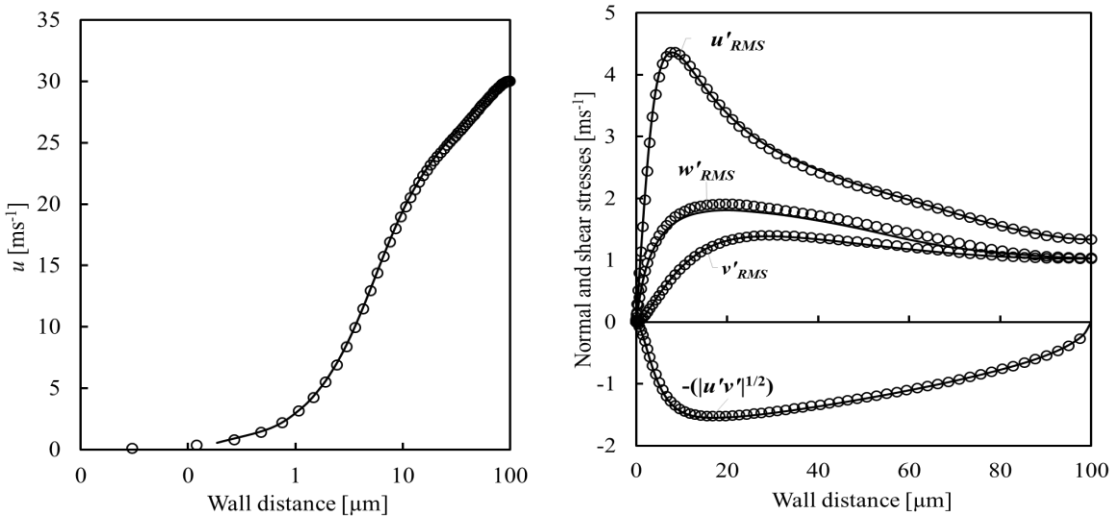

Figure 66. Comparison of fluid velocity profiles: (Left) streamwise mean velocity, (Right) normal and shear stresses (— present, ○ Moser et al, 1999).

Figure 67 considers the effect of two-way coupling on the fluid normal and shear stresses in order to determine how the particles modify the turbulence properties of the flow. The results demonstrate that two-way coupling has only a small influence on these statistics. Specifically, all three components of the normal stress and the Reynolds shear stress are attenuated, indicating that the presence of nanoparticles at the concentration considered reduces slightly the magnitude of turbulence in the flow. Since the effect is strongest in those regions which show greatest deviation between particle stresses and those of the unladen flow, this is likely due to greater slip velocities in those regions, meaning that the particles work to dampen the energy in the local turbulent eddies.

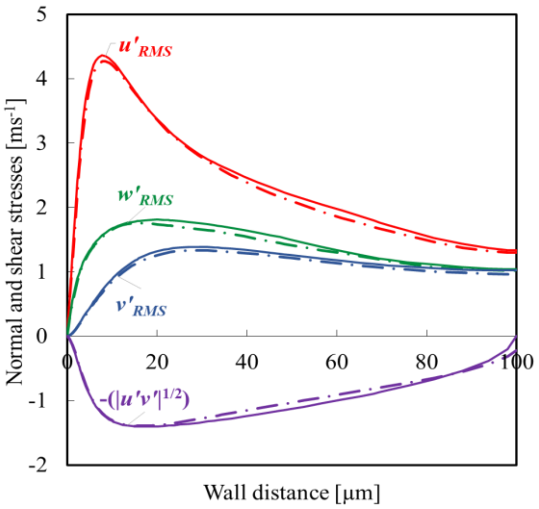

Figure 67. Fluid normal and shear stress profiles (— unladen flow, –·– two-way).

The left side of Figure 68 compares the particle mean streamwise velocity for each coupling mechanism considered. It is observed that for all the coupled cases, the particles lag slightly behind the unladen fluid flow between the turbulent region and the channel centre. This indicates that the coupling and interaction mechanisms all have only a slight effect on the mean streamwise motion of the particles, albeit of the same order. However, the right side of Figure 68 shows the root-mean-square of the particle velocity fluctuations, a measure of turbulence intensity, in each coordinate direction. In this case it is clear that for two-way and four-way coupling, the particulate phase exhibits similar velocity fluctuations in all three directions. More specifically, reduced turbulence fluctuations are observed compared to the single phase in the spanwise and wall normal directions, whilst the streamwise normal stress is greater in the turbulent region of the flow, but lower close to the channel centre. On introduction of the DLVO attractive and repulsive forces, a further slight increase in the streamwise normal stress is observed which is most significant in the turbulent region. This is likely due to the aggregation of particles in this region which leads to increased particle inertia due to their larger size, with such particles exhibiting greater decoupling from the local fluid velocities.

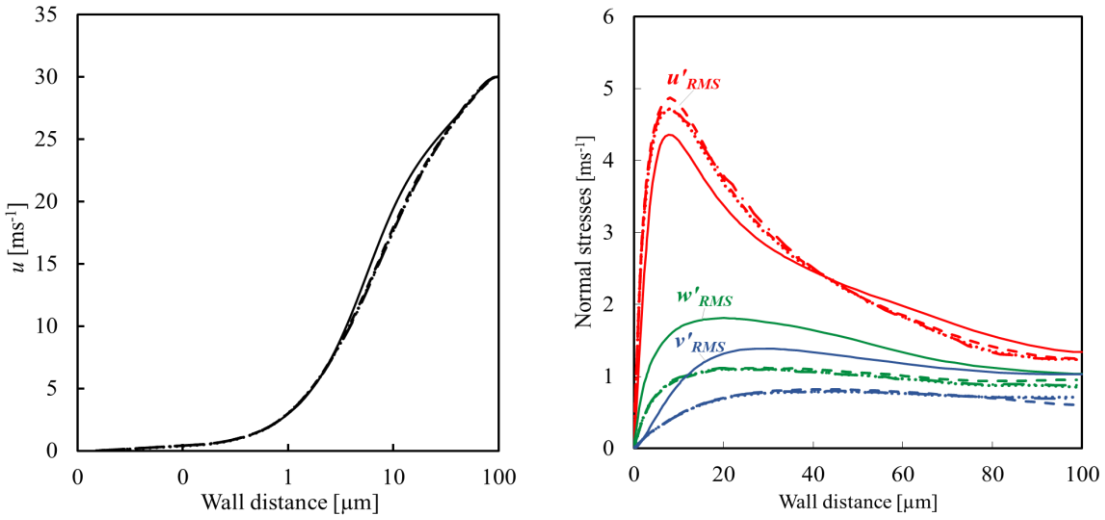

Figure 68. Comparison of velocity profiles: (Left) mean streamwise velocity, (Right) normal stresses (— unladen flow, – · – particles (two-way), · · · particles (four-way), – – particles (four-way + agglomeration).

Furthermore, Figure 69 compares the particle concentration distribution relative to the initial concentration, C_0, during the simulation. It is clear from the results that over the course of the simulation turbophoresis takes place, with a similar qualitative behaviour observed at all times. Over time this leads to a build-up of nano-particulate concentration close to the walls. This has consequences for the agglomeration rate since the local concentration in these regions is nearly 100 times greater than the initial concentration once the system has reached a steady state.

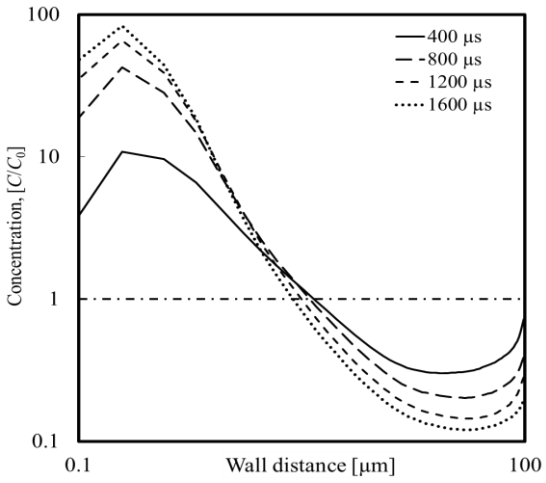

Figure 69. Particle concentration relative to homogenously distributed concentration, C_0 (-. -.) for the isothermal four-way coupled with agglomeration water based nanofluid configuration. —: Initial injection; – –: 800 μs; – –: 1600 μs; · · · :2000 μs.

Instantaneous particle distributions near the channel boundary obtained from various timesteps throughout the simulation are presented in Figure 70. Results from the initial

stages of the run, when initial injection of the particles occurred, have been included here to provide a more in-depth overview of the response of near-wall particle segregation with time. The overall trend is clear; particles at t = 400 μs are homogenously distributed near the wall, showing very little indication of their location within low speed streaks. As the time of simulation increases to t = 800-1200 μs, the level of order increases likewise, and the results indicate a maximum level of order by inspection at t = 1600 μs. Above this value, the change in the streaks begins to become much less clear, thus particles tend to remain trapped within the low speed streaks near the wall.

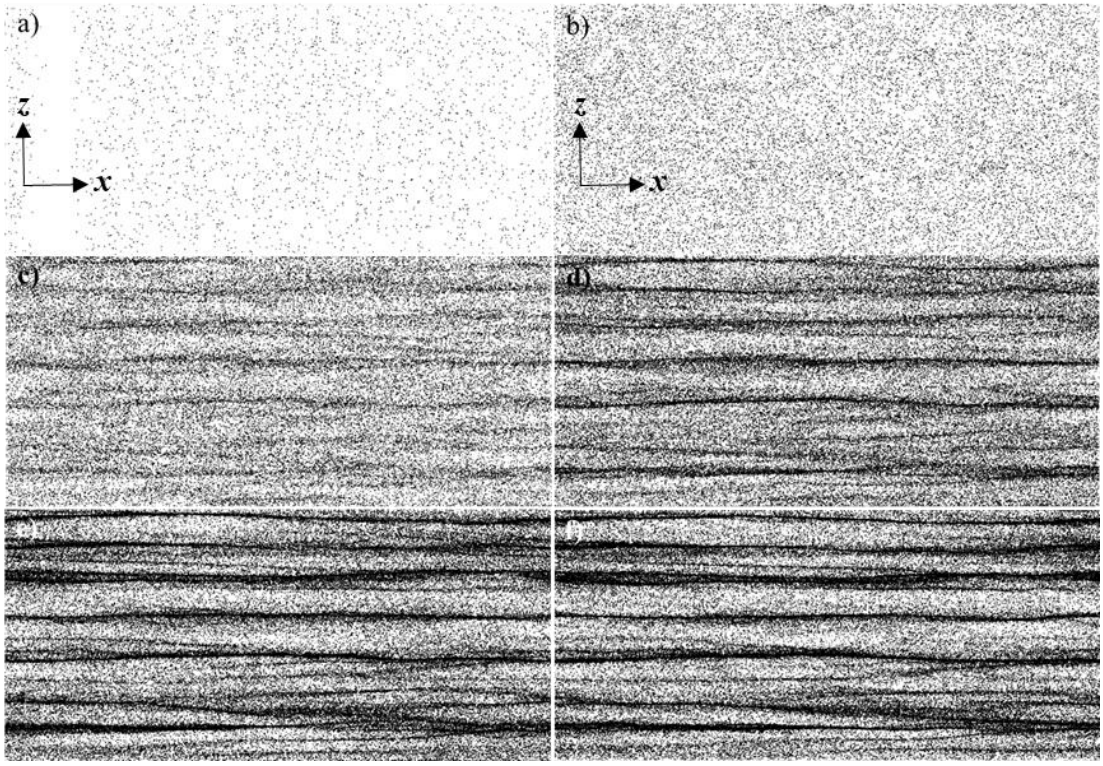

Figure 70. Instantaneous near-wall particle distributions taken from the simulations at: a) Initial injection; b) 400 μs; c) 800 μs; d) 1200 μs; e) 1600 μs; f) 2000 μs;. Showing particle entrainment in low speed streaks close to the wall.

6.3 Isothermal molten salt nanofluid simulation, *T*= 410°C

For this section, the molten salt-based nanofluid will be investigated. As before, the simulation parameters are chosen to represent a typical situation of relevance to thermo-solar power plant. In addition, the thermophysical characteristics of the multiphase system are modelled dynamically. A description of the thermal properties of the solar salt mixture used in the code was given earlier in section 3.2.10., the details of which is given with sources[163, 164] in Table 5. Also the mechanical characteristic (e.g. modulus of

elasticity, rigidity and Poisson's ratio) of the alumina ceramic nanoparticles in the fluid change as a function of temperature[161], as described earlier in section 3.4.7.

The knowledge from this type of study provides both a more in-depth understanding of how particles affect the turbulence properties of molten salt (in such system as a thermal energy storage) within a channel flow, as well as laying the foundations for investigating the heat transfer behaviour of molten salt nanofluids at a more fundamental level, as will be carried out in the following sections. Thus the simulation has been set to have an isothermal boundary condition with a uniform fluid temperature. Chemical and mechanical properties were chosen to match Al_2O_3 in molten salt at 410 °C (set to have a high Prandtl number, Pr = 5), with the parameters used in the simulations provided in Table 9.

Table 9. Parameters used in the simulations.

Parameter	**Carrier phase ($NaNO_3$-KNO_3)**	**Particle phase (Al_2O_3)**
Shear Reynolds number, Re_τ	180	-
Bulk Reynolds number, Re_B	2800	-
Particle diameter, d_p / nm	-	100
Number of particles, N_p	-	500,000
Volume, V / m^3	1.58×10^{-10}	4.07×10^{-13}
Volume fraction, Φ / vol %	-	0.26
Temperature, T / °C	410	410
Bulk velocity, U_B / m s^{-1}	25.67	25.68
Density, ρ / kg m^{-3}	1830	3850
Kinematic viscosity, ν_F / m^2 s^{-1}	0.974×10^{-6}	-

The simulations were initialised using the same procedure as detailed earlier in Section 6.2. Particles were then injected uniformly throughout the channel, this time leaving a small gap between the wall and the first particle in order to more closely observe any wall migration effects such as turbophoresis and thermophoresis. As before, the collection of turbulence statistics and averaging of both particles and fluid statistics are similar to those described earlier in Section 6.2. All simulations were performed with all levels of coupling switched on, however two-way coupling effects were minimal throughout.

To explore the dynamics associated with both the fluid and particle phase, mean velocity and RMS velocity fluctuation statistics were obtained. Figure 71 compares the mean streamwise velocity of the fluid flow with that of the particles. As expected, particles follow the fluid streamlines very closely and act as tracers.

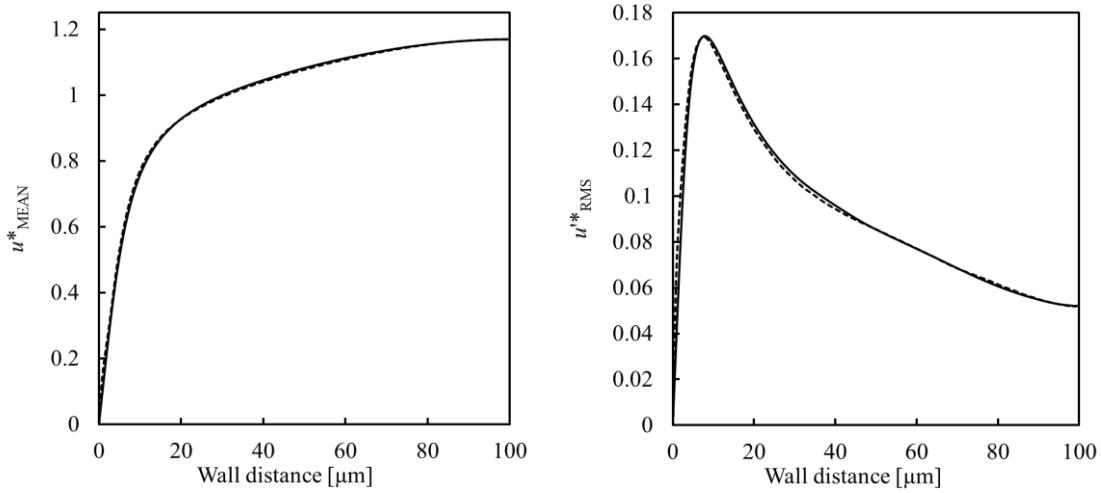

Figure 71. (Left) Mean streamwise velocity comparison, (Right) Root-mean-square of velocity fluctuations, streamwise. (—: fluid; – –: particles).

Similarly, the streamwise RMS velocity fluctuations for both the unladen fluid and particles are presented in Figure 71-Right. For the particle statistics, the streamwise component is close to that of the unladen flow, especially in the near wall region. With regard to the turbulent intensity of both isothermal simulations: water at 25°C (shown as dimensional in Figure. 68) and the dimensionless molten salt at 410°C (Figure 71), the results shows that the Root-mean-square of the velocity fluctuations are qualitatively alike. This indicates that there is no obvious difference from both simulations in terms of the streamwise velocity fluctuations under such isothermal conditions.

Moreover, both fluid and particles RMS velocities are plotted in Figure 72. It can be seen from the spanwise and wall-normal RMS components that there are slight deviations between the unladen fluid and the particles. We observe slight differences in the spanwise fluctuations of the particles from the unladen flow. This is even more noticeable in the wall-normal components which increase slightly in both the near wall region and bulk flow region. This difference between the unladen flow and that of particles can be attributed to the statistical sampling time, as they are very close as expected for such low Stokes numbers. Also the slight deviations in the unladen flow and that of particles at increased Stokes numbers are usually due to collisions which primarily add deviations to the spanwise and wall-normal velocities.

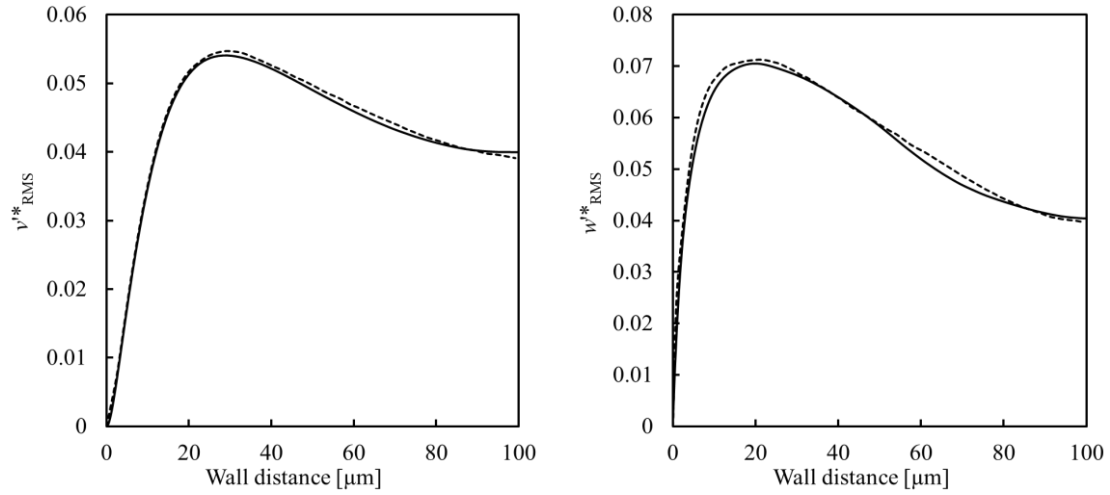

Figure 72. Root-mean-square of velocity fluctuations. (Left) wall-normal; (Right) spanwise. (—: unladen flow; – –: particles).

Particle distribution across the wall-normal direction of the channel, as well as the dispersive motion of particles towards the near-wall region, were then explored. To illustrate this, Figure 73 shows the mean particle concentration across the channel sampled at t = 600 μs. Figure 74 demonstrates the evolution of the near-wall particle concentration relative to a homogenously distributed concentration over time. As a reminder, for the present simulation the near-wall concentration is zero at injection since particles are distributed with a gap between the wall and the first particle. To generate this quantity, the number of particles in each statistical region was recorded at each time step and divided by the volume of the enclosed regions to generate a concentration C. This was then divided by the mean initial concentration measured across the entire channel after injection, C_0, to obtain a relative concentration.

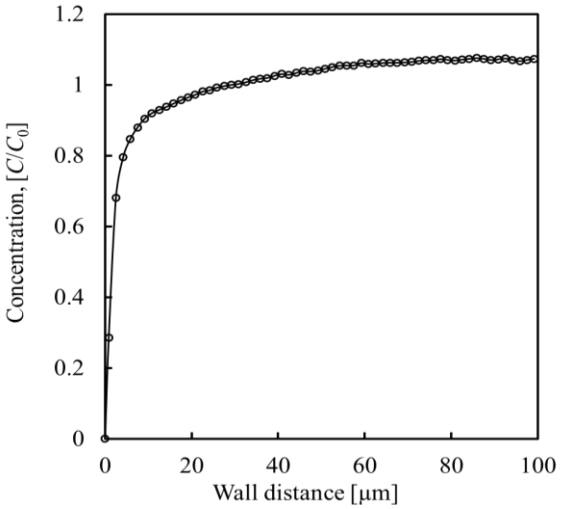

Figure 73. Mean particle concentration across the channel. ○○: present work at t = 600 μs.

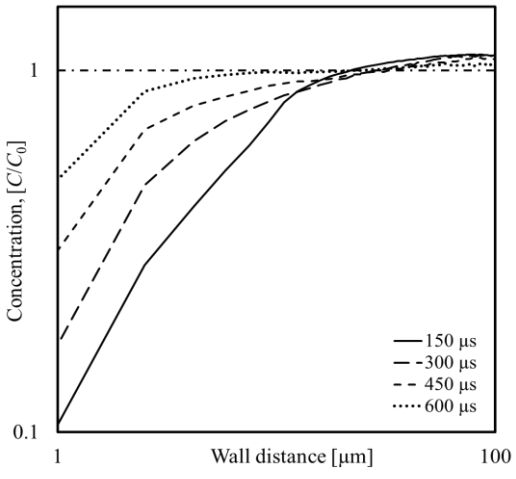

Figure 74. Particle concentration relative to a homogenously distributed concentration, C_0 (-. -.) for the isothermal configuration at T = 410 °C. —: 150 μs; − −: 300 μs; – –: 450 μs; · · · : 600 μs.

Figure 74 shows that there is an increase in particle concentration near the wall during the stabilising period, which remained consistent for the remainder of the simulation time considered from 150-600 μs. This is explicable by the tendency for particles to accumulate in elongated streamwise regions of low speed present in such flows[133], which will be demonstrated later. This phenomena is further explained by Mortimer et al.[227], as inertial particles entering these regions will slow down, reducing the rate at which they return to the outer layer. The concentration effects in the near-wall region are related to turbophoresis, which has been observed earlier by a number a researchers[229-231].

According to Arcen at el.[229] the physical accumulation of particles in the proximity of the near wall region can be explained by the presence of typical vortices, which was referred to as "offspring vortices''. In addition to this, Marchioli and Soldati[233] described these vortices to be responsible for the particle accumulation under the low-speed streaks, which are known as a long-lived wall structures. Zhao at el.[231] also pointed out the accumulation of small particles with high inertia such as those considered in this study would strongly affect the fluid turbulence in the near wall region. According to Zhao at el. [231] this is caused by the large and slow vortices (usually referred to as "sweeps") sweep the fluid and particles towards the wall, therefore, the particles preferentially accumulate in the low speed streaks very near the wall. The influence of turbophoresis with the presence of thermal gradients and its impact on the particle concertation in the near wall region will be discussed further in the following section.

6.4 Turbulent heat transfer in nanoparticulate multiphase channel flows with a high Prandtl number molten salt fluid

In this section, the focus of the simulations relies on modelling the heat transfer in nanoparticulate multiphase channel flows with a high Prandtl number fluid (i.e. molten salt). A similar turbulent heat transfer model to that of Kawamura et al.[133] was utilized in the current work. However, we here aim to expand on this work by seeding the continuous phase with nanoparticles to determine turbulence quantities such as the turbulent heat flux and temperature variance of the multiphase system considered with $Pr = 5$ (defined earlier in section 3.4.5) and $Re_\tau = 180$.

In order to relate the present work to the systems present in solar thermal power plants, we consider mechanical and chemical properties matching those of Al_2O_3 nanoparticles in molten salt ($NaNO_3$-KNO_3, 60-40 weight ratio), which is a simulant for proposed heat

transfer fluids and thermal energy storage media, with the parameters used in the simulations provided in Table 11.

Table 10. Parameters used in the simulations.

Parameter	**Carrier phase ($NaNO_3$-KNO_3)**	**Particle phase (Al_2O_3)**
Shear Reynolds number, Re_τ	180	-
Bulk Reynolds number, Re_B	2800	-
Prandtl number, Pr	5	-
Particle diameter, d_p / nm	-	100
Number of particles, N_p	-	500,000
Volume, V / m^3	1.58×10^{-10}	4.07×10^{-13}
Volume fraction, Φ / vol %	-	0.26
Temperature, T / °C	CW= 250, HW= 500	410
Bulk velocity, U_B / m s^{-1}	25.67	25.68
Density, ρ / kg m^{-3}	2263.628 – 0.636 (T)	3850
Kinematic viscosity, ν_F / m^2 s^{-1}	0.974×10^{-6}	-

In addition, a novel method is used here to describe the oscillating layered structure of molten salt fluids (represented by the matrix of liquid molecules around the nanoparticles), and the influence of the interfacial layer thickness on the system conductivity, further details of which can be found in Section (3.4.6). This innovative approach allows for the simulation of different flows, and modifications to them to gain a better understanding of the nanoparticle dynamics and heat transfer characteristics of the system. The final outcome is expected to provide the optimum characteristics of the nanofluid flows that can be used in solar power plants.

Eqns. 3-40 to 3-46 are solved to perform two simulations with different heat flux boundary conditions. The first simulation has a fixed hot wall boundary with an associated temperature of 500°C, whereas the second had a fixed cold wall boundary with an associated temperature of 250°C. The fluid Prandtl number (Pr = 5) used is representative of molten salt at 410°C. Both of these simulations used a non-isothermal boundary condition with different heat transfer configuration, as shown in Figure 75 and Figure 76. Thus q_w is positive on both walls if $T_w \geq T^*$ for the hot wall case. Conversely q_w is negative on both walls when $T_w \leq T^*$ for the cold wall case. The statistics obtained from these simulations are presented and discussed in the following sections.

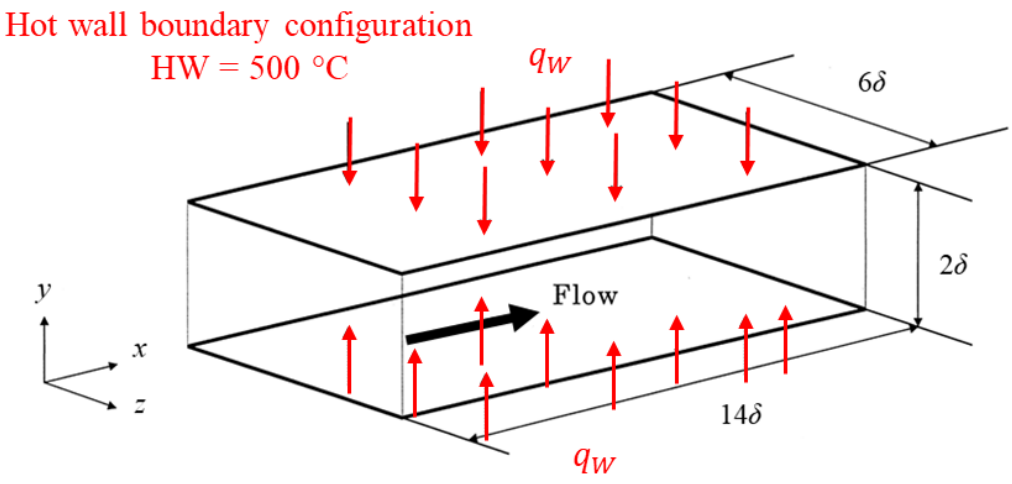

Figure 75. Configuration of DNS for turbulent heat transfer channel flow for hot wall case. Heat transfer occurs from the hot wall (500°C) to fluid (410°C), as indicated by the direction of q_w.

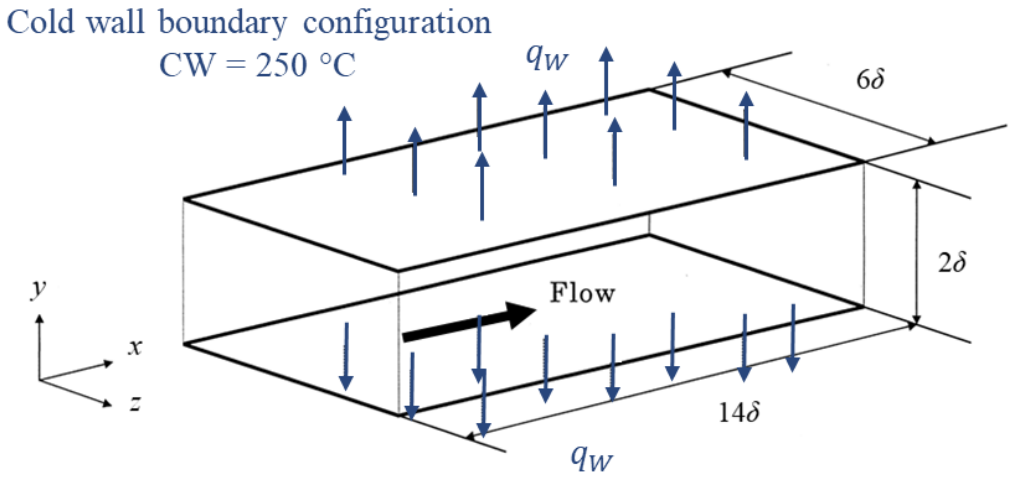

Figure 76. Configuration of DNS for turbulent heat transfer channel flow for cold wall case. Heat transfer occurs from the hot fluid (410°C) to the cold wall (250°C), as indicated by the direction of q_w.

6.4.1 Non-isothermal molten salt simulation, single-phase

The simulations were first performed as an unladen single-phase molten salt flow using an arbitrary initial turbulence profile with added chaotic terms in the wall-normal and spanwise directions. Once turbulence was established, fluid statistics were monitored every 150 μs until the mean and fluctuating velocity and temperature fields reached a statistically steady state.

Profiles of the mean temperature and RMS of temperature fluctuations are presented in Figure 77 for the single-phase flow. The statistics of the DNS performed in Kawamura et

al[133] which simulated turbulent heat transfer in a channel flow at Re_τ = 180 and Prandtl number Pr = 5 are used for comparison and found to be in qualitatively good agreement. However, significant discrepancies are apparent between the two set of results, but these may be attributed to be a consequence of computational issues due to differences in the number of nodes and elements used in each simulation, with the present work using an order of magnitude higher number of nodes. Furthermore, statistical sampling periods in order to obtain a smooth profile were very long since the energy equation solver increased the computational cost per timestep greatly. The turbulent heat fluxes in the streamwise and spanwise directions are also presented in Figure 78. These determine the rate and direction of heat energy transfer via turbulence either towards (cold wall) or away (hot wall) from the wall.

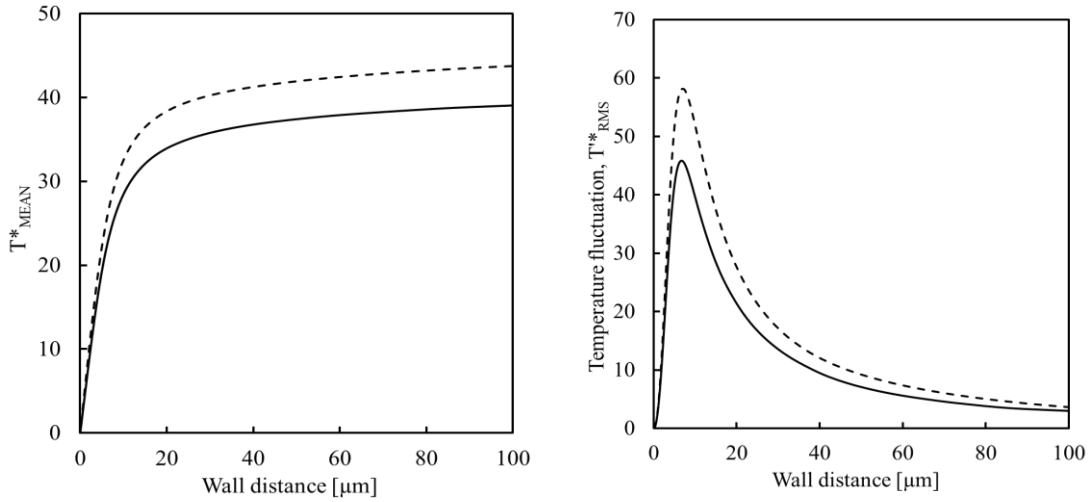

Figure 77. (Left) Comparison of Mean temperature profiles, (Right) Comparison of Root-mean-square of temperature fluctuations. (— present, – – Kawamura et al[133], 1998).

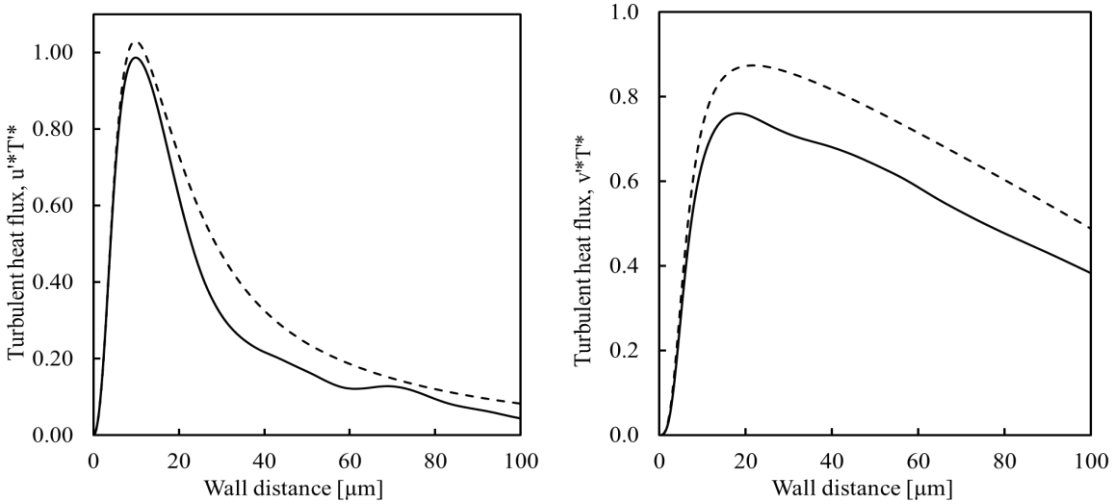

Figure 78. (Left) Comparison of Turbulent heat flux components: streamwise, (Right) Comparison of Turbulent heat flux components: spanwise. (— present, – – Kawamura et al[133], 1998).

6.4.2 Non-isothermal molten salt simulation, multi-phase

Particles were injected using the same procedure as applied for the isothermal molten salt simulations in section 6.3. The results of each simulation were analysed to explain the flow and heat flux behaviour of the fluid and the nanoparticles within the channel. Figure 79 shows the instantaneous fluid temperature at the top of the figure, as well as illustrating the location of the nanoparticles in a zoomed in portion of the channel with hot walls in the lower part of the figure. Considering the results of Figure 79, a trend in preferential concentration of particles within the coldest regions is noticeable. It is also evident that the particles exhibit increased concentrations in the centre of the channel. The reasons for this will be discussed later.

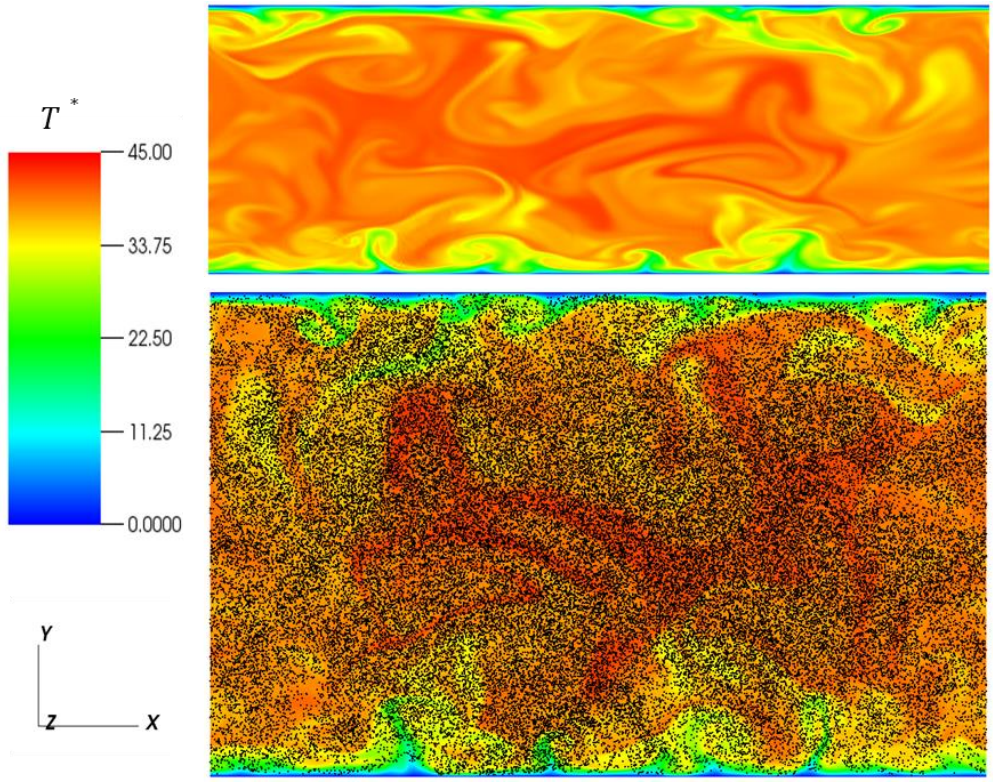

Figure 79. Instantaneous temperature distribution in unladen flow (top), and a zoomed in portion with nanoparticles for the hot wall case (bottom).

Profiles of the streamwise mean particle velocity and the RMS of particle streamwise velocity fluctuations are shown in Figure 80.

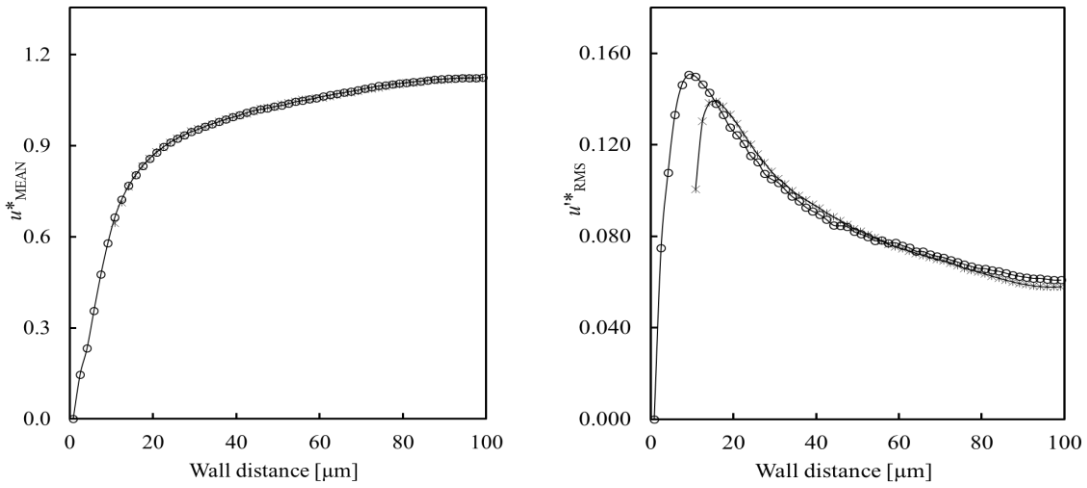

Figure 80. (Left) Streamwise mean particle velocity profiles, (Right) Root-mean-square of particle velocity fluctuations, streamwise. (✱✱: Hot wall; ○○: Cold wall).

It is clear that the streamwise mean particle velocity distributions are similar for both the cold and hot wall configurations. This is likely due to the low particle Stokes number and the lack of dependence of mean streamwise flow behaviour on the temperature field. In the case of the hot wall, the statistics near the walls are not plotted due to insufficient particles in these regions to obtain meaningful averages. However, the RMS of velocity fluctuation profiles show variation between the two configurations. In the case of the cold wall, the peak is closer to the wall, indicating that the particles behave in a more turbulent fashion within the near-wall region. This is likely to be due to thermophoresis causing a drift in the wall-normal direction towards the wall. For the hot wall case, the peak particle RMS value is reduced and shifted towards the channel centre slightly, since particles which approach the wall are encouraged to move away from it due to increased local temperatures, although the spread of streamwise RMS velocities further from the wall is maintained. Comparing with Figure 71, in both the hot wall and cold wall cases the streamwise RMS velocity fluctuation is reduced with respect to the isothermal case. The peaks are also shifted closer to the centre of the channel, so that the same qualitative turbulent profile is observed but acts over a region with a lower spread of velocities.

The RMS of velocity fluctuations in the wall-normal and spanwise directions is illustrated in Figure 81. It can be seen that the wall-normal particle fluctuations exhibit similar behaviour near the wall, but the fluctuations are slightly increased for the cold wall configuration in the outer layer. This is likely to be due to turbophoresis and thermophoresis working together to give the particles greater distributions in wall-normal

velocity. The spanwise distributions exhibit similar behaviour, as expected since this direction is homogeneous in both fluid temperature and velocity distributions.

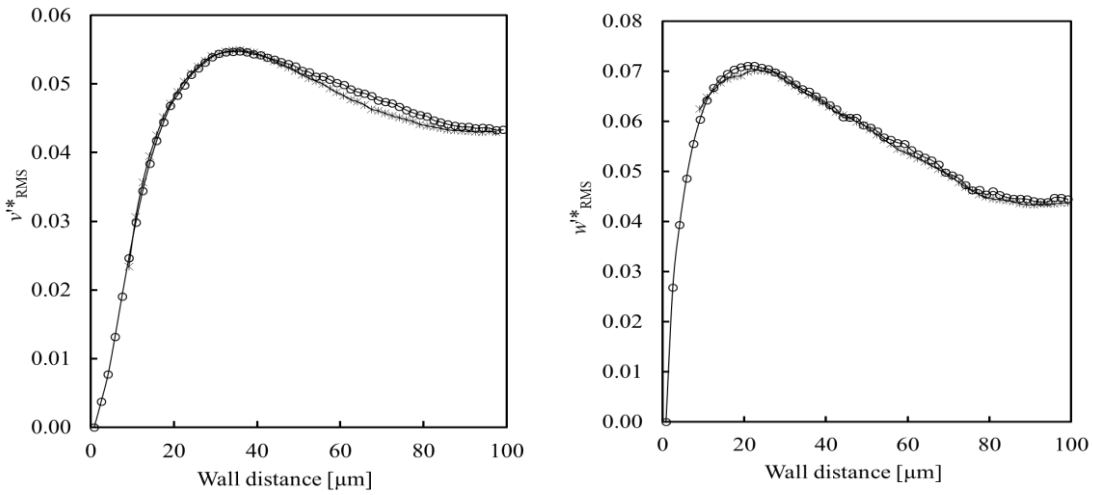

Figure 81. (Left) Root-mean-square of particle velocity fluctuations, wall-normal, (Right) Root-mean-square of particle velocity fluctuations, spanwise. (✱✱: Hot wall; ○○: Cold wall).

The predictions also demonstrate how particle concentrations differ in the near-wall regions due to thermophoresis, as illustrated in Figure 82.

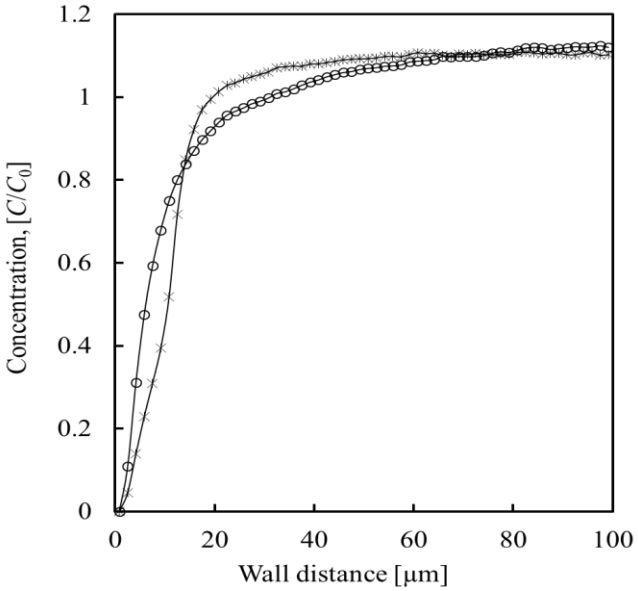

Figure 82. Comparison of mean particle concentrations across the channel. ✱✱: Hot wall; ○○: Cold wall.

Over the course of the cold wall simulation it is clear that both turbophoresis (as observed in the isothermal case) and thermophoresis take place, encouraging the particles to migrate to regions of low turbulence kinetic energy and temperature (i.e. near the walls). Over time this leads to a build-up of nano-particulate concentrations close to the wall.

This has implications for particle collision and agglomeration rates since the local concentration in these regions is greater than the initial concentration once the system has reached a steady state. This also implies that, with time, particle deposition rates on the walls will likely increase due to migration towards the walls (see Figure 83. Conversely, the results for the hot wall boundary condition show particles are migrating away from the walls towards the channel centre, as shown in Figure 83. The preferential concentration of particles within the hottest zones of the channel in this case was also noted previously through the observations in regards to the results of Figure 79.

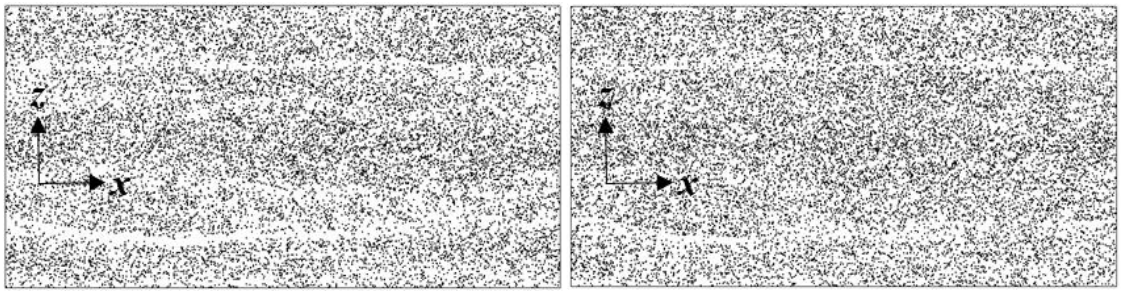

Figure 83. Instantaneous near-wall particle distributions taken from the salt based nanofluid simulations at 2000 μs showing particle migration in the near-wall regions. (Left) Hot wall: (Right) Cold wall.

The particle concentration distribution relative to the initial concentration, C_0, for both non-isothermal molten salt simulations (hot and cold configurations) are shown in Figure 84.

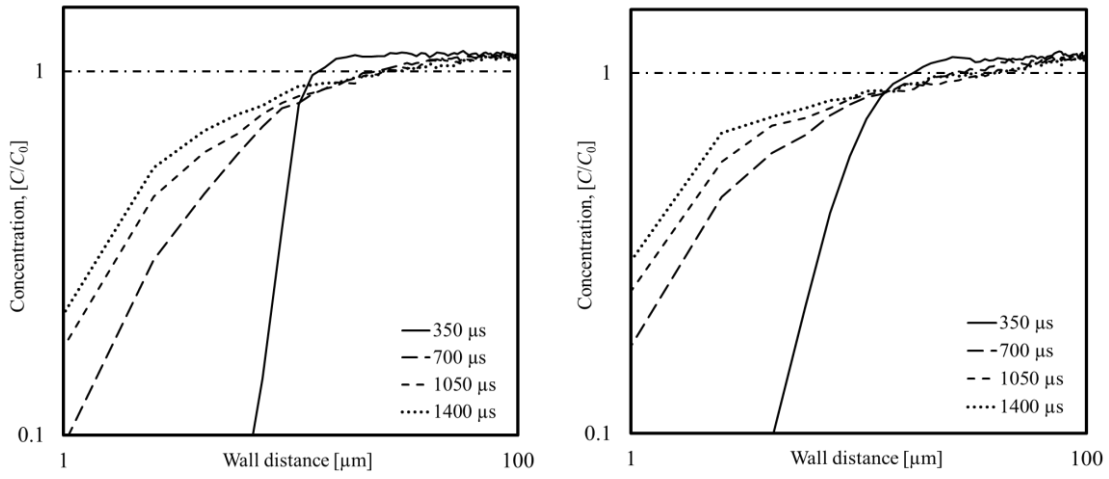

Figure 84. Particle concentration relative to homogenously distributed concentration, C_0 (-. -.). (Left) hot wall configuration; (Right) cold wall configuration. —: 350 μs; – –: 700 μs; – –: 1050 μs; · · · :1400 μs.

It is clear from the results of the cold wall configuration that there is a build-up of nano-particulate concentrations close to the walls. This also implies that, with time, particle

deposition rates will likely increase due to the migration towards the walls. Conversely, the hot wall encounters particle migration towards the centre of the channel, as illustrated in the Figure 84 - left. In all cases, the near-wall concentration reached an approximately statistically steady state after t > 1050 μs; however, this period still exhibited a slow and uniform particle accumulation rate. When these predictions are compared with the isothermal molten salt predictions (previously discussed in Figure 74) where turbophoresis was clearly observed, it can be concluded that the additional concentration differences are due to Brownian motion and thermophoresis taking place over the course of the hot and cold wall simulations.

Brownian motion and thermophoresis effects in nanofluid systems have also been observed in previous numerical simulations such as that by Anbuchezhian at el.[126]. In their study, the important role of thermophoresis in both laminar and turbulent nanofluid flow was discussed[126]. It was also pointed out that the size of nanoparticles, can greatly affect thermophoresis and particle deposition with Brownian motion, in the presence of thermal stratification, and hence have a substantial effect on the boundary layer flow field. This further impacts therefore on the heat transfer properties and nanoparticle volume fraction rate from the sheet to the carrier fluid. The results of another numerical investigation conducted by Wen at el.[234] using a non-homogeneous equilibrium model, revealed that both Brownian diffusion and thermophoresis forces were the two migration mechanisms in the boundary layer, which lead to nanoparticle migration in the turbulent flow regime similar to those found in this study.

To conclude, the developed molten salt turbulent heat transfer model exceed those used by other researchers[126, 133, 231, 234] in various ways. First the model is capable of predicting both isothermal and non-isothermal conditions, as well as presenting particle distribution in hot- and cold-wall configurations, with operating conditions being chosen to match those found in a real solar thermal power plant. Moreover, in addition to the role of inter-particle forces (e.g. Brownian motion, fluid viscous drag, collisions and DLVO) on the physical and thermal behavior of nanofluid, the incorporation of the oscillatory force, is considered a novelty. Further analysis of these forces may generate proposals for future research to perform a sensitivity analysis in order to identify the relevance of all small-scale forces used in both the stagnant simulations, as well as under turbulent flow conditions where drag force and heat transfer are increased.

6.5 Summary and conclusions

The dispersion properties of two isothermal nanoparticle-laden channel flow (water- and salt- based nanofluids) have been studied using various coupling mechanisms between the particles and the fluid flow. The particles are found to be slightly decoupled from the fluid flow in that they lag behind the mean flow beyond the turbulent region for all coupling regimes. Velocity fluctuations indicate that the particles exhibit increased normal stresses in the streamwise direction in the turbulent region, but reduced values in the other two directions. Interestingly, from the water-based nanofluid simulation the inclusion of particle agglomeration increases the magnitude of this effect in the streamwise direction. Two-way coupling is shown to lead to a slight dampening effect on the flow turbulence. Concentration plots also indicate a time varying particle distribution, with a noticeable increase in particle concentration in the near-wall regions over the run times considered that is insensitive to the mode of coupling. The molten-salt nanofluid simulation exhibits the same effects, with a clear tendency for particles to migrate towards the near-wall region. Future work should further consider relating the effects observed to the rate of particle collision and agglomeration within the channel in order to better understand the dynamics which lead to the particle behaviour observed, and to allow conclusions to be reached regarding the implications for thermal energy storage systems using nanofluids.

Direct numerical simulations of turbulent nanofluid flow with heat transfer mechanisms were performed for two different thermal wall configurations (cold and hot walls) using a high Prandtl number fluid, and the effect on nanoparticle motion statistical quantities was investigated. Concentration plots indicate a notable difference in particle distributions between the cold and hot wall boundary conditions. Specifically, it was observed that an increase in particle concentration in the near-wall regions occurred over the run times considered for the cold wall configuration. The particles were found to behave in a more turbulent fashion in the near-wall regions, due to thermophoresis causing a drift in the wall-normal direction towards the wall. Combined turbophoresis and thermophoresis effects were also found to give the particles larger distributions in the wall-normal velocity. For the hot wall case, particle migration was observed to be in the opposite direction, away from both of the walls towards the channel centre, as particles that approach the wall are encouraged away due to the increased wall temperature. The results obtained highlight differences in particle migration due to the wall temperature

boundary condition, which over time will lead to a build-up of a non-homogeneous particulate concentrations within the channel. Future work should further consider the influence of turbophoresis and thermophoresis in more detail, and this will allow conclusions to be reached regarding the implications for thermal energy storage systems using nanofluids.

A number of conclusions can be drawn from the nanofluid flow and heat transfer simulations presented in this chapter. First from the water based nanofluid simulation it was observed that there is a noticeable increase in particle concentrations in the near-wall region over time due to turbophoresis, and with the addition of particle agglomeration augmenting this effect. However, this change in the streaks build up due to particle concentration begin to become much less clear beyond a certain period of time, thus a small proportion of nanoparticles tends to remain trapped within the low speed streaks near the wall and away from the bulk fluid motion.

In terms of nanofluid stability (particle dispersion and settling behaviour), if water based nanofluid is to be used in cooling and heat transfer applications, it should be pointed out that nanoparticles may likely settle out and form a deposit on the inner surface of the transferring equipment (i.e. piping systems with elevated temperatures), which may trigger equipment fouling in the long term. In such cases, the deposited layer of nanoparticles would act as a thin layer of inner-pipe coating. This situation may sometimes be favoured as nano-coating has the advantage of reducing the pipe surface roughness, thus minimizing the influences of shear stress between the surface and the thermofluid. The other advantage of this thin layer of nano-coating is that it is highly conductive and so it may enhance the heat transfer rate in the heat exchanging equipment.

Also, it was seen from the molten salt base nanofluid flow simulations that there is more stability and uniform particle dispersion, which could be related to the contribution of the oscillatory structural forces between charged particle surfaces flowing in an ionic liquid (molten salt). With regard to the heat transfer performance our findings revealed that molten salt nanofluids are highly influenced by the wall temperature (heating/cooling from both walls). These findings are of importance if this type of nanofluid is to be used in a thermos-solar power plant. For instance, when the process equipment is in the ‘heating mode’ the hot wall configuration applies, and as such nanoparticles are expected to migrate to the centre region of the closed conduit. This may lead to disturbed heat fluxes, and non-uniform heat distribution, especially towards the centre point of the heat

transfer equipment. Conversely, when the heat exchanging equipment is in the ‘cooling mode’ the migration of nanoparticles is expected to be in the opposite direction, which may lead to enhanced levels of fouling or/and erosion-corrosion at the pipe walls or process equipment. It is suggested that the thermo-solar power plant design and operation philosophy would have to be set to cope with this type of flow and heat transfer behaviour, if water- or molten salt-based nanofluids are to be used as the thermal heat transfer and storage media.

7 CONCLUSIONS

7.1 Review of methods and results

Motivated by the exploration of novel types of hybrid nanofluids that can be used as thermal storage media and heat transfer fluid in solar power plants, a set of novel experimental and numerical techniques have been developed, tested, validated and employed on multiple scales in this study. These techniques aimed at generating new understanding surrounding the thermophysical property, as well as the flow and heat transfer behaviour of nanofluids in both stagnant and flow conditions. This new knowledge can be used to develop understanding surrounding, nanoparticle interaction, dynamic forces, stability and thermal enhancement of nanofluid on a fundamental level. By doing so, we possess the ability to improve current conventional fluids and design safer and more energy-efficient solar thermal storage systems in the future. This chapter shall summarise the findings of this research study and provide concepts for further work in this field.

Different types of nanofluids, preparation methods, diagnostic techniques, fluid properties, and nanosuspension stability have been explored first. The study extends to the thermophysical properties of nanofluids, covering the theoretical, experimental and numerical aspects in a great depth. According to our literature review, various studies have described the potential heat transfer enhancement of nanofluids, but only a few discussed the reasons and mechanisms responsible for the enhanced thermal properties of nanofluids. It was also found that the stability and dynamic properties of nanofluids are affected by a range of key parameters including: the preparation technique, nanoparticle characteristics such as size, concentration, type, shape, pH value and external driving forces, as well as the effect of base-fluid properties and temperature on the overall thermal properties of the system.

With emphasis on developing our understanding on the thermophysical properties of nanofluids an ultrasonic techniques was used. Two types of acoustic test cells were developed to allow measurements of the speed of sound in both low temperature (water based) and high temperature (salt based) nanofluids. Measurements were made using a high temperature ultrasonic probes at different operating conditions (i.e. temperature and particle concentration), as well as an ultrasonic waveguide which was used with the

standard transducer. The observed relationships between the measured parameters and speed of sound variation were presented, and found to be in good agreement with both theoretical and experimental results available in the literature. Moreover, available theoretical approaches are reviewed and applied to the data of the study. The speed of sound data together with measurements of physical properties and predictions of thermal conductivity, derived from Lagrangian particle tracking (LPT) simulations, were used to determine the ratio of specific heats of nanofluids using a modified version of the Bridgman equation. The results demonstrate the effectiveness of the measurement technique, with outcomes elucidating the dependence of the speed of sound on temperature and particle concentration. Using the speed of sound approach and LPT simulations, the predicted thermal values, which have an estimated accuracy of 5-10%, show good agreement with theoretical and experimental results available in the literature for similar operating conditions. Such findings forms the basis for the use of novel acoustic techniques for online, *in situ* measurement of nanofluids and their potential applications in solar thermal power systems.

The specific heat capacity of nanofluids was measured within a wide temperature range of 0 to 85^{o}C (water-based) and 0 to 500°C (salt-based), using differential scanning calorimetry (DSC). The effect of particle mass fraction and temperature on the heat capacity values of nanofluids was considered. The results of water based nanofluids revealed that the addition of Al_2O_3 nanoparticles decreased the heat capacity from a minimum of 1.53% at 0.5 wt.% to around 11.44% at 2.0 wt.%. Conversely, for the salt based nanofluids the heat capacity increased with increasing temperature. The addition of 1.0 wt. % Al_2O_3 nanoparticles, to binary nitrate salt based nanofluids displayed a slight reduction of around 2.1% in the specific heat capacity. It appears that there is an optimum nanoparticle concentration, which may likely be below 1.0 wt. %, for maximizing the specific heat of salt base nanofluids. These findings in turn suggests that there are competing mechanisms (i.e. oscillating particle-fluid interactions) affecting the specific heat enhancement in such an ionic based nanofluid. However, more work is needed in this area to identify these phenomena.

In the second results chapter, a computational modelling technique has been developed to assess the thermal conductivity of nanoparticle suspensions in fluids using a Lagrangian particle tracker. A three-dimensional, multiphase fluid-solid model is developed which predicts the motion of suspended nanoparticles. The system considered

consists of 25, 50 and 71 nm diameter Al_2O_3 ceramic nanoparticles suspended in water, with homogeneous temperature distributions ranging from 25 to 85°C, and at various volume fractions between 1 and 5%. The results of the simulations demonstrate the effectiveness of the presented technique, with predictions elucidating the role of Brownian motion, fluid viscous drag, inter-particle collisions and DLVO attraction and repulsion forces on nanofluid stability. Results also indicate that aggregated nanoparticles formed in the suspensions, at various particle concentrations, play an important role in the thermal behaviour of the nanofluids. Predictions are in agreement with theoretical and experimental results obtained in related studies. Using this model, the thermal characteristics of nanofluids were also considered as a function of temperature, system chemistry and time (measured from an initially homogeneously dispersed state). The proven enhancement in the conductivity of fluids affected by the addition of nanoparticles found to have great potential to assist the development of commercial nanofluid technology aimed at energy efficient and sustainable processes.

Similar multiscale simulations were carried out, this time using key variables related to the oscillatory structural force acting between two spherical nanoparticles, and the thermal conductivity of salt-based ionic nanofluids (from 250 to 500°C). The examined thermal properties of nanofluids were found to be enhanced compared to those of the pure molten salt bulk fluid. The model has been found to perform well in comparison with similar studies, and provides confirmation of the effect of interparticle distance, particle concentration, temperature, and the formation of nanolayer and percolation networks, on the thermal conductivity of nano-salts.

The current model was extended further to include the aforementioned dynamic forces considered to be important in three-dimensional flows, by coupling the tracking approach with direct numerical simulations. The behaviour of dispersed nanoparticles within a turbulent wall-bounded flow was investigated, with the fluid phase properties chosen to represent a thermofluid flow typical of those present in solar thermal power plants. Mean fluid and particle velocities, and turbulence statistics, were obtained, to investigating the effect that the turbulence field has on the dispersion properties of the solid nano-particulate phase. Particle mean velocities were observed to lag behind the fluid flow in the outer layer for all coupling methods (one-, two- and four-way coupling between the fluid and discrete phases). The result also indicated that particle streamwise velocity fluctuations were lower than those of the fluid in the bulk region of the flow, but were

greater than the latter in the buffer layer, with the addition of particle agglomeration augmenting this effect. Particle concentrations in the near-wall region were observed to increase over time due to turbophoresis.

To develop further understanding surrounding the heat transfer behaviour of a nanofluid within a turbulent wall-bounded flow, the direct numerical simulations was developed and implemented to run the non-dimensional conservation equation for energy transport with Nek5000. The fluid phase properties chosen to represent a solar molten salt ($NaNO_3$-KNO_3, 60:40 weight ratio) thermofluid typical of those present in solar thermal power plants. Predictions of a statistically steady turbulent channel flow at high turbulent Prandtl number $Pr = 5.0$ were obtained and validated. The effect of nanoparticles on the turbulent heat flux and temperature field was investigated, by the concentration response to temperature variations and turbulence across the channel, and with the associated first and second-order flow and temperature field statistics presented. The advantage of the model developed is its ability to study in detail phenomena such as interparticle collisions, agglomeration, turbophoresis and thermophoresis, with the approach also being of value in investigations of the heat transfer performance and long-term thermal stability of nanoparticle dispersions which as yet have not been considered in detail. The interesting indication of this work was that particle deposition rates on the cold walls were increased due to nanoparticle migration (regions of low turbulence kinetic energy and temperature). Conversely, the results for the hot wall boundary condition showed particles are migrating away from the walls towards the channel centre. The outcome of this study allows conclusions to be reached regarding the implications of nanoparticle-seeded molten salts for solar thermal energy storage systems.

This study provides a combined experimental and computational approach which have been developed to target the generation of new understanding of nanofluids for thermal application. For the first time, new acoustic method were developed to allow the determination of thermophysical properties of different nanofluids from speed of sound measurements, and over a wide temperature range. Furthermore, there are a number of novel features in the developed stagnant model, which was described in the second result chapter. As far as the authors are aware, there is no such analysis of the key dynamic factors affecting the stability and thermal conductivity of nanofluids using a similar multiscale computational modelling approach, more on the novelty of this model is in section 5.1.1. The nanoparticulate turbulent heat transfer model described in the final

result chapter provided explanations for phenomena such as nanoparticles migration and concentration distribution with respect to wall temperature configurations. All of this understanding can be used to make better decisions when considering nanofluids, whether that be in solar thermal power plant or any other industry which deals with such nanofluid.

7.2 Suggestions for future exploitation

The nature of the work performed here clearly opens up new avenues of research with which to explore the dynamics of nanofluids for thermal energy storage applications. It also brings new scientific challenges around our current understanding of these types of systems. There follows a numbered list of suggestions, by topic, for future work, based on the findings of this study.

1. *Nanofluid stability*. The preparation methods of nanofluids used in this study was discussed in section 3.2.4 and 3.2.10. Both mechanical mixing and ultrasonic homogenization techniques were applied to achieve nanofluid stability. The main advantage of these techniques was that shot-term stability can be achieved during the course of the experiments. The technique also has the advantages of preventing the addition of chemicals (such as those needed to control the pH or act as surfactants) and their side-effects, which could raise a concern, especially for nanofluid under high temperature. The main shortcoming of this arrangement, however, was the sedimentation of nanoparticles over time. Future research could therefore focus on developing new nanofluid fabrication methods to improve the stability of nanoparticles. The stability can be obtained when the pH value is far from isoelectric point (IEP), thus give maximum repulsion between the nanoparticles. For nanofluids the increase in zeta potential can be archived by the addition of chemicals with high-temperature thermal stability. Zeta potential techniques can then be used for the evaluation of nanoparticles behavior in the base fluid and the stability of the system.

2. *Ultrasonication*. With regard to the preparation approach of the water based nanofluids (see section 3.2.4), it is very important to point out the usefulness of ultrasonication to ensure the physical stability of nanofluids. But on the other hand, the use of an ultrasonic device will gradually increase the temperature of the nanofluid during the preparation process, which may possibly alter the

thermophysical properties. Further research initiatives in this area is therefore recommended.

3. *Ultrasonic probe*. The high temperature probe (Ionix, Huddersfield, UK) presented in 3.2.6, and were used in this study is rated to 380°C (for long term use). It was noticed that excursions at ≥ 400°C were fine as observed during the experiments, but with longer periods of probe exposure in the molten salt at such high temperature, the signal amplitude reduction was clearly noticed. Therefore it has been decided to keep exposure periods as limited as possible at temperatures above 380°C, thus to avoid damaging the probe. The manufacturer was consulted and noted that they are now working on a newer version of this probe, with higher temperature capabilities (T ≥ 500°C). It is recommended to test the performance of the new probe using the high temperature acoustic test cell, thus to obtain multiple speed of sound measurements of salt based nanofluids, over the widest range possible.

4. *Ultrasonic waveguide*. The development of a an ultrasonic waveguide sensor that can be used as buffer-rod in high temperature nanofluids was discussed in section 3.2.12 and the results of which are discussed in section 4.5. As part of the continuous improvement of the devices, work is ongoing on cladding them, which it is thought will help to improve the received signal. This will also help in reducing the trailing echoes further, making the waveguides more promising and cost-effective not just for the desired nanofluid application but also for many other industrial applications such as liquid metals.

5. *Differential scanning calorimetry*. It appears from the results shown in section 4.6 that there is an optimum nanoparticle concentration for maximizing the specific heat of nanofluids. This concertation may likely be below 1.0 wt. %, and so more experimental and theoretical modelling should be conducted, in order to identify the exact mechanisms affecting the specific heat of nanofluids, thus to identify the optimum nanoparticle concentration for the best enhancement in heat capacity. Also more theoretical work is needed to the type of solid-liquid interaction, which may have altered the specific heat capacity, especially those found in an ionic salt based nanofluid.

6. *Thermophysical properties of nanofluids*. A detailed discussion of the thermophysical property enhancement of nanofluids was given throughout this study, such as those covered in section 2.7. and the rest which were presented in the first result chapter of this thesis. However, the comparison of results such as those presented in Figure 40, shows that there are some discrepancies in the results obtained for the same type of nitrate salts. This could be due to the trace minerals and different composition of impurities present within the purchased salts. These impurities may also have an impact on the thermodynamic properties of the nanofluid mad out of the salt. Great deal of chemical analysis could be performed to identify these impurities and hence their effect on the thermal properties (thermal conductivity and heat capacity), which would have to be investigated further both experimentally and theoretically, and over a wide range of temperature. Typically, variation in the thermophysical results of a nanofluid may also be due to the: different instrumentation techniques, sample preparation and the actual physical characteristics of nanoparticles that have been used. It can therefore be said that these issues are yet to be explored and more work is necessary on this topic.

7. *Stagnant model*. The results of the stagnant model were discussed in the second result chapter. A key task for future work will be to extend the advances made in the current study to include a broader selection of thermofluids such as ionic liquids and other types of molten salts under a wide range of operating conditions, especially temperature, to cover those ranges found in solar thermal heat storage systems. Moreover, the current model includes the role of oscillatory structural forces, i.e. non-DLVO forces between ceramic nanoparticles, which can be extended to study the effect of non-spherical particles (i.e. nanotubes) and their influence on the thermal conductivity of ionic-based nanofluids. This may also be extended further to flow situations by coupling the tracking approach described with direct numerical simulations. Also experimental research needs to be conducted to support the development of this numerical model.

8. *Performance and flow behavior of nanofluids.* The effects of turbophoresis and thermophoresis on nanoparticle concentration were presented in Sections 6.3 and 6.4. Based on the results of the third result chapter, the presence of huge quantities of nanoparticle in the near wall region (in the case of cold wall configuration) of

a conduit could increase the viscosity and that may lead to higher shear stress between the fluid and the surrounding surface. This might be seen as a drawbacks of using nanofluids in some of the heat transfer equipment (e.g. piping system and heat exchangers). Also the pumping power and efficiency of the mixing systems would have to be designed to handle this increase in the viscosity, thus further research in this area is needed.

9. *Sensitivity analysis*. A sensitivity analysis could be performed to determine the effect of all small-scale forces used in both the stagnant and flow simulations, thus to predict which are relevant under turbulent flow conditions when heat transfer and drag forces are increased.

8 REFERENCES

1. Gautam, A.; Chamoli, S.; Kumar, A.; Singh, S. A review on technical improvements, economic feasibility and world scenario of solar water heating system. *Renew Sustain Energy Rev* **2017**, 68, 541– 62.

2. Lovering, D. G., ed. In Molten Salt Technology, Plenum Press: New York, 1982.

3. Dell, R.M.; Rand, D.A.J. Energy storage - a key technology for global energy sustainability. *Journal of Power Sources* **2001**, 100, 2–17.

4. Rajamani, L. Ambition and Differentiation in the 2015 Paris Agreement: Interpretative Possibilities and Underlying Politics. I*nternational and Comparative Law Quarterly* **2016**, 65, 493– 514.

5. KISR, 2015. Kuwait Institute for Scientific Research [Online]. Available: http://www.kisr.edu.kw/en, accessed on Jun. 27, 2019.

6. Mount Holyoke, Concentrated Solar Power: Parabolic Trough Plant [online] Available at: https://www.mtholyoke.edu/~wang30y/csp/PTPP.html [Accessed 27 Jul. 2019].

7. Adinberg, R.; Zvegilsky, D.; Epstein, M. Heat Transfer Efficient Thermal Energy Storage for Steam Generation. *Energy Conversion and Management* **2010** ,51, 9–15.

8. Kearney, D.; Herrmann, U.; Nava, P.; Kelly, B.; Mahoney, R.; Pacheco, J.; Cable, R.; Potrovitza, N.; Blake D.; Price, H. Assessment of a Molten Salt Heat Transfer Fluid in a Parabolic Trough Solar Field. *Sol. Energy Eng.* **2003**, 125, 170– 176.

9. Kruizenga, A.; David, M.; Gill, D.; LaFord, M.; McConohy, G. Corrosion of high temperature alloys in solar salt at 400, 500, and 680°C. *SANDIA Report* **2013**, 8256, 1– 45.

10. Siegel, R. Solidification of low conductivity material containing dispersed high conductivity particles. Inter. *J. Heat Mass Transf.* **1977**, 20, 1087– 9.

11. Parameshwaran, R.; Kalaiselvam, K. Thermal Energy Storage Technologies for Sustainability: Systems Design, Assessment and Applications, 1st ed. New York, NY, USA: Academic, 2014.

12. Lasfargues M (2014) Nitrate based high temperature nano-heat-transfer-fluids: formulation & characterisation. PhD thesis. University of Leeds.

13. Meriem, C.; Sébastien, V. Benchmark of Concentrating Solar Power plants: historical, current and future technical and economic development. *Proc. Comp. Sci.* **2016**, 83,782– 789.

14. Ralon, P.; Taylor, M.; Ilas, A. Electricity storage and renewables: Costs and market to 2030. Abou Dabi 2017. [online] Available at: www.irena.org/ publications/2017/Oct/Electricity-storage-and-renewables-costsand-markets [Accessed 1 Sep. 2019].

15. Tian, Y.; Zhao, C.Y. A review of solar collectors and thermal energy storage in solar thermal applications. *Applied Energy* **2013**, 104, 538– 553.

16. Rosenthal, M.W.; Kasten, P.R.; Briggs, R.B. Molten-Salt Reactor History, Status and Potential. Nuclear Applications and Technology, vol. 8, 1970.

17. Gil, A.; Medrano, M.; Martorell, I.; Lázaro, A.; Dolado, P.; Zalba, B.; Cabeza, L.F. State of the art on high temperature thermal energy storage for power generation. Part 1 - concepts, materials and modellization. *Renew. Sust. Energ. Rev.* **2010**, 14, 31– 55.

18. T. Ehresman (ed.), "Molten Salt Reactor (MSR)," (Fact Sheet), 08-GA50044-17-R1 R6-11 (Idaho National Laboratory), [Online]. Available: https://inl.gov/research/molten-salt-reactor, accessed on Jun. 27, 2019.

19. Lane, G.A. Solar heat storage—latent heat materials, vol. I. Boca Raton, FL: CRC Press, Inc.; 1983.

20. Atkins, P., & Jones, L. Chemical principles: The quest for insight (3rd ed.). New York: Freeman, 2005.

21. Pfleger, N.; Bauer, T.; Martin, C.; Eck, M.; Wörner, A. Thermal energy storage - Overview and specific insight into nitrate salts for sensible and latent heat storage, *Beilstein J. Nanotechnol.* **2015**, 6, 487– 1497.

22. Pecora, R. Dynamic Light Scattering Application of Photon Correlation Spectroscopy; Plenum Press: New York, 1976.

23. Dukhin, A.S. Goetz, P.J. Characterization of Liquids, Nano- and Microparticulates, and Porous Bodies Using Ultrasound, second ed. Elsevier, Oxford, 2010.

24. Choi, S. U. S. Nanofluids: from vision to reality through research. *J. Heat Transf.* **2009**, 131, 033106/1– 033106/9.

25. Xuan, Y. and Li, Q. Heat transfer enhancement of nanofluids. *Int. J. Heat Fluid Flow* **2000**, 21, 58– 64.

26. Wang X.Q.; Mujumdar A.S. Heat transfer characteristics of nanofluids: a review. *Int. J. Therm. Sci.* **2007**, 46, 1– 19.

27. Shin, D.; Banerjee, D. Effects of silica nanoparticles on enhancing the specific heat capacity of carbonate salt eutectic (work in progress). *IJASE* **2010**, 2, 25– 31.

28. Wang, X.Q.; Mujumdar, A.S. A Review on Nanofluids – Part I: Theoretical and Numerical Investigations. *Braz. J. Chem. Eng.* **2008a**, 25, 613– 630.

29. Wang, X.Q.; Mujumdar, A.S. A review on Nanofluids – Part II: Experiments and Applications. *Braz. J. Chem. Eng.* **2008b**, 25, 631– 648.

30. Ganvir, R.B.; Walke, P.V.; Kriplani V.M. Heat transfer characteristics in nanofluid-a review. *Renew. Sustain. Energy Rev.* **2017**, 75, 451– 460.

31. Raja, M.; Vijayan, R.; Dineshkumar, P.; Venkatesan, M. Review on nanofluids characterization, heat transfer characteristics and applications, *Renew. Sustain. Energy Rev.* **2016**, 64 163– 173.

32. Bhanushali, S.; Jason, N. N.; Ghosh, P.; Ganesh, A.; Simon, G.P.; Cheng, W. Enhanced Thermal Conductivity of Copper Nanofluids: The Effect of Filler Geometry. *ACS Appl. Mater. Interfaces* **2017**, 9, 18925− 18935.

33. Azizi, M.; Hosseini, M.; Zafarnak, S.; Shanbedi, M.; Amiri, A. Experimental analysis of thermal performance in a two-phase closed thermosiphon using graphene/water nanofluid *Ind. Eng. Chem. Res.* **2013**, 52, 10015– 10021.

34. Shima, P. D.; Philip, J. Role of Thermal Conductivity of Dispersed Nanoparticles on Heat Transfer Properties of Nanofluid *Ind. Eng. Chem. Res.* **2014**, 53 (2) 980– 988.

35. Murshed S.M.S.; Leong K.C.; Yang C. Thermophysical and electrokinetic properties of nanofluids—a critical review. *Appl. Therm. Eng.* **2008**, 28, 2109– 2125.

36. Yu W.; France D.M.; Routbort J.L.; Choi S.U.S. Review and comparison of nanofluid thermal conductivity and heat transfer enhancements. *Heat Transf. Eng.* **2008**, 5, 432– 460.

37. Chandrasekhar M.; Suresh S. A review on the mechanisms of heat transport in nanofluids. *Heat Transf. Eng.* **2009**, 30, 1136– 1150.

38. Wen D.; Lin G.; Vafaei S.; Zhang K. Review of nanofluids for heat transfer applications, *Particuology* **2009**, 7, 141– 150.

39. Keblinski, P.; Phillpot, S. R.; Choi, S. U. S.; Eastman, J. A. Mechanisms of heat flow in suspensions of nano-sized particles (nanofluids). *Inter. J. of Heat Mass Transf.* **2002**, 45, 855– 863.

40. Eastman, J. A.; Phillpot, S. R.; Choi, S. U. S.; Keblinski, P. Thermal transport in nanofluids. *Annu. Rev. Mater. Res.* **2004**, 34, 219– 46.

41. Hong, Y.; Ding, S.; Wu, W.; Hu, J.; Voevodin, A. A.; Gschwender, L.; Snyder, E.; Chow, L.; Su, M. Enhancing Heat Capacity of Colloidal Suspension Using Nanoscale Encapsulated Phase-Change Materials for Heat Transfer. *ACS Appl. Mater. Interfaces* **2010**, 2, 1685– 1691.

42. Das, S.K.; Choi S.U.; Patel H.E. Heat Transfer in Nanofluids – A Review. *Heat Transfer Eng.* **2006**, 27, 3– 19.

43. Sen, S.; Govindarajan, V.; Pelliccione, C. J.; Wang, J.; Miller, D. J.; Timofeeva, E. V. Surface modification approach to TiO_2 nanofluids with high particle concentration, low viscosity, and electrochemical activity, *ACS Appl. Mater. Interfaces* **2015**, 7, 20538– 20547

44. Lee, J.; Mudawar, I. Assessment of the effectiveness of nanofluids for singlephase heat transfer in micro-channels. *Inter. J. Heat Mass Transf.* **200**7, 50, 452– 463.

45. Li, Y.; Zhou, J.; Tung, S.; Schneider, E.; Xi, S. A review on development of nanofluid preparation and characterization. *Powder Technol.* **2009**, 196, 89– 101.

46. Das SK, Choi SUS, Yu W, Pradeep T: Nanofluids: Science and Technology. New Jersey: Wiley; 2008.

47. Solangi, K.H.; Kazi, S.N.; Luhur, M.R.; Badarudin, A.; Amiri, A.; Sadri, R.; Zubir, M.N.M.; Gharehkhani, S.; Ten, K.H. A comprehensive review of thermo-physical properties and convective heat transfer to nanofluids. *Energy* **2015**, 89,1065– 86.

48. Starov, V.M., Nanoscience: Colloidal and Interfacial Aspects, Fla.: CRC; London: Taylor & Francis, 2010.

49. Israelachvili, J.N. Intermolecular and Surface Forces, 2nd Edition, Academic Press, London, 1992.

50. Zeinali, H.S.; Nassan, T.H.; Noie, S.H.; Sardarabadi, H.; Sardarabadi, M. Laminar convective heat transfer of Al2O3/water nanofluid through square cross-sectional duct. *Int. J. Heat Fluid Flow* **2013**, 44, 375– 82.

51. Chougule, S.S.; Sahu, S.K. Comparative study of cooling performance of automobile radiator using Al_2O_3-water and carbon nanotube-water nanofluid. *J. Nanotech. Eng. Med.* **2014**, 5, 1– 6.

52. Chougule, S.S.; Sahu, S.K. Thermal performance of automobile radiator using carbon nanotube/water nanofluid—experimental study. *J. Therm. Sci. Eng. Appl.* **2014**, 6, 041009– 041014.

53. Ghassemi, M.; Shahidian A. Nano and Bio Heat Transfer and Fluid Flow, Academic Press, 2017.

54. Wang, X.Q.; Xu, X.; Choi, S.U.S. Thermal Conductivity of Nanoparticle Fluid Mixture. *J. Thermophys. Heat Tr.* **1999**, 13, 474– 480.

55. Saha, G.; Paul, M. C. Numerical analysis of the heat transfer behaviour of water based Al2O3 and TiO2 nanofluids in a circular pipe under the turbulent flow condition. *Intl Communication Heat Mass Transfer* **2014**, 56, 96– 108.

56. Keblinski, P.; Prasher, R.; Eapen, J. Thermal Conductance of Nanofluids: Is the Controversy Over? *J. Nanopart. Res.* **2008**, 10, 1089– 1097.

57. Eastman, J. A.; Phillpot, S. R.; Choi, S. U. S.; Keblinski, P. Thermal transport in nanofluids. *Annu. Rev. Mater. Res.* **2004**, 34, 219– 46.

58. Sloan, G.; Feng, Z.-G.; Bhaganagar, K.; Banerjee, D. Coupled Direct Numerical Simulation and Experimental Approach to Develop Framework for Nanofluids. *ASME International Mechanical Engineering Congress and Exposition, Houston, USA*: **2012**, 7, 2877– 2882.

59. Beck, M.P.; Yuan, Y.; Warrier, P.; Teja, A.S. The Effect of Particle Size on the Thermal Conductivity of Nanofluids. *J. Nanopart. Res.* **2009**, 11, 1129– 1136.

60. Lee, S.; Choi, S.U.S.; Li, S; Eastman, J.A. Measuring Thermal Conductivity of Fluids Containing Oxide Nanoparticles. *J. Heat Transfer* **1999**, 121, 280– 289.

61. Xie, H.; Wang, J.; Xi, T.; Liu, Y.; Ai, F.; Wu, Q. Thermal conductivity enhancement of suspensions containing nanosized alumina particles. *J. Appl. Phys.* **2002**, 91, 4568– 4572.

62. Pantzali, M.N.; Mouza, A.A.; Paras, S.V. Investigating the efficacy of nanofluid as coolants in plate heat exchangers (PHE). *Chem. Eng. Sci.* **2009**, 64, 3290–3300.

63. Gherasim, I.; Roy, G.; Nguyen, C.T.; Vo-Ngoc, D. Experimental investigation of nanofluids in confined laminar radial flows. *Int. J. Therm. Sci.* **2009**, 48, 1486–1493.

64. Leong, K.Y.; Saidur, R.; Mahlia, T.; Yau, Y.H. Performance investigation of nanofluid as working fluid in a thermosyphon air preheater. Int. Commun. *Heat Mass Transf.* **2012**, 39, 523– 532.

65. Hung, Y.; Teng, Tun-Ping; Teng, Tun-Chien; Chen J. Assessment of heat dissipation performance for nanofluid. *Appl. Therm. Eng.* **2012**, 32, 132– 140.

66. Das, S.K.; Putra, N.; Thiesen, P. Temperature dependence of thermal conductivity enhancement for nanofluids. *J. Heat Transf. Trans. ASME* **2003**, 125, 567– 574

67. Eastman, J. A.; Choi, S. U. S.; Li, S.; Thompson L. J.; Lee, S. Enhanced thermal conductivity through the development of nanofluids, Fall Meeting of the Materials Research Society (MRS), Boston, USA, 1996.

68. Nguyen, C.T.; Galanis, N.; Polidori, G.; Fohanno, S.; Popa, C.V.; Bechec, A.L. An experimental study of a confined and submerged impinging jet heat transfer using Al2O3-water nanofluid. *Int. J. Therm. Sci.* **2009**, 48, 401– 411.

69. Asirvathama, L.G.; Rajab, B.; Lal, D.M.; Wongwises, S. Convective heat transfer of nanofluids with correlations. *Particuology* **2011**, 9, 626– 631.

70. Naphon, P.; Assadamongkol, P.; Borirak, T. Experimental investigation of titanium nanofluids on the heat pipe thermal efficiency. *Inter. Communication Heat Mass Transf.* **2008**, 35, 1316– 1319.

71. Cao, J.; Ding, Y.; Ma, C. Aqueous Al2O3 nanofluids: the important factors impacting convective heat transfer. *Heat and Mass Transf.* **2014**, 50, 1639– 1648.

72. Coscia, K.; Elliott, T.; Mohapatra, S.; Oztekin, A.; Neti, S. Binary and Ternary Nitrate Solar Heat Transfer Fluids. J. Solar Energy Eng. 2013, 135, 021011–.

73. Raade, J.W.; Padowitz, D. Development of molten salt heat transfer fluid with low melting point and high thermal stability. J. Solar Energy Eng. 2011, 133, 031013–.

74. Pielichowska, K.; Pielichowski, K. Phase change materials for thermal energy storage. *Progress in Materials Science* **2014**, 65, 67– 123.

75. Zhao, Q.; Hu, C.; Liu, S.; Guo, H.; Wu, Y. The thermal conductivity of molten $NaNO_3$, KNO_3, and their mixtures. *Energy Procedia* **2017**, 143, 774– 779.

76. Mahian, O.; Kianifar, A.; Kalogirou, S.S.; Pop, I.; Wongwises, S. A review of the applications of nanofluids in solar energy. *Int. J. Heat Mass Transf.* **2013**, 57, 582– 594.

77. Kalaiselvam, S.; Parameshwaran, R. Thermal energy storage technologies for sustainability: systems design, assessment and applications. Elsevier 2014, 163– 192.

78. Bozorgan, N.; Shafahi, M. Performance evaluation of nanofluids in solar energy: a review of the recent literature. *Micro Nano Syst. Letters* **2015**, 3:5, 1– 15.

79. Chieruzzi, M.; Cerritelli, G.F.; Miliozzi, A.; Kenny, J.M. Effect of nanoparticles on heat capacity of nanofluids based on molten salts as PCM for thermal energy storage. *Nanoscale Research Letters* **2013**, 8:448, 1– 9.

80. Dudda, B.; Shin, D. Effect of nanoparticle dispersion on specific heat capacity of a binary nitrate salt eutectic for concentrated solar power applications. *Inter. J. Therm. Sci.* **2013**, 69, 37– 42.

81. Lu, M.C.; Huang, C.H. Specific heat capacity of molten salt-based alumina nanofluids. *Nanoscale Research Letters* **2013**, 8, 292– 299.

82. Tiznobaik, H.; Shin, D. Enhanced specific heat capacity of high temperature molten salt-based Nanofluids. *Inter. J. Heat Mass Transfer* **2013**, 57, 542– 548.

83. Jo, B., Banerjee, D. Enhanced specific heat capacity of molten salt based nanomaterials: Effects of nanoparticle dispersion and solvent material. *Acta. Mater* **2014**, 75, 80– 91.

84. Nagasaka, Y.; Nagashima, A. The thermal conductivity of molten $NaNO_3$ and KNO_3. *Inter. J. Thermophysics* **1991**, 12, 769– 781.

85. Muñoz-Sánchez, B.; Nieto-Maestre, J.; Iparraguirre-Torres, I.; García-Romero, A.; Sala-Lizarraga, J.M. Molten salt-based nanofluids as efficient heat transfer and storage materials at high temperatures. An overview of the literature. *Renew. Sustain. Energy. Rev.* **2018**, 82, 3924– 3945.

86. Wang, W.; Wu, Z.; Li, B.; Sunden, B. A review on molten-salt-based and ionic-liquid-based nanofluids for medium-to-high temperature heat transfer. *J. Therm. Analysis Calorimetry* **2019**, 136, 1037– 1051.

87. Bauer, T.; Laing, D.; Tamme, R. Recent progress in alkali nitrate/nitrite developments for solar thermal power applications. *Molten Salts Chem. Technol.* **2011**, No. June, 1– 10.

88. Muñoz-sánchez, B.; Nieto-maestre, J.; Iparraguirre-torres, I.; García-romero, A.; Sala-lizarraga, J.M. Molten salt-based nano fluids as e fficient heat transfer and storage materials at high temperatures. An overview of the literature. *Renew. Sustain. Energy Rev.* **2018**, 82, 3924– 3945.

89. Ueki, Y.; Fujita, N.; Kawai, M.; Shibahara, M. Thermal conductivity of molten salt-based nanofluids. *AIP Advances* **2017**, 7, 055117.

90. Ma, B.; Banerjee, D. Experimental measurements of thermal conductivity of alumina nanofluid synthesized in salt melt. *AIP Advances* **2017**, 7, 115124.

91. Sumair, F. A. Preparation and characterisation of eutectic nanofluids for heat transfer enhancement in flat plate solar collectors, 2018, Ph.D. thesis, University of Nottingham, Nottingham, UK.

92. Bellos, E.; Tzivanidis, C.; Tsimpoukis, D. Thermal, hydraulic and exergetic evaluation of a parabolic trough collector operating with thermal oil and molten salt based nanofluids. *Energy Convers. Manag.* **2018**,156, 388– 402.

93. Shin, D.; Banerjee, D. Enhanced thermal properties of SiO_2 nanocomposite for solar thermal energy storage applications. *Int. J. Heat Mass Transf.* **2015**, 84, 898–902.

94. Jeyaseelan, T.R.; Azhagesan1, N.; Pethurajan, V. Thermal characterization of $NaNO_3/KNO_3$ with different concentrations of Al_2O_3 and TiO_2 nanoparticles. *J. Therm. Analysis & Calorimetry* **2018**, 136, 235– 242.

95. Bianco, V.; Manca, O.; Nardini, S. Numerical investigation of transient single phase forced convection of nanofluids in circular tubes. *WIT Trans. Eng. Sci.* **2008**, 61, 3– 12.

96. Halelfadl, S.; Maré ,T.; Estelle, P. Efficiency of carbon nanotubes water based nanofluid as coolants. *Exp. Therm. Fluid Sci.* **2014**, 53, 104– 110.

97. Ghanbarpour, M.; Bitaraf Haghigi, E.; Khodabandeh, R. Thermal properties and rheological behavior of water based Al_2O_3 nanofluid as a heat transfer fluid. *Exp. Therm. Fluid Sci.* **2014**, 53, 227– 235.

98. Namburu, P.K.; Das, D.K.; Tanguturi, K.M.; Vajjha, R.S. Numerical study of turbulent flow and heat transfer characteristics of nanofluid considering variable properties. *Int. J. Therm. Sci.* **2009**, 48, 290– 302.

99. Ray, D.R.; Das, D.K.; Superior performance of nanofluid in an automotive radiator. *J. Therm. Sci. Eng. Appl.* **2014**, 6 1– 16.

100. Puliti, G.; Paolucci, S.; Sen, M. Nanofluids and their properties, *ASME Appl. Mech. Rev.* **2011**, 64, 031002– 031025.

101. Bergman, T. Effect of reduced specific heats of nanofluids on single phase, laminar internal forced convection. *Int. J. Heat Mass Transf.* **2009**, 52, 1240– 1244.

102. Vajjha, R. S.; Das. D. K. Specific heat measurement of three nanofluids and development of new correlations. *J. Heat Transf.* **2009**, 131, 071601.

103. Zhou, S.-Q.; Ni, R. Measurement of the specific heat capacity of water-based Al_2O_3 nanofluid. *Appl. Phys. Lett.* **2008**, 92, 093123.

104. Nelson, I. C.; Banerjee, D.; Ponnappan, R. Flow loop experiments using polyalphaolefin nanofluids. *J. Thermophys. Heat Trans.* **2009**, 23, 752– 761.

105. Shin, D., Banerjee. D. Enhancement of specific heat capacity of high-temperature silica-nanofluids synthesized in alkali chloride salt eutectics for solar thermal-energy storage applications. *Int. J. Heat Mass Transf.* **2011**, 54, 1064–1070.

106. Azari, A.; Kalbasi, M.; Rahimi, M. CFD and experimental investigation on the heat transfer characteristics of alumina nanofluids under the laminar flow regime. *Braz. J. Chem. Eng.* **2014**, 31, 469– 481.

107. Doostmohammadi, A.; Dabiri, S.; Ardekani, A. M. A numerical study of the dynamics of a particle settling at moderate Reynolds numbers in a linearly stratified fluid, *J. Fluid Mech.* **2014**, 750, 5– 32.

108. Kuznetsov, A.V.; Nield, D.A. Natural convective boundary-layer flow of a nanofluid past a vertical plate. *Inter. J. Therm. Sci.* **2009**, 49, 243– 247.

109. Kowsari, F. Numerical investigation into the heat transfer enhancement of nanofluids using a nonhomogeneous model. *J. Enhanced Heat Trans.* **2011**, 18, 81– 90.

110. Xuan, Y.; Yao, Z. Lattice Boltzmann model for nanofluids. *Heat Mass Trans.* **2005**, 41, 199– 205.

111. Xue, L.; Keblinski, P.; Phillpot, S. R.; Choi, S. U. S.; Eastman, J. A. Effect of liquid layering at the liquid-solid interface on thermal transport. *Inter. J. Heat Mass Trans.* **2004**, 47, 4277–4284.

112. Njobuenwu, D. O. Lagrangian particle tracking methods for slurry flow. Ph.D. (transfer report), The University of Leeds, 2007.

113. Crowe, C. T., Engineering fluid mechanics / Clayton T. Crowe, Donald F. Elger, John A. Roberson, New York ; Chichester :, Wiley, 2006.

114. Derjaguin, B.; Landau, L. Theory of the stability of strongly charged lyophobic sols and of the adhesion of strongly charged particles in solutions of electrolytes. *Acta Physicochim* **1941**, 14, 633– 662.

115. Verwey, E.J.W.; Overbeek, J.T.G. Theory of the stability of lyophobic colloids. *J. Colloid Sci.*, 1955, 10, 224– 225.

116. Kang, U.; Kim, W.; Kim, S.H. Effect of particle migration on the heat transfer of nanofluid. *Korea Australia Rheol J* **2007**, 19, 99– 107.

117. Lee, S.-H.; Jang, S.P. Mechanisms and Models of Thermal Conductivity in Nanofluids, in Heat Transfer Enhancement with Nanofluids, Bianco, V.; Manca, O.; Nardini, S.; Vafai, K. (Eds.). CRC Press, Boca Raton, Florida, 2015, 78– 98.

118. Ren, Y.; Xie, H.; Cai, A. Effective Thermal Conductivity of Nanofluids Containing Spherical Nanoparticles. *J. Phys. D Appl. Phys.* **2005**, 38, 3958–3961.

119. Murshed, S.M.S.; Leong, K.C.; Yang, C. A Combined Model for the Effective Thermal Conductivity of Nanofluids. *Appl. Therm. Eng.* **2009**, 29, 2477– 2483.

120. Xuan, Y.; Li, Q.; Hu, W. Aggregation Structure and Thermal Conductivity of Nanofluids. *AIChE J.* **2003**, 49, 1038– 1043.

121. Prasher, R.; Bhattacharya, P.; Phelan, P.E. Thermal Conductivity of Nanoscale Colloidal Solutions (Nanofluids). *Phys. Rev. Lett.* **2005**, 94, 025901/1–025901/4.

122. Prasher, R.; Phelan, P.E.; Bhattacharya, P. Effect of Aggregation Kinetics on the Thermal Conductivity of Nanoscale Colloidal Solutions (Nanofluid). *Nano Lett.* **2006**, 6, 1529– 1534.

123. Prasher, R.; Evans, W.; Meakin, P.; Fish, J.; Phelan, P.; Keblinski, P. Effect of Aggregation on Thermal Conduction in Colloidal Nanofluids. *Appl. Phys. Lett.* **2006**, 89, 143119/1– 143119/3.

124. Prasher, R.; Song, D.; Wang, J.; Phelan, P. Measurements of Nanofluid Viscosity and its Implications for Thermal Applications. *Appl. Phys. Lett.* **2006**, 89, 133108/1– 133108/3.

125. Goodarzi, M.; Safaei, M.R.; Vafai, K.; Ahmadi, G.; Dahari, M.; Kazi, S.N. Jomhari, N. Investigation of nanofluid mixed convection in a shallow cavity using a two-phase mixture model. *Int. J. Therm. Sci.* **2014**, 75, 204– 220.

126. Anbuchezhian, N.; Srinivasan, K.; Chandrasekaran, K.; Kandasamy R. Thermophoresis and Brownian motion effects on boundary layer flow of nanofluid in presence of thermal stratification due to solar energy. *Appl. Math. Mech.* **2012**, 33, 765– 780.

127. Mohammed, H.A.; Gunnasegaran, P.; Shuaib, N.H. Heat transfer in rectangular microchannel heat sink using nanofluid. *Int. Commun. Heat Mass Transf.* **2010**, 37, 1496– 503.

128. Seyf, H.R.; Feizbakhshi, M. Computational analysis of nanofluid effects on convective heat transfer enhancement of micro-pin-fin heat sinks. *Int. J. Therm. Sci.* **2012**, 58, 168– 79.

129. Ebrahimnia-Bajestan, E.; Niazmand, H.; Duangthongsuk, W.; Somchai, W. Numerical investigation of effective parameters in convective heat transfer of nanofluid flowing under a laminar flow regime. *Int. J. Heat Mass Transf.* **2011**, 54, 4376– 88.

130. Ahmed, M.A.; Shuaib, N.H.; Yusoff, M.Z.; Al-Falahi, A.H. Numerical investigations of flow and heat transfer enhancement in a corrugated channel using nanofluid. *Int. Commun. Heat Mass Transf.* **2011**, 38, 1368– 75.

131. Moraveji, M.K.; Esmaeili, E. Comparison between single-phase and two-phases CFD modeling of laminar forced convection flow of nanofluid in a circular tube under constant heat flux. *Int. Commun. Heat Mass Transf.* **2012**, 39 1297– 302.

132. Gori, F.; Boghi, A. A three dimensional exact equation for the turbulent dissipation rate of Generalised Newtonian Fluids. *Int. Commun. Heat Mass Transf.* **2012**, 39, 477– 85.

133. Kawamura, H.; Ohsaka, K.; Abe, H.; Yamamoto, K. DNS of turbulent heat transfer in channel flow with low to medium-high Prandtl number fluid. *Int. J. Heat and Fluid Flow* **1998**, 19, 482– 491.

134. Povey, M.J.W. Ultrasonic techniques for fluids characterization, Academic Press, San Diego, 1997.

135. Wedlock, D.J.; McConaghy, C.J.; Hawksworth, S. Automation of ultrasound velocity scanning for concentrated dispersions. Colloids and Surfaces *A: Phy. Eng. Aspects* **1993**, 77, 49– 54.

136. Locatelli, F.; François, P.; Laurent, J.; Lawniczak, F.; Dufresne, M.; Vazquez, J.; Bekkour, K. Detailed velocity and concentration profiles measurement during activated sludge batch settling using an ultrasonic transducer. *Sep. Sci. and Tech.* **2015**, 7, 1059– 1065.

137. Rice, H.P.; Fairweather, M.; Peakall, J.; Hunter, T.N.; Mahmoud, B.; Biggs, S.R. Measurement of particle concentration in horizontal, multiphase pipe flow using acoustic methods: Limiting concentration and the effect of attenuation. *Chem. Eng. Sci.* **2015**, 126 , 745– 758.

138. Rice H.P.; Fairweather M.; Peakall J.; Hunter T.N.; Mahmoud B.; Biggs S.R. Constraints on the functional form of the critical deposition velocity in solid-liquid pipe flow at low solid volume fractions. *Chem. Eng. Sci.* **2015**, 126, 759– 770.

139. Wood, A.B.A. Textbook of sound, Bell and Sons, London, 1941.

140. Urick, R.J. A sound velocity method for determining compressibility of finely divided substances. *J. of Appl. Phy.* **1947**, 18, 983– 987.

141. Hirschfelder, J.O.; Curtiss, C.F.; Bird R.B. Molecular theory of gases and liquids, John Wiley and Sons, New York, 1954.

142. Bridgman, P.W. The compressibility of thirty metals as a function of pressure and temperature. *Proc. Am. Acad. Arts Sci.* **1923**, 58, 165– 242.

143. Bird, B.R.; Stewart, W.E.; Lightfoot, E.N. Transport phenomena. John Wiley & Sons, New York, 2007.

144. Lin J.Y.; Pate M.B.; A thermal conductivity prediction method for refrigerant mixtures in the liquid phase. IRACC 175 1992.

145. Powell, R.E.; Roseveare, W.E.; Eyring, H. The constants of the Beattie-Bridgeman equation. *Ind. Eng. Chem.* **1941**, 33, 430– 435.

146. Chakraborty, S.; Saha, S.K.; Pandey, J.C.; Das, S. Experimental characterization of concentration of nanofluid by ultrasonic technique, *Powder Technol.* **2011**, 210, 304– 307.

147. Bockris, J. O. M.; Richards, N. E. The Compressibilities, Free volumes and equation of state for molten electrolytes: Some Alkali Halides and Nitrates. *Proc. R. Soc. London* **1957**, 241, 44– 66.

148. Asher, R.C. Ultrasonic Sensors, Institute of Physics, London, 1997.

149. National Institute of Standards and Technology, Gaithersburg MD, 20899, https://doi.org/10.18434/T4D303, (accessed December 9, 2018).

150. Kell, G.S. Density, thermal expansivity, and compressibility of liquid water from 0° to 150°C: Correlations and tables for atmospheric pressure and saturation reviewed and expressed on 1968 temperature scale. *J. of Chem. and Eng. Data* **1975**, 20, 97– 105.

151. Blitz, J. Fundamentals of ultrasonics, Butterworth & Co. Ltd., London, 1963.

152. Touloukian, Y.S.; Makita, T. Thermophysical properties of matter, - The TPRC data series, Volume 6, Specific heat - Nonmetallic liquids and gases, Plenum Press, New York, 1970.

153. Parthasarathy, S. The ratio of specific heats as a fundamental physical property of liquids. *Annalen der Physik* **1956**, 452, 178– 184.

154. Bardakov, R.N.; Kistovich, A.V.; Yu. D. Chashechkin calculation of the sound-propagation velocity in inhomogeneous liquid. *Doklady Akademii Nauk* **2008**, 420, 324– 327.

155. Richards, N.E.; Brauner E.J.; Bockris, J.O.'M. Determination of the velocity of ultrasonic vibrations in molten salts. *B. J. Appl. Phys.* **1955**, 6, 387– 390.

156. Chebbi, R. A theoretical model for thermal conductivity of nanofluids. *Mater. Express* **2017**, 7, 51– 58.

157. Mahmoud, B.H.; Fairweather, M; Mortimer, L.F.; Peakall J.; Rice, H.R.; Harbottle, D. Prediction of stability and thermal conductivity of nanofluids for

thermal energy storage applications. *Computer-Aided Chem. Eng.* **2018**, 43, 61–66.

158. US Research Nanomaterials Inc., 2018. [online] Available at: www.us-nano.com/inc/sdetail/13136 [Accessed 25 Nov. 2018].

159. Bilaniuk, N.; Wong, G.S.K. Speed of sound in pure water as a function of temperature. *J. Acoust. Soc. America* **1993**, 93, 1609– 1612.

160. Yaws, C.L. Chemical Properties Handbook. McGraw-Hill: New York, 1999.

161. Lide, D.R. Handbook of chemistry and physics, 71st Edition, CRC Press, Boca Raton, 1990.

162. Auerkari, P. Mechanical and physical properties of engineering alumina ceramics. Technical Research Centre of Finland, ESPOO, 1996.

163. Nissen, D.A. Thermophysical properties of the equimolar mixture $NaNO_3$-KNO_3 from 300C to 600C. *J Chem Eng Data* **1982**, 27, 269– 73.

164. D'Aguanno, B.; Karthik, M.; Grace, A. N.; Floris, A. Thermostatic properties of nitrate molten salts and their solar and eutectic mixtures. *Scientific Reports 8*, **2018**, 10485.

165. Jen, C. K.; Legoux, J. G.; Parent, L. Experimental evaluation of clad metallic buffer rods for high temperature ultrasonic measurements. *NDT&E International* **2000**, 33, 145– 153.

166. Burhan, D. Ihara, I. Seda, Y. In Situ observations of solidification and melting of Aluminium alloy using ultrasonic waveguide sensor, *Materials Transactions* **2005**, 46, 2107– 2113.

167. Murayama, R. Kobayashi, M. Matsumoto, K. Kobayashi, M. Ultrasonic inspection system using a long waveguide with an acoustic horn for high-temperature structure, *J. Sensor Tech.* **2014**, 4, 178– 185.

168. Lasfargues, M. Nitrate Based High Temperature Nano-Heat-Transfer-Fluids: Formulation & Characterisation, The University of Leeds, 2014.

169. P.F Fischer, J.W. Lottes, S.G. Kerkemeier, 2008, Nek5000 [online] Available at: http://nek5000.mcs.anl.gov [Accessed 20 Jul. 2019].

170. Maday, Y.; Patera, A.T. Spectral element methods for the incompressible Navier-Stokes equations. *In: State-of-the-art Surveys on Computational Mechanics* **1989**, 71– 143.

171. Mortimer, L.; Fairweather, M.; Njobuenwu, D.O. Particle Concentration and Stokes Number Effects in Multi-Phase Turbulent Channel Flows. *5th International Conference on Particle-Based Methods, Hannover, Germany:* **2017**, 859– 869.

172. Israelachvili, J.N. Intermolecular and Surface Forces, Academic Press, Elsevier, London, 2011.

173. Timoshenko, S.P.; Goodier, J.N. Theory of Elasticity, 3rd Ed., McGraw-Hill, New York, 1970.

174. Fujita, M.; Yamaguchi, Y. Multiscale Simulation Method for Self-Organization of Nanoparticles in Dense Suspension, *J. Comput. Phys.* **2007**, 223, 108– 119.

175. Butt, H.-J.; Kappl, M. Surface and Interfacial Forces, Wiley VCH, 2009.

176. Hiemenz, P. C. Principles of Colloid and Surface Chemistry, Marcel Dekker, New York, 1997.

177. Kim, M.; Zydney, A.L. Effect of Electrostatic, Hydrodynamic, and Brownian Forces on Particle Trajectories and Sieving in Normal Flow Filtration. *J. Colloid Interface Sci.* **2004**, 269, 425– 431.

178. Denkov, N.D.; Kralchevsky, P.A. Colloid Structural Surface Forces in Thin Liquid Films, *Prog. Colloid Polymer Sci.* **1995**, 98, 18– 22.

179. Carnahan, N.F.; Starling, K.E. Equation of State for Nonattracting Rigid Spheres, *J. Chem. Phys.* **1969**, 51, 635– 637.

180. Timoshenko, S.P.; Goodier, J.N. Theory of Elasticity, McGraw-Hill, New York, 1970.

181. Kim, J.; Kim, J.; Bae, M.; Ha, K.; Kim, M.; Chu, M. Analysis of the dependence of the sound speed in a nano-particle suspension on the concentration of nano-paticles. *New Physics: Sae Mulli* **2017**, 67, 243– 247.

182. Rice H.P.; Fairweather M.; Hunter T.N.; Mahmoud B.; Biggs S.; Peakall J. Measuring particle concentration in multiphase pipe flow using acoustic backscatter: Generalization of the dual-frequency inversion method. *J. Acoust. Soc. America* **2014**, 136, 156– 169.

183. Piotrowska, A. Propagation of ultrasonic waves in suspensions and emulsions, 1. Investigation of emulsions and pigment suspensions by an acoustic method. *Ultrasonics* **1971**, 9, 14– 20.

184. Coker, A.K. Ludwig's applied process design for chemical and petrochemical plants, Gulf Professional Publishing, Houston, 2007.

185. Kaye, G.W.C. and Laby, T.H.. Tables of physical and chemical constants, Longmans Green and Co. Ltd., London, 1995.

186. O'Connor, J.J.; Robertson, E.F.; Laplace, P.-S. 1999. [online] Available at: http://www-groups.dcs.stand.ac.uk/~history/Biographies/Laplace.html [Accessed 5 Dec. 2018].

187. Fleming, P. Adiabatic compressibility, 2017. [online] Available at: https://chem.libretexts.org [Accessed 9 Dec. 2018].

188. Rice, H. P. Transport and deposition behaviour of model slurries in closed pipe flow, 2013, Ph.D. thesis, University of Leeds, Leeds, UK.

189. Ferrer, G.; Barreneche, C.; Solé, A.; Martorell, I.; Cabeza, L.F. New proposed methodology for specific heat capacity determination of materials for thermal energy storage (TES) by DSC. *Journal of Energy Storage* **2017**, 11, 1– 6.

190. Tian, Y.; Zhao, C.Y. A review of solar collectors and thermal energy storage in solar thermal applications. *Applied Energy* **2013**, 104, 538– 553.

191. Pfleger, N.; Bauer, T.; Martin, C.; Eck, M.; Wörner, A. Thermal energy storage – Overview and specific insight into nitrate salts for sensible and latent heat storage. *Beilstein J. Nanotechnology* **2015**, 6, 1487– 1497.

192. Bauer, T.; Laing, D.; Tamme, R. Overview of PCMs for concentrated solar power in the temperature range 200 to 350 °C. *Advances in Science and Technology* **2010**. 74, 272– 277.

193. Wu, Y.; Li, J.; Wang, M.; Wang, H.; Zhong, Y.; Zhao, Y.; Wei M.; Li. Y. Solar salt doped by MWCNTs as a promising high thermal conductivity material for CSP. *RSC Advances* **2018**, 8, 19251– 19260.

194. Dudda, B.; Shin, D. Effect of nanoparticle dispersion on specific heat capacity of a binary nitrate salt eutectic for concentrated solar power applications. *International Journal of Thermal Sciences* **2013**, 69**,** 37– 42.

195. Perry, R.H. Perry's chemical engineers' handbook. Seventh Edition. New York Mc Graw Hill; 1999.

196. Zavoico, A. B. Solar power tower design basis document. SAND2001-2100, Technical Report July, Sandia, National Laboratories, 2001.

197. Lu, M.C.; Huang, C.H. Specific heat capacity of molten salt-based alumina nanofluids. *Nanoscale Res Lett* **2013**, 8, 292– 299

198. Schuller, M.; Shao, Q.; Lalk, T. Experimental investigation of the specific heat of a nitrate–alumina nanofluid for solar thermal energy storage systems. *International Journal of Thermal Sciences* **2015**, 91, 142– 145.

199. Shin, D.; Tiznobaik, H.; Banerjee, D. Specific heat mechanism of molten salt nanofluids. *Applied Physics Letters* **2014**, 104, 121914.

200. Ho, M.X.; Pan, C. Optimal concentration of alumina nanoparticles in molten Hitec salt to maximize its specific heat capacity. *Int J Heat Mass Transfer* **2014**, 70, 174– 184.

201. Paul, T.C. Investigation of thermal performance of nanoparticle enhanced ionic liquids (NEILs) for solar collector applications, 2014, PhD thesis, University of South Carolina, USA.

202. Xuan, Y.; Roetzei, W. 2000. Conceptions for heat transfer correlation of nanofluids. *International Journal of Heat and Mass Transfer* **2000**, 43, 3701–3707.

203. Sekhar, Y.R.; Sharma, K.V. Study of viscosity and specific heat capacity characteristics of water-based Al_2O_3 nanofluids at low particle concentrations. *Journal of Experimental Nanoscience* **2013**, 10, 86– 102.

204. Vajjha, R. S.; Das, S, D. K. Specific heat measurement of three nanofluids and development of new correlations. *J Heat Transfer* **2009**, 131, 071601 (7 pages).

205. Kim, H.; Buongiorno, J'; Hu, L.W.; McKrell, T. Nanoparticle deposition effects on the minimum heat flux point and quench front speed during quenching in water based alumina nanofluids. *Int. J Heat Mass Transf.* **2010**, 53, 1542– 1553.

206. Nguyen, C.; Laplante1, G.; Cury, M.; Simon, G. Experimental investigation of impinging jet heat transfer and erosion effect using Al_2O_3-water nanofluid. *Inter. Conference on Fluid Mechanical and Aerodynamics* **2008**, 20– 22.

207. Maxwell, J. C. A Treatise on Electricity and Magnetism, 3rd Ed., Clarendon Press, Oxford, 1892.

208. Nan, C.W.; Birringer, R.; Clarke, D.R.; Gleiter, H. Effective Thermal Conductivity of Particulate Composites with Interfacial Thermal Resistance. *J. Appl. Phys.* **1997**, 81, 6692– 6699.

209. Feng, Y.; Yu, B.; Xu, P.; Zou, M. The effective thermal conductivity of nanofluids based on the nanolayer and the aggregation of nanoparticles. *J. Phys. D: Appl. Phys.* **2007**, 40, 3164– 3171.

210. Yu, W.; Choi, S.U.S. The Role of Interfacial Layers in the Enhanced Thermal Conductivity of Nanofluids: A Renovated Maxwell Model. *J. Nanopart. Res.* **2003**, 5, 167– 171.

211. Warrier, P.; Yuan, Y.; Beck, M.P.; Teja, A.S. Heat Transfer in Nanoparticle Suspensions: Modeling the Thermal Conductivity of Nanofluids; *AIChE J.* **2010**, 56, 3243– 3256.

212. Hamilton, R. L.; Crosser, O. K. Thermal Conductivity of Heterogeneous Two-Component Systems. *Ind. Eng. Chem. Fundam.* **1962**, 1, 182– 191.

213. Hojjat, M.; Etemad, S.G.; Bagheri, R.; Thibault, J. The Thermal Conductivity of Non- Newtonian Nanofluids, 8th World Congress of Chemical Engineering, Montreal, Canada, 2009.

214. Ramires, M.L.V.; Nieto de Castro, C.A.; Nagasaka, Y.; Nagashima, A.; Assael, M.J.; Wakeham, W.A. Standard Reference Data for the Thermal Conductivity of Water. *J. Phys. Chem. Ref. Data* **1995**, 24, 1377– 1382.

215. Touloukian, Y.S. Thermophysical Properties of High Temperature Solid Materials. Macmillan, New York, 1967.

216. Kell, G. S. Thermodynamic and Transport Properties of Fluid Water, in Water A Comprehensive Treatise, Vol. 1, F. Franks (Ed.), Plenum Press, New York, 1972; 363– 412.

217. Sridhara, V.; Satapathy, L.N. Effect of Nanoparticles on Thermal Properties Enhancement in Different Oils – A Review. *Critical Reviews in Solid State and Material Sciences* **2015**, 40, 399– 424.

218. Yopps, J. A.; Fuerstenau, D. W. The Zero Point of Charge of Alpha-Alumina, *J. Colloid. Sci.* **1964**, 19, 61– 71.

219. Singh, B.P; Menchavez, R.; Takai, C.; Fuji, M.; Takahashi, M. Stability of Dispersions of Colloidal Alumina Particles in Aqueous Suspensions. *J. Colloid Interface Sci.* **2005**, 291, 181– 186.

220. Kim, D. J.; Kim, H.; Lee, J. K. Dependence of the Rheological Behavior of Electrostatically Stabilized Alumina Slurries on pH and Solid Loading. *J. Mater. Sci.* **1998**, 33, 2931– 2935.

221. Lee, D. J.; Kim, W.; Kim, B. G. A New Parameter to Control Heat Transport in Nanofluids: Surface Charge State of the Particle in Suspension, *J. Phys. Chem. B* **2006**, 110, 4323– 4328.

222. Ganesan, V.; Louis, C.; Damodaran, S.P. Novel nanofluids based on magnetite nanoclusters and investigation on their cluster size-dependent thermal conductivity. *J. Phys. Chem. C* **2018**, 122, 6918– 6929.

223. Kwak K.; Kim, C. Viscosity and Thermal Conductivity of Copper Oxide Nanofluid Dispersed in Ethylene Glycol. *Korea-Aust. Rheol. J.* **2005**, 17, 35– 40.

224. Pang, C.; Lee, J.W.; Kang, Y.T. Enhanced Thermal Conductivity of Nanofluids by Nanoconvection and Percolation Network, *Heat Mass Transfer* **2016**, 52, 511– 520.

225. Lenert, A.; Wang, E.N. Optimization of nanofluid volumetric receivers for solar thermal energy conversion. *Sol. Energy* **2012**, 86, 253– 265.

226. Nguyen, C.; Galanis, N.; Polidori, G.; Fohanno, S.; Popa, C.; Bechec, A. An experimental study of a confined and submerged impinging jet heat transfer using Al2O3-water nanofluid. *Int. J. Therm. Sci.* **2009,** 48, 401– 411.

227. Mortimer, L.F.; Njobuenwu, D.O.; Fairweather, M. Near-wall dynamics of inertial particles in dilute turbulent channel flows. *Phys. Fluids* **2019**, 31, 063302.

228. Henry, C.; Minier, J.P.; Pozorski, J.; Lefèvre, G. A new stochastic approach for the simulation of agglomeration between colloidal particles. *Langmuir* **2013**, 29, 13694– 13707.

229. Arcen, B.; Tanière, A.; Oesterlé, B.; On the influence of near-wall forces in particle-laden channel flows, *Int. J. Multiphase Flow* **2006**, 32, 1326– 1339.

230. Marchioli, C.; Soldati, A.; Kuerten, J.; Arcen, B.; Taniere, A.; Goldensoph, G.; Squires, K.; Cargnelutti, M.; Portela, L. Statistics of particle dispersion in direct numerical simulations of wall-bounded turbulence: Results of an international collaborative benchmark test, *Int. J. Multiphase Flow* **2008**, 34, 879– 893.

231. Zhao, F.; George, W. K.; Van Wachem, B. Four-way coupled simulations of small particles in turbulent channel flow: The effects of particle shape and Stokes number, *Phys. Fluids* **2015**, 27, 083301.

232. Mortimer, L.F. Particle transport, interaction and agglomeration for nuclear reactor and nuclear waste flow applications, 2019, Ph.D. thesis, University of Leeds, Leeds, UK.

233. Marchioli, C.; Soldati, A. Mechanisms for particle transfer and segregation in a turbulent boundary layer. *J. Fluid Mech.* **2002**, 468, 283– 315.

234. Wen, D.; Zhang, L.; He, Y. Flow and migration of nanoparticle in a single channel. *Heat Mass Transfer* **2009**, 45, 1061– 1067.

235. Bux, J.; Peakall, J.; Rice, H.R.; Manga, M.S.; Biggs, S.; Hunter T.H. Measurement and density normalisation of acoustic attenuation and backscattering constants of arbitrary suspensions within the Rayleigh scattering regime. *Applied Acoustics* **2019**, 146, 9– 22.

APPENDIX-A: THE RATIO OF SPECIFIC HEATS

The model of O'Connor and Robertson[186] proposed by Fleming[187] is used to define the adiabatic compressibility, κ_s, of compression waves as:

$$\kappa_s = -\frac{1}{V}\left(\frac{\partial V}{\partial P}\right)_s \qquad 8\text{-}1$$

Since the entropy, *S*, is defined by:

$$dS = \frac{dq_{rev}}{T} \qquad 8\text{-}2$$

it follows that any adiabatic pathway (dq = 0) is also isentropic (dS = 0), or proceeds at constant entropy. Similarly, the isothermal compressibility, κ_T, can be found from:

$$\kappa_T = -\frac{1}{V}\left(\frac{\partial V}{\partial P}\right)_T. \qquad 8\text{-}3$$

The derivation of an expression for the speed of sound in which sound waves are modelled as adiabatic compression waves starts by expanding the description of κ_s using a type II partial derivative transformation, as suggested by Fleming[187]. By applying this to Eqn. (8-1), the adiabatic compressibility can be expressed as:

$$\kappa_s = \frac{1}{V}\left(\frac{\partial V}{\partial S}\right)_p \left(\frac{\partial S}{\partial P}\right)_v, \qquad 8\text{-}4$$

and if transformation type I is used such that:

$$\kappa_s = \frac{1}{V}\frac{\left(\frac{\partial S}{\partial P}\right)_v}{\left(\frac{\partial S}{\partial V}\right)_p}, \qquad 8\text{-}5$$

the partial derivatives can be expanded using the chain rule as follows:

$$\kappa_s = \frac{1}{V}\frac{\left(\frac{\partial S}{\partial T}\right)_v \left(\frac{\partial T}{\partial P}\right)_v}{\left(\frac{\partial S}{\partial T}\right)_p \left(\frac{\partial T}{\partial V}\right)_{vp}} \quad , \tag{8-6}$$

where

$$\left(\frac{\partial S}{\partial T}\right)_v = \frac{C_v}{T}, \tag{8-7}$$

$$\left(\frac{\partial S}{\partial T}\right)_p = \frac{C_p}{T}, \tag{8-8}$$

Accordingly, Eqn. (8-6) can be simplified to:

$$\kappa_s = \frac{C_v}{C_p}\left(\frac{1}{V}\frac{\left(\frac{\partial T}{\partial P}\right)_v}{\left(\frac{\partial T}{\partial V}\right)_{vp}}\right), \tag{8-9}$$

Further simplification yields:

$$\kappa_s = \frac{C_v}{C_p}\left(\frac{1}{V}\left(\frac{\partial T}{\partial P}\right)_v \left(\frac{\partial V}{\partial T}\right)_p\right), \tag{8-10}$$

$$\kappa_s = \frac{C_v}{C_p}\left(-\frac{1}{V}\left(\frac{\partial V}{\partial P}\right)_T\right), \tag{8-11}$$

And the final expression can now be expressed as:

$$\kappa_s = \frac{C_v}{C_p}\kappa_T \qquad 8\text{-}12$$

The ratio of heat capacities may now be written as $\gamma = C_p/C_v$ and after substituting the compressibility relations, Eqn. (8-1) for κ_s and Eqn. (8-3) for κ_T, into Eqn. (8-12) the following expression is obtained:

$$\gamma = \frac{C_p}{C_v} = \frac{\kappa_s}{\kappa_T} = \left(\frac{\partial V}{\partial P}\right)_s / \left(\frac{\partial V}{\partial P}\right)_T \qquad 8\text{-}13$$

It should be noted here that C_p is always larger than C_v. This ratio of heat capacities (also known as the isentropic index) is used in this study to convert the isothermal compressibility, κ_T, to the adiabatic compressibility, κ_s, which is derived from the propagation of sound compressing the fluid adiabatically. Consequently, the speed of sound in a fluid of density ρ can be expressed by the following relation[152]:

$$C = \left(\frac{\partial P}{\partial \rho}\right)_s^{1/2} = (\kappa_s \rho)^{1/2}. \qquad 8\text{-}14$$

Substituting this relation into Eqn. (8-13) gives:

$$\gamma = -\frac{C^2}{V^2}\left(\frac{\partial V}{\partial P}\right)_T, \qquad 8\text{-}15$$

According to Touloukian and Makita[152], the difference between C_p and C_v can be presented using the first and second laws of thermodynamics as:

$$C_p - C_v = T\left(\frac{\partial V}{\partial T}\right)_p \left(\frac{\partial P}{\partial T}\right)_v \qquad 8\text{-}16$$

$$C_p - C_v = -T\left(\frac{\partial V}{\partial T}\right)_p^2 / \left(\frac{\partial V}{\partial P}\right)_T \qquad 8\text{-}17$$

Therefore, the ratio of heat capacities can be derived from experimental values of the speed of sound together with a knowledge of P-V-T relations. Moreover, combining Eqn. (8-15) with Eqn. (8-16) or (8-17), the values of C_p and C_v may be written as:

$$C_v = \frac{T(\partial P/\partial T)_v^2 \, (\partial V/\partial P)_T}{(C^2/V^2) + (\partial P/\partial V)_T} \qquad 8\text{-}18$$

$$C_p = \frac{T(\partial P/\partial T)_v^2}{1 + (V^2/C^2)} \qquad 8\text{-}19$$

This method allows the indirect experimental determination of specific heats from speed of sound data and can be applied for gases, liquids[152] and suspensions.

APPENDIX-B: PROPAGATION OF EXPERIMENTAL ERRORS

There are three main sources of uncertainty in the directly measured quantities, as follows: the perpendicular distance of the probe, *h*, the oscilloscope peak-to-peak time resolution, *t*, and the temperature, *T*. The effect of these uncertainties on measurements of the speed of sound and thermal conductivity are assessed for representative example runs, and the total and relative contribution of the various uncertainties are compared and discussed.

The example for which errors have been quantified is a set of speed of sound runs with pure water over a temperature range of 25-90℃. Data from the 4MHz high-temperature probe mounted vertically were used. The total uncertainties in the acoustic system used for the speed of sound experimental measurements can be expressed as:

$$\underbrace{\left(\frac{dC}{|C|}\right)^2}_{\text{Total error in acoustic system}} = \underbrace{\left(\frac{dh}{h}\right)^2}_{\text{Probe distance and orientation}} + \underbrace{\left(\frac{dt}{t}\right)^2}_{\text{Oscilloscope peak}-\text{to}-\text{peak resolution}} \qquad 8\text{-}20$$

where dh is the uncertainty in the probe distance, dt is the oscilloscope peak-to-peak time resolution.

B.1 PROBE POSITION

The uncertainty in the measured probe distance consists of both an angular error h_1 and a linear error h_2, which can be expressed as:

$$(dh)^2 = (dh_1)^2 + (dh_2)^2. \qquad 8\text{-}21$$

The angular error h_1 may be caused by a slight mispositioning of the probe at a nominal measurement distance, h, with an acoustic beam divergence angle Θ radians, as illustrated in Figure 85. The maximum possible deviation in the position of the measurement point from the perpendicular distance from the probe along its axis is denoted as dh_1.

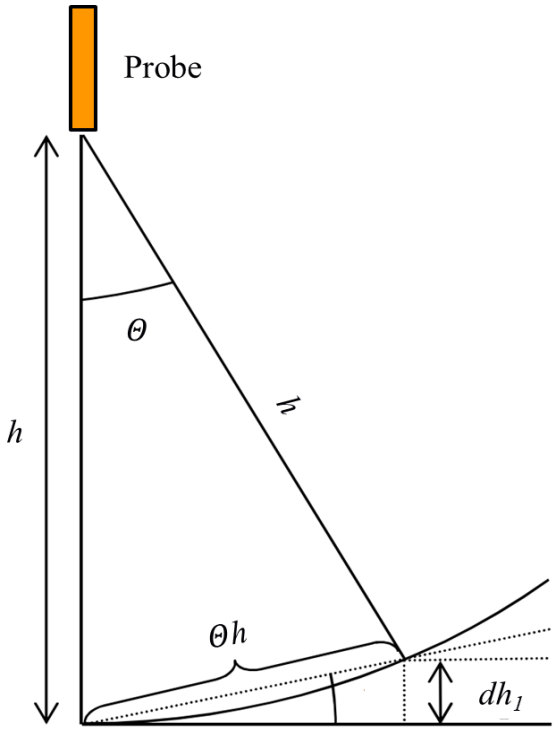

Figure 85. The maximum possible deviation in the position of the probe measured distance, *h*, from the perpendicular distance of the probe along its axis, resulting in an uncertainty denoted as dh_1, Θ is the probe divergence angle. [Adapted from[188]]

For the maximum angular error Θ to be approximated, the following expression can be used:

$$\cos\Theta \approx \frac{h}{h + dh_1} \qquad 8\text{-}22$$

and if the angular error is assumed to be $d\Theta$ = 1°, at h=100 mm, Eqn. (8-22) then gives:

$$100 + dh_1 = 100 / (\cos 1°) \Rightarrow dh_1 = \pm\ 0.15 \text{ mm}.$$

As to the linear error in the measured distance, that can be obtained directly from the height gauge standard uncertainty (given by the manufacturer), dh_2 = ± 0.07 mm. However, this is the resolution of the instrument, and not how precise it can be positioned in reality. To be more realistic, it has been estimated to be 0.1 mm.

Substituting the calculated values of dh_1 and dh_2 into Eqn. (8-21) results in a total uncertainty in the measured probe distance dh = ± 0.17mm.

B.2 PEAK-TO-PEAK TIME RESOLUTION

For the uncertainties in the peak-to-peak measurement due to the oscilloscope, example runs with pure water over the temperature range of 25-90℃ are again employed. The recorded variation in the time of flight, t, in these runs is used to make an estimation of the uncertainty in the speed of sound, assuming the maximum oscilloscope resolution to be dt = +/- 0.25 μs, as listed in Table 11.

Table 11. List of time resolution uncertainties over the temperature range of 25-90℃.

T [℃]	t [μs]	dt/t
25.00	141.40	0.00177
30.00	140.20	0.00178
35.00	139.20	0.00179
40.00	138.40	0.00180
45.00	137.80	0.00181
50.00	137.20	0.00182
55.00	136.80	0.00182
60.00	136.50	0.00183
65.00	136.20	0.00183
70.00	136.10	0.00183
75.00	136.10	0.00183
80.00	136.10	0.00183
85.00	136.40	0.00183
90.00	136.80	0.00182

B.3 TEMPERATURE

The speed of sound, *C*, is a function of temperature, *T*. The uncertainty in *C*, dC, is then expressed as:

$$dC = \left|\frac{\partial C}{\partial T}\right| dT. \qquad 8\text{-}23$$

As stated by Kaye and Laby[185], at T = 10, 20 and 30°C, C = 1447.28, 1482.36 and 1509.14 ms^{-1}, respectively, in distilled water. Using the values of C at T = 10 and 30°C, an estimate of $\partial C/\partial T$ may be made, as follows[188]:

$$\frac{dC}{dT} \approx \frac{C(T = 30°C) - C(T = 10°C)}{30 - 10} \qquad 8\text{-}24$$

Measurement uncertainty of the temperature sensor is provided by the manufacturer as, $T = \pm 0.1$°C that gives a value of $dC/dT \approx 3.10$ ms^{-1} K^{-1} at $T = 20$ °C (i.e. standard ambient temperature in the laboratory). This in turn gives $dC \approx 3.10 \times 0.1$, so dC/|C| = 0.31/1500 = 0.021%. It should be noted that this dC/dT value was chosen because the magnitude of the gradient is largest in this region, and so the error is also greatest. The error in the temperature was therefore neglected because it was found to be an order of magnitude smaller that the errors in the probe position.

B.4 SUMMARY OF UNCERTAINTIES

The nominal values of the probe distance, oscilloscope resolution and temperature, with corresponding uncertainties as estimated in the preceding sections, are summarized in Table 12.

Table 12. Summary of nominal values of measured quantities in the example run, with corresponding uncertainties. All the results are for 4 MHz high-temperature probe, used in the speed of sound run for pure water over a temperature range of 25-90°C.

Quantity	**Symbol**	**Nominal or mean value**	**Uncertainty**	
			Symbol	**Estimated value**
Probe distance	h	100 mm	dh	± 0.17mm
Time of flight	t	137 μs	dt	± 0.25 μs
Temperature	T	25°C	dT	± 0.1°C

Although the results are only presented for one example run with pure water, this run was chosen as being representative of other runs performed. The analysis that was presented in this section was applied to all other experimental runs described in this study. Although the magnitude of the errors varied slightly between runs, the trends presented in this appendix apply for all runs.

The uncertainty in the probe distance was found to produce the most significant error in the measurements. In addition, the angular error exceeds the linear error. The time resolution of the oscilloscope when finding the peak-to-peak distance was found to produce errors that were slightly lower in magnitude than those due to positioning of the probe. It was also found that the error due to temperature is generally negligible and less likely to influence the measurement by the acoustic system.